Study and realisation of micro/nano photovoltaic cells and their concentration systems

Florian Proise

École Doctorale 397

Thèse de doctorat

Spécialité : Physique et Chimie des Matériaux

présentée par

Florian Proise

pour obtenir le grade de

DOCTEUR DE L'UNIVERSITÉ PIERRE ET MARIE CURIE

Study and realisation of micro/nano photovoltaic cells and their concentration systems

---

Soutenue le 30 septembre 2014 devant le jury composé de :

M. Christian Seassal	INL	Rapporteur
M. Abdelilah Slaoui	Icube	Rapporteur
M. Gérard Aka	IRCP	Examinateur
M. Uwe Rau	Forschungszentrum Julïch	Examinateur
M. Jean-Jacques Greffet	LCFIO	Examinateur
M. Jean-François Guillemoles	IRDEP	Directeur de thèse
M. Jean-Luc Pelouard	LPN	Co-Directeur de thèse
M^{me} Anne-Laure Joudrier	IRDEP	Encadrante

École Doctorale 397

Thèse de doctorat

Spécialité : Physique et Chimie des Matériaux

présentée par

Florian Proise

pour obtenir le grade de

DOCTEUR DE L'UNIVERSITÉ PIERRE ET MARIE CURIE

Étude et réalisation de cellules photovoltaïques micrométrique / nanométriques et de leurs systèmes de concentration

---

Soutenue le 30 septembre 2014 devant le jury composé de :

M. Christian Seassal	INL	Rapporteur
M. Abdelilah Slaoui	Icube	Rapporteur
M. Gérard Aka	IRCP	Examinateur
M. Uwe Rau	Forschungszentrum Julïch	Examinateur
M. Jean-Jacques Greffet	LCFIO	Examinateur
M. Jean-François Guillemoles	IRDEP	Directeur de thèse
M. Jean-Luc Pelouard	LPN	Co-Directeur de thèse
M^{me} Anne-Laure Joudrier	IRDEP	Encadrante

Institut de Recherche et Développement sur l'Énergie Photovoltaïque
6, quai Watier
78 401 Chatou

École doctorale Physique et Chimie des Matériaux 397
4, place Jussieu
75 252 Paris cedex 05

Il arrivera nécessairement un jour où, faute de combustible, elle [l'industrie] sera bien forcée de revenir au travail des agents naturels. Que les dépôts de houille et de pétrole lui fournissent longtemps encore leur énorme puissance calorifique, nous n'en doutons pas. Mais ces dépôts s'épuiseront sans aucun doute : le bois qui, lui, cependant, se renouvelle n'est-il pas devenu plus rare qu'autrefois ? Pourquoi n'en serait-il pas de même un jour d'une provision de combustible où l'on puise si largement sans jamais combler les vides qui s'y forment ?[. . .] On ne peut s'empêcher de conclure qu'il est prudent et sage de ne pas s'endormir à cet égard sur une sécurité trompeuse
Augustin MOUCHOT, 1869

Acknowledgements

Un travail de thèse de trois ans, c'est un peu comme un oxymore : un travail d'équipe solitaire. Il est grand temps ici de remercier ceux sans qui ce travail n'aurait pas pu être mené comme il l'a été. Je souhaite remercier en premier lieu les membres de mon Jury qui ont eu la gentillesse d'avoir évalué mon travail. J'ai été honoré de leur présence et de leur enthousiasme à l'égard de ce travail. En particulier merci à Christian Seassal et Abdelilah Slaoui d'avoir accepté d'être rapporteur, et merci à Gérard Aka, Uwe Rau et Jean-Jacques Greffet d'avoir accepté d'être examinateur.

Cette formidable expérience n'a été possible que grâce à la confiance que m'ont accordé mes directeur et co-directeur de thèse Jean-François et Jean-Luc. Merci à vous deux pour m'avoir accueilli dans vos laboratoire respectifs et pour avoir accepté de travailler avec moi pendant trois ans. Merci Jean-François, pour toutes tes remarques / idées qui m'ont véritablement permis de progresser et d'approfondir mon travail. Je suis fier d'avoir produit ce travail de thèse sous ta supervision. Le rôle de Jean-Luc a été déterminant pour moi. Hormis sa connaissance très fines des dispositifs, ses points de vue / suggestions, tant sur l'interprétation de données expérimentales que sur la relecture d'article, de brevet et de présentations ont toujours été d'une très grande pertinence.

Cette thèse n'a pas été que supervisée, elle a aussi été encadrée par Anne-Laure. Je tiens à la remercier pour la grande disponibilité qu'elle a eu (même en vacances) et pour son aide qui m'a fait gagner un temps précieux. Je tiens aussi à remercier Daniel Lincot, directeur de l'IRDEP pour son enthousiasme communicatif et nos discussions très instructives. Mathieu Versavel aussi mérite d'être présent dans ces quelques lignes. Récent co-directeur de l'IRDEP, j'ai grandement apprécié son support et nos discussions. Merci aussi à Yves Schlumberger pour m'avoir accepté dans ce groupe.

Plus prosaïquement, je remercie le CNRS et EDF d'avoir financé mes trois ans de recherche : cela m'a permis d'assaisonner mes pâtes !

Ce travail étant très collaboratif, je remercie les laboratoires qui m'ont accueilli. Outre l'IRDEP, j'ai eu grand plaisir à travailler au Laboratoire de Photonique et Nanostructures, doté d'une superbe salle blanche. Je tiens à remercier aussi le Laboratoire de Génie Electrique de Paris et l'Institut Lavoisier de Versailles pour m'avoir ouvert leurs portes.

Derrière ces noms de laboratoires il y a des gens. Je remercie mes collègues de l'IRDEP, du LPN et d'ailleurs. Myriam pour son aide tout au long de ma thèse dont il serait trop long de faire la liste ici et aussi pour l'encadrement de mon stage. Toujours disponible, j'ai eu grand plaisir à travailler avec elle. Laurent L. pour son aide précieuse sur les mesures de luminescence et son accent du Sud. Toujours en luminescence, merci à Gilbert et Daniel pour

leur aide en TRPL. Christophe et Nathalie, les magiciens de la salle blanche. Non seulement très compétents, ils m'ont permis de travailler en salle blanche dans une excellente ambiance. Tant que je suis en salle blanche je continue sur ma lancée. Je remercie Nicolas P.-L. mon deuxième mentor technologique après Christophe, qui m'a appris cette formidable leçon : « Tu dois rincer au moins autant de temps qu'a duré la réaction chimique ». Stéphane G. pour la gravure sèche, Laurence pour m'avoir formé sur la RIE, Stephan pour les images MEB, Andrea pour ses conseils divers, Nicolas V. pour son extrême gentillesse, ses dépannages fort utiles et pour m'avoir permis de comparer mon code avec Reticolo. Je ne veux pas oublier tous les autres membres du LPN en Salle blanche qui m'ont ponctuellement aidé, comme débugger une tournette ou trouver de la verrerie.

La partie simulation a été importante pour moi. Je remercie donc Eric pour sa connaissance du Monte Carlo, Gary pour l'optimisation du code, Clément et Inès pour nos interprétations (parfois fumeuses) de tel ou tel mécanisme de résonance, et bien sûr Fabrice, sans qui je n'aurais pas pu modéliser les nanorésonateurs.

La fabrication de concentrateur luminescent et de micro cellules est le fruit du travail de nombreuses personnes. Merci à Fred et Marie pour la fourniture du CIGS (et pour les soirées coinches !), merci à Valérie et Laurent M. pour le CdS, Gilles et Benoit pour le ZnO. Merci à Tarik pour ses connaissances approfondies de l'emplacement de la verrerie, de son aide en chimie et au polissage. La mesure des échantillons a souvent été faite par Enrique. Merci à lui pour sa disponibilité à toute épreuve.

Je remercie aussi José pour m'avoir formé sur l'AFM-CP et m'avoir grandement aidé à faire des mesures. Côté passivation, je remercie Christian et Anne-Marie pour le polyphosphazène et cette superbe collaboration. Merci à Claire et Mireille pour leur aide administrative plus que nécessaire.

Il y a aussi les collègues avec qui on ne travaille pas directement, mais qui font que cette expérience fut si agréable. Merci à Hugo pour avoir supporté mes chansonnettes et autres imitations de sonneries en tout genre, Julien pour ses points de vue très intéressants et son pouvoir d'animation. Merci au triumvirat, Amaury, Jorge et Torben. Que de bons souvenirs, que ce soit au labo, à Berlin, à Barcelone ou pendant nos nombreuses soirées. Ils ont très fortement contribué au plaisir que j'ai eu à faire cette thèse. Merci aux deux Sébastien pour nos discussions sur Skype entre 21h et 23h, loots à D3 et carrying/support à LOL.

Je remercie aussi Rémy et Winny, mes deux stagiaires. J'ai pris beaucoup de plaisir à travailler avec eux.

En vrac, je remercie les autres membres de l'IRDEP et du LPN : Alexandre, Sophie, Cathy, Aurélien, Negar, Serena, Thibault, Corentin, Stéphane C., Benoit B., Grégory, Emilie, Jean R. (bis), Alain, Nicolas L., Sana, Romain et Lorraine. J'ai toujours pris plaisir à discuter avec vous.

Merci à mon club de Karaté, qui pendant les deux premières années de thèse m'a permis de ne pas grossir et d'obtenir la fameuse ceinture noire. Je remercie très sincèrement l'autoradio de ma voiture qui a rendu moins longs les bouchons au retour de Marcoussis, WordReference et Linguee pour leurs traductions, parfois hasardeuses.

La famille et les amis « de l'extérieur » ont aussi été déterminants. Je remercie Aurélie pour m'avoir supporté, m'écouté parler de ma thèse, et m'avoir permis de passer de super moments, que ce soit dans notre belle Capitale ou en vacances. Merci à mes parents qui m'ont toujours soutenu (et même hébergé !), et plus généralement ma famille, oncles et tantes, cousins et cousines... Merci à Léo et Brice, indéfectibles soutiens depuis plus de 13 ans ! Merci à mon petit Chesnel, à qui je dois mon entrée à Normale Sup en me convaincant de faire 5/2. Que de superbes souvenir, que ce soit en colle, à Morzine, en Andalousie ou à Cherbourg. Je souhaite remercier aussi toutes les autres personnes que j'ai pu côtoyer pendant ma thèse.

Merci enfin à ceux qui m'ont fait la gentillesse d'être présents à ma thèse.

Abbreviations and acronyms list

- α_i (cm^{-1}): Absorption coefficient (i=matrix or dye)
- A: Dye absorbance
- $\mathcal{A}_e$ (cm): Luminescent solar concentrator edge area
- $\mathcal{A}_f$ (cm): Luminescent solar concentrator front area
- d (cm): photon traveled distance
- $\overline{d}$ (cm): mean traveled distance per photon
- $\overline{d}_{PV}$ (cm): Mean distance required to be collected
- dz (cm): LSC thickness
- c: Speed of light ($\approx 3.10^8$ m.s^{-1})
- c_{max} / C_{max}: Maximum internal / total concentration factor
- C: Concentration factor
- C_{geo}: Geometrical gain (or geometrical concentration factor)
- ΔE (eV): Dye Stokes shift
- η (%): Power conversion efficiency
- η_{opt} (%): Optical efficiency
- ξ: Random number with uniform distribution in the interval $]0\,1[$
- e: Emission coefficient
- E (eV): Photon energy
- E_c (eV): Conduction band edge
- E_f (eV): Fermi level
- E_g (eV): Energy bandgap
- E_v (eV): Valence band edge
- f: Coverage fraction
- FF (%): Fill Factor

- $\mathcal{G}_{coll.}$ (%): Collected photons
- h: Planck constant ($\approx 6.63.10^{-34}$ J.s)
- $\overline{hit}_{f,b}$: Mean front,back absorption event, per photon
- J_0 (mA.cm^{-2}): Saturation current density (or dark current density)
- J_{00} (mA.cm^{-2}): Reference current density
- J_{sc} (mA.cm^{-2}): Short-circuit current density.
- k (J/K): Boltzmann constant
- λ (nm): Wavelength
- $\mathcal{L}_i$ (%): Loss channels (i= Ext., Front, Back, mat., QY, side)
- n: Refractive index or diode ideality factor
- $\bar{n}_{\text{abs}}^{\text{dye}}$: mean dye absorption events per photon
- ν (s^{-1}): Photon frequency
- p (nm): Period
- ρ ($C.cm^{-3}$) : Charge density
- φ (rad or °): Azimuth angle
- Φ_{bb} (s^{-1}): Spectral photon density of a black body
- P_{max} (W.cm^{-2}): Maximum power density generated by a solar cell
- P_{tot} (W.cm^{-2}): Total power density received by a solar cell
- $\mathcal{P}_{em}$ Emission probability distribution function
- q (C): Elementary charge
- R_i: Reflection coefficient (i=Fresnel, PBS or back)
- S (J.K^{-1}): Entropy
- θ (rad or °): Polar angle
- θ_{acc} (rad or °): Acceptance angle
- θ_c (rad or °): Critical angle
- T (K): Temperature
- T: Transmission coefficient
- t_{mean} (nm): Mean thickness
- V_{app} (V): External applied potential
- V_{bi} (V): Built-in potential

- V_{oc} (V): Open-circuit voltage
- $\widetilde{V}_{oc}$: Normalized open cicruit voltage
- w (nm): Width
- AIBN: azobisisobutyronitrile (PMMA initiator)
- AM1.5: Air Mass 1.5
- ARC: Anti-Reflection Coating
- CIGS: Cu(In,Ga)Se_2-based solar cell
- CPV: Concentrated photovoltaics
- (H/M/L)CPV: (High/Medium/Low) Concentrated photovoltaics
- CW-PL: Constant Wave PhotoLuminescence
- EDX: Energy-dispersive X-ray spectroscopy
- FDTD: Finite-Difference Time-Domain
- I/O: Input/Output
- ICP: Inductively Coupled Plasma
- IEA: International Energy Agency
- LSC: Luminescent Solar Concentrator
- MBEO: Mean Basic Event Occurrence
- MIBK: Methyl isobutyl ketone
- MRCD: Mono-Resonant Concentration Device
- PBS: Photonic Band Stop
- PC: Photonic crystal
- (PL)QY: (PhotoLuminescent) Quantum Yield
- PMMA: Poly methyl methacrylate
- PV: PhotoVoltaic
- QD: Quantum dot
- R305: Lumogen® Red 305 dye
- RMCA: Rigorous Maxwell Constitutive Approximation
- SCR: Space Charge Region
- SEM: Scanning Electron Microscope
- SRH: Shockley Read Hall

- TEOS: TetraEthyl OrthoSilicate
- TIR: Total Internal Reflection
- TR-PL: Time-Resolved PhotoLuminescence
- XPS: X-Ray photo-electron spectrometry

Contents

General introduction

Although considered as a "new energy", photovoltaics history started in the 1800s and, strangely, is intimately associated to Paris. In this city, Volta presented to Napoleon in 1800 the first electrochemical battery. 39 years later, Edmond Becquerel discovered the photovoltaic effect [1]. Still in Paris, the world first demonstration of solar energy was carried out in 1860s by Augustin Mouchot and one century later in 1973, the first conference on the Sun as an energy source was held. Almost unknown to the general public twenty years ago, photovoltaics has become a key player in the world energy landscape.
Photovoltaics has won the economic battle against some energy sources in sunny parts of the world and gains ground day after day. Citizens, local, regional and central governments begin to take over this energy. Yet uncertainties remain and efforts must be made to improve efficiency, cost, sustainability and social acceptance.

Among explored solutions, light concentration on photovoltaic cells has the potential to combine a better efficiency, a lower cost and a better sustainability. By its very nature, photovoltaic cells working under light concentration are small. Even more, the smaller the better. In this context, this thesis studies the possibility to concentrate light on photovoltaic cells no larger than few hundreds of micrometers. The unique character of this thesis is double. We endeavour to couple two photovoltaic domains: micro-cells and luminescent solar concentrator. On the other hand, we push the miniaturization logic to its limits designing a novel photovoltaic concept which lies between luminescent solar concentrators and nanophotonics.

This thesis is organized in two parts and six chapters. Chapter 1 sets the scene and replaces this work in a general context. Energy and photovoltaics pictures are given. Focusing on photovoltaics, general operating principle is exposed and light concentration techniques are reviewed.

Part 1 comprises chapters 2, 3 and 4. It is dedicated to the study of LSC and microcells. Chapter 2 focuses on the luminescent solar concentrator basis and present the code I have fully developed. Chapter 3 aims at grasping the physics of luminescent solar concentrators by modeling and analyzing them with the algorithm detailed in the previous chapter. Finally, chapter 4 is an experimental contribution dealing with the coupling between microcells array and luminescent solar concentrator. Part 1 underlines, among others, the potential interests of having photovoltaic devices exhibiting light absorption cross-section larger than their metallurgical areas. Part 2 studies this possibility by miniaturizing.

Part 2 comprises chapters 5 and 6. It is devoted to the design of a novel photovoltaic device taking advantage of light properties at the sub-wavelength scale to fabricate nano-antenna. Chapter 5 explores the advantages that can be derived from the luminescent solar concentrators and nano-antenna coupling. Then a review of light absorption strategies is done to motivate

our choice of using a Metal-Insulator-Metal nano-antenna. Chapter 6 exposes how the device design is done. Then fabrication and experimental characterizations will be shown.

This transverse work reflects the results of collaborations among four laboratories. I would like to precise what has been my contribution from theirs. I have spent around two third of my time at the Institut de Recherche et Développement sur l'Energie Photovoltaïque (IRDEP) and one third at the Laboratoire de Photonique et de Nanostructures (LPN). Occasionally, I have been at Institut Lavoisier de Versailles (ILV) and Laboratoire de Génie Electrique de Paris (LGEP).

Concerning part 1, the study was almost entirely held at IRDEP. I have done all the theoretical work by myself. Luminescent solar concentrators being a novel activity at IRDEP, I have developed and exploited the modeling algorithm by myself. Experimentally, I have fabricated the luminescent solar concentrator but I have received substantial help for the microcells fabrication. The process have been developed by a former PhD student and the deposition of Mo / CIGS / CdS / ZnO:i / ZnO:Al has been done by colleagues from IRDEP laboratory platform. I have done the micro-structuring lithography whereas dielectric/metal deposition has been done by co-workers either at IRDEP and LPN. Luminescent solar concentrator and microcell coupling with resist pillars was done only partly by myself. Pillars lithography and buffer layer development/optimization was carried out by IRDEP co-worker, as well as opal photonic filters fabrication.

Part 2 crystallized most of the collaborations. Modeling algorithm has been developed by LPN co-workers. I have only added some secondary features (such as parallelization or code coupling). I have done all the nano-antenna design. I have devoted a large amount of time to the nano-antenna fabrication in clean-room. I have been trained by LPN colleagues, and became independent on most of the sample process steps. Yet epitaxy and electronic lithography has been performed by LPN co-workers. SEM images have been produced both by LPN and IRDEP co-workers. ILV collaboration has dealt with InP passivation. I have only done constant wave photoluminescence measurements. Time-resolved photoluminescence was done by IRDEP colleagues. Finally, AFM-based electric characterization was held at LGEP. They have done some measurements but they have trained me on AFM, consequently I managed to do majority of measurements.

Chapter 1

Photovoltaics, one answer to energy challenge

Contents

1.1 Energy issues

This PhD thesis, devoted to photovoltaics, falls within an unprecedented energy context. Our current energy mix is questioned, energy sources choice is debated in numerous countries, between fossil energy (oil, natural gas, shale gas, nuclear power) and renewable energy (biomass, hydro, wind-power, photovoltaics...). Under the current circumstances, Science must be involved to provide a better understanding of these different technologies, but also to improve existing technologies in order to give different viable energy alternatives, with their pro and cons. Thus, with a deep knowledge of all different technologies, policy makers and individual citizens may choose an appropriate energy mix in term of cost, environmental damage and local criteria.

My work seems to be far from this preoccupation, especially because I deal with new concepts far from industrialization, but this context was a motivation source for me. That is why I begin this introduction by few lines about our fascinating energy situation.

Seventies' has been the decade from which, for the first time, energy crisis shook our certainties. The first oil crisis happened in 1973 and one of its consequences, in addition of recession, was the nagging question: "What if our abundant and cheap oil-based energy sources may be possibly depleted in a near future?". Since a scarcer resource leads to more expensive prices and economic concerns drive our modern societies, all the conditions were meet together to look for alternative energies. The dynamics was created and the first European R&D program on renewable energy was launched in 1975.

1.1.1 Current situation

Earth average temperature has risen of 0.85 °C compared to pre-industrial period. In its latest report [2], the Intergovernmental Panel on Climate Change evaluates that its anthropogenic origin is 95% probable. To limit the temperature rise to +2°C in 2100 (which will be already huge of consequence), the worldwide green-house effect gases emission must drop of 40-70 % in 2050 with almost 0 emission in 2100. This requires a real paradigm shift and a total mutation of our energy systems. In that context, the need of alternative energy source becomes obvious and renewable energies are one of the keys to succeed. Research in the field of renewable energy is not luxury, it is a contribution to the huge challenge the world must address.

Before giving trends or projections, I would like to mention some key facts in the energy landscape. In 2012, more than 25 PWh (10^{15} Wh) of electricity have been produced worldwide, of which 20.8% comes from renewable sources [3] (143.7 TWh for non hydro-renewable source against 4556 TWh for hydro). Between 2000 and 2013, renewable energy achievements are tremendous, as shown in table 1.1:

Wind, PV, bio-power achievements		
	Power capacity (GW)	New jobs (million)
World	510 (47)	5.7
Europe	213 (11)	1.2
Germany	75 (0)	0.38

Table 1.1: Achievements of some renewable energy source in 2013. Numbers in brackets are for year 2000 [4]

The renewable energy perspectives are also bright. According to the International Energy Agency (IEA), renewable electricity production will be increased of 40 % from 2012 to 2018, with a symbolic step in 2016: IEA 2016 projections forecast that renewable electricity production will exceed gas-fired electricity generation and will be two time higher than nuclear production.

1.1.2 PV in the electricity mix

The first significant impulse on photovoltaic research was given by a UNESCO congress in 1973 in Paris titled "Le Soleil au service de l'Homme" (The Sun in The Service of Mankind). This congress has been the recognition of pressing energy problem on human scale (because of global climate change and limits of fossil resources) as well as an increase of political concerns

for national energy independence, the sun being available everywhere. After around 30 years of R&D, PV begins to appear in the energy statistics and was not limited to off-grid application. The PV evolution since 2000 to 2013 is shown below:

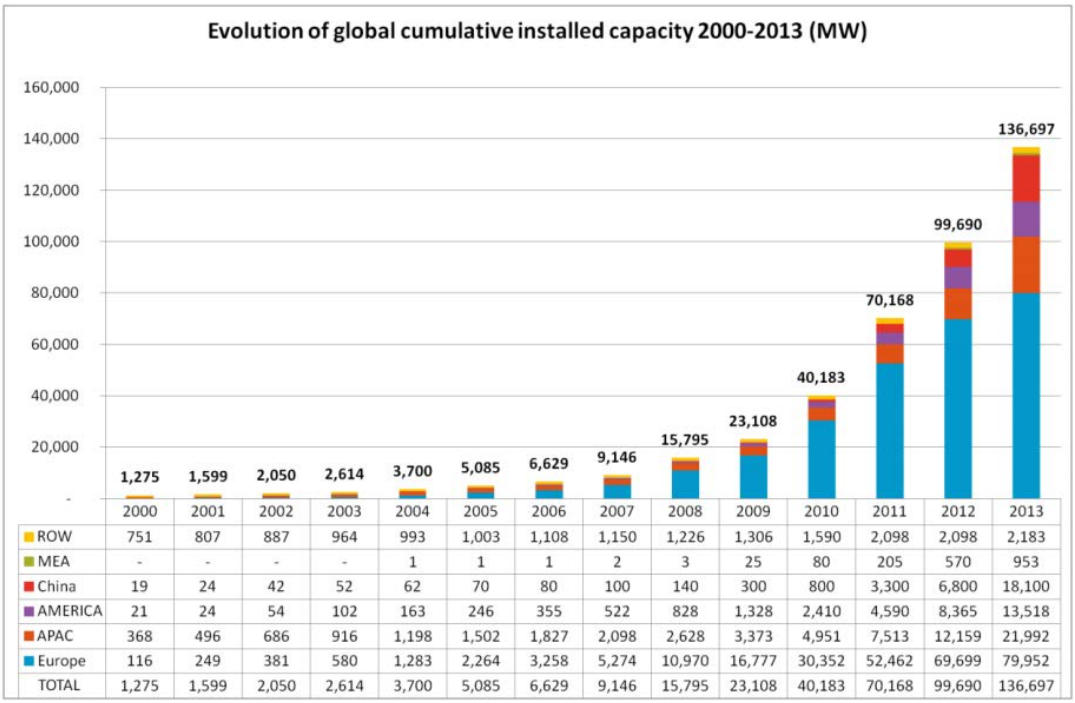

	2000	2001	2002	2003	2004	2005	2006	2007	2008	2009	2010	2011	2012	2013
ROW	751	807	887	964	993	1,003	1,108	1,150	1,226	1,306	1,590	2,098	2,098	2,183
MEA	-	-	-	-	1	1	1	2	3	25	80	205	570	953
China	19	24	42	52	62	70	80	100	140	300	800	3,300	6,800	18,100
AMERICA	21	24	54	102	163	246	355	522	828	1,328	2,410	4,590	8,365	13,518
APAC	368	496	686	916	1,198	1,502	1,827	2,098	2,628	3,373	4,951	7,513	12,159	21,992
Europe	116	249	381	580	1,283	2,264	3,258	5,274	10,970	16,777	30,352	52,462	69,699	79,952
TOTAL	1,275	1,599	2,050	2,614	3,700	5,085	6,629	9,146	15,795	23,108	40,183	70,168	99,690	136,697

Figure 1.1: Evolution of global PV cumulative installed capacity 2000-2013 (MW) [5]

PV reaches 136.7 GW installed power (1.4 GW in 2000) worldwide, among them 80 are in Europe (less than 0.1 GW in 2000). This success has not been anticipated at all, as illustrated by these citations about 2010 PV production:

- "The official installed target scenario for 2010 [..] represents a global forecast of 11.3 GW." [1]
- "By 2010, installed solar power capacity would be 500 MW resulting in power generation of 0.7 TWh." [2]
- "Solar cell/module manufacturing to rapidly increase from 4 GW in 2007 to 13.35GW in 2010." [3]

The reality is that in 2010 PV reached 40 GW. Yet these global key facts mask the huge inhomogeneity of the solar production worldwide. Until 2012, more than half of the PV production was located in Europe, which is changing now with the arrival of new players such as China.

When PV production is compared with the global electricity production, it may seem rather low. Nevertheless symbolic steps have been achieved recently. In France, more than 1% of

1. Solar Electricity in 2010, Installed Target Scenarios by EPIA published in 1995
2. IEA World Energy Outlook, published in 1998
3. Solar Annual 2007, Micheal Rogol, Photon Consulting

the electricity consumption was provided by PV in 2013. In Germany, May, 25th 2012 was the record day with more than 22 GW peak PV power production, leading to around 14 % (190 GWh) of the total electricity consumption in Germany this day [6].

Now, the PV industry enters a restructuring period: many firms collapsed, unstable feed-in tariff and so on. According executive director of the IEA, the PV future is based on two levers:

- Cost drop
- Technology diffusion

In a context of cost reduction, many strategies are studied, among them light concentration. This thesis falls within this problematic with a specificity: the low PV size (from micro to nano meter scale). Before getting to the heart of the subject, a very short description of PV technology is needed.

1.2 Photovoltaics: from principles to technology

1.2.1 PV basic principles

Photovoltaic cell is one of the few energy sources which does not require a turbine to produce electricity. This tour de force originates from the direct conversion of solar (photon) energy to electricity. Basically three steps are required:

1. Photon absorption and electron-hole pair creation
2. Charge carriers separation
3. Charge carriers collection in the external circuit

To fulfill these 3 steps, ideally a solar cell must have the following features:

- All the incident light must be absorbed by the solar cell (point 1)
- Each absorbed photon generates one electron-hole pair (point 1)
- Charges must be separated to avoid recombination (point 2)
- Charges must be collected in the external circuit without loss in the contact (point 3)

These requirements are explained in more details in the next sections.

1.2.1.1 Photo-carriers generation

In a solar cell, the layer dedicated to the photon absorption is called the absorber layer, and is always a semiconductor for inorganic photovoltaic devices. A semiconductor has the same energy diagram than a dielectric except that its bandgap (E_g) is smaller (between 0.5 and 2.5 eV). If enough energy is supplied to the semiconductor (i.e. higher than the bandgap), an electron of the valance band may be promoted to the conduction band. This surplus of energy is supplied in the case of a photovoltaic cell by the sunlight. Each photon carries an energy $E = \frac{h \times c}{\lambda}$($h$ is the Planck's constant, c the velocity of light and λ the wavelength) which may be lower, equals or higher than the bandgap. This is represented in fig. 1.2

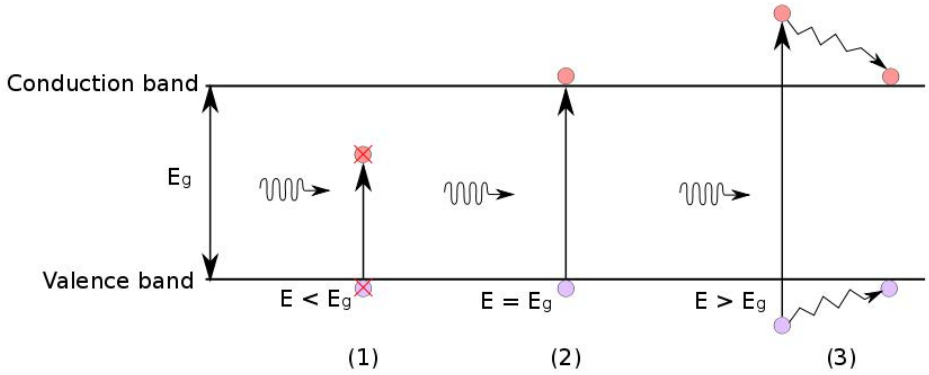

Figure 1.2: Photon absorption in a semiconductor. (1) photon energy is lower than E_g. No electron-hole pair is created and the photon is not absorbed. (2) photon energy matches E_g. An electron-hole pair is created. (3) photon energy is greater than the bandgap. Electron hole pair is created but the excess energy is lost by thermalization

A low energy photon (compared to E_g) (case (1)) is lost for the PV cell because non absorbed, whereas a high energy photon may create an electron-hole pair with an excess of energy. Indeed, an electron which was initially bond to the semiconductor crystal is freed by the energy brought by the photon (passing from valence to conduction band). If the excited electron has a greater energy than the band gap (case (3)), the excess energy in the form of kinetic energy is dissipated by electron-crystal multiple collisions creating phonons. It lasts until the thermodynamic equilibrium is reached, which corresponds to the charge carriers reaching the valence (hole) / conduction (electron) band edges. The thermalization process has a duration around 1 ps, which makes it much faster than the electron-hole pair separation (see next section). Consequently a photon of higher energy will be considered to create an electron-hole pair of the bandgap energy, assuming a fully thermalization process has occurred.

Thus, the photo-carriers generation relies only on two conditions. The first one has been detailed above, the photon must have an energy equals or higher than the bandgap. The second condition seems trivial: the photon must be able to reach to semiconductor layer, which means it should not be reflected or absorbed in another layer. After being absorbed in the semiconductor and allowing the generation of electron-hole pair, the charge carriers must be separated.

1.2.1.2 Charge carrier separation

After creating an electron-hole pair, its recombination must be avoided at all cost. Separating the charge is therefore of the greatest importance. Because this manuscript deals only with inorganic PV, we will mention only one mean of separating the charge: the pn junction.

The pn junction (or diode) consists in putting a n-doped together with a p-doped semiconductor. The doping asymmetry leads to charge diffusion close to the metallurgical junction creating a space charge region (SCR). The charge density ρ is not equal to zero in the SCR. We assume shallow doping and abrupt junction (fig. 1.3a). Solving Poisson equation, the electric field becomes non zero (fig. 1.3b). Consequently it gives rise to a potential, called built-in potential (V_{bi}) (fig. 1.3c). Therefore, an energy barrier is created along the pn junction (fig. 1.3d). The barrier height can be modulated by an external applied potential (V_{app}). When an electron-hole pair is generated in the SCR, electron flows toward the n-region whereas holes heads toward the p-region: the charges have been separated. A complete theoretical derivation of the pn junction can be found in [7]. The pn junction is one way to separates charges but others strategies may be applied. Among them, we can cite a structure in which there is no pn junction but selective contacts.

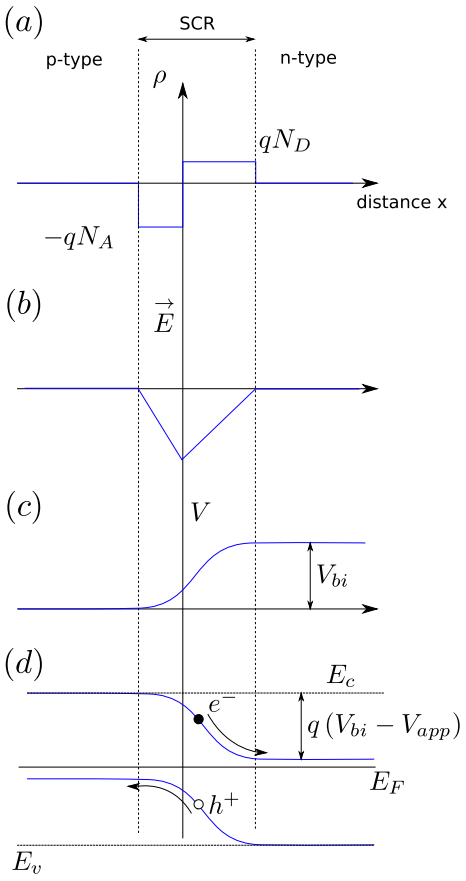

Figure 1.3: pn junction scheme.

A way of separating charges is essential. Yet charges need to be collected by electrodes.

1.2.1.3 Charge collection

On their way to be collected to the electronic contacts, separation is important but still, recombination process may occur. The three main recombination mechanisms are given below:

Radiative recombination: An electron in the conduction band recombines with a hole in the valence band (band-to-band recombination), producing a photon with an energy equals to the bandgap. This mechanism is the inverse of the generation mechanism explained in section 1.2.1.1 and cannot be avoided. [8] gives a model to calculate radiative recombination.

Defect-assisted recombination: The presence of a defect state (due to impurity for example) in the bandgap may ease recombination in lowering the energy required. The defect acts as a charge trap. This type of recombination is called Shockley Read Hall (SRH) [9, 10] and produces heat. Two SRH contributions can be highlighted: bulk and surface. Bulk SRH occur when the semiconductor crystal is not defect-free and therefore reducing it implies to improve the material quality. Besides, semiconductor surfaces (or interfaces) are, by nature, high density defect areas and consequently SRH may be enhanced.

Auger recombination: When Auger recombination occurs, electron and hole recombine and emit energy neither in the form of light or heat, but transfer it to a third electron. The energy

excess of this electron is then lost by thermalization. From this description, it is straightforward that the higher is the doping, the higher is the Auger recombination probability. A quite recent description of Auger recombination can be found in [11].

These recombination mechanisms are general and co-exist (with different amplitudes) in all solar cells. More specifically, it will be seen in chapter 6 that since we are doing nano-structured devices, surface SRH may be a big issue (the ratio Surface/Volume being really high). One strategy to limit surface recombination (surface passivation) will be exposed.

1.2.1.4 Efficiency

The three main operating steps of a PV cell described above are quantified by the efficiency (η) of the cell. It is defined as the ratio between the maximum operating power and the total power. To be able to compare solar cell, a standard defines the reference solar spectrum (light intensity, temperature, humidity, molecules concentration in air and so on) . For terrestrial application the AM1.5G, normalized to 1000 W.cm^{-2} is used. It can be found in [12] as well as its precise definition. It means that P_{tot} in eq. (1.1) worth 1000 W.cm^{-2}

$$\eta = \frac{P_{max}}{P_{tot}} = \frac{(V \times J)_{max}}{P_{tot}} = \frac{V_{oc} \times J_{sc} \times FF}{P_{tot}} \tag{1.1}$$

The maximum operating power can be described by the open-circuit voltage V_{oc}, the short-circuit current J_{sc} and the fill factor FF. They can be defined graphically:

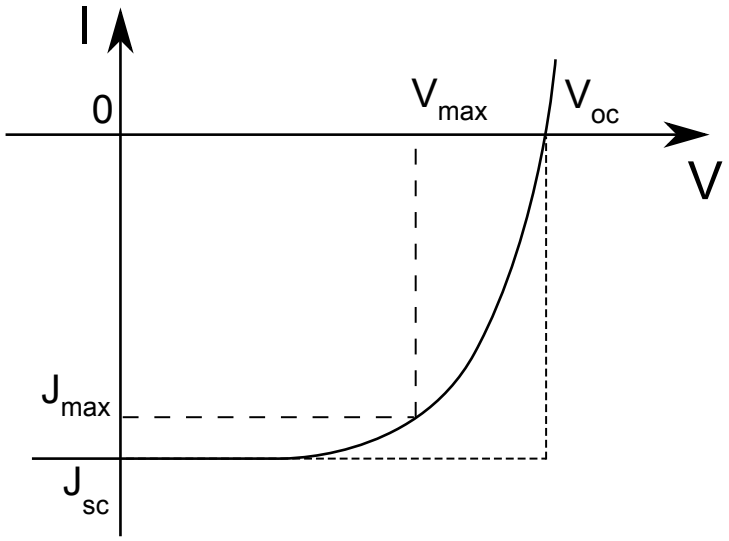

Figure 1.4: Current-Voltage plot of an illuminated solar cell. The fill factor FF quantify the square shape of the plot and worth $\frac{V_{max}J_{max}}{V_{oc}J_{sc}}$

Light concentration on PV cell has the potential to increase the solar cell performance, therefore its influence must appear in the efficiency expression. Sticking to the fact, a solar cell working under concentration at a concentration factor C experiences an higher short-circuit current and receive an higher total power. These two terms vary linearly with C. Consequently, the gain in J_{sc} is not directly responsible of efficiency gain because it cancels out with the total power. The benefit of concentration on the cell efficiency is mainly due to V_{oc}.

V_{oc} can be expressed by setting the net current to 0. Neglecting parasitic resistance, we have:

$$0 = J_0 \left(e^{\frac{q.V_{oc}}{n.k.T}} - 1 \right) + J_{sc} \cdot C \tag{1.2}$$

With q the elementary charge, k the Boltzmann constant, T the temperature, n the ideality factor and J_0 the dark current density. We can re-write J_0 in $J_0 = J_{00} e^{-\frac{E_g}{n.k.T}}$ with E_g the solar cell bandgap and J_{00} a pre-factor (reference current density). When $e^{\frac{q.V_{oc}}{n.k.T}} >> 1$, eq. (1.2) simplifies in:

$$V_{oc} = \frac{n.k.T}{q} ln \left(\frac{J_{sc} \cdot C}{J_0} \right) = \frac{E_g}{q} + \frac{n.k.T}{q} \left(ln(C) + ln \left(\frac{J_{sc}}{J_{00}} \right) \right) = V_{oc}(C=0) + \frac{n.k.T}{q} ln(C) \tag{1.3}$$

Light concentration leads to V_{oc} increase of $25 \cdot n \cdot ln(C)$ meV. Interestingly the higher is the ideality factor, the higher is the concentration benefit. As an example if $C = 100$ and $n = 2$, V_{oc} increases by 240 mV. In addition, the fill factor is also dependent on V_{oc}, as shown by the following equation [13]

$$FF = \frac{\widetilde{V}_{oc} - ln(\widetilde{V}_{oc} + 0.72)}{\widetilde{V}_{oc} + 1}, \text{ with } \widetilde{V}_{oc} = \frac{q}{n.k.T} V_{oc} \tag{1.4}$$

This function is an increasing function of V_{oc} which strengthens concentration positive influence on the efficiency.

1.2.2 PV technologies

Now that PV cell functioning has been reviewed, a brief description of the main PV technologies will be given to highlight the PV landscape and look at how this thesis work fits in.

PV technologies are traditionally divided in 3 generations. The first one consists in single-crystal silicone (c-Si) solar cell. This technology produces high quality material with few defects, enabling to get high conversion efficiency. The other side of the coin is that fabrication process uses energy and time intensive techniques.

The second generation, known as thin-film technologies, aims at reducing process costs with fabrication techniques using less energy and being less time consuming. Doing thin-film enables to use less expensive material and deposit the material in less time than for a thick c-Si cell. Certain thin-film photovoltaic cells can be fabricated with non vacuum techniques, which greatly reduces their costs. Up-to-now the second generation efficiency is still lower than the first generation, which explains why the market share of c-Si is still so important.

The third generation encompasses the remaining technologies. Some of them may exceed the classical mono junction efficiency limit. Among third generation technologies, we can give the non-exhaustive following list:

- Multi-junctions
- Organic photovoltaic (OPV)

- Quantum dot cells
- Hot carrier
- Up and down conversion

Without giving details about these examples, fig. 1.5 illustrates the philosophy behind the three generations.

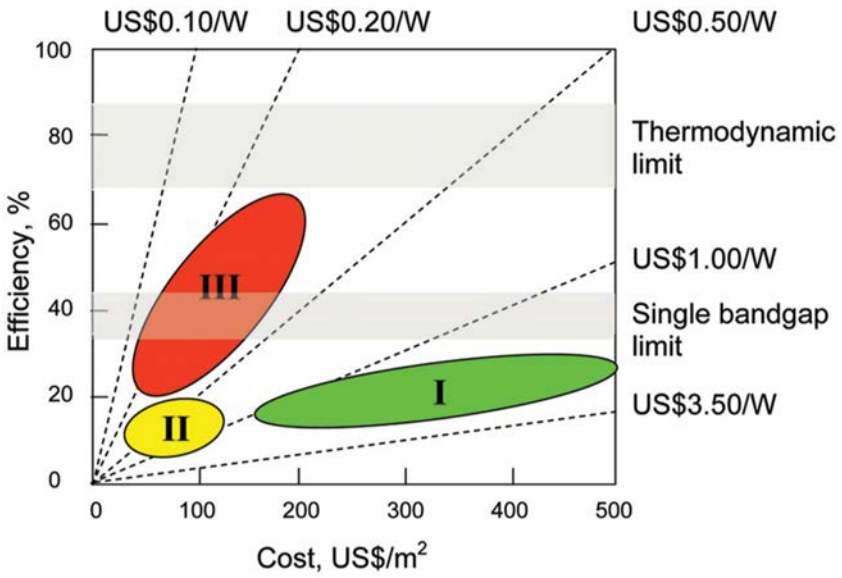

Figure 1.5: The three PV generations [14]. First generation is the most expensive but experiences fairly high efficiency. Second generation is cheapest but efficiencies can be low. The third generation aims at combining both advantages: efficient and low-cost. In practice, highly efficient cells are extremely expensive for now.

Record efficiencies of these different technologies has been compiled by NREL in fig. 1.6:

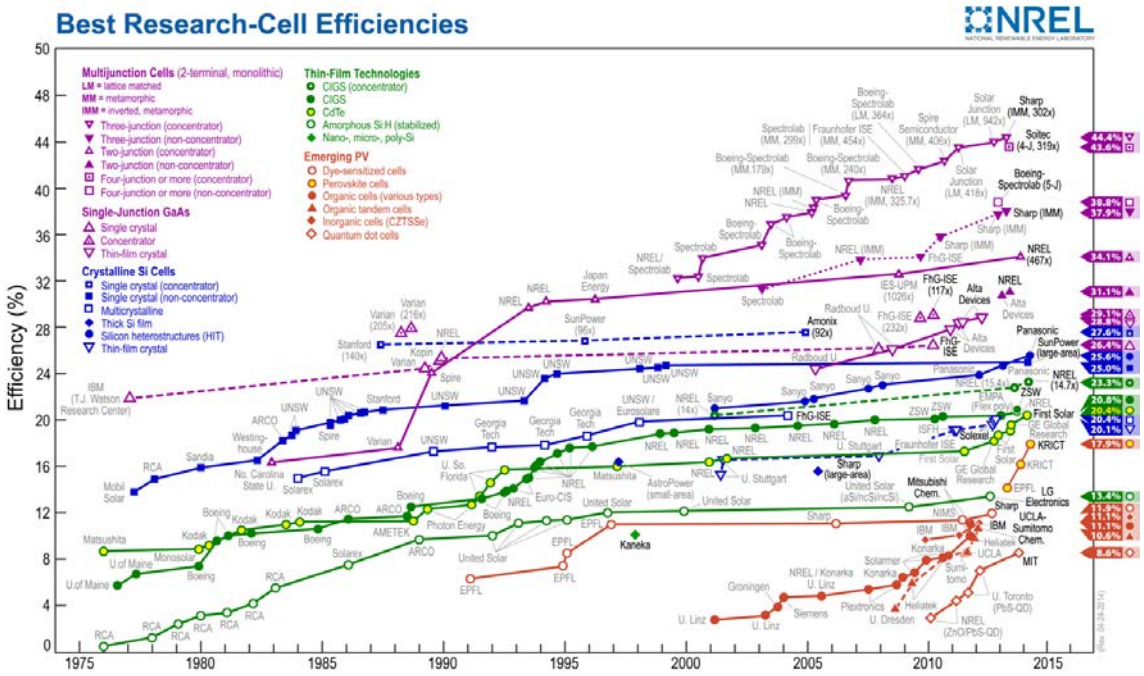

Figure 1.6: Best efficiency of the different PV technologies [15].

Figure 1.6 shows that numerous technologies exist. The first generation is represented by plain blue square and the second generation is in green. All other technologies belong to the third generation. c-Si is still better than thin film but the gap is narrowing. It is worth noting that mutli-junction technologies (in violet in the chart), have better efficiencies than c-Si but are fare more expensive and are used when the cost is not an issue, mainly in the space industry. Despite their high cost, they are still classified in the third generation. Figure 1.6 shows also that multi-junction cells are used under concentration. As we will see later, our goal is not to challenge these technologies but rather explore light concentration for cheaper solar cells. Open green circles represent CIGS (thin-film) records. The best value is obtained for a concentration factor X 14.7. This thesis will be focused on this concentration range.

In the next section, we review light concentration applied to photovoltaics.

1.3 State of the Art on photovoltaics light concentration

Up to now, our guiding principle was that photovoltaics needs cost reduction to be more competitive and that it may be solved by light concentration. It has been said without justification. This is why the first part of this section aims at explaining why concentration may reduce cost. Secondly, we will detail the different three concentration categories giving some technology examples. From there, pros and cons of the different light concentration systems will be highlighted, which will justify why this thesis deals with the Luminescent Solar Concentrator (LSC) technology.

1.3.1 CPV: interests & features

When light concentration is used on a photovoltaic system, we enter the domain of Concentrating PhotoVoltaics (CPV). A large area of sunlight is focused onto a small area solar cell

with the help of an optical device, the concentrator.

Two ideas stand behind optical concentration, both contributing to improve PV competitiveness. The first one is the material saving. Indeed, if the light hits a given area and can be concentrated in a solar cell ten times smaller, then a factor 10 on material amount can be saved to absorb light. As a consequence, the material cost in the total PV module cost can be significantly lowered, both in term of raw material and fabrication time saving (whereas one must add concentrator cost and its maintenance).

The second idea is that the open-circuit voltage varies with the concentration factor in a logarithmic way (see section 1.2.1.4) and therefore contributes to improve the system efficiency. On the other hand, if concentration is too high, resistive loss may limit the solar cell, which results in a low FF. Paire and co-workers [16] showed that resistive loss is reduced when cell size is also reduced. This justifies this work frame limited to photovoltaic cells no larger than few hundreds of microns.

Light concentrator is characterized by a concentration factor C, which is the product between a geometrical concentration factor (C_{geo}) and the optical efficiency (η_{opt}):

$$C = C_{geo} \times \eta_{opt} \tag{1.5}$$

The main concern in CPV is that the Sun has not always the same position in the sky at two time scales: day and season. During 24 hours, incident sunlight varies from -90° to +90° in the east-west direction whereas a 24° shift occur from winter to summer in the north-south direction. CPV should be designed to be efficient throughout the year during daytime, which force to consider incidence angle variation. This notion is taken into consideration with the acceptance angle θ_{acc}. By definition it is the maximum angle at which incident light can be concentrated by the CPV. If θ_{acc} is to small to allow the CPV system to be efficient all the day, then tracking is needed to align the CPV with the Sun. Concentration systems can be sorted in two categories. Some of them have a limited θ_{acc} whereas others exhibit $\theta_{acc} = \pi/2$. For a given acceptance angle, the maximum concentration C_{max} achievable is given by the following equation, derived from the second law of thermodynamics [17]:

$$C_{max} = \frac{n^2}{sin^2\theta_{acc}} \tag{1.6}$$

n is the refractive index in which the concentrator is located. Equation (1.6) states that the lower is the acceptance angle, the higher is the concentration factor. On the other hand, Sun-concentrating optics alignment will be more challenging. In addition, sunlight can be either direct or diffuse. Diffuse light has been scattered from direct solar beam by molecules in the atmosphere. Unfortunately, direct and diffuse light are not concentrated with the same efficiency in CPV. This is linked to the notion of acceptance angle. Diffuse light has a 90° incidence angle (2π steradian in solid angle) whereas direct light exhibits only one incidence angle, depending on the sun position. Thus, concentration systems with $\theta_{acc} \neq \pi/2$ cannot concentrate diffuse light but seems to be limited to a concentration factor of n^2.

The next question is: what is the average proportion of diffuse and direct light? Figure 1.7 shows the monthly proportion of diffuse over global (diffuse + direct) light, in two cities in France, Paris and Marseille. Paris is generally cloudy whereas Marseille, in the south of France, is rather sunny.

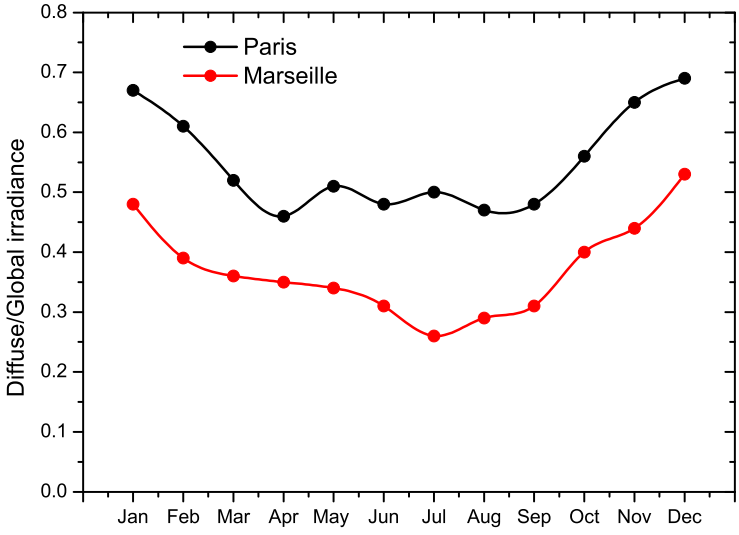

Figure 1.7: Diffuse over global irradiance in Paris (black) and Marseille (red) during a year. Data available in [18].

Throughout a year, diffuse light reaches 55.0 % (37.2%) of the global irradiance in Paris (Marseille) respectively. In sunny places, more than 1/3 of light can be diffuse, whereas in cloudy places, this proportion can exceed 50%. In places similar to Paris, the use of concentration systems which are not able to concentrate diffuse light means to loose straight away more than half of the light.

1.3.2 Different concentration levels for different targets

1.3.2.1 High Concentration PhotoVoltaics HCPV

HCPV is the most common CPV systems with the best industrial maturity. HCPV concerns concentration factors higher than 150, which are mainly obtained using Fresnel lenses and to a lesser extent micro-dish or dense array receivers [19]. All these technologies are called "imaging" (by definition they form the source image on the focal point) and consequently can concentrate only direct sunlight. As seen above, they are interesting only in sunny regions.

Fresnel lenses have the same optical function than conventional lenses, their particularity lies in the fact that all the material not needed to perform concentration has been removed (see fig. 1.8).

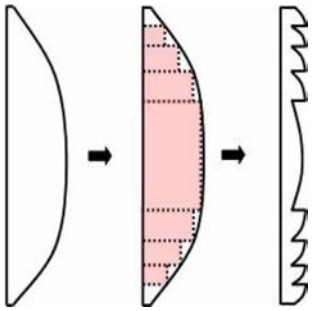

Figure 1.8: Fresnel lens scheme. A Fresnel lens is made by removing the non-refractive part of a conventional lens, leaving the lens with a thin profile [20]

This design makes lens more compact, which eases their implementation, reduces the concentrator weight as well as wind pressure. More details on Fresnel lens concentrator can be found in this seminal paper [21].

Common HCPV concentration factors vary between 400 and 700, but values higher than 2000 have been reported [22]. The world record, (in terms of module efficiency) is hold by Semprius with 35.5% efficiency for $C_{geo} = 1100$ ($\eta_{opt} \approx 0.8$) [23]. It is worth noting that eq. (1.6) corollary is that sun tracking system must be extremely accurate to achieve good light concentration with such high concentration factors. In addition, HCPV requires active cooling to keep a reasonable temperature in the solar cells.

What should be understood is that HCPV goal is to achieve cost reduction through expensive semi-conductor material saving. Because concentrating optics is expensive (mainly tracker), targeted solar cells for HCPV are the most efficient (III-V multi-junctions). High concentration optics cost plus additional cost of highly efficient cells (compared to c-Si or thin film) is counterbalanced by the material saving granted by HCPV. Rather, HCPV seems not adapted to concentration on "low cost" solar cells because the material saving induced cost reduction is not high enough.

1.3.2.2 Medium Concentration PhotoVoltaics MCPV

Medium CPV is a kind of trade off between high optical concentration and high industrial capacity ($10 < C_{geo} < 150$). It is usually done on c-Si PV cells and requires less accurate sun tracker than HCPV. Even a one axis tracking system is sometimes sufficient [24]. Popular optics for MCPV is Fresnel mirror, which are based on the same technology than Fresnel lens. Fresnel mirror enables to make thin a parabola cutting it in different segments. Concentration factors are lower than parabolic compounds but industrialization is easier and cheaper. Figure 1.9 illustrates an example of MCPV:

Figure 1.9: MCPV with Fresnel mirror from Axiosun. Concentration factor is around 15. Downloadable in [25]. Red arrows point solar cells.

Achieving higher concentration requires other optics, such as prismatic lenses reaching $C_{geo} = 120$ [26]. Going lower in concentration level, we end up with low concentration photovoltaics.

1.3.2.3 Low Concentration PhotoVoltaics LCPV

Concentration factor lower than 10 belongs to low CPV. Generally LCPV does not require sun tracking system (or simple ones) and consequently are not expensive. Furthermore, the low concentration factor does not require heat dissipation systems. Compatible with low cost cells (thin films or c-Si), LCPV can be a way to increase module performances with a soft extra-cost.

Different technologies have been studied. Among them we can highlight:

- Prism Array Concentrator
- Parabolic mirror
- Non fluorescent flat plate concentrator
- Luminescent solar concentrator

Prism Array Concentrator consists in a coupling between a transparent prism (glass or plastic) and a mirror, as illustrated in fig. 1.10:

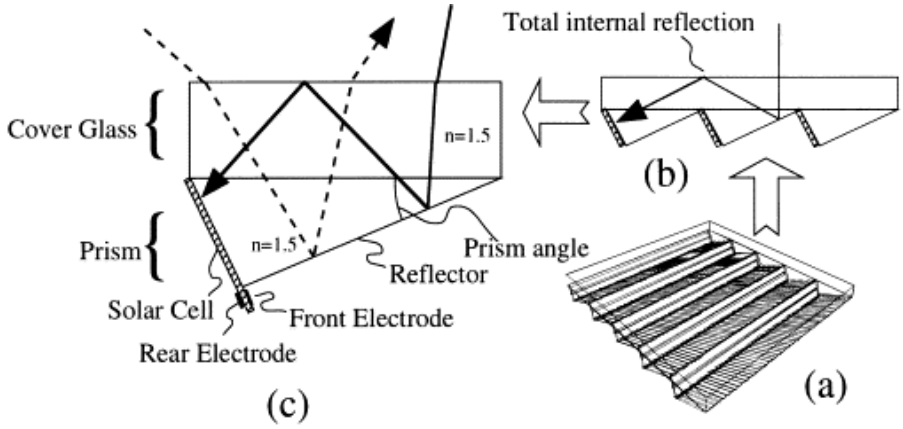

Figure 1.10: (a) Prism array concentrator scheme. (b) Cross-section view. (c) Principle scheme of a Prism array concentrator elementary unit. Taken from [27]

Prism Array Concentrator key parameters are prism refractive index and inclination angle. They rule the light concentration based on total internal reflection. Authors claim an annual concentration factor (averaged over azimuth and polar angles) of 1.77.

An other strategy consists in using parabolic mirrors, as depicted in fig. 1.11:

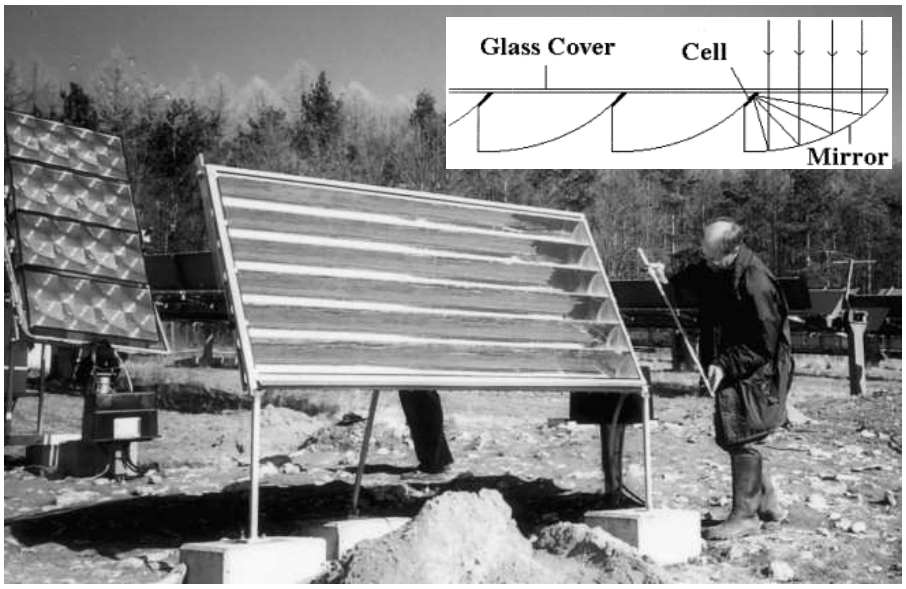

Figure 1.11: Picture of a parabolic mirror LCPV. Inset, diagram of the general principle. Taken from [28]

This concentrator enables geometrical concentration factor of X6 (but the optical efficiency is not given [28]). The acceptance angle is only 7°, which implies the use of a 1-axis sun tracker in the North-South direction. Indeed, the daytime variation is not an issue here (except side effect) but a bad North-South alignment leads to a off-centered focal plan.

Closer to the heart of this thesis we have the non fluorescent flat plate concentrator. The idea behind non fluorescent flat plate concentrator is to receive light on a large area and guide

it onto low-area solar cells. The guiding is performed by avoiding light (trapping) to get out the collector. Light trapping is promoted by TIR and mirror reflection, as shown below:

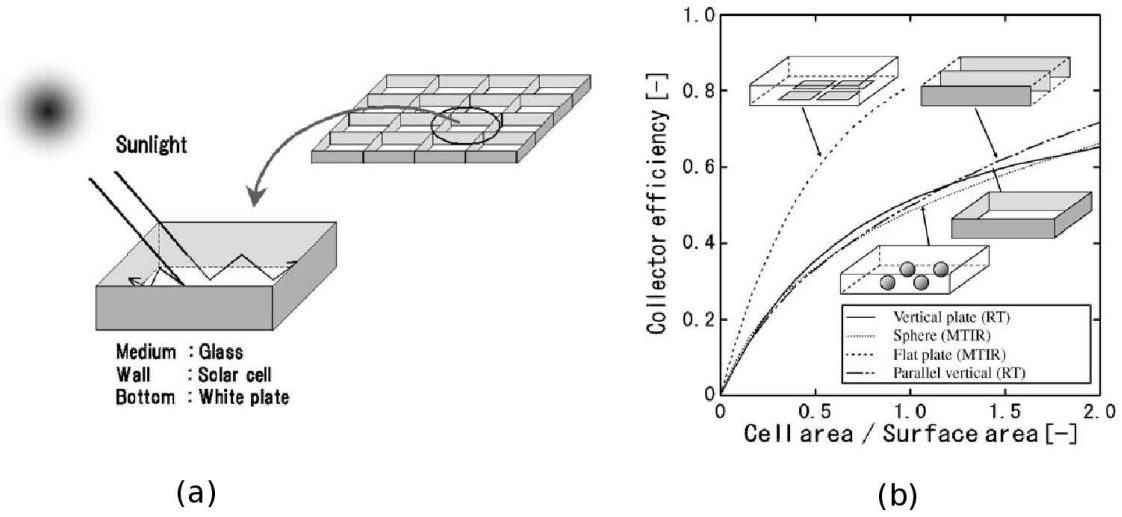

Figure 1.12: (a) Scheme of a vertical solar cell with a flat plate concentrator. (b) Collector efficiencies for various concentrators as a function of cell to glass area ratio. Taken from [29]

Whatever the configuration is, concentration is still low. Morimoto et al. [29] have obtained in the best case X1.44 concentration. We have not yet mention the concentration system which is of interest for us (luminescent solar concentrator) for highlighting its place in the CPV picture.

1.3.2.4 Luminescent Solar Concentrator place in CPV landscape & consistency with low size PV cells

Working with low cost photovoltaic cells (thin films), concentrator must be low-cost to preserve the whole system competitiveness. In this respect, concentration optics should not comprise expensive sun-tracker, and consequently θ_{acc} should not be to low. Typically, a value of $\theta_{acc} \approx 7.5°$ allows to track the sun only one time per hour. HCPV is therefore not adapted (see eq. (1.6)). Taking this line of thought further, any concentration system with $\theta_{acc} \neq \pi/2$ concentrates light on a focal point, which can be an additional challenge if used with extremely low size PV cells. Superimposing micron-size focal points to micron-size solar cells taking into account Sun movement is challenging. As such, $\theta_{acc} = \pi/2$ systems become even more interesting when PV cell has micron size. In addition, these systems can concentrate diffuse light, whose proportion exceeds 50% in temperate regions. Unfortunately, eq. (1.6) greatly limits the concentration factor.

Luminescent Solar Concentrator may be an alternative because this technology has numerous desired benefits ($\theta_{acc} = \pi/2$, low-cost) but also may have concentration factors exceeding the n^2 limit derived of eq. (1.6). For all these reasons, we have chosen to evaluate the light concentration potential on micro CIGS-based solar cell with a luminescent solar concentrator (part I). Part II of this work intends to study an innovative light concentration alternative inspired from LSC, in response to LSC fundamental limitations.

1.4 Big picture

This introductory chapter was an opportunity to give some context elements of this work. Energy is absolutely fundamental and the need to diversify our production technologies is pressing. Photovoltaics plays an ever-growing role in the energy mix, supported by a ratio cost over efficiency drop. The idea of using light concentration contributes to achieve this goal.

The majority of concentrated photovoltaics comprises expensive III-V multi-junction cells. We restrain ourselves to study concentration on low-cost thin-films solar cells. As a proof of concept, it will be done with Cu(In,Ga)Se_2-based solar cells (abbreviated CIGS). Moreover, substantial resistive loss limits light concentration benefits if no appropriate measures are made. Solar cell size reduction is one of them, that is why we study CIGS-based microcells.

Given that, we need to find a light concentration system adapted to our constraints, namely low size ($\sim 100\ \mu m$) and concentration factors around X10 to X100. Luminescent Solar Concentrator is a possible candidate.

Part I

Luminescent solar concentrator based concentration

Chapter 2

Basics of Luminescent Solar Concentrators

Contents

This second chapter, divided in two main sections, is dedicated to Luminescent Solar Concentrator (LSC) basics. The first section reviews LSC. After a reminder of our motivations, LSC operating principles will be given from the point of view of ray-tracing. The different loss mechanisms will be identified and the physical parameters ruling LSC performance will be highlighted. Thereafter, optical filter use at the LSC front surface will be introduced. Optical filters will be used in the theoretical study of chapter 3. The thermodynamics section explains why LSC can outperform the maximum concentration factor n^2 derived from eq. (1.6). Finally best achievements and literature efficiency records will be given.

The second section addresses LSC modeling. We have chosen to develop a ray-trace program called LSC-VMCA (Luminescent Solar Concentrator - Vectorized Monte Carlo Algorithm) to analyze LSC physics. The code description is given in this section.

2.1 Luminescent Solar Concentrator: State of the art

2.1.1 Motivations

The origin of LSC can be found in the field of fluorescent collection which was previously applied in display or scintillator technologies. For the first time in 1976, W.H. Weber and J. Lambe extrapolate this concept to solar concentration [30]. One year later, A. Goetzberger and W. Greubel published a paper [31] in which a theoretical evaluation of LSC capabilities is done: a new research thematic was born. Two years later, Batchelder and co-workers [32] published a seminal paper on LSC. In particular they derive analytically the different loss channels independently. Because the loss channels are highly interdependent, they solve the problem only for ideal or highly symmetrical systems. From their work is born the idea of using numerical tools to take into account the loss channels interdependency.

Ideas behind LSC are pretty intuitive. In its simplest form, a LSC comprises a rectangular cavity containing luminescent particles and a solar cell located at one edge of the cavity (fig. 2.1 left). Photons enter the cavity through the front cavity area ($\mathcal{A}_f$), are absorbed by luminescent molecules and isotropically re-emitted at a longer wavelength, making possible light guiding toward solar cell at the cavity edge (area $\mathcal{A}_e$). The ratio $\frac{\mathcal{A}_f}{\mathcal{A}_e}$ is called geometrical concentration factor or geometrical gain (C_{geo}). If $C_{geo} > 1$, light concentration is achievable.

As previously mentioned in section 1.3.2.4, this way of light concentration has two main advantages compared to imaging concentrators:

- Concentration of the diffuse component of the solar spectrum
- Low cost system:
  - Cheap materials (plastic cavity and organic dye)
  - Light tracking system not mandatory

The straightforward corollary is the possible light concentration even with a cloudy sky (diffuse light important), which is appealing under our latitudes (cf fig. 1.7 page 30). Nevertheless, LSC experiences losses mitigating its advantages. That is why a complete LSC description is required to identify all loss mechanisms and then to assess their respective weights.

Because the luminescent solar concentrator acts as a waveguide, the isotropic nature of dye emission is not optimal. As such, Verbunt and co-workers [33] have shown that an assembly of isotropic molecule may not be considered as globally isotropic. In PMMA, isotropic emission leads to around 25% loss (through the front surface) whereas it rises to almost 30% when the anisotropic behavior is taken into consideration. This refinement has not been taken into account in this manuscript and does not modify its conclusions. Uncontrolled anisotropy can be prejudicial, but introducing smart anisotropy can be on the contrary an asset (see section 2.1.4).

2.1.2 Description via geometrical optics

This section aims at giving all the useful background to study LSC. The concentrator principle will be given as well as the different loss mechanisms. The physical parameters involved in the loss mechanisms will be detailed, a glimpse of the complexity of LSC will be presented but the study in itself will be performed in the next chapter, once the fundamentals have been presented. Finally, the LSC thermodynamics aspect will be envisaged.

As explained in the previous chapter, we are interested in the bottom-mounted rather than edge-mounted LSC configuration. Figure 2.1 shows a schematic of these two configurations.

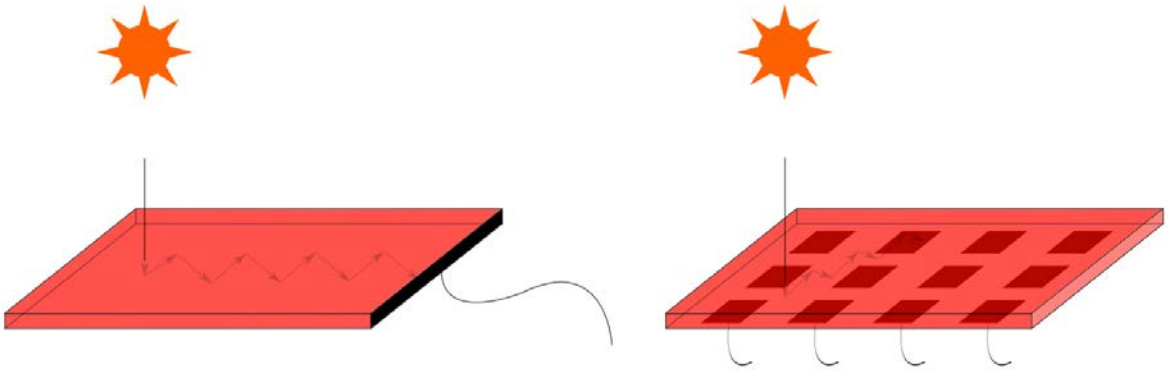

Figure 2.1: The two LSC configurations. *Left*: Edge-mounted. *Right*: Bottom mounted

The bottom-mounted configuration is far much convenient to couple microcells at the LSC back surface rather than at its edges. In addition, Pronneke et al. [34] showed that theoretical performances of the two configurations are almost similar. These two reasons contribute to opt for bottom-mounted LSC. Although the physical principles are the same, a bottom-mounted LSC can be viewed as a cavity in which light is trapped until it reaches solar cells. Figure 2.2 depicts a bottom-mounted LSC with all its loss channels.

Sunlight may be transmitted in the cavity and absorbed by a dye molecule. Radiative isotropic emission may occur leading to a photon trapped inside the cavity until it reaches the solar cell (7). The trapping is performed by reflecting photons with mirrors at the edges and at the back surface (between solar cells) and by Total Internal Reflection at the front surface. However, loss channels sketched in fig. 2.2 (noted $\mathcal{L}$) contribute to reduce the LSC performance.

2.1.3 Loss channels

Sunlight may be reflected before entering the device by Fresnel reflection $\mathcal{L}_{ext}$. Once absorbed, dye-emission may not occur due to non ideal photoluminescence quantum yield (PLQY), leading to photon loss through heat $\mathcal{L}_{QY}$. Being isotropically re-emitted, photon may reach the front surface at an angle below the critical angle (θ_c) and consequently be transmitted and lost $\mathcal{L}_{front}$. θ_c forms a cone called "escape cone". Every photons in the escape cone will not be reflected by total internal reflection. The host matrix in itself may not be totally transparent, which leads to a non-zero probability matrix absorption and the photon is also lost through heat $\mathcal{L}_{mat}$. Light is naturally guided toward edges. Photon may escape through the lateral surface $\mathcal{L}_{side}$. Mirrors reflection coefficients can be non ideal and photon is lost by absorption $\mathcal{L}_{back}$. Finally, photons can be absorbed by solar cells ($\mathcal{G}_{coll}$), which obviously is the channel we try to favor. By construction, we have the following relationship:

$$\mathcal{L}_{ext.} + \mathcal{L}_{QY} + \mathcal{L}_{front} + \mathcal{L}_{mat.} + \mathcal{L}_{side} + \mathcal{L}_{back} + \mathcal{G}_{coll.} = 1 \tag{2.1}$$

To go further, a more detailed and quantitative analysis of each loss mechanisms is required:

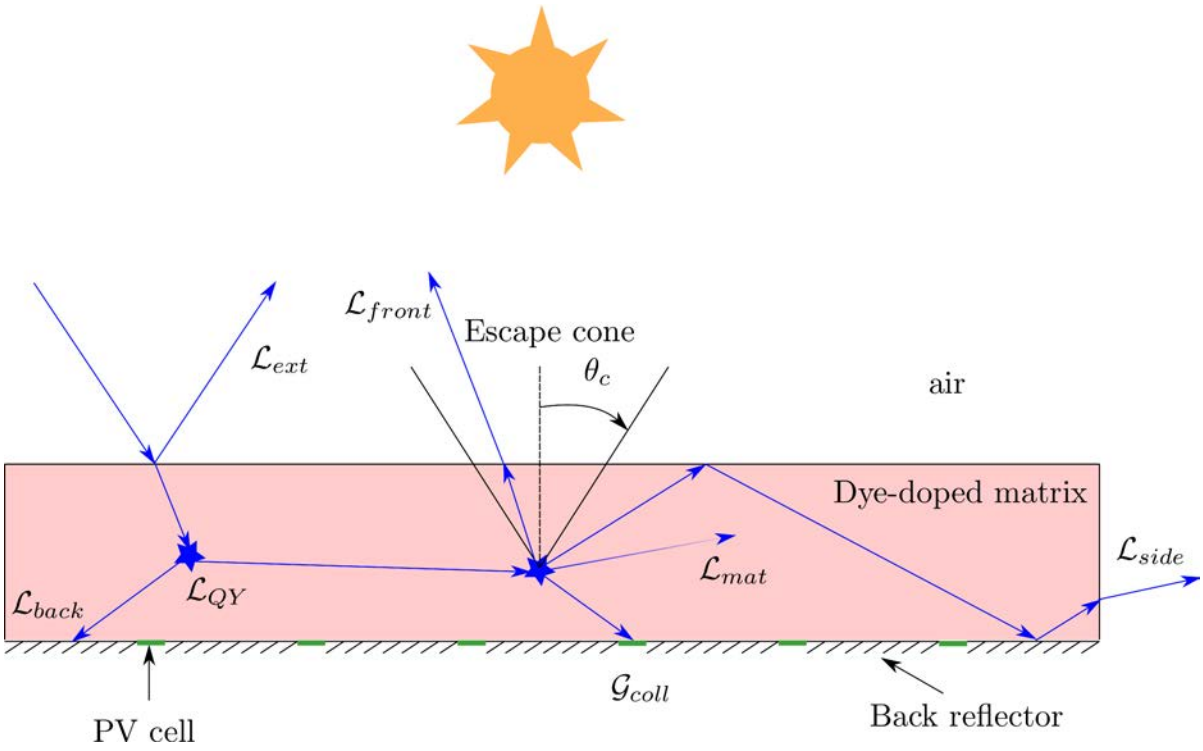

Figure 2.2: Schematic of a BM-LSC comprising loss channels. External loss $\mathcal{L}_{ext}$. Internal losses: Non radiative deexcitation $\mathcal{L}_{QY}$, Non trapping at the front surface $\mathcal{L}_{front}$, Absorption by the host matrix $\mathcal{L}_{mat}$, Back reflector absorption $\mathcal{L}_{back}$, Edge loss $\mathcal{L}_{side}$, Collected photons $\mathcal{G}_{coll}$

External loss $\mathcal{L}_{ext}$: Photons come from air and must be transmitted in the cavity. Since the refractive indexes (R) of these two media are different ($n_{\text{air}} = 1 \neq n_{\text{mat}}$), it gives rise to a reflection coefficient (so-called Fresnel reflection coefficient). Typical values for n_{mat} are 1.3-1.5. Fresnel reflection coefficients depend on the light polarization, refractive indexes and incidence angle (θ_{i}) and are given in equations eqs. (2.2) to (2.4) and plotted in fig. 2.3.

$$R_{\text{TE}}^{\text{air}\to\text{mat}} = \left| \frac{n_{\text{air}}\cos\theta_{\text{i}} - n_{\text{mat}}\sqrt{1-\left(\frac{n_{\text{air}}}{n_{\text{mat}}}\sin\theta_{\text{i}}\right)^2}}{n_{\text{air}}\cos\theta_{\text{i}} + n_{\text{mat}}\sqrt{1-\left(\frac{n_{\text{air}}}{n_{\text{mat}}}\sin\theta_{\text{i}}\right)^2}} \right|^2 \tag{2.2}$$

$$R_{\text{TM}}^{\text{air}\to\text{mat}} = \left| \frac{n_{\text{air}}\sqrt{1-\left(\frac{n_{\text{air}}}{n_{\text{mat}}}\sin\theta_{\text{i}}\right)^2} - n_{\text{mat}}\cos\theta_{\text{i}}}{n_{\text{air}}\sqrt{1-\left(\frac{n_{\text{air}}}{n_{\text{mat}}}\sin\theta_{\text{i}}\right)^2} + n_{\text{mat}}\cos\theta_{\text{i}}} \right|^2 \tag{2.3}$$

$$R_{\text{Fresnel}}^{\text{air}\to\text{mat}} = \frac{R_{\text{TE}}^{\text{air}\to\text{mat}} + R_{\text{TM}}^{\text{air}\to\text{mat}}}{2} \tag{2.4}$$

Sunlight is not polarized and it will be assumed in this thesis that sunlight is normal with respect to the cavity. Consequently $R_{\text{Fresnel}} = 4\%$. Note that this loss is qualified of external because it occurs prior entering the device and is totally independent of others loss mechanisms.

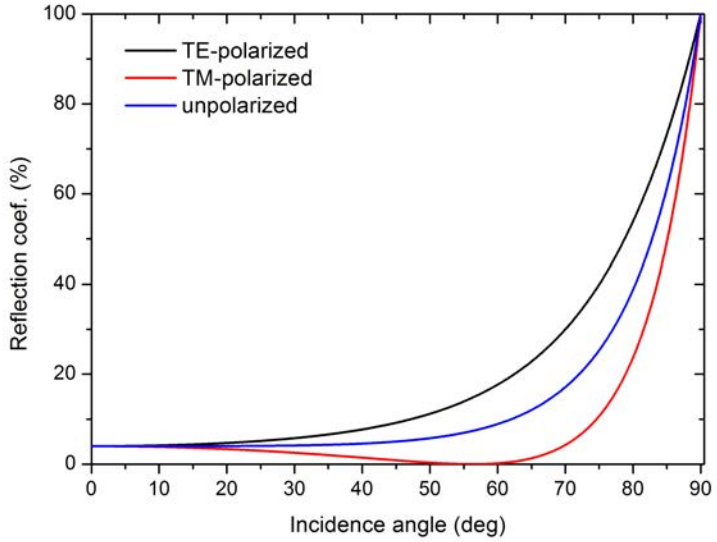

Figure 2.3: Fresnel reflection coefficients for polarized and unpolarized light from air to matrix

Non radiative deexcitation $\mathcal{L}_{QY}$: The ability to emit a photon after its absorption by a dye is quantified by the dye photoluminescence quantum yield (PLQY):

$$PLQY = \frac{\text{number emitted photons}}{\text{number excited molecules}} * 100\% \tag{2.5}$$

It is generally admitted that PLQY is wavelength-independent. Values of PLQY vary from almost 0 to 100 % and depend also on the solvent. It will be seen in chapter 3 that for this application, interesting dyes must absorb most of the solar spectrum and re-emit just above the solar cell bandgap. It means that emission wavelength should be preferentially in the red or near-infrared region. Fig. 2.4 shows typical PLQY values for different dyes.

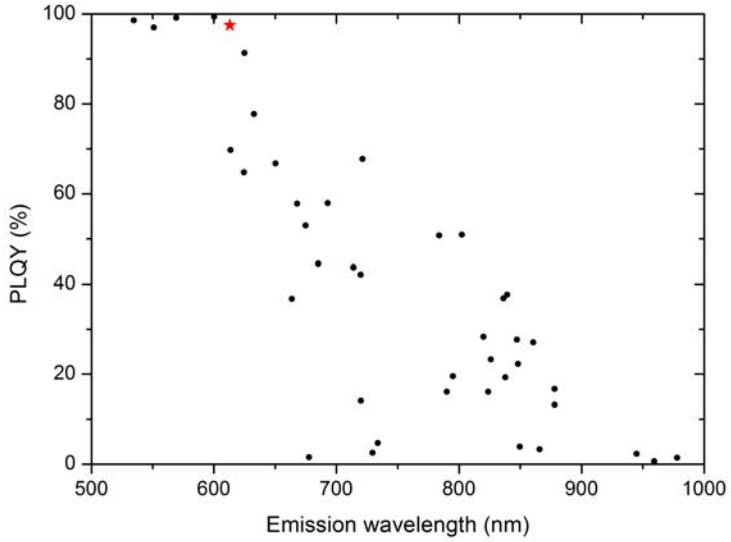

Figure 2.4: PLQY versus emission wavelength of different dyes. Adapted from [35, 36]. The red star corresponds to Lumogen® RED 305 from BASF

The longer is the emission wavelength, the lower is the PLQY. It can be understood knowing that the energy difference between the excited and ground state of a dye molecule is lower at long-wavelength emission. As a consequence, the number of options to get rid of the excited-state energy by non radiative process increases and so PLQY decreases. The dye Lumogen® Red 305 (red star in Fig. 2.4, abbreviated R305) is a standard dye used in LSC because it exhibits high quantum yield, relatively small overlap, high stability and is easy to dissolve in common matrix. For all these reasons, R305 will be largely used in this thesis.

Front escape loss $\mathcal{L}_{front}$: Front loss trapping is basically performed by TIR. The derivation of the reflection coefficient from the high to low refractive index material, n_{mat} and n_{air} must be inverted in eqs. eqs. (2.2) to (2.4) and result is shown in Fig. 2.5 (left) in the case of a PMMA matrix ($n_{PMMA} = 1.5$) .

For angles higher than the critical angle θ_{c}, the reflection is total and polarization independent. This behaviour is the reason why LSC may act as a concentrator by waveguiding, but conversely may cause high loss since the critical angle is rather large for common matrix. Fig 2.5 (right) shows the critical angle dependence versus the refractive index.

To be accurate, one can argue that TIR efficiency cannot be exactly 100 % because of impurities such as dust or moisture droplets on the surface. Study has been performed by Thomas et al. [37] and they conclude that TIR efficiency was 0.9998. The influence of this effect will be considered negligible throughout this thesis.

Matrix absorption $\mathcal{L}_{mat}$: Matrix absorption of photon is detrimental since excited matrix molecules deexcite via radiativeless vibration mode. The key physical parameter is the wavelength-dependent matrix absorption coefficient α_{mat}. Typical values for α_{PMMA} is $10^{-4} - 10^{-3}$ cm^{-1}. This loss can be neglected for low dimension LSC (typically 5x5x0.2 cm^3) but may

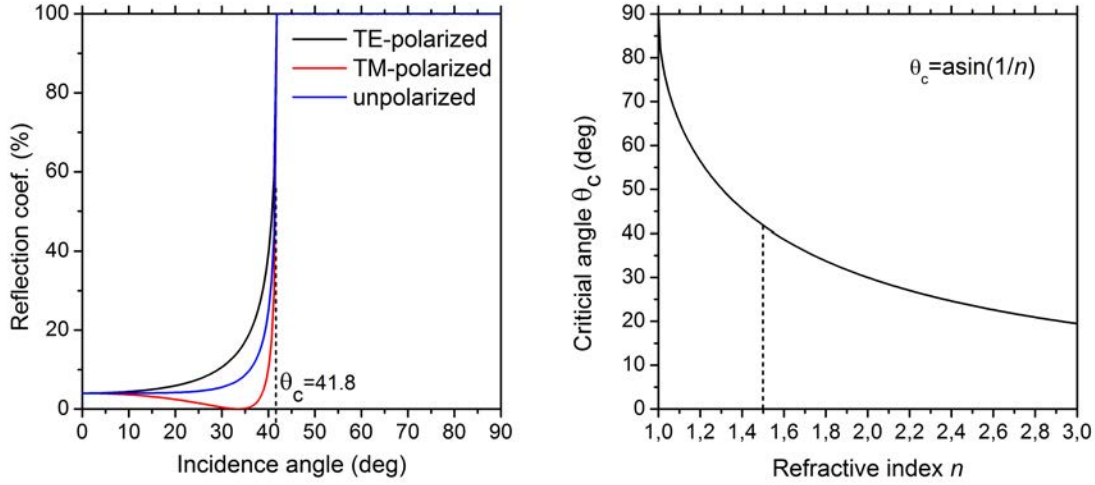

Figure 2.5: *Left*: Fresnel reflection coefficients for polarized and unpolarized light from PMMA to air. *Right*: Critical angle versus refractive index

be of importance for larger size due to the increase of the photons mean free path (more details in section 3.1.3.1).

Back reflector absorption $\mathcal{L}_{back}$: Reflection coefficient of mirrors is not ideal and is wavelength dependent. Absorption may occur and has exactly the same effect that matrix absorption. This loss channel is really different between bottom and edge mounted configuration, and care must be taken in the bottom mounted configuration since the reflection coefficient is not 100% contrary to TIR. Furthermore, the nature of the reflector, specular [1] or lambertian [2], is of importance. It will not affect the back reflector loss since it is only driven by the reflection coefficient, but changing the light angle after reflection can disrupt the trapping at the front surface. Indeed photons with angle higher than θ_c can be reflected at an angle becoming lower than θ_c. This effect will be studied later section 4.2.2.5.

Side loss $\mathcal{L}_{side}$: Bottom mounted LSC is exposed to side loss since it is the "natural" behavior to guide light to the cavity edges. Two options will be envisaged. One is to put a reflector on the edges the same way than on the back surface, the other is to do nothing and side reflection will be then driven by Fresnel reflection. Side loss is really sensitive to lateral LSC size, which will be also viewed later.

Another loss mechanism commonly attributed to LSC is the emitted photon energy loss. Indeed LSC is a down-shifting device and the photon has a lower energy after being emitted. However it will not be considered throughout all this thesis as a LSC loss because this loss would have occurred in the solar cell in the form of thermalization. We will see in section 2.1.5 that the down-shifting process is a beneficial loss because it creates entropy, which is at the origin of making high concentration factors achievable.

1. By definition, a specular surface reflects a beam of light so that the angle of reflection is equal to the angle of incidence.
2. By definition, a lambertian surface reflects radiance equally into all directions.

As written in numerous papers, the overall LSC optical efficiency $\left(\eta_{\text{opt}} = \frac{\text{nb.incidentphotons}}{\text{nb.collectedphotons}}\right)$ can been described by the following equation:

$$\eta_{\text{opt}} = \eta_{\text{ext}}.\eta_{\text{int}} = \eta_{\text{ext}}.\eta_{\text{PLQY}}.\eta_{\text{Front}}.\eta_{\text{Matrix}}.\eta_{\text{side}}.\eta_{\text{Back}} \tag{2.6}$$

Where the right part efficiencies can be trivially linked to the loss mechanisms described below. This elegant formula cannot be used to precisely find out the LSC efficiency because all loss mechanisms are interdependent (except for η_{ext}) which makes difficult to find analytical description of these intermediate efficiencies. As an example, if we look at η_{PLQY}, an intuitive expression is:

$$\eta_{\text{PLQY}} = (\text{PLQY})^{\bar{n}_{\text{abs}}^{\text{dye}}} \tag{2.7}$$

Where $\bar{n}_{\text{abs}}^{\text{dye}}$ is the mean dye absorption event. $\bar{n}_{\text{abs}}^{\text{dye}}$ is unknown and depends on all others LSC parameters. Thus computational techniques are required to derive η_{PLQY}. The one used in this thesis will be described later.

In eq. 2.6, we have divided losses in two categories, external and internal. External loss occurs outside the concentrator whereas internal losses concern mechanisms occurring inside the concentrator. Yet we would like to emphasize on another way of dividing the losses: both external and front loss are not arising from non ideal LSC physical parameters contrary to the others losses:

- $\mathcal{L}_{QY} = 0$ if $\text{PLQY} = 1$
- $\mathcal{L}_{back} = 0$ if $\text{R}_{\text{back}} = 1$
- $\mathcal{L}_{mat} = 0$ if $\alpha_{\text{mat}} = 0\ cm^{-1}$
- $\mathcal{L}_{side} = 0$ if $\text{R}_{\text{side}} = 1$

Which means that $\mathcal{L}_{ext}$ and $\mathcal{L}_{front}$ cannot be avoided even for an all ideal device and are inherent to LSC. Consequently, LSC optimization can be also divided in two parts:

- Find ideal parameters/materials → act principally on avoidable loss.
- Find different strategies or configurations → act principally on intrinsic loss.

Anti-reflection coating (ARC) for instance is a way of reducing $\mathcal{L}_{ext}$. The next section will be devoted to an additional optical compound aiming at tackling $\mathcal{L}_{front}$.

2.1.4 Lowering front loss: Photonic Band Stop & dye anisotropic emission

As previously written, front trapping is performed by TIR whose efficiency depends only on refractive indexes and photons angle. Enhancing TIR efficiency requires:

1. Increase $\Delta n = n_{\text{mat}} - n_{\text{air}}$
2. Anisotropic dye emission to reduce emission in the escape cone

Implementing the first solution implies an increase of $\mathcal{L}_{ext}$ not mentioning difficulties to find a proper material which is still transparent and able to host dyes. Nevertheless clearly a trade-off must be found on refractive index between $\mathcal{L}_{ext}$ and $\mathcal{L}_{front}$, which will be done later. The second solution would have been far more efficient except that anisotropic dye molecules

are hard to conceive and not as efficient (PLQY, absorption and emission spectra). Some work on this field can be found in [38]. A third solution is to take advantage of the fact that photon wavelength after dye emission is red shifted and use an optical filter designed to reflect luminescence. This concept was first proposed by U. Rau [39].

Indeed, the incoming solar spectrum is broad-band but the dye action enables to differentiate three spectral regions illustrated in fig. 2.6.

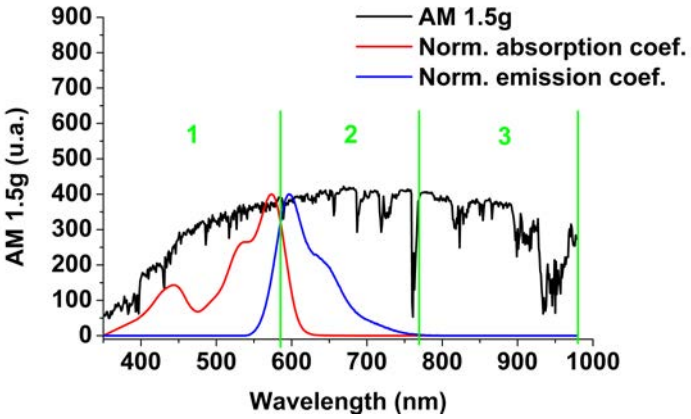

Figure 2.6: The three different spectral regions illustrated in the case of R305. 1: Dye absorption region. 2: Dye emission region. 3: Unaffected by dye

The idea underlying the photonic band stop (PBS) use is to add an optical filter at the front surface, which transmits light in regions 1 and 3 and reflects light in region 2, acting as an optical band-stop filter. The PBS highly reflective property in the region 2 enables to trap light even if photons are not reflected by TIR, making the trapping insensitive to photons angle and consequently greatly reduces front loss. Note that region 3 could be avoided if solar cells bandgap matches dye emission. The mismatch will be studied later in this thesis. It can be easily seen from Fig. 2.6 that the PBS must be chosen accordingly to the dye to match the three spectral regions described above. Reflecting photons in region 2, the PBS will enhance the external loss in this region so a trade-off must be done. A more detailed study of the PBS is beyond the scope of this introduction. The next question is how a PBS can be fabricated? All known PBSs belong to a material class named photonic crystals (PC).

Photonic crystals optical properties were first studied by Yablonovitch [40] and John [41] in 1987. It consists in a refractive index periodic structure giving rise to a photonic-gap: no photonic modes are allowed within the bandgap energy range and so reflection occurs [42]. Photonic crystals are classified from their dimensions, from 1D (infinite layer) to 3D crystals. 1D-PC and 3D-PC were studied for LSC applications. Bragg reflector or Rugate filters [43] are examples of 1D-PC in which the refractive index varies along one dimension. In a Bragg reflector, the refractive index periodicity follows a step function whereas Rugate filters exhibits a sinusoidal periodicity. Bragg reflectors are usually prepared by layer-by-layer deposition of alternative refraction index materials. Rugate filters can be made by varying the material porosity. The stop band is defined by setting appropriate refractive indexes difference and layer thickness. Reference [44] illustrates how a Rugate filter can be coupled to LSC. Concerning 3D-PC, famous structures are the opal and the inverse-opal. An opal consists in a

close package of spheres leading to a natural 3D periodic structure. The inverse opal being an opal in which the sphere volume has a lower refractive index than the surrounding medium. In an opal structure, the stop band is defined by the refractive index of the spheres as well as their diameters (affecting the filling ratio). Experimental works on opals (edge-mounted LSC) have been reported in [45], yet efficiency is still low because of opal structural defects. A complete review on photonic crystals applied to photovoltaics can be found in [46] as well as a comparative study between LSC with and without optical filter [47].

An other way of reducing front loss is to take advantage of anisotropic dye emission. Assuming that organic dye emission dipoles are oriented parallel to the normal of the LSC plane, the $\sin(\theta)^2$ emission pattern reduces the escape cone loss from 25% to 9.2% [32]. More generally, dye orientation favoring photon emission outside the escape cone is beneficial. We have not considered this option in this manuscript because homogenous dye orientation is extremely challenging, and require the use of particular matrix (liquid crystal, [48, 49]) which has lower optical properties than classical matrix such as PMMA. A complete study of anisotropic dye emission can be found in [50].

At this point the LSC has been introduced as well as the PBS which can be advantageously used to improve the LSC performance. Yet the dye role may be not so clear. One may think dye is used only to isotropically emit photons to be able to trap them by TIR. Following this reasoning, one may conclude that dye is not mandatory and a simple lambertian reflector is sufficient. PBS cannot be used without dye but still there is a fundamental reason explaining why dye is essential. The answer lies in thermodynamics.

2.1.5 Thermodynamics consideration

To deny the previous assertion, one can look at the etendue conservation law, which states that a light beam energy can not increase through passive optical systems and therefore can be seen as a consequence of the second thermodynamics Law. Etendue and entropy S are linked by eq. (2.8):

$$S \approx k \log(\text{etendue}) + \text{cst} \tag{2.8}$$

The etendue is proportional to the areas of emitting or receiver element, their refractive index and the emitting or crossed solid angle. In solar concentrating devices, the "entrance" area is larger than the solar cells surfaces but in the LSC case, the acceptance angle is 2π steradian, which is the same as the solid angle illuminating the solar cells. As a consequence, only a refractive index difference can counterbalance the area differences to conserve the etendue. That is why concentration is possible even in a purely diffusive concentrator, but only via the refractive indexes difference, which greatly limits achievable concentration factors.

The dye role is to create entropy by absorbing a high energy photon ν_1 and emitting it at a lower energy $\nu_2 \leq \nu_1$. This excess of entropy enables to break the etendue conservation law while respecting the second thermodynamics law. To be more quantitative, it has been shown that, under terrestrial conditions, the concentration factor C may be approximated by the following equation [51]:

$$C \leq \frac{n_2^2 \nu_2^2}{n_1^2 \nu_1^2} . \exp \frac{h(\nu_1 - \nu_2)}{kT} \tag{2.9}$$

Where the subscript 1 refers to the external medium (air), and 2 to the matrix cavity. In a purely diffusive concentrator (without energy shift) the concentration factor can not exceed the ratio $\frac{n_2^2}{n_1^2}$, which is consistent with eq. (2.9) with $\nu_1 = \nu_2$. Practically, a diffusive PMMA LSC of refractive index 1.5 enables a maximum concentration factor of 2.25. Adding a dye with $\nu_1 = 2.14$ and $\nu_2 = 2.02$ eV leads to a maximum concentration factor of 113.

To summarize, the dye has two main roles, one is to emit isotropically the light to allow Total Internal Reflection, the other one is to make high concentration possible by breaking the etendue conservation law through heat creation. Having said that, what are the efficiency record of LSC?

2.1.6 Record efficiencies

The first 3.2 % LSC conversion efficiency has been published in 1980 by Friedman [52]. This record was followed by another one in 1984 published by Goetzberger and Wittwer [53]. They manage an LSC efficiency of 4% with two $40 \times 40 \times 0.3$ cm^3 plates coupled to c-Si cells and GaAs cells. This record has been surpassed many years later by several teams. Slooff et al. [54] published the world record of 7.1% LSC efficiency. This concentrator consists in a $5 \times 5 \times 0.5$ cm^3 with four GaAs cells coupled to the matrix cavity, which leads to $C_{geo} = 2.5$. They do not precise the GaAs cells efficiencies without LSC. The matrix was doped with two dyes (Coumarine CRS040 from Radiant Color and R305) concentrated at 30 and 100 ppm respectively. An other excellent result has been achieved almost simultaneously by Goldschmidt [44]. 6.8 % efficiencies with two dyes BA241 and BA8756 (5.1 % with one dye BA241) has been reported with four GaInP cells (15.4% efficiency without LSC). Collector size was $2 \times 2 \times 0.6$ cm^3. It means that the geometrical gain was 0.83, lower than 1.

Desmet et al. [55] published a 4.2% record efficiency using two edge-mounted c-Si cells (15.6% mean efficiency) with two dyes mixture R305 and blue dye perylene perinone. LSC dimension was $5 \times 5 \times \times 0.5$ cm^3, leading to a geometrical gain of 5. Optical efficiency was 22%, leading to 1.11 concentration factor.

Some research has also been done using quantum dots (QD) instead of organic dye. Qualitative arguments in favor of QDs are better stability, high brightness and large Stokes shift [56]. One of their drawbacks is a greater difficulty to add QD in a matrix [57, 58, 59, 60]. QD quantum yield is also an issue compared to organic dyes. 60% PLQY has been reported [61] for CdSe core/multishell quantum dots. 3.97% efficiency has been reported [62] with a CdSe/ZnS core/shell QD (PLQY 57%). Collector size was $6.2 \times 6.2 \times 0.3$ cm^3 ($C_{geo} \approx 5$), solar cell efficiency was 18.3% efficiency without LSC. In this paper the matrix was liquid (toluene), which raises stability issue. Advanced QD luminescence spectra computation has also been treated in [63] to have a better knowledge of QD LSC. A recent article [64] presents encouraging results by engineering QD to improve its Stokes shift. They reach a concentration factor of 4.4 ($C_{geo} = 43$ and $\eta_{opt} = 0.102$).

For a more complete LSC efficiencies review, see [65, 66]. From the literature survey, the conclusions we can draw are that the high efficiency LSC share two common points: low lateral size and highly efficient bare PV cell. This remark leads us to make the choice of not choosing the power conversion efficiency η as the main figure of merit but rather the optical efficiency η_{opt} (or in a similar way the concentration factor $C = \eta_{opt} \times C_{geo}$). Choosing an highly efficient solar cell increases the global LSC efficiency, but does not reflect the intrinsic LSC quality.

Literature results cited above fall under the first generation of LSC. The concept of LSC generation was first introduced by D.J. Farrell in 2012 [67]. Idea of first generation assumes the existence of a second generation. D.J. Farrell defines a second generation LSC as a system in which photon transport is enhanced thanks to molecular (anisotropic dye for example) or optical methods. However in practice more efficient, second generation LSC lacks in maturity and are far more challenging to fabricate. In this regard, part II of this thesis deals with a system which can be qualified of second generation, even if it goes beyond the concept of LSC.

An overwhelming majority of literature results have been obtained for edge-mounted LSC configuration. Very few studies have been carried out on bottom-edge mounted LSC configuration since it goes against the "natural" LSC waveguiding. Consequently, a majority of available ray-trace programs are designed for edge-mounted LSC. Therefore a specific algorithm modeling bottom-mounted LSC was required.

2.2 Modeling: Algorithm & Flowchart

Following the LSC description adopted in this thesis, there are two main technical solutions to compute a LSC: ray trace and thermodynamic modeling. Thermodynamics-based calculation was not addressed in this thesis, but explanations can be found in A. Chatten and co-workers publications [68, 69], as well as a comparison between the two approaches [70], which concludes that both methods are accurate. A third way of modeling, in Finite-Difference Time-Domain (FDTD), has been investigated [71] in the case of LSC embedded in a photonic crystal (to reduce Self-Absorption). Although efficient, it was done only in 2D.

Ray trace technique is a very common way of modeling LSC using a Monte Carlo algorithm [72, 73, 74]. A home-made code (LSC Vectorized Monte-Carlo Algorithm LSC-VMCA) has been written during this thesis in order to be able to modify it and obtain all the desired data. This section describes its principle, considered events and the inputs/outputs.

By definition a Monte-Carlo method is based on random events to determine a numerical value. In our case the numerical value will be the LSC optical efficiency $\eta_{\text{opt}} = \left(\frac{\text{nb. incoming photons}}{\text{nb. collected photons}}\right)$. Derive η_{opt} is interesting but do not help to understand the physics of LSC. Yet, knowing how the remaining photons $(1 - \eta_{\text{opt}})$ have been lost (which loss channels, which spectral repartition) contributes to understand the value of η_{opt}. Monte-Carlo technique is really well suited for this task since no additional work is required, except putting flags on the correct code lines. Finally, since Monte Carlo is based on random events, statistics must be done to have accurate results. Statistical data are also available and will be used in this thesis.

This code runs in 3 dimensions and uses Cartesian coordinates. 10^5 photons coming at normal incidence will be tested to be in a statistical regime and are treated independently. The independence property enables to parallelize the code to run faster. The photons have a spectral density similar to the AM1.5G which can be found on this website [12] [3]. LSC-VMCA flowchart is shown in fig. 2.7 and the main blocks will be described.

2.2.1 Flowchart: global-description

3. AM1.5G is a terrestrial reference for photovoltaic performance evaluation

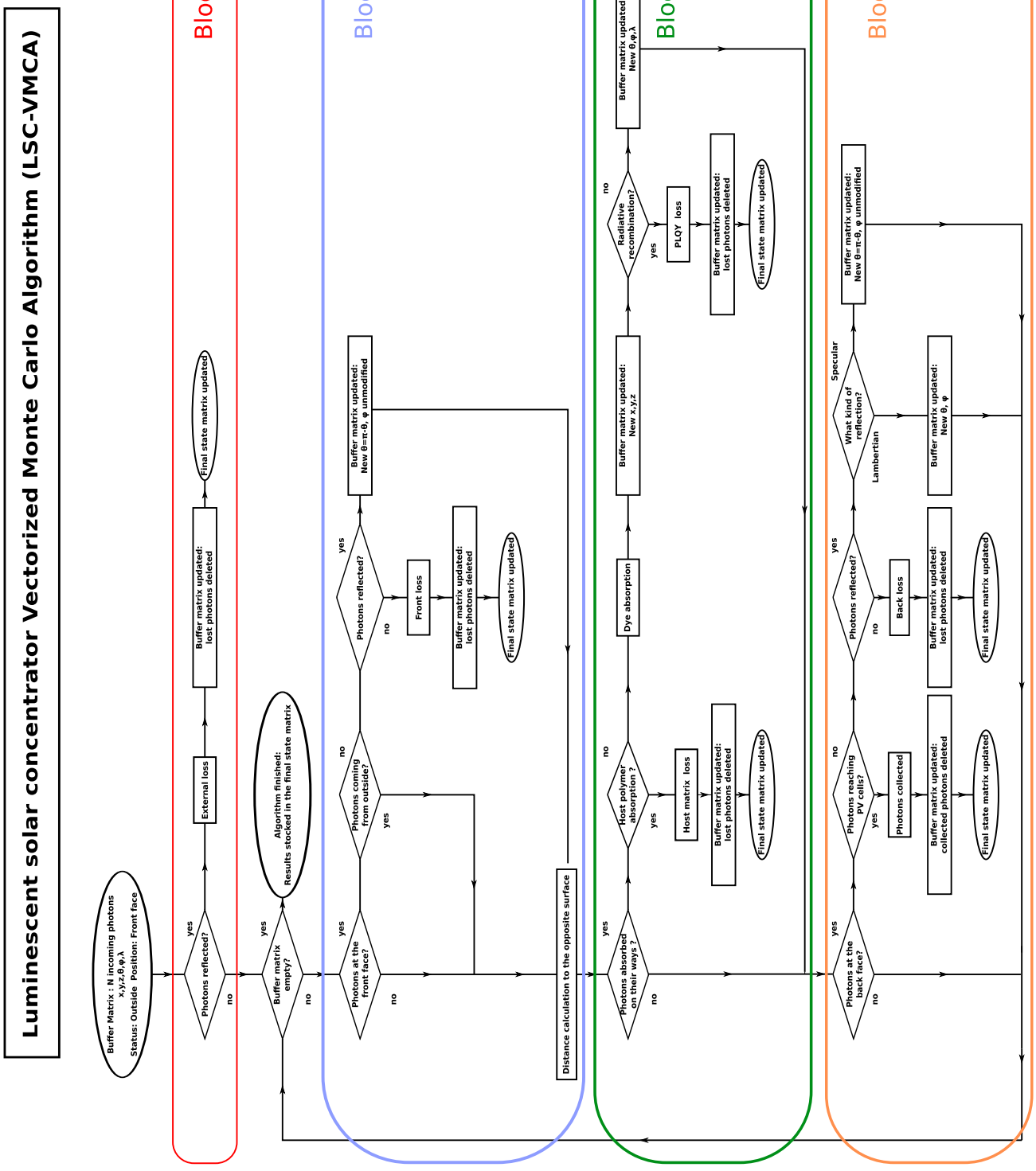

Figure 2.7: LSC-VMCA flow chart. Red block 0 corresponds to external loss. Blue (orange) block 1 (3) deals with all front (back) surface events respectively. Green block 2 deals with events inside the LSC

Photons must first enter the device and a random number for each photon is compared to the Fresnel reflection coefficient given in eq. (2.4). It corresponds to fig. 2.7 **block 0**. Once entered, photons are located on the front surface and are traveling toward the back surface. Inside the cavity, three situations are possible:

Block 1 : Photon is located at the front surface. Reflection is tested to know if it is transmitted (lost) or reflected (trapped). Reflection is tested according to $R_{\text{Fresnel}}^{\text{mat}\to\text{air}}$ if no PBS (cf. fig. 2.5) or to R_{PBS}.

Block 3 : Photon is located at the back surface. A test is performed to know if the photon hits a solar cell (collected) or the back reflector. If not collected, a test is done to know if it is reflected (trapped) or absorbed (lost). Then the new angles (θ and φ) are set according the reflector nature (specular or diffusive).

Block 2 : Photon is not on front or back surface. This situation is possible if a photon has been absorbed before reaching the surfaces. Matrix absorption is automatically a loss whereas dye absorption can be a loss or a re-emission, according the dye photoluminescence quantum yield. Re-emission leads to new wavelength and new azimuth and polar angles.

After solving an event and if the photon outcome is still not decided, then the distance separating the photon to the surface (to which it points at) is calculated and the probability of being absorbed along this distance is computed. If the photon is heading toward the front (back) surface and is not absorbed, it corresponds to block 1 (block 3) respectively. Block 2 occurs after photon absorption. Finally, if the photon coordinates are outside the edges, boundary conditions apply (periodic conditions or reflected/absorbed by a mirror).

2.2.2 Flowchart: quantitative description

The algorithm description has been up to now more qualitative than quantitative. The last part of this section deepens and quantifies the mathematical expressions used and will be summarized in table 2.1. All events will be tested by a random number $\xi \in]0,\ 1[$ (standard uniform distribution). Figure 2.8 depicts the conventions used in the code.

Each block is treated as follows:

Block 0, External External loss is dealt comparing ξ and $R_{\text{Fresnel}}^{\text{air}\to\text{mat}}(\theta, n_{\text{mat}})$ or $R_{\text{PBS}}(\lambda)$ if PBS is used.

Block 1, Front surface If no PBS is used, only Fresnel reflection can trap photons: ξ and $R_{\text{Fresnel}}^{\text{mat}\to\text{air}}(\theta, n_{\text{mat}})$ are compared. If a PBS is used, only its reflection coefficient $R_{\text{PBS}}(\lambda)$ is taken into consideration.

Block 2, Inside

- The distance d is calculated as follows:

$$\begin{aligned} d &= \frac{dz - z}{\cos\theta} \text{ if } \theta \leq \pi/2 \\ d &= \frac{-z}{\cos\theta} \text{ if } \theta \geq \pi/2 \end{aligned}$$

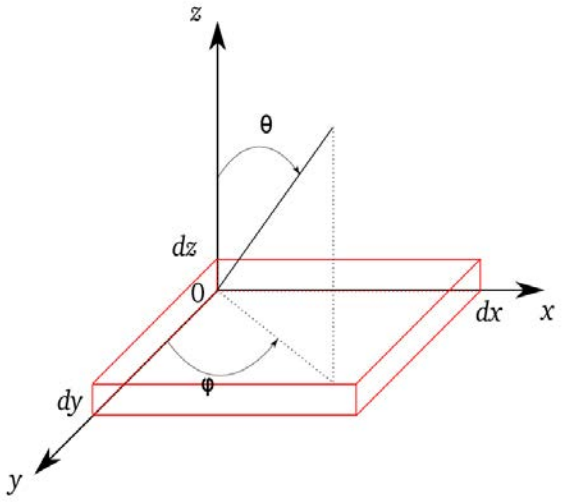

Figure 2.8: LSC schematic and axis definition

dz being the vertical dimension of the LSC.

- The probability of being absorbed on this distance d is: $\exp(-(\alpha_{\text{mat}}(\lambda) + \alpha_{\text{dye}}(\lambda)).d)$.
- If absorbed, the photon has only traveled a distance $d_{new} = \frac{-\log \xi}{\alpha_{\text{mat}}(\lambda)+\alpha_{\text{dye}}(\lambda)}$ with ξ being the same than the one used to determine the absorption.
- To know what kind of absorption occurs, the expressions $\frac{\alpha_{\text{mat}}(\lambda)}{\alpha_{\text{mat}}(\lambda)+\alpha_{\text{dye}}(\lambda)}$ or $\frac{\alpha_{\text{dye}}(\lambda)}{\alpha_{\text{mat}}(\lambda)+\alpha_{\text{dye}}(\lambda)}$ are tested against ξ.
- Radiative emission is dealt comparing ξ with PLQY.
- After emission, the new wavelength is set using the emission probability distribution function: $\mathcal{P}_{em}(\lambda) = \int_{q=\lambda_{min}}^{\lambda} e(q)dq$ (fig. 2.9).
- Emission is isotropic so photons are emitted uniformly into 4π steradians. New direction is computed by sampling uniformly φ_{em} in the range [0,2π] and $\cos(\theta_{em})$ in the range [-1,1], thus:

$$\begin{cases} \theta_{em} &= \text{acos}(2\xi - 1) \\ \varphi_{em} &= 2\pi\xi \end{cases}$$

Block 3, Back surface

- The probability to hit a solar cell (leading to photon collection) is given by the coverage fraction $f = \frac{1}{C_{\text{geo}}}$.
- If not collected, the photon has reached the back reflector. ξ is compared to R_{back} to test the reflection.
- If reflection occurs, the new angles are defined according the reflector nature:

Specular : $\begin{cases} \theta_r &= \pi - \theta_i \\ \varphi_r &= \varphi_i \end{cases}$ Lambertian : $\begin{cases} \theta_r &= \text{acos}(\sqrt{\xi}) \\ \varphi_r &= 2\pi\xi \end{cases}$

The demonstration of $\theta_r = \text{acos}(\sqrt{\xi})$ can be found in appendix A.

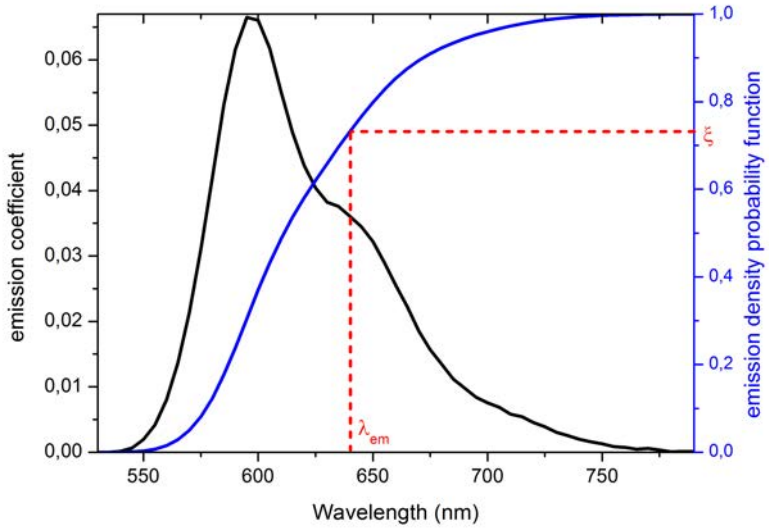

Figure 2.9: Emission probability distribution function $\mathcal{P}_{em}(\lambda)$ is derived from the emission coefficient $e(\lambda)$ and compared to ξ. In red: example for $\xi = 0.73$ giving $\lambda_{em} = 640$ nm

Table 2.1 summarizes the different events which may occur in a LSC as well as their location inside the LSC and their key parameters.

LSC-VMCA		
Where?	*Event?*	*Key expression(s)*
Outside	Enter LSC or reflected?	$R_{\text{Fresnel}}^{\text{air}\to\text{mat}}(\theta, n_{\text{mat}})$ or $R_{\text{PBS}}(\lambda)$
Front surface	Trapped or escaped?	$R_{\text{Fresnel}}^{\text{mat}\to\text{air}}(\theta, n_{\text{mat}})$ or $R_{\text{PBS}}(\lambda)$
Back surface	PV cell or reflector?	C_{geo}
	Reflected or absorbed?	$R_{\text{back}}(\lambda)$
Inside	Absorbed on a distance d?	$exp(-(\alpha_{\text{mat}}(\lambda) + \alpha_{\text{dye}}(\lambda)).d)$
	If absorbed, emitted?	PLQY
	If emitted, which wavelength?	$\mathcal{P}_{em}(\lambda)$

Table 2.1: Summary of LSC-VMCA events

Now that LSC-VMCA has been described, the next sections will be devoted to highlight this code capabilities.

2.2.3 Inputs/Outputs

Quality, usefulness and adaptability of a code are dependent on its Inputs/Outputs (I/Os). A high input number makes the code more versatile and able to deal with numerous situations and a high output number gives more information and enables a better understanding of the modeled device. We try to give the code as many degree freedoms as possible. Yet the geometry

was set to a rectangular homogeneous (n) cavity, mainly because of algorithmic and time issues. I/Os are given in tables 2.2 and 2.3:

Inputs							
LSC block	Ph. spectrum	Matrix	Dye	Back refl.	PBS	Geometry	Boundary cond.
Parameters	λ	$\alpha(\lambda)$	$\alpha(\lambda)$	$R_{\text{back}}(\lambda)$	with / without	x, y, z	periodic
	nb.	n	$e(\lambda)$	specular or lambertian	R_{PBS}	C_{geo}	R_{side}
	θ, φ	concentration	PLQY nb. (1-3)	with / without air gap			mat/air interface

Table 2.2: LSC-VMCA Inputs

Output							
Loss channels	Ext L.	Front L.	Back L.	Matrix L.	PLQY L.	Side L.	Collected
Statistical data		$\overline{hit}_f$		$\overline{hit}_b$		$\overline{abs}_{dye}$	$\overline{d}$

Table 2.3: LSC-VMCA Output. Loss channels: photon outcome is filed in the appropriate loss matrix as well as its wavelength. Statistical data: $\overline{hit}_f$ and $\overline{hit}_b$ corresponds to the number of times a photon hits the front (back) surface respectively. $\overline{abs}_{dye}$ is the number of times a photon is absorbed by the dye and $\overline{d}$ is the mean traveled distance before being lost or collected (in cm)

2.2.4 Algorithmics

Each time an event occur (for $\overline{hit}_f$, $\overline{hit}_b$ and $\overline{abs}_{dye}$), a counter is incremented whereas a distance counter is incremented after each elementary photon traveled distance (for $\overline{d}$). At the end of the calculation, these counters are normalized by the number of photons which are entered the LSC (total number of photons minus external loss).

Before ending with the code description, we would like to precise the algorithmic of LSC-VMCA. This code has been modified throughout this thesis to perform as fast as possible. 10^5 photons have to be tested as well as different LSC parameters. In addition, to study interdependencies, multiple parameters were tested simultaneously. In the case of two tested parameters, 50 values each, it leads to $10^5 * 50 * 50 = 2.5.10^8$ different photons, which themselves experience numerous events (absorption, reflection and so on). The solution adopted was to vectorize the main algorithm (dealing with one LSC configuration), and parallelize the input file to run multiple LSC configurations in parallel. The vectorization of the main algorithm is efficient especially as Matlab® is optimized for matrix operations. Instead of having a loop on each photon, the vectorization consists in creating a matrix with 10^5 lines which shrinks along with the number of photons treated (lost or collected). The parallelization of the input file is simply done using the Matlab® Parallel Computing Toolbox "parfor" function. As an example, a typical LSC simulation takes $\sim$ 4 seconds.

2.3 Big picture

Luminescent Solar Concentrator is a 40 years old concept which is experiencing renewed interest due to the rise of photovoltaics and more performing dyes. Its main interest is that it may combine high and low concentration advantages (high concentration factor without accurate sun tracking system). The LSC community goal is to achieve good optical efficiency with the larger geometrical gain. Multiple strategies have been explored to limit the different loss channels responsible to the rather low optical efficiency (generally less than 10%).

The different approaches to improve performance as well as most of the fabricated LSC concerns edge-mounted configuration (solar cell at the concentrator edges). This is due to the natural guiding effect to the edges. Although bottom-mounted LSC configuration has not been extensively studied in the literature, this thesis considers only this configuration. This choice makes sense for microcells array concentration because of fabrication issue and good theoretical potential.

To understand the bottom-mounted LSC, a modeling tool is mandatory. We have presented LSC-VMCA, which has been developed throughout this work. This tool enables to model numerous LSC systems with a vectorized Monte Carlo algorithm. It provides photon spectral repartition in the different loss channels completed by statistical data. Our first step in the study of microcells array and LSC coupling is to extensively use our numerical tool to evaluate theoretical LSC performances but also, even more importantly, understand what are the physics insights behind these results.

Chapter 3

LSC Physics

Contents

We have seen in the chapter 2 that the luminescent solar concentrator (LSC) is a device, which traps light until it reaches a solar cell or is lost. Although less popular than edge-mounted configuration (solar cells on luminescent sheet edges), we focus our study on the bottom-mounted configuration. Less intuitive, this configuration is best suited to concentration on micro-cells array because of fabrication issue.

LSC is ruled by 6 loss channels (external losses, non radiative deexcitation loss, front escape loss, host matrix absorption loss, back reflector loss, edge loss) plus one collection channel. As a reminder, LSC scheme and loss channels are reproduced below:

Optimizing LSC leads to reduce loss channels contributions for the benefit of the collection channel, i.e. an increase of the optical efficiency η_{opt}. We have also seen that aside from the optical efficiency, the concentration factor C requires a high ratio LSC area over PV cells areas (geometrical gain, C_{geo}). Since the optical efficiency is a decreasing function of the geometrical

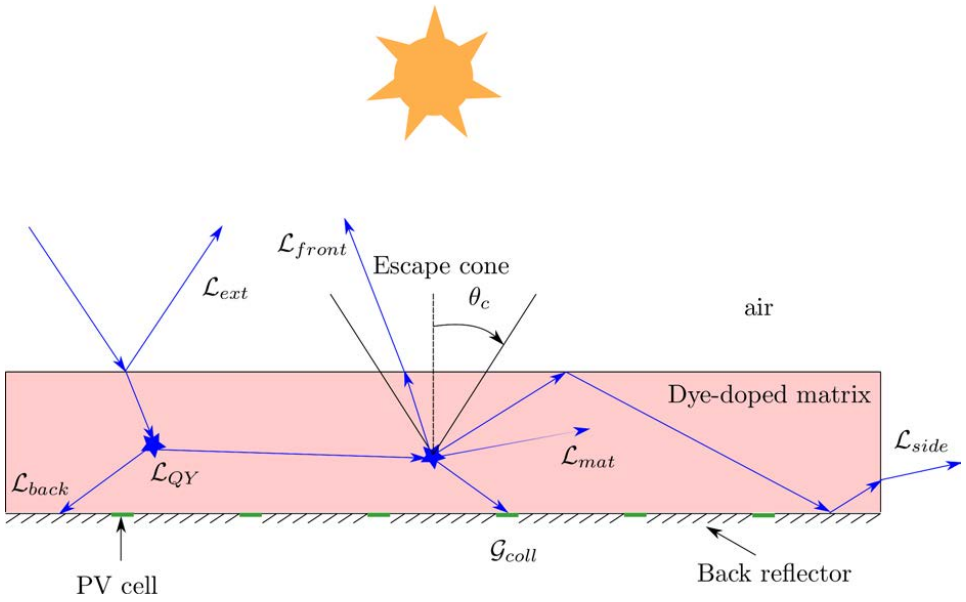

Figure 3.1: Schematic of a BM-LSC comprising loss channels. External loss $\mathcal{L}_{ext}$. Internal losses: Non radiative deexcitation $\mathcal{L}_{QY}$, Non trapping at the front surface $\mathcal{L}_{front}$, Absorption by the host matrix $\mathcal{L}_{mat}$, Back reflector absorption $\mathcal{L}_{back}$, Edge loss $\mathcal{L}_{side}$, Collected photons $\mathcal{G}_{coll}$

gain, the optimum trade-off must be found and consequently the physics of LSC must be understood in detail.

The luminescent solar concentrator is a highly interdependent system (an example has been presented in section 2.1.2), which complicates its comprehension. Although there are numerous physical parameters involved, they are limited in number. As a consequence, fine understanding of the all system may be achievable. This chapter exposes all the theoretical results obtained in this thesis regarding the classical LSC.

The first part deals with ideal and semi-ideal LSC. Indeed, the starting point of this chapter is to look at the all-ideal thermodynamic case to assess what is the LSC upper limit (section 3.1.2). This study has already been done by Rau et al. [75] which allows to compare our results to theirs. A good accordance is the first step to validate our code (the second step will be comparison to experiment, shown in section 4.2.2.3). Then LSC system will be progressively degraded, first by changing only one LSC material parameters among the following:

- Photoluminescence quantum yield QY
- Back mirror reflection coefficient R_{back}
- Photonic band stop reflection coefficient R_{PBS}

We call this case the semi-ideal LSC (section 3.1.3 to section 3.1.5). We choose to present these results by first giving numerical results, then by discussing them with simplified models. It helps to grab the physics and draw conclusions more general than the ones we have obtained on an particular configuration.

After that, reflection on the mismatch effect between dye and solar cell will be studied (section 3.2). The next step is to modify the dye absorption/emission spectra to design a semi-ideal dye before considering a real dye R305. While the ideal dye enables to simulate LSC system as close as possible to thermodynamic limits, R305 enables to assess what can be expected in practice whereas the semi-ideal dye (section 3.1) highlights how the transition between these two extreme cases occurs, and helps illustrating where to search for improved dyes.

Because sometimes numerical calculation may be a black box regarding physical phenomenon understanding, section 3.4 is a contribution to understand LSC behavior through a semi-analytical model. Based on results found so far, we will highlight what we believe to be the LSC fundamental contradiction and what kind of rupture can be brought as a response (section 3.5).

3.1 Thermodynamics limit: ideal dye case

3.1.1 Method

Loss mechanisms are studied modeling a rectangular bottom-mounted with a coverage fraction $f = \frac{1}{C_{geo}}$. Homogeneous PV cell repartition at the rear surface and periodic boundary conditions are used to avoid scaling effects compared to edge-mounted LSC. In such a system, only 5 basic loss mechanisms exist ($\mathcal{L}_{side} = 0$ due to periodic boundary condition).

The different LSC parameters are described below. We used a typical case for application, a cavity consisting of a transparent matrix (ideal transmission T=1 for all wavelengths) of refractive index 1.5 (close to Polymethyl methacrylate, a widely used polymer for LSC) with a thickness d of 5 mm. The host matrix is doped with a dye characterized by its photoluminescence quantum yield (QY) which is set to unity in the all-ideal case and will be lowered later.

The PV cells bandgap is set to 1.55 eV (800 nm) to match R305 (same emission tail) and was not optimized (bandgap choice will be discussed in section 3.3.3). A GaAlAs solar cell (with 8% Al), for instance, would have a suitable bandgap. 10^5 photons with AM1.5 spectral repartition are tested in parallel by LSC-VMCA algorithm. They all hit the LSC at normal incidence, with a random distribution along the x and y direction.

3.1.2 All-ideal system

In this section we use an ideal dye. Its absorption coefficient α_{dye} is taken constant over two ranges of the spectrum, $\alpha_{dye} = 3/d$ for $\lambda < \lambda_c$ and $\alpha_{dye} = 0.03/d$ for $\lambda_c < \lambda < \lambda_g$. λ_c stands for the cut-off wavelength and λ_g the solar cell bandgap wavelength (see fig. 3.2). $3/d$ ensures that almost all photons are absorbed at least one time (95% absorption probability on a single pass and 99.8% on a double pass). On the contrary $0.03/d$ implies that single-pass absorption probability is less than 3%. In addition, these values allow comparison to the literature [75]. It corresponds to a good balance between absorption of incoming light and self absorption of luminescent light. The emission spectrum is deduced from Kirchhoff's law [76]:

$$e(E) \propto n_{mat}.\alpha_{dye}(E).E^2.e^{-\frac{E}{kT}} \tag{3.1}$$

In addition, the use of a photonic band-stop filter (PBS) at the front interface improves the light trapping inside the LSC [77]. As seen before, its role is to transmit light absorbable by the dye (T=1 and R=0 for $\lambda < \lambda_c$), and reflect the emitted light (T=0 and R=1 for $\lambda_c < \lambda < \lambda_g$). Figure 3.2 shows the absorption and emission spectra for the ideal and R305 dye.

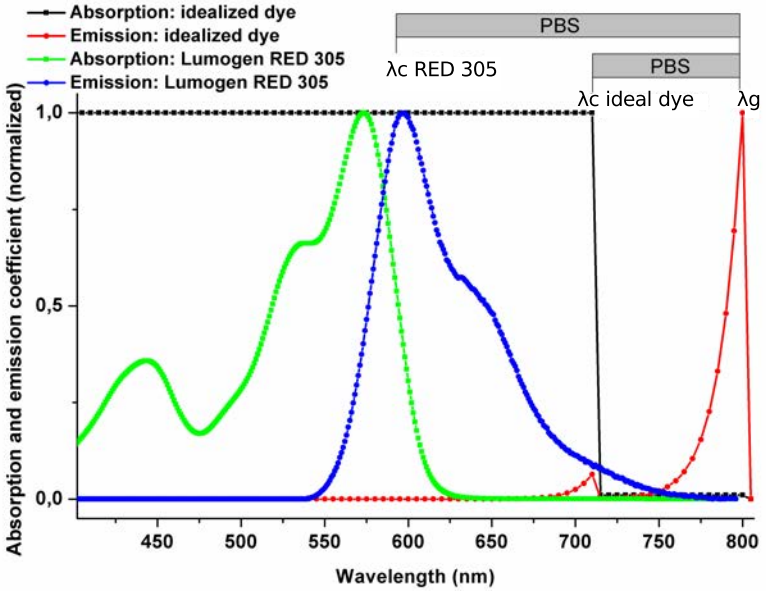

Figure 3.2: Normalized absorption and emission coefficients of R305 and an ideal dye with $\alpha_{dye} = 3/dz$ when $0 < \lambda < \lambda_c$ and $\alpha_{dye} = 0.03/dz$ when $\lambda > \lambda_c$, with $\lambda_c = 715$ nm (dz stands for the LSC thickness)

In an all-ideal configuration ($R_{back} = 1$, $PLQY = 1$, $\alpha_{mat} = 0\ cm^{-1}$), the two only ways of losing photons are photon reflection at the front surface before entering the device $\mathcal{L}_{ext}$ and front escape due to photons redirected into escaping modes because of self-absorption $\mathcal{L}_{front}$. These unavoidable losses can be minimized tuning the Stokes shift of the ideal dye for different coverage fractions, which is shown in fig. 3.3:

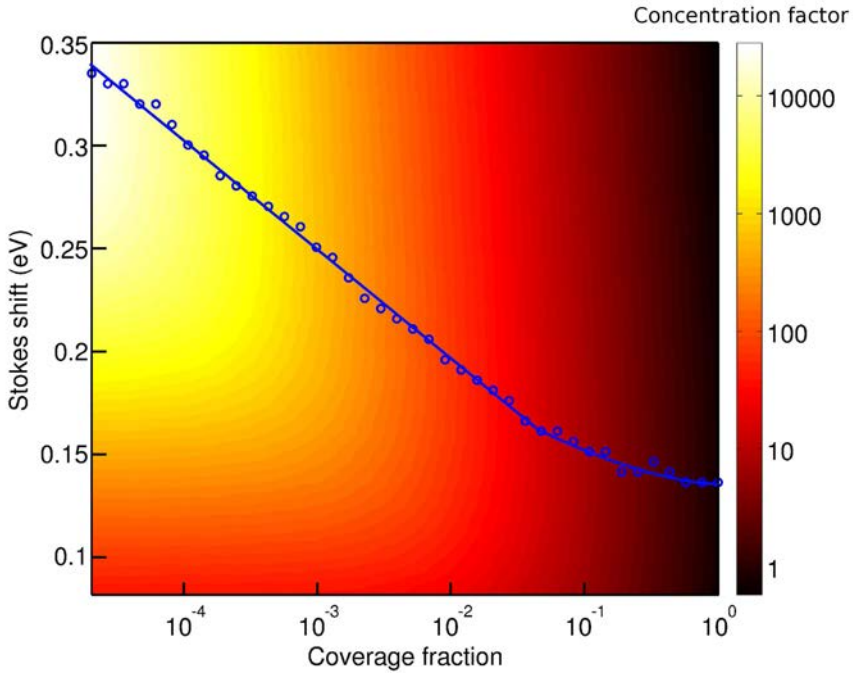

Figure 3.3: Color map of the effective concentration factor (logarithmic scale) as a function of the coverage fraction and the dye Stokes shift. Blue open circles correspond to the Stokes shift resulting in the best concentration factor at a given coverage fraction. The blue line is a guide for the eye of the optimum Stokes shift versus the coverage fraction.

Figure 3.3 shows that the Stokes shift should increase when the coverage fraction decreases to perform optimally. It is understandable considering that for a low coverage fraction, the mean optical path of photons must be high enough to reach a PV cell, resulting in a necessarily high optical efficiency and consequently a high Stokes shift. Indeed a high Stokes shift implies an efficient trapping by lessening low wavelength re-emission probability therefore self-absorption probability. However, it also involves more external loss (broader PBS reflection, which leads to a trade-off based upon the need for both high photons amount admitted in the LSC and efficient trapping).

In this simple situation, the concentration factor may be expressed as a function of the only two loss contributions, the coverage fraction and the Stokes shift ΔE:
$C = \frac{1}{f}.(1 - \mathcal{L}_{ext}(\Delta E) - \mathcal{L}_{front}(\Delta E, f))$

$\mathcal{L}_{ext}(\Delta E)$ is a monotonic decreasing function whereas $\mathcal{L}_{front}(\Delta E, f)$ is a monotonic increasing function of ΔE. Additionally, $\mathcal{L}_{front}(\Delta E, f)$ is negligible with respect to $\mathcal{L}_{ext}(\Delta E)$ for low (high) C_{geo} (f), that is why low ΔE is preferred for high f and high ΔE preferred for low f.

We now choose an ideal dye Stokes shift of 0.2 eV, which is an optimum for a coverage fraction around 0.01. Figure 3.4 presents the all-ideal LSC performance, with and without PBS, and table 3.1 recapitulates the all-ideal LSC features

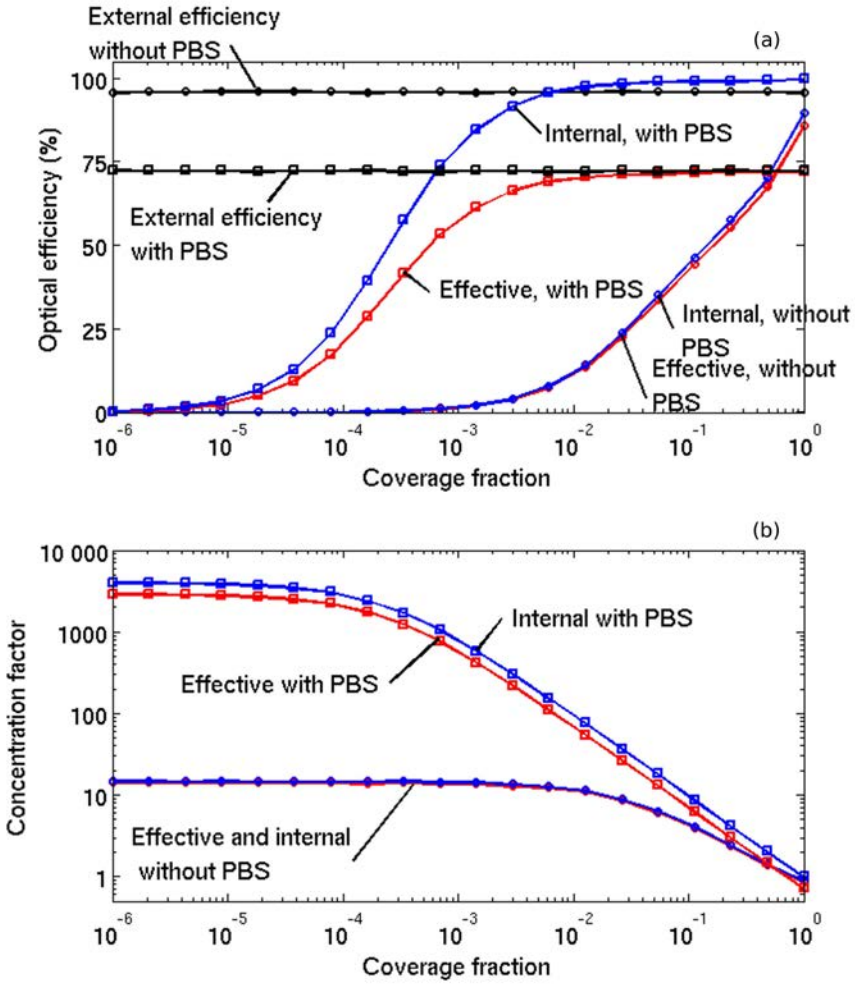

Figure 3.4: (a) Dependence of optical efficiency and (b) concentration factor versus the coverage fraction, for an ideal system with and without PBS. Internal values (blue lines) take into consideration only internal losses whereas effective ones (red lines) account for both internal and external losses. The two horizontal lines in (a) represent the external efficiency with and without PBS. It does not depend on the coverage fraction. Effective efficiency is the product of the internal and external efficiency.

All-ideal LSC parameter		
Matrix	*Dye*	*Reflector*
$n_{mat} = 1.5$	PLQY=1 $\Delta E = 0.2\ eV$	Specular
$\alpha_{mat} = 0\ cm^{-1}$	$\alpha_{max} = 3/dz$ $\Delta\alpha = 100$	$R_{back} = 1$

Table 3.1: All ideal system parameters

Figure 3.4 is in accordance with [39] which also used a ray-tracing algorithm. Optical efficiency is a monotonically increasing function of the coverage fraction f, whereas the concentration factors is a monotonically decreasing function of f. Optical efficiency tends to (without reaching) 0 at low coverage fraction as fast as the coverage fraction decreases, leading to a concentration factor saturation, which strongly depends on the use of PBS. The PBS increases the maximum concentration factor $c_{max} = 4058$ by more than two orders of magnitude and stabilizes the optical efficiency until $f \approx 10^{-2}$. Without PBS, the trapping depends only on total internal reflection (TIR).

$f \approx 10^{-2}$ threshold, found numerically, can be derived by a simple reasoning. The PBS high efficiency results from different conditions met together:

- Low absorption coefficient for emitted photon wavelength (ie. low Stokes Shift): $\alpha(\lambda_c < \lambda < \lambda_g) = \frac{3}{100dz}$
- Low probability to be emitted outside the photonic band-stop region: $\mathcal{P}_{em}^{esc} = \frac{\alpha_{\lambda<\lambda_c}}{P} \int_{E_{th}}^{\infty} E^2.exp\left(-{}^{E}/_{kT}\right) \approx 0.05$. P is a normalization factor, ensuring an unity probability to be emitted whatever the wavelength is.

With $\mathcal{P}_{em}^{esc} = 0.05$, 20 absorption events (on average) are necessary to be emitted outside the band-stop spectral range. Yet the mean distance to be absorbed is given by $\frac{1}{\alpha} = \frac{dz}{3}$ for the first absorption and $\frac{1}{\alpha} = \frac{100dz}{3}$ for the other 19 absorption events. Thus the mean distance to be emitted $\overline{d}_{em}^{esc} = \frac{dz}{3} + 19 \times \frac{100dz}{3} \approx \frac{1900*dz}{3}$. This number should be compared to the mean distance required to be collected $\overline{d}_{PV}$.

At a given coverage fraction, the mean number of back surface hit required is $1/f$, and the distance traveled on a back and forth is $2 \times 2 \times dz$ (first factor 2 comes from a back and forth, second factor 2 arises because photons evolve in 3D without being normal to the surface [78]), so $\overline{d}_{PV} = \frac{4dz}{f}$. On average, the PBS traps efficiently all the photons until $f < \frac{\overline{d}_{PV}}{\overline{d}_{em}^{esc}} = 6.3.10^{-3}$, which is in good accordance with fig. 3.4.

The maximum concentration factor can be analytically expressed writing it is related to the ratio of the incoming / outgoing photon density flux. It depends on the matrix refractive index and the dye Stokes Shift [75]:

$$c_{max}^{theo} = n_{mat}^2 \frac{\int_{E_g}^{\infty} \Phi_{bb}(E)dE}{\int_{E_c}^{\infty} \Phi_{bb}(E)dE} = n_{mat}^2 \left(1 + \frac{\int_{E_g}^{E_c} E^2 exp(-E/kT)}{\int_{E_c}^{\infty} E^2 exp(-E/kT)}\right) \tag{3.2}$$

With $\Phi_{bb} \propto E^2 e^{-E/kT}$ the black body spectrum. In our conditions, $c_{max} = 4058$, which is in good agreement (0.35% discrepancy) with the maximum concentration factor (4044) we have found with the use of our Monte Carlo code (see fig. 3.4). To summarize these results, we work on four values extracted from fig. 3.4. Two of them are written with lowercase letters and take into consideration only internal losses. The two other values describe the effective performance of the system (uppercase letters), taking into account all losses (both internal and external). They are listed in table 3.2.

	Internal losses		Total losses	
	c_{max}	f_{80}	C_{max}	F_{80}
no PBS	15	8.4 10^{-1}	14.4	5 10^{-1}
PBS	4044	1.1 10^{-3}	2937	NA

Table 3.2: Calculated key values of an ideal LSC system with and without PBS. C_{max}/c_{max} is the maximum effective/internal concentration factor. $C_{max} = \frac{N_{coll}}{N_{tot}}$ and $c_{max} = \frac{N_{coll}}{N_{tot}-N_{ext}}$. N_{ext} is the number of photons lost before entering the system, N_{tot} the total number of incoming photons and N_{coll} the number of photons reaching PV cells.

We can define F_{80}, the minimal coverage fraction needed to have an effective optical efficiency of 80% and f_{80}, the minimal coverage fraction needed to reach an optical efficiency of $0.8.\eta_{opt}(f = 1)$. In the PBS case, there is no coverage fraction enabling an effective optical efficiency of 80% because external losses are higher than 20% whatever the value of f. These above defined parameters will be used later to analyze the LSC robustness against non ideality and to easily compare the three different dyes. At this point, for an all ideal LSC system, concentration factor can be higher than 1000 for coverage fraction lower than 5.10^{-3}. In order to find out why real LSC devices have concentration factor several order of magnitude lower, non ideality are introduced.

3.1.3 Semi-ideal case: sensitivity analysis

We now investigate non ideal parameters influence on the system performances. We use the ideal dye (absorption and emission spectra) with non ideal LSC parameters. We restrict ourselves to studying only the LSC used with a PBS, because performances are too low without PBS.

3.1.3.1 Matrix absorption

The first parameter to be discussed is the matrix absorption coefficient α_{mat}. Figure 3.5 displays the concentration factor versus α_{mat} and C_{geo}.

Figure 3.5 shows that best concentration factors are obtained for high C_{geo} and low α_{mat}, which is perfectly intuitive. Indeed, the higher is C_{geo}, the higher will be the photon traveled distance before reaching the PV cell and therefore the larger will be matrix loss. More precisely, at a given geometrical gain, we can define a threshold value α_{mat}^{th} at the colormap bends (see fig. 3.5). For example $\alpha_{mat}^{th} \approx 2.10^{-3}\ cm^{-1}$ at $C_{geo} = 20$. Below α_{mat}^{th}, the concentration factor is almost unchanged, whereas an abrupt drop occurs above α_{mat}^{th}. The matrix absorption coefficient is not a cause of loss if its value is kept below α_{mat}^{th}. The threshold matrix absorption coefficient value is intimately linked with the geometrical gain and the matrix choice must be thought with a clear idea of the LSC geometrical gain. It is worth noting that for real system with more losses, tolerance on α_{mat} is better because it will reduce the photon mean pathlength.

Aside from α_{mat}^{th}, an other interesting parameter is the matrix absorption coefficient leading to 50% concentration factor drop (black dots on fig. 3.5). Additionally, some analytical elements can helps to give insight to numerical results.

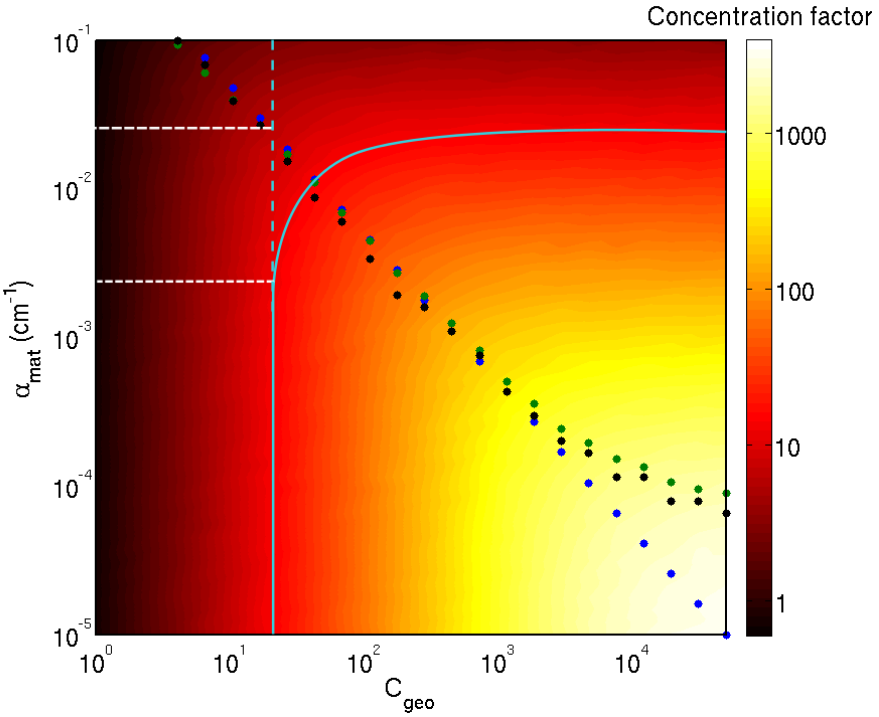

Figure 3.5: Color map of the maximum concentration factor (logarithmic color scale) for different α_{mat} and C_{geo}. Black dots corresponds to α_{mat} leading to 50% loss on the concentration factor. Blue dots represents eq. (3.3). Green dots is a variant of eq. (3.3) in which $4dzC_{geo}$ is replaced by $\overline{d}_{\alpha_{mat}=0}$. Turquoise plain line is an iso-concentration curve and turquoise dotted line is the deviation to the maximum concentration factor at $C_{geo} = 20$. The maximum value of α_{mat} not leading to concentration drop is called α_{mat}^{th}

On average, matrix absorption occurs on a pathway of $1/\alpha_{mat}$. On the other side, on average, photon collection in a PV cell occurs on a distance of $\overline{d}_{PV} = 4.dz.C_{geo} = {}^{4.dz}/_{f}$, as explained in the previous section. Thus, if $1/\alpha_{mat} = 4.dz.C_{geo}$, the two phenomena (matrix absorption / PV collection) are equiprobable. Working with the absorbance $A = \alpha dz$, the previous condition becomes:

$$A = \frac{1}{4C_{geo}} \tag{3.3}$$

If we compare the blue and black dots in fig. 3.5, results are in good agreement except at high geometrical gain ($C_{geo} > 1000$). To understand the deviation, one must compare α_{mat} to the mean photon traveled distance before being lost (or collected) when $\alpha_{mat} = 0$. This parameter will be noted $\overline{d}_{\alpha_{mat}=0}$. When no loss is taken into consideration (which is not physical but corresponds to a mathematical asymptotic limit), $\lim_{loss \to 0} \overline{d}_{\alpha_{mat}=0} = 4dzC_{geo}$, which corresponds to eq. (3.3), but in real devices $\overline{d}_{\alpha_{mat}=0} \ll 4dzC_{geo}$. Even in the all ideal case, the higher is the geometrical gain, the higher becomes the front escape loss, which lowers $\overline{d}_{\alpha_{mat}=0}$ from its limit $4dzC_{geo}$. The variable $\overline{d}_{\alpha_{mat}}$ cannot be given analytically but can be extracted from numerical calculation. It corresponds to green dots in fig. 3.5, which nicely fit black dots. Thus analytical approximation of some numerical result can be derived.

3.1.3.2 Back loss

The reasoning used in the previous section can be adapted to study the back loss. The mean back hit event before being lost by reflector absorption is $^1/_{1-R_{back}}$. Consequently, the mean distance before reflector loss is $\overline{d}_{back} = \frac{4dz}{1-R_{back}}$. In order to have equiprobability between back loss and collection, the following equality must be respected : $\overline{d}_{back} = \overline{d}_{PV}$ and consequently:

$$\frac{4dz}{1-R_{back}} = 4.dz.C_{geo} \text{ ie. } R_{back} = 1 - \frac{1}{C_{geo}} \tag{3.4}$$

Equation (3.4) shows that for C_{geo} higher than 100, R_{back} as high as 0.99 is the minimum to have 50% loss. Section 3.1.3.2 and section 3.1.3.2 shows the concentration factor as a function of $R_{back} \in [0-1]$ and $\in [0.9-1]$ respectively.

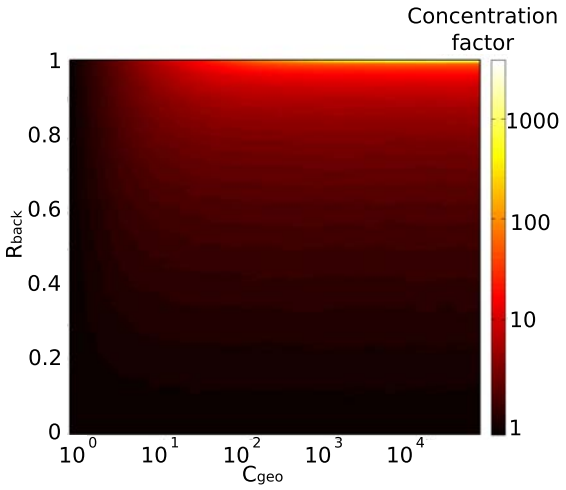

Figure 3.6: Concentration factor versus R_{back} and C_{geo}

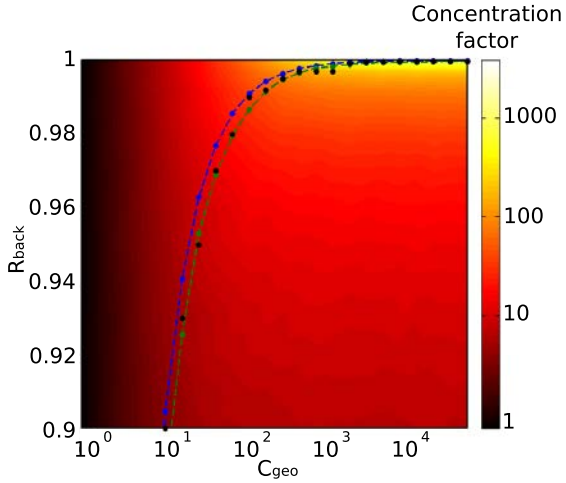

Figure 3.7: Zoom of section 3.1.3.2 for $R_{back} \in [0.9 - 1]$. Black dots represent, for a given C_{geo}, the reflector coefficient required to reduce fc by 50%. Blue, fit using eq. (3.4). Green: variant of eq. (3.4) replacing $4dzC_{geo}$ by $\overline{d}_{back}$.

3.1.3.3 R_{PBS} loss

As a reminder, R_{PBS} modification concerns only the PBS band stop spectral range. Transmission range is always 0 but reflection will vary between 1 (ideal PBS used before) and 0. Varying R_{PBS} influences front and external losses. The trade-off between these two losses depends on the geometrical gain, as shown in fig. 3.8:

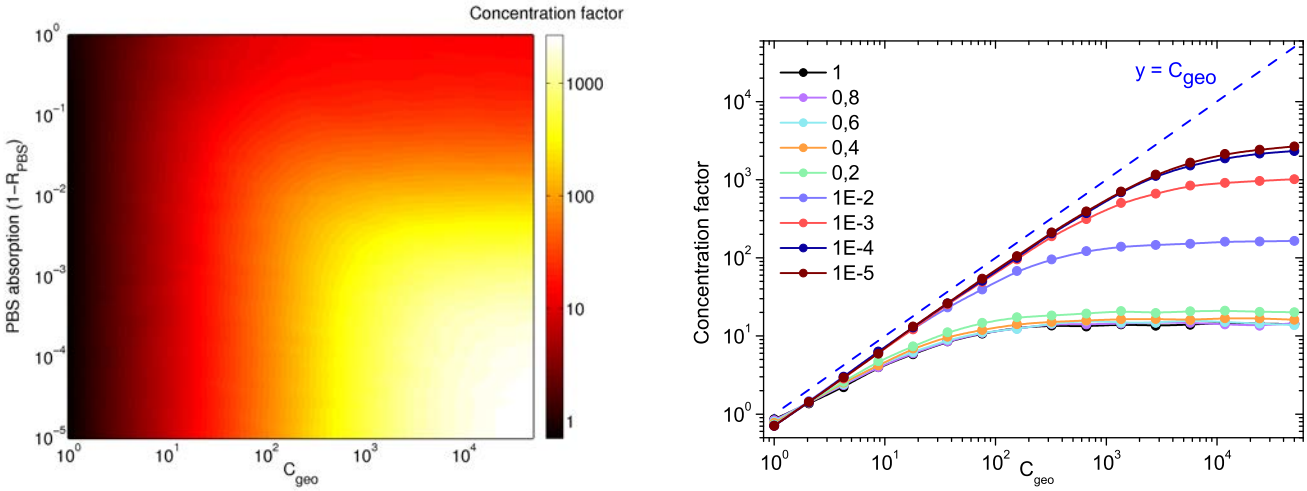

Figure 3.8: *Left*: Concentration factor versus $1 - R_{PBS}$ and C_{geo}. *Right*: Section view of the left plot for few values of $1 - R_{PBS}$. As a guide for the eyes, the plot $y = C_{geo}$ is shown.

Figure 3.8 shows that whatever the value of the PBS coefficient reflection, concentration factor is higher for high C_{geo}. For very low geometrical gain (smaller than 2), PBS is detrimental because it involves spectral shading (high $\mathcal{L}_{ext}$) which cannot be counterbalanced by a better front trapping (too high $\mathcal{L}_{front}$). When C_{geo} becomes higher than 2, PBS becomes beneficial. Yet if R_{PBS} is lower than 80% ($1 - R_{PBS} < 0.2$), concentration factor never exceeds 20.

Ideality discrepancy should be lower than 10^{-2} to gain order of magnitude for concentration factor. Last observation we can make is as follows: concentration factor decrease due to R_{PBS} ideality discrepancy is noticeable only for geometrical gain exceeding a certain threshold. This threshold value is low for high ideality discrepancy and reciprocally. It means that if an LSC has a geometrical gain lower than 10 (for example), the system will be quite tolerant on R_{PBS} ($R_{PBS} = 1$ leads to $C = 6$ against $C = 4$ $R_{PBS} = 0$). The lower is the geometrical gain, the more tolerant the system will be on R_{PBS}.

Finding analytical explanation of PBS sensitivity is more difficult compared to R_{back} and α_{mat} because photon wavelength plays a big role with a PBS. Averaged value must be taken over two spectral ranges. The last difficulty is that photon populations in these two spectral ranges are dynamic: shift occur because of absorption/emission process. For all these reasons, we won't investigate further the case of R_{PBS}.

3.1.3.4 PLQY loss

The last parameter analyzed is the photoluminescence quantum yield. The LSC tolerance on PLQY is shown in fig. 3.9:

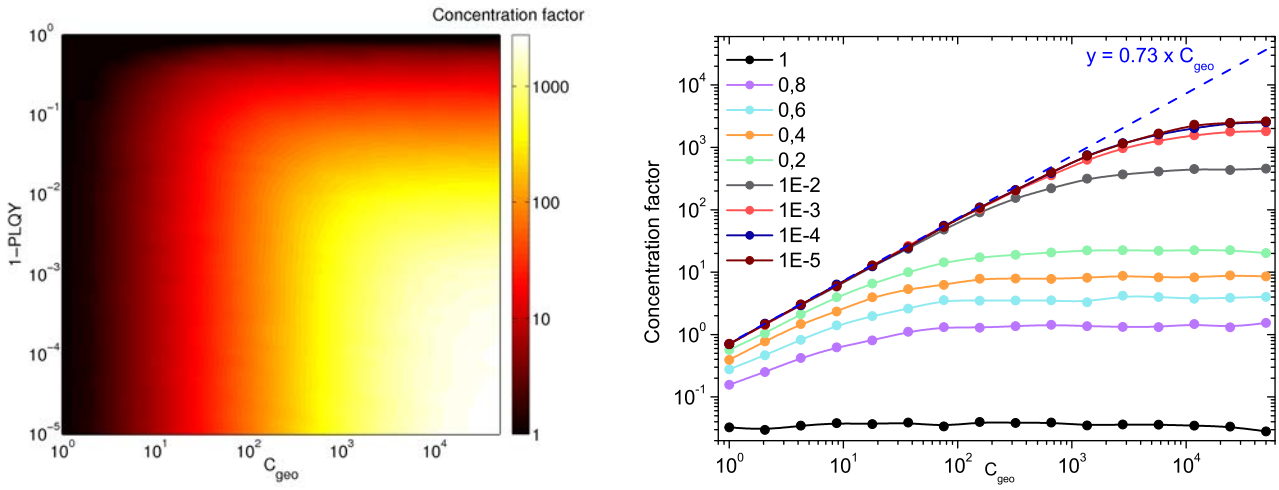

Figure 3.9: *Left*: Concentration factor versus $1-QY$ and C_{geo}. *Right*: Section view of the left plot for few values of $1-QY$. As a guide for the eyes, the plot $y = 0.73 \times C_{geo}$ representing the maximal concentration factor achievable is shown. 0.73 corresponds to the maximal optimal efficiency due to PBS when $R_{PBS} = 1$, which reflects 27% of photons.

PLQY sensitivity is quite different from R_{PBS}. Yet a common observation is that there is no point working at a high geometrical gain if PLQY is far from ideality. At PLQY=80% (green curve), concentration factor saturates at $C_{geo} \approx 100$. A huge difference with R_{PBS} is PLQY influence even at low geometrical gain. Indeed, dye absorption is a process which must occur at least once (ideally only once without self-absorption) whatever the value of C_{geo}. As a consequence, low QY is always detrimental.

For PLQY=0.95 (not shown in 3.9), C saturates at 100 at $C_{geo} \approx 1000$ and the concentration factor is almost ideal until $C_{geo} \approx 10$. The teaching from this number is that for low C_{geo} (in this case 10), there is no need to have extremely high PLQY since concentration factor is

(almost) the same for $PLQY \in [0.95 - 1]$. In others words, the sensitivity on PLQY is lesser at low geometrical gain. This is intuitive, true for all parameters and so quantification elements have been given.

The semi-analytical study of PLQY loss is complex because a photon loss requires an absorption, which is wavelength dependent, and a non radiative deexcitation. The mean absorption event number to be lost by PLQY is $\frac{1}{1-QY} = 1 + \frac{QY}{1-QY}$, with $QY \in]0, 1]$. The first absorption occurs with an absorption coefficient of $3/dz$ whereas the following ones should be treated with $\alpha = 3/100dz$. Thus the mean distance $\overline{d}_{QY}$ is given by:

$$\overline{d}_{QY} = \frac{dz}{3}\left(1 + \frac{QY}{1-QY}.100\right) \tag{3.5}$$

In conclusion, LSC sensitivity on non ideality varies according to the physical parameters and the geometrical gain. What is always true is that the sensitivity will be higher at high geometrical gain because all loss mechanisms are strongly dependent on the mean pathlength $\overline{d}$. The next step is to quantify the hierarchy between these losses.

3.1.4 Non ideality comparison

To compare the different losses contributions and their hierarchy, we find for R_{back}, R_{PBS}, $PLQY$ and α_{mat} the ideality discrepancy required to reduce fc_{max} $(= \frac{c_{max}}{C_{geo}})$ by 50, 90 and 99%. This study is done with various C_{geo}, ranging from 1 to 10^5 (fig. 3.10)

The discussion of these data must differentiate $1-R_{back}$, $1-R_{PBS}$ and $1-PLQY$ from α_{mat}. The first three parameters can be considered as efficiencies (of reflection or radiative emission), without unit, $\in [0, 1]$ whereas α_{mat} is the absorption coefficient and has a unit (cm^{-1} in fig. 3.10, m^{-1} in international system unit), $\in [0, +\infty[$. Yet, they all represent ideality discrepancy.

In these LSC systems, the sensitivity hierarchy differs with the geometrical gain. At high geometrical gain, sensitivity hierarchy is $PLQY < R_{PBS} < R_{back}$ ($<$ means "less sensible than"). As C_{geo} reduces, PLQY becomes more and more sensible compared to the two others considered parameters, to the point where PLQY sensibility becomes higher than R_{back} or R_{PBS} for very low C_{geo}. Indeed, the lower is C_{geo}, the lower is the necessity to have a good trapping at back and front surface, and consequently the lower is the sensitivity on LSC parameters ruling these two reflections. On the other hand, even at $C_{geo} = 1$, dye single-pass absorption probability is 95% (see section 3.1.1) and therefore LSC is still sensitive to PLQY.

It is worth noting that the back reflection coefficient is always more sensible than the PBS reflection coefficient. It can be understood knowing that reflection at the back surface depends only on R_{back} whereas both TIR and R_{PBS} contributes to the front reflection. Even if there is no PBS, total internal reflection contributes to front reflection whereas back reflection is impossible without back reflector.

Matrix absorption coefficient is also a sensitive parameter. However, α_{mat} values ranging from 10^{-4} to 10^{-2} are more realistic for real materials than for absorption coefficient (1-R) or non radiative probability (1-PLQY).

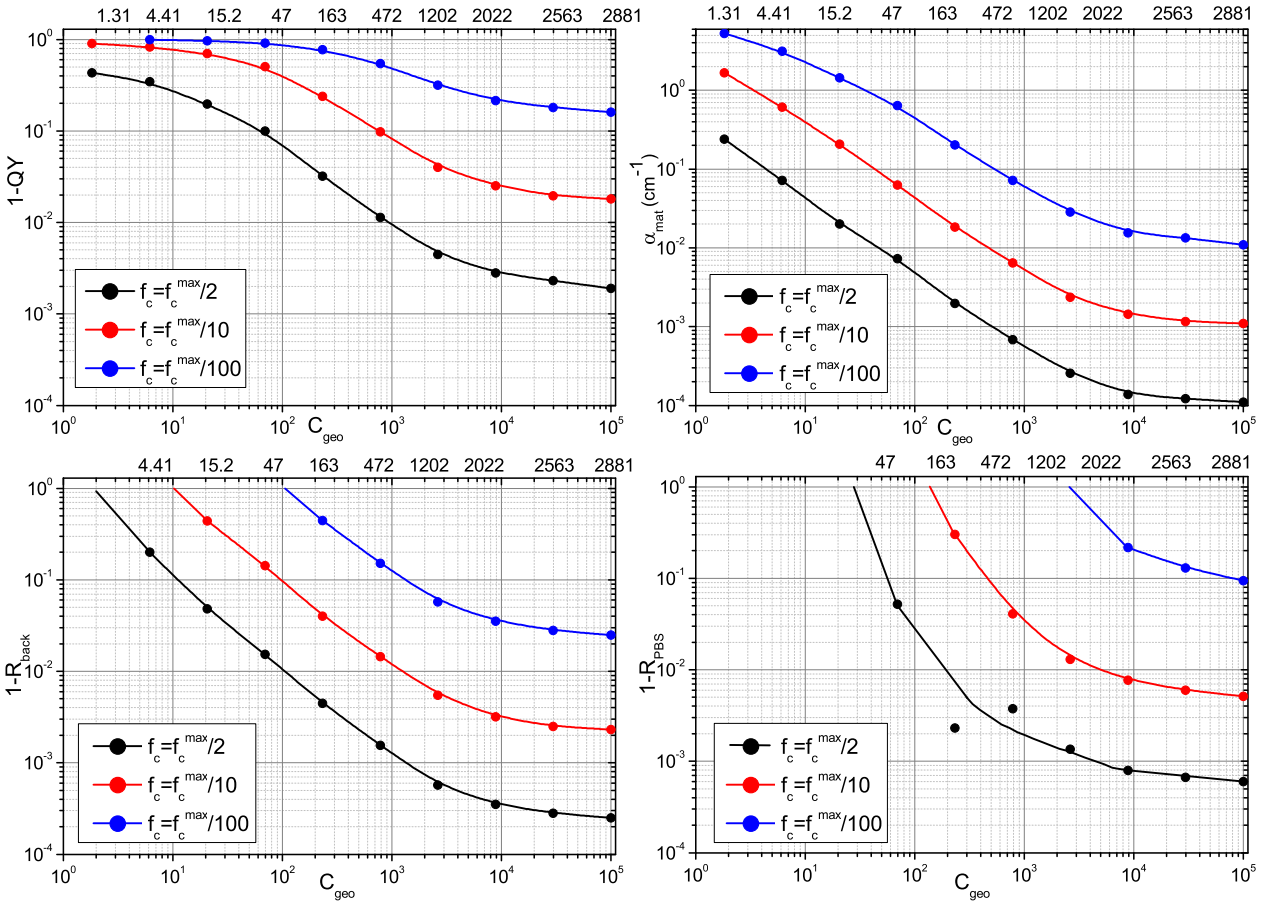

Figure 3.10: Effect R_{back}, R_{PBS}, $PLQY$ and α_{mat} on the concentration factor. On each Y axis is represented the ideality discrepancy. *Top left*: non radiative probability $(1 - PLQY)$. *Top right*: the matrix absorption coefficient which represents the ideality discrepancy if non zero. *Bottom left*: the reflector absorption coefficient $(1 - R_{back})$. *Bottom right*: the transmission coefficient (assuming the PBS does not absorb) $(1 - R_{PBS})$. The top X axis represents, for each C_{geo}, the maximum concentration factor fc_{max}. The ideality discrepancy required to divided fc_{max} by 2, 10 or 100 is given by the curves in black red and blue respectively.

3.1.5 Interdependencies of non ideality

A LSC is a system which exhibits highly correlated parameters. An intuitive example is the correlation between the PLQY and the dye spectral overlap. The overlap between absorption and emission spectra rules the probability of self absorption, which will enhance non radiative losses if the PLQY is not ideal. Thus, the sensitivity on the PLQY will be higher with a greater overlap. More generally, all parameters are correlated together, even if they seem independent. As an example, the interdependency between R_{back} and $PLQY$ is presented in fig. 3.11.

Figure 3.11 does not exhibit a diagonal symmetrical axis meaning that one loss is more damaging than the other one. The iso-loss boundary (blue curve) is shifted up with respect to the diagonal axis, meaning that R_{back} is more prejudicial than PLQY, which is consistent with fig. 3.10. This is confirmed by iso-concentration factor curves (black) which have a non unity slope (0.58). Thus, the level of performance degradation due to non-ideal quantum yield is strongly correlated to R_{back} and reciprocally.

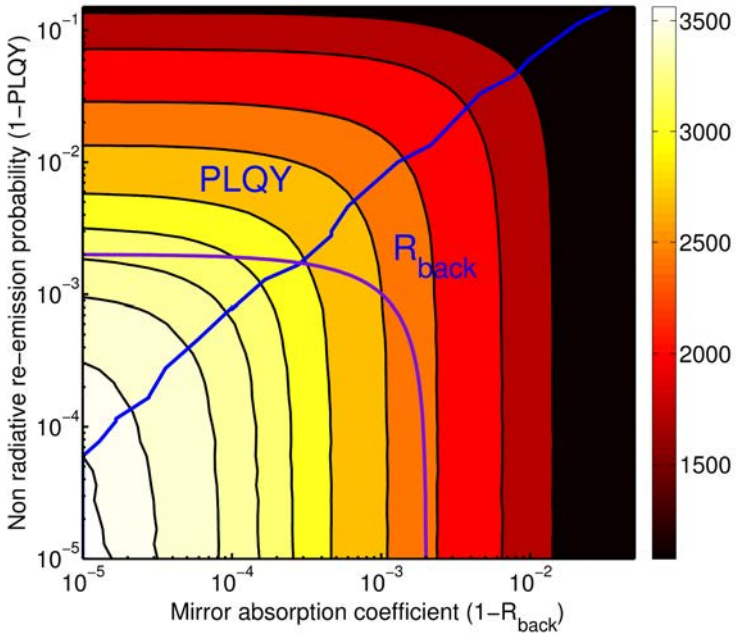

Figure 3.11: Color map of the maximum concentration factor (logarithmic color scale) for different reflector absorption coefficient ($1 - R_{back}$) and non radiative loss probabilities ($1 - PLQY$) at $f = 10^{-6}$. Black curves are iso-concentration, the blue line separates the two domains in which the PLQY loss is higher than R_{back} loss (upper domain) and reciprocally (lower domain). As a guide for the eye, the violet curve represents a linear plot.

Even if there is no trivial relation between R_{back} and PLQY, they are linked somehow and this link may explain the non linear correlation. The link on all LSC parameters is hidden in their influences on what we call "mean basic event occurrence" (MBEO). Some have already been used in this chapter. We define four MBEOS: mean front and back hits event ($\overline{hit}_f$ and $\overline{hit}_b$), mean dye absorption event ($\overline{abs}_{dye}$), and mean traveled distance ($\overline{d}$). One illustration is the example already given on overlap and the quantum yield correlations. Non radiative deexcitation depends on $\overline{abs}_{dye}$, which in turn depends on the overlap: $\overline{abs}_{dye} \leq 1$ if the overlap is zero but can be higher for non zero overlap. However $\overline{abs}_{dye}$ does not depend only on the overlap. A high mean optical path (corresponding for instance to a low coverage fraction) will enhance the probability of self absorption and so will increase $\overline{abs}_{dye}$. This is also the case for others LSC parameters such as the back reflection coefficient. A low R_{back} greatly reduces the mean optical path, which in turn reduces $\overline{abs}_{dye}$, and consequently reduces the effect of a non ideal photoluminescence quantum yield.

Reciprocally, the value of PLQY affects the system sensitivity on R_{back} by the same mechanism. Thus, there is a fine balance to find, in order to perform optimally, knowing that each loss depends on its LSC parameter (PLQY for non radiative loss, R_{back} for back loss and so on) but also on all other parameters via MBEOs which make them non linearly interdependent. Since MBEOs are correlated in a complex way with LSC parameters, predicting analytically the system losses is challenging. That explains why numerical simulation is used to understand the physics of LSC.

At this point, we have seen that non ideal parameters drastically lower LSC concentration factor. We have also seen that the loss channels are inter-dependent and we have investigated in more depth some particular behaviors. A part of the non-ideality interdependency is due to Self-Absorption. Self-Absorption is not a loss mechanism in itself but contributes greatly to enhance losses inside the device. Without PBS, its detrimental effect is straightforward. Indeed, the front trapping is due to TIR, which is based on photons angle conservation (to avoid escape cone emission): SA gives at least a second opportunity to re-emit photons in the escape cone. A second obvious effect of SA is $\mathcal{L}_{QY}$, which directly depends on the number of dye absorption $\overline{abs}_{dye}$.

Aside from these two effects, Self-absorption influences all internal loss channels via MBEOs. Indeed, the MBEO representing self-absorption is $\overline{abs_{dye}}$ and we will see in section 3.4.3 that it indirectly influences all loss channels equations.

Before moving to more realistic dyes, we want to highlight the effects of dye / solar cell gap mismatch.

3.2 Mismatch effect between dye and solar cell bandgap

Before introducing non ideal dye, it is interesting to understand the effect of the mismatch between the dye and the solar cell bandgap. To introduce a mismatch, one can keep the ideal dye and decrease E_g or keep E_g and shift the dye absorption coefficient to higher energies. We have chosen to keep the solar cell bandgap to be able to have a better comparison. Indeed playing on E_g will reduce the open circuit voltage and therefore make the comparison less conclusive. So the Stokes shift is conserved and is fixed to 0.2 eV.

For different C_{geo}, the dye absorption is shifted and the PBS modified accordingly ($R_{PBS} = 1$ only on the 0.2 eV range after the dye bandgap) as shown in fig. 3.12a. Results are displayed in fig. 3.12b

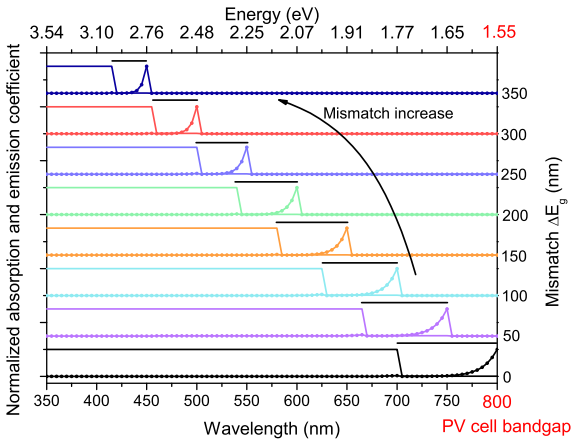

(a) Dye emission and absorption coefficient introducing a mismatch with the solar cell bandgap. Black lines represents the PBS reflecting spectral range

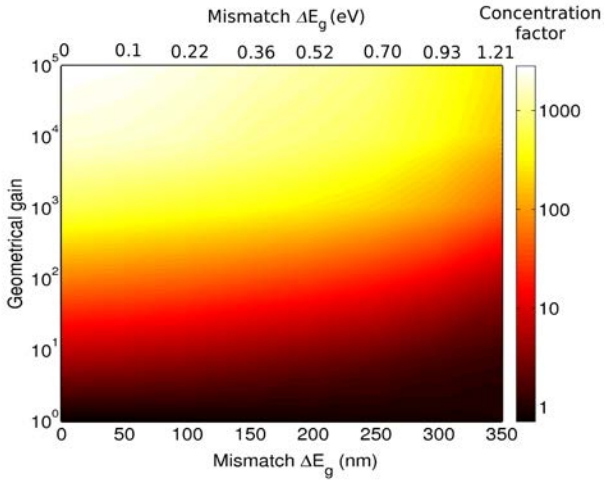

(b) Concentration factor as a function of the mismatch and geometrical gain

Figure 3.12: Effect of a mismatch between dye and solar cell bandgap.

$\mathcal{L}_{ext}$ decreases as the mismatch increases because the PBS spectral range of reflection shrinks (see fig. 3.12a). $\mathcal{L}_{ext}$ being independent of the geometrical gain, at a given mismatch the geometrical gain (or coverage fraction) influence is exerted only on $\mathcal{L}_{front}$, which is the only other loss mechanism possible in this ideal LSC.

Without mismatch, the optical efficiency experiences a plateau on the coverage fraction interval $[10^{-3}, 1]$ (see fig. 3.4). Aside from shortening this plateau, the mismatch shifts it to lower coverage fraction (x-axis) and lower optical efficiency (y-axis), as shown in fig. 3.13a.

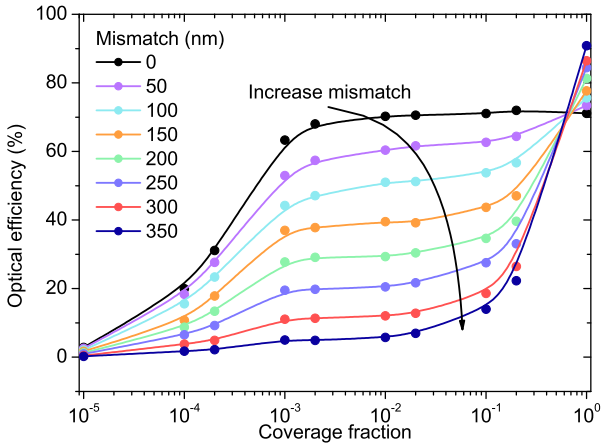

(a) Optical efficiency as a function of the mismatch and coverage fraction.

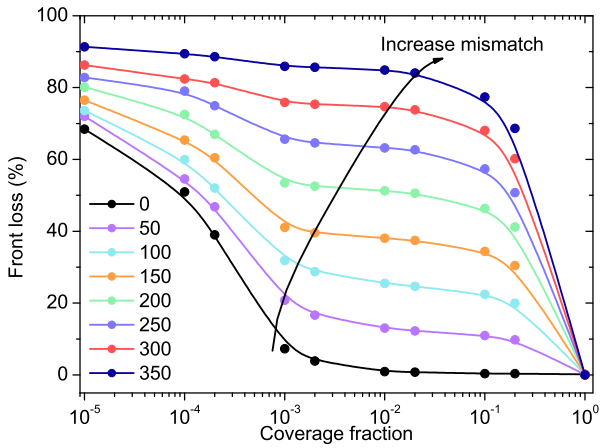

(b) Front loss as a function of the mismatch and coverage fraction.

Figure 3.13: Effect of a mismatch between dye and solar cell bandgap on the optical efficiency (a) and the front loss (b)

The plateau behavior on the optical efficiency is directly correlated with the front loss shown in fig. 3.13b. The mismatch induces a spectral range (larger with a high mismatch) with no dye emission or absorption. In this interval, the probability for a photon to be collected is only $1/C_{geo}$ without PBS trapping opportunity, which greatly reduces the optical efficiency.

Finally one can introduce non ideality discrepancies to assess the mismatch influence in the semi-ideal LSC case. We introduce two ideality discrepancies, $R_{back} = 0.95$ and $PLQY = 0.95$. Results are displayed in fig. 3.14:

With ideality discrepancies, the concentration factor fig. 3.14f is far more sensitive to the mismatch and very low (highest value around 12). $\mathcal{L}_{back}$ and $\mathcal{L}_{QY}$ exhibit the same sensitivity to C_{geo} and ΔE (high loss at high C_{geo} and low ΔE) to the detriment of $\mathcal{L}_{front}$, which becomes very low at low ΔE. When looking at $\mathcal{G}_{coll.}$, the mismatch improves the number of collected photons at very low geometrical gain. This is due to the fact that for this range of C_{geo}, a dye induces more loss than benefits. An increased mismatch tends to minimize the dye influence and therefore converges to the case without dye. On the contrary at high geometrical gains ($C_{geo} > 100$), the number of collected photons is almost zero and very slightly dependent on the mismatch.

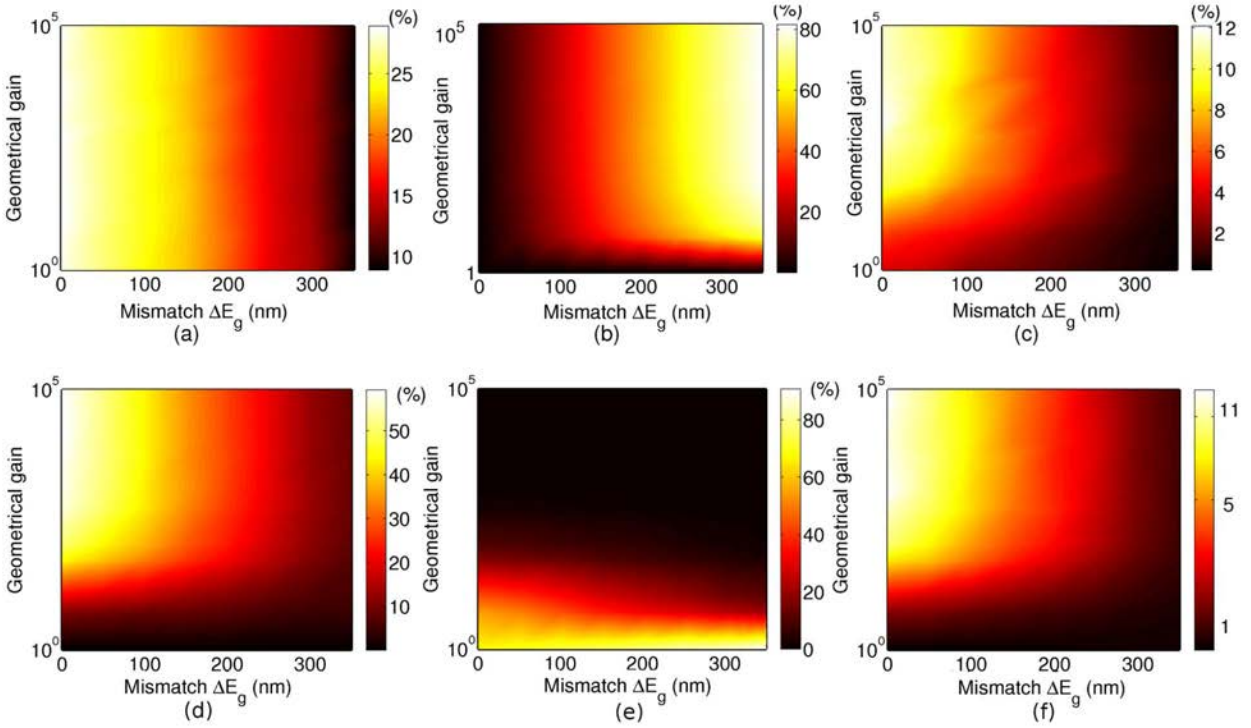

Figure 3.14: Effect of a mismatch between dye and solar cell bandgap with $R_{back} = 0.95$ and $PLQY = 0.95$. (a) $\mathcal{L}_{ext}$. (b) $\mathcal{L}_{front}$. (c) $\mathcal{L}_{QY}$. (d) $\mathcal{L}_{back}$. (e) $\mathcal{G}_{coll.}$. (f) Concentration factor.

We may conclude that the mismatch between the dye and the solar cell bandgap can be very prejudicial, even at high coverage fraction. This dependency is exacerbated when LSC parameters are not ideal, which will be the case in real systems. In the real system case (section 3.3.2), we will see that a mismatch of more than 50 nm exists, which will automatically reduces the performances.

3.3 Toward realistic LSC

3.3.1 Semi-ideal dye

To be able to compare a realistic LSC with a commercial dye to an idealized concentrator, we adapt the ideal dye to the commercial one with the help of a semi-ideal dye. This dye absorption spectrum has the same absorption and emission shape as the ideal dye but is modified to better match R305.

The absorption spectrum is modified in order to fit the emission probability density function (abbreviated epdf, cumulative sum of the normalized emission coefficient) and the absorption probability of R305, keeping the absorption stair shape of the ideal dye. The fit leads to a semi-ideal dye with $\alpha = 3/d$ when $0 < \lambda < \lambda_c$ and $\alpha = 0.003/d$ when $\lambda_c < \lambda < \lambda_g$, with $\lambda_c = 615$nm and $\lambda_g = 675$ nm (d stands for the LSC thickness). The new absorption spectrum and emission probability density function are shown in fig. 3.15.

The semi-ideal dye exhibits a higher probability to emit in the low wavelength emission peak as compared to the ideal dye. This leads to two main consequences: higher PLQY losses

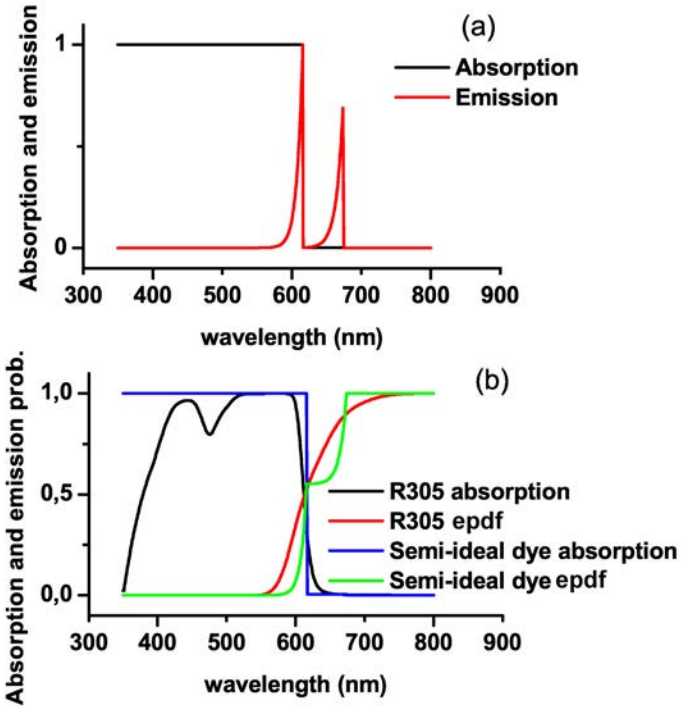

Figure 3.15: (a) Normalized absorption and emission spectra of the semi-ideal dye. (b) Comparison of R305 and semi-ideal dye absorption and emission probability density function. The emission probability function is preferred to the emission coefficient because this function is used by the Monte Carlo algorithm to compute the dye emission (see section 2.2.1).

through more SA processes and less efficient PBS trapping. The maximum concentration factor achievable is 1904 against 4044 for the ideal dye, which is the direct consequence of the lower Stokes shift (0,179 < 0,200 eV). These results are also consistent with fig. 3.3.

The conclusion is that the Stokes shift is not the main cause for losses, but rather the lack of abruptness of the absorption threshold.

3.3.2 Real dye

To address the realistic LSC issue, we have modeled the real dye with the absorption and emission spectrum of R305 described in section 2. The dye concentration is 270 ppm, which corresponds to a probability of 0.99 for a photon of 475 nm (valley in the absorption coefficient spectrum in fig. 3.15) to be absorbed on twice the LSC thickness.

Before going further, one can compare on fig. 3.16 the influence of R_{back}, $PLQY$ and R_{PBS} for the three dyes considered: the ideal, semi-ideal and R305 dye. The PLQY is not a free parameter for the R305 dye but varying its value highlights the influence of the absorption and emission spectra shape on non radiative loss.

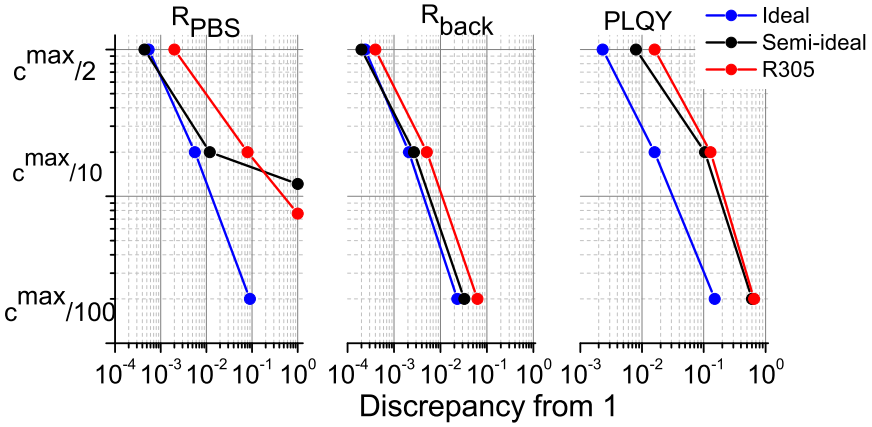

Figure 3.16: Effect of R_{back}, PLQY, R_{PBS} non ideality on the concentration factor for three different dyes.

Concentration factors in fig. 3.16 are normalized to the maximum achievable concentration factor C_{max}, but C_{max} is different for the three dyes: 4044, 1904, 1440 for ideal, semi-ideal, R305 dye respectively. These concentration ratios are still high (above 1000), even in the case of the commercial dye. As expected, non ideality tolerance with the semi-ideal dye is lower compared to R305 but higher than the ideal dye. This trend may be explained knowing that a high c_{max} implies a high mean optical path and consequently a high LSC parameter sensitivity. The accident point for R_{PBS} in the semi-ideal case arises because the PBS trapping effect is poor and consequently even with no PBS ($R_{PBS} = 0$), the drop of concentration factor cannot reach $C_{max}/100$. The bad trapping property is due to a higher probability of re-emission at wavelength not reflected by the PBS (see fig. 3.15a).

3.3.3 Realistic system

In this section we introduce a real LSC with R305 dye and realistic parameters. We address a LSC system with a PBS at the front surface. The considered PBS is an opal filter, which reflects or transmits photons according to the reflection spectrum shown in fig. 3.17left. This opal is far from ideal but is a reasonable example of an optical filter which may be used with LSC. Opal optical properties are angular dependent but we use only the normal incidence spectrum for the sake of simplicity. Boundary conditions are taken periodic. It will be seen in section 4.2.2.4 that potential side loss may be avoided by increasing LSC surface, which makes the periodic boundary condition hypothesis reasonable. The dye concentration value has been

optimized and worth 200 ppm to reconcile a high absorption and a low self-absorption. Results are shown in fig. 3.17 right:

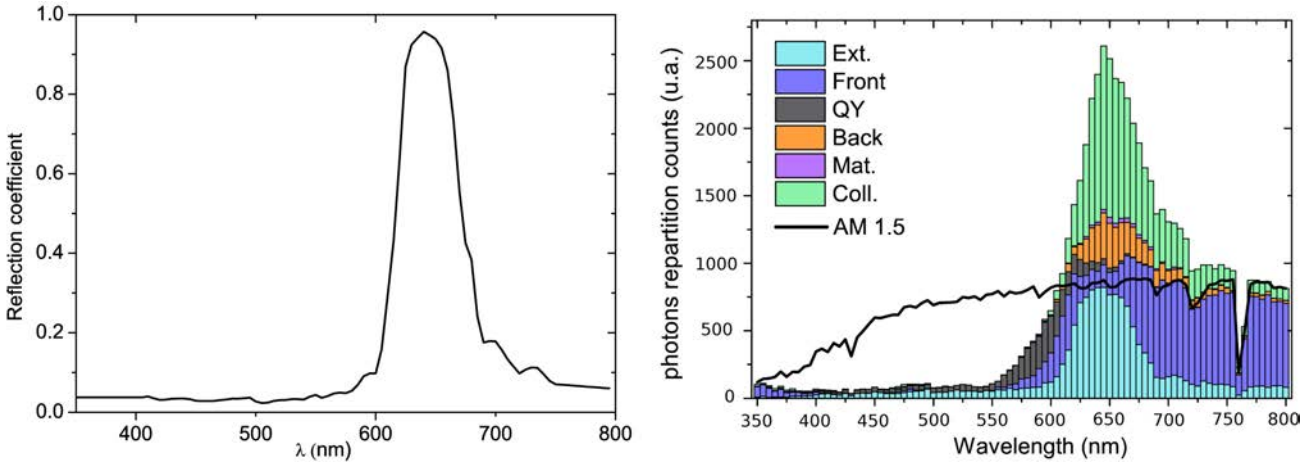

Figure 3.17: *Left*: Normal incidence reflection coefficient of a simulated opal, adapted from [79] shifting the entire plot of 50 nm to the high wavelength, which corresponds to a larger sphere size. *Right*: Spectral repartition of photons according to the different loss mechanisms. The LSC parameters have been set to: PLQY= 0.95, $R_{back} = 0.97$, $\alpha_{PMMA} = 10^{-3}\ cm^{-1}$ and $C_{geo} = 10$.

This LSC has a concentration factor of 2.64, which is a direct consequence of a 26.4% effective optical efficiency and $C_{geo} = 10$. This is far from the effective optical efficiency of the all ideal case of 72% (see fig. 3.4) or even the 53.8% in the case of a 100 nm mismatch (see fig. 3.13a for $f = 0.1$). This is mainly due to high external loss (23.7%) and a poorly effective PBS trapping (Front loss 35.4%). The bad trapping originates mainly from 700 to 800 nm (dye/solar cell mismatch) wavelength photons, which are not trapped by the PBS. There is almost no loss below 600 nm, which means that the dye is concentrated enough to absorb photons on two LSC thicknesses. One straightforward consequence is that reflection coefficients have to be close to unity only between 600 and 700 nm (after 700 nm, photons are not absorbed by dye and will be lost at the front surface), which releases the constraint on the reflection coefficient. Back loss is higher than PLQY loss, even though $R_{back} = 0.97$ is higher than PLQY = 0.95, which confirms the trend of a higher sensitivity of R_{back} than PLQY. Yet it can't be generalized for all dyes, especially those with a high overlap and highly concentrated. The matrix loss is less than 1% because in this particular case, the photon mean traveled distance $\overline{d}$ is around 10 cm and $\alpha_{PMMA} = 10^{-3}\ cm^{-1}$. Finally, side losses are not too detrimental in this configuration because $\overline{d}$ is only two times higher than lateral dimensions.

The main limitation of this configuration comes from the non optimal dye emission spectrum, which almost nullified the decrease in the front loss by increasing the external loss. Indeed, the emission spectrum is broad-band (200 nm width from 550 to 750 nm) and large compared to the useful solar spectrum for a 1.55 eV bandgap solar cell (450 nm width from 350 to 800 nm). Reflecting the emitted photons means blocking a high amount of incoming photons (due to broad-band emission at wavelength corresponding to high solar radiation) and a high fraction of useful photons. A more favorable case is to have a thinner emission spectrum to block less incoming photons while trapping them efficiently. An emission shifted to the near infrared

would also helps to increase the proportion of useful photons and also to use solar cells with a lower bandgap.

Briefly mentioned in the previous paragraphs, solar cells and dye bandgaps present a mismatch. One can illustrates the effect of the mismatch on the cell conversion efficiency η (and not only optical efficiency). To do that, the first step is to reduce λ_g from 800 to 600 nm and look at the loss channels evolutions. Then, we calculate the conversion efficiency using the following procedure:

- The short-circuit current (J_{sc}) is calculated as follows: $J_{sc} = \eta_{opt} \times \int_{350\ nm}^{\lambda_g} AM1.5(\lambda)$
- The open-circuit voltage (V_{oc}) is deduced from J_{sc} and C_{geo}: $V_{oc} = (E_g - 0.5) + ln(C_{geo} * \eta_{opt})$. The term 0.5 corresponds to $k.Tln\left(\frac{J_{sc}}{J_0}\right)$. This term is considered constant since it is greatly dominated by the dark current J_0. This formula is wrong for low J_{sc} (low λ_g consequence) but this range is of little interest since performances are bad.
- The Fill Factor (FF) is deduced from V_{oc} according the empirical formula [13] : $FF = \frac{\widetilde{V}_{oc} - ln(\widetilde{V}_{oc}+0.72)}{\widetilde{V}_{oc}+1}$, with $\widetilde{V}_{oc} = \frac{q}{k.T}V_{oc}$

Loss channels evolution as a function of λ_g is shown in fig. 3.18:

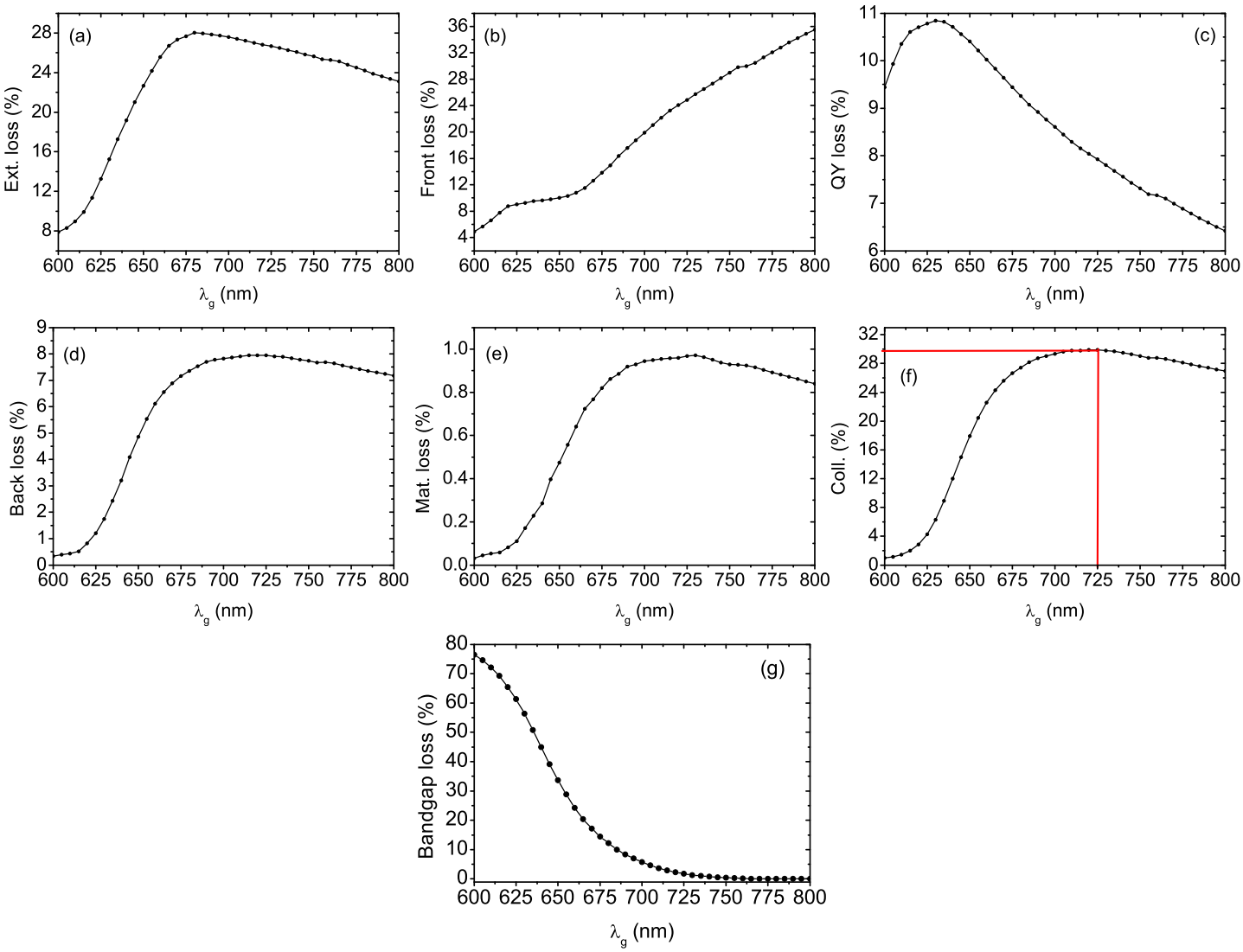

Figure 3.18: Effect of the photovoltaic bandgap on the LSC loss channels. (a) External loss, (b) Front loss, (c) PLQY loss, (d) Back loss, (e) Matrix loss, (f) Collected photon, (g) Bandgap loss. Maximum optical efficiency of 29.9 % is reached at $\lambda_g = 725\ nm$

Some comments can be done.

External loss: Reducing λ_g increases $\mathcal{L}_{ext}$ because opal reflection coefficient plays a more important role. Yet below 675 nm, the opal spectral spectral range shortens and $\mathcal{L}_{ext}$ decreases.

Front loss: $\mathcal{L}_{front}$ always decreases when reducing λ_g. However, reasons explaining this behaviour are different depending on whether λ_g is high or low. For $675 < \lambda_g < 800$, the spectral range which is not affected by the dye, highly responsible for front loss (fig. 3.17) shortens. Below 675 nm, $\mathcal{L}_{front}$ decreases to the benefit of bandgap loss (fig. 3.18g).

PLQY loss: $\mathcal{L}_{QY}$ spectral range is 350 - 650 nm (fig. 3.17). This loss is not modified for $650 < \lambda_g < 800$ but total number of photons reduces, so "mechanically" $\mathcal{L}_{QY}$ increases. For

low λ_g, we enter the spectral range in which PLQY loss occurs, which reduces $\mathcal{L}_{QY}$.

Back and matrix losses: These two losses behaviours are identical. This can be explained because their spectral range is also identical (fig. 3.17). They are not intrinsically changed when modifying λ_g, this is mainly a question of photon proportion.

Bandgap loss: Decreasing λ_g leads to some photons emitted at wavelength which does not allow PV cell absorption (photon energy is not high enough). Therefore, bandgap loss always increases when λ_g decreases.

Collection Optical efficiency is a consequence of the different loss channels evolution discussed above. the function $\eta_{opt}(\lambda_g)$ has a maximum at $\lambda_g = 725$ nm. The consequences on the PV cell efficiency are discussed with the help of the figure below:

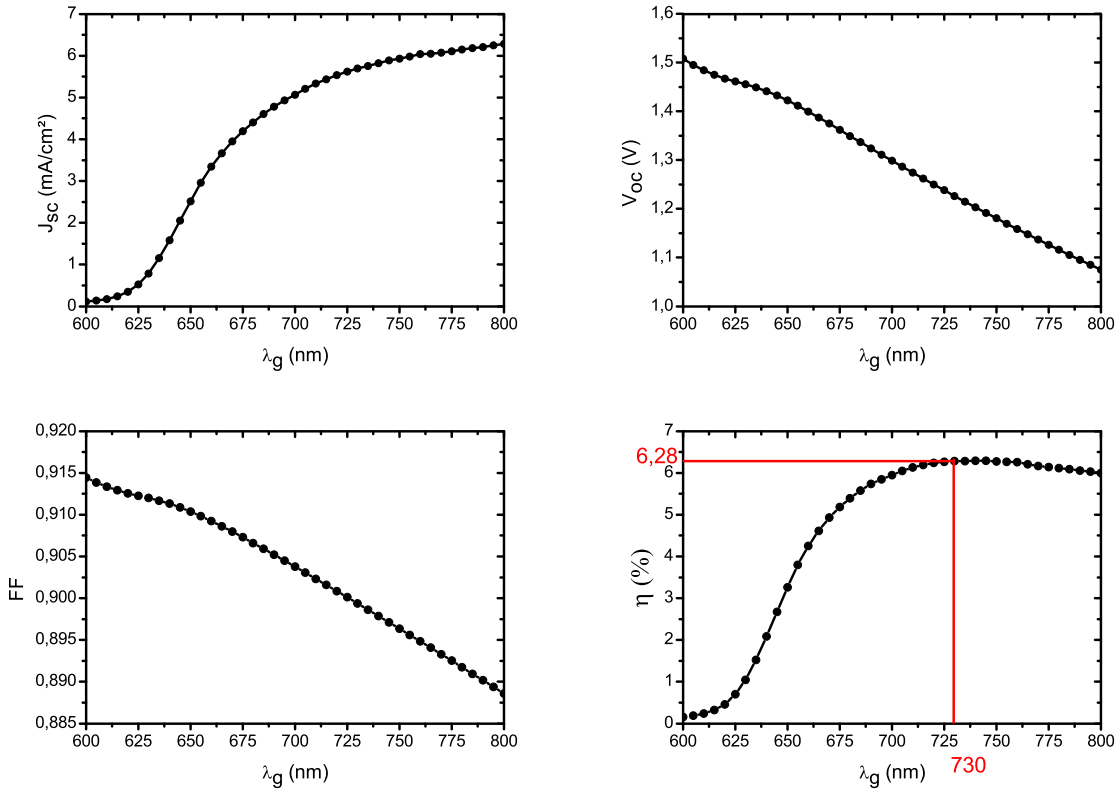

Figure 3.19: Influence of the photovoltaic bandgap on the LSC performances. Top left J_{sc}, top right V_{oc}, bottom left FF, bottom right η. Best efficiency of 6.28% is reached at $\lambda_g = 730$ nm

Decreasing the solar cell bandgap reduces the short circuit current (fig. 3.19 top left) even if optical efficiency is improved until $\lambda_g = 725$ nm (fig. 3.18f). In other terms, light collection improves but does not compensate the reduced amount of concerned photons. On the contrary, the open circuit voltages follows $E_g - 0.5$ (fig. 3.19 top right). The effect of the concentration is low. In the best case, concentration factor is 3 (leading to around 0.025 V gain on V_{oc}). Fill factor follows V_{oc} trend (fig. 3.19 bottom left). As a consequence, η is almost stable between 700 and 800 nm because V_{oc} and FF increase compensates J_{sc} decrease. Below 700 nm, J_{sc}

sharply drops leading to η drop as well (fig. 3.19bottom right). Working at $\lambda_g = 800\ nm$ is therefore close to optimal condition.

It is worth noting that the value of the constant (previously 0.5) in V_{oc} formula slightly changes our conclusion. Obviously, the lower this constant the higher η but $\eta(\lambda_g)$ shape changes. For low constant (typically 0.3), η is stable between 700 and 800 nm whereas the maximum efficiency is more pronounced for high constant (typically 0.8), from 4.62 % at 725 nm to 4.17 % at 800 nm.

3.4 Semi-analytical formulation with MBEOs

Throughout this chapter, we have studied the loss mechanisms to highlight some main trends in the LSC behavior. We have seen that LSC parameters impact on loss mechanisms is not straightforward since all LSC process are inter-correlated. Yet finding analytical formulas to describe LSC loss mechanisms seems almost insoluble. Despite that, we propose in this section (semi)analytical expressions using statistical data. The prefix "semi" means that these statistical data are found with numerical calculation. The difficulty varies according to the loss channel considered.

3.4.1 Expressions derivation

$\mathcal{L}_{ext}$ is particular because this loss channel does not depend on MBEOs and can be rigorously expressed analytically. Nevertheless it depends on the PBS. If no PBS is used, then $\mathcal{L}_{ext}$ corresponds exactly to Fresnel reflection. When a PBS is used, we use its reflection coefficient and we consider that in its transmission spectral range, Fresnel reflection apply. Therefore we have:

$$\mathcal{L}_{ext} = \begin{cases} \left(\frac{n_{mat}-n_{air}}{n_{mat}+n_{air}}\right)^2 & \text{if no PBS} \\ 1 - \widetilde{R}_{PBS} + \widetilde{R}_{PBS} \times \left(\frac{n_{mat}-n_{air}}{n_{mat}+n_{air}}\right)^2 & \text{if PBS} \end{cases} \tag{3.6}$$

With $\widetilde{R}_{PBS} = \frac{\int_0^{\lambda_g} AM(\lambda)(1-R_{PBS}(\lambda))d\lambda}{\int_0^{\lambda_g} AM(\lambda)d\lambda}$, the fraction of incident light reflecting by the PBS.

Now we can expressed $\mathcal{G}_{coll.}$, the optical efficiency. It can be approximately derived with the geometrical gain and the MBEO $\overline{hit}_b$ (defined in section 2.2.4):

$$\mathcal{G}_{coll.} = (1 - \mathcal{L}_{ext}) \times \left(1 - (1 - \frac{1}{C_{geo}})^{\overline{hit}_b}\right) \tag{3.7}$$

This equation simply expresses that the probability of being collected by a solar cell is $1/C_{geo}$, and that this probability must be weighted by the number of time photons hit the back surface. This expression is enough to assess the device performance but does not provide information on the other loss channels.

$\mathcal{L}_{back}$ is similar to $\mathcal{G}_{coll.}$:

$$\mathcal{L}_{back} = (1 - \mathcal{L}_{ext}) \times \left(1 - R_{back}^{\overline{hit}_b}\right) \tag{3.8}$$

$\mathcal{L}_{QY}$ is expressed in eq. (3.9), which is close to the previous expression.

$$\mathcal{L}_{QY} = (1 - \mathcal{L}_{ext}) \times \left(1 - QY^{\overline{abs}_{dye}}\right) \tag{3.9}$$

This simple expression states that $\mathcal{L}_{QY}$ depends on PLQY through $\overline{abs}_{dye}$, which quantify the self-absorption. This expression is less accurate for low PLQY. Indeed this equation takes into account the proportion of photons absorbed by dye only through $\overline{abs}_{dye}$. The lower is PLQY, the lower is the influence of $\overline{abs}_{dye}$: asymptotically, PLQY = 0 leads to full PLQY loss, which is not true since a part of photons is not absorbed (red photons). The accuracy of this formula will be studied in more details in the next section.

$\mathcal{L}_{mat}$ will be influenced by the matrix absorption coefficient as well as the mean traveled distance $\overline{d}$:

$$\mathcal{L}_{mat} = (1 - \mathcal{L}_{ext}) \times \left(1 - exp\left(-\alpha_{mat} \times \overline{d}\right)\right) \tag{3.10}$$

$\mathcal{L}_{front}$ is more complicated than others loss mechanisms because its resolution requires a succession of events. It also depends on the presence of a PBS. Without PBS, front surface trapping requires

1. Dye absorption
2. Radiative emission
3. Outside escape cone emission

If there is SA, the event succession must be repeated according to $\overline{abs}_{dye}$. So we obtain:

$$\mathcal{L}_{front}^{noPBS} = (1 - \mathcal{L}_{ext}) \times \left(1 - (\tau.QY.cos(\theta_c))^{\overline{abs}_{dye}}\right) \tag{3.11}$$

With $\tau = \frac{\int_0^{\lambda_g} AM(\lambda).exp(-\alpha_{dye}.2dz)d\lambda}{\int_0^{\lambda_g} AM(\lambda)d\lambda}$ the proportion of photon absorbed on a distance $2dz$ (dz being the thickness). The factor 2 in $2dz$ originates from the round-trip and photons normal incidence angle. It is worth noting that eq. (3.11) is false if $\overline{abs}_{dye} >> 1$ because after 1 absorption, the photon spectrum has been red shifted (with respect to AM 1.5) and therefore τ is not valid ($AM(\lambda)$ should be replaced by $e(\lambda)$). Yet this approximation is quite good if the dye overlap is reasonable.

With a PBS the expression becomes far more complex, reflection being ensured either by R_{PBS} and TIR and will not be considered later. In addition, because all loss channels plus $\mathcal{G}_{coll.}$ must equal 100 %, the last loss channel may still be derived.

Equations (3.6) to (3.11) must be verified against numerical results.

3.4.2 Validation

For each loss channel (except $\mathcal{L}_{ext}$, which is ruled by Fresnel reflection), we compute the difference between numerical and semi-analytical results ($\Delta = |\mathcal{L}^{num} - \mathcal{L}^{ana}|$) against PLQY, R_{back} and n_{mat}. In this section we show only results when no PBS is used and with $C_{geo} = 100$ (fig. 3.20). Three other cases have been analyzed (PBS and $C_{geo} = 100$, no PBS and $C_{geo} = 5$, PBS and $C_{geo} = 5$) and are displayed in appendix B.

In order not to limit ourselves to the ideal case, we use R305 dye (concentration of 200 ppm) in these simulations. Boundary conditions are periodic and the number of photons tested in parallel is 65000. Back reflector is specular.

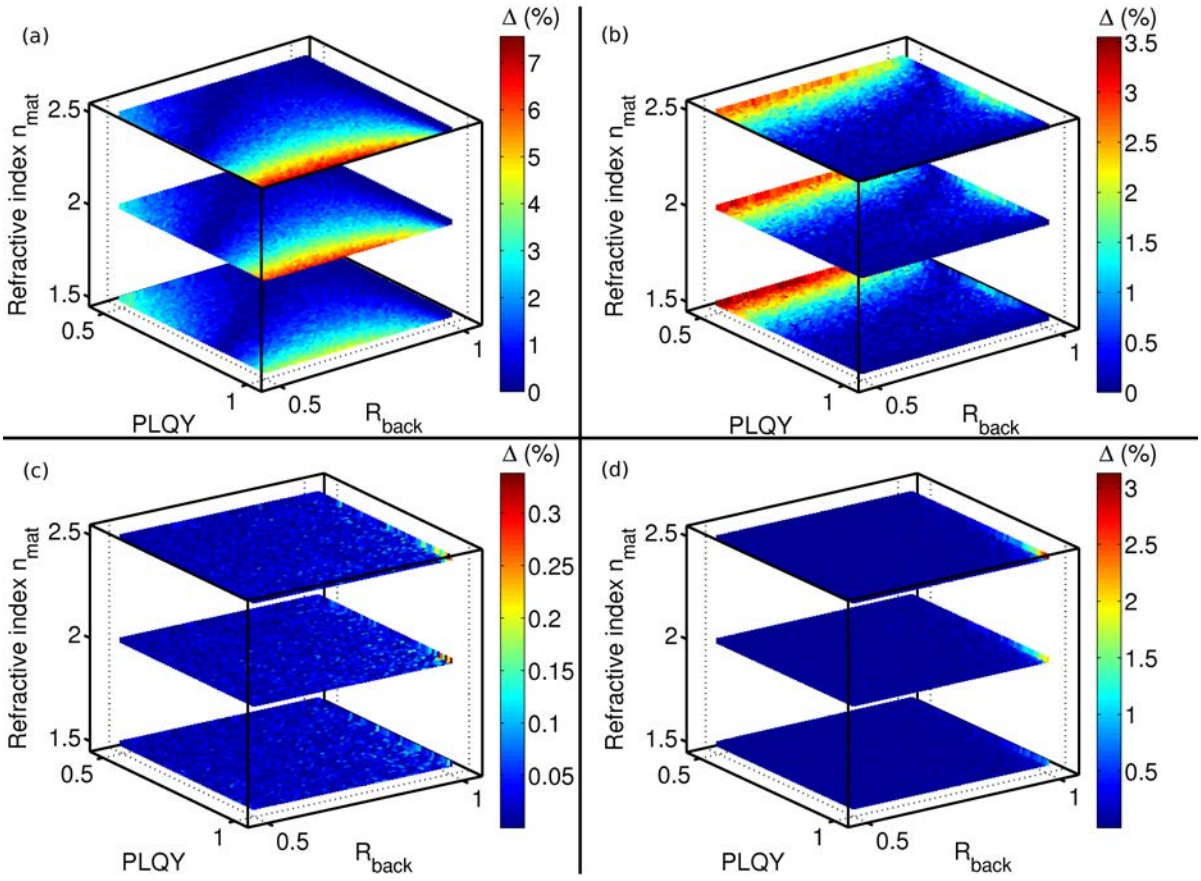

Figure 3.20: Comparison between numerical and semi-analytical loss channels derivations without PBS and at $C_{geo} = 100$. Colormap is in absolute percentage ($\Delta = |\mathcal{L}^{num} - \mathcal{L}^{ana}|$). (a) $\mathcal{L}_{back}$, (b) $\mathcal{L}_{QY}$, (c) $\mathcal{L}_{mat}$, (a) $\mathcal{G}_{coll.}$

The discrepancy between numerical and semi-analytical results varies in the same way whatever the value of n_{mat} is. Generally the error is reduced at low refractive index (in practice n_{mat} is close to 1.5), except for $\mathcal{L}_{QY}$. Yet error is relatively low for formulas describing physical phenomena at the first order (the inter-correlation complexity being taken into consideration mainly through MBEOs). As predicted in eq. (3.9), error increases if PLQY decreases. The error on $\mathcal{L}_{back}$ is less intuitive: it is higher for high PLQY values / non ideal R_{back} (loss underestimation) and low PLQY / low R_{back} (loss overestimation). $\Delta\mathcal{L}_{mat}$ and $\Delta\mathcal{G}_{coll.}$ are lower

than 3%, and lower than 1% with $n_{mat} = 1.5$. fig. 15 in appendix B shows that the error on $\Delta\mathcal{G}_{coll.}$ increases at low coverage fraction (worst case 7%).

In the real case studied previously fig. 3.17, the two means of derivation (numerical and semi-numerical) are consistent, as shown in table 3.3:

Numerical vs. semi-analytical methods						
	$\mathcal{L}_{ext}$	$\mathcal{L}_{front}$	$\mathcal{L}_{QY}$	$\mathcal{L}_{back}$	$\mathcal{L}_{mat}$	$\mathcal{G}_{coll.}$
Numerical	23.7	35.4	6.6	7.2	0.7	26.4
Semi-analytical	23.7	NA	6.4	7.7	0.8	23.4
Δ (%)	0.0	NA	0.2	0.5	0.1	3.0

Table 3.3: Parameter which can be tuned in the optical design. We vary simultaneously the width, period and InP thickness. After that, the dye concentration is optimized. It would have been too time consuming to optimize this four parameters together.

From all loss mechanisms, formulas are in good accordance with the numerical derivation. It means that the complexity of loss mechanisms interdependences can be treated with only four "a priori unknown" MBEOs.

3.4.3 Reducing MBEOs only to $\overline{d}$

Among the four MBEOs used to derive loss mechanisms, mathematical relationship exists. $\overline{hit}_f$ and $\overline{hit}_b$ must be extremely close because dye emission is isotropic (as many photons emitted toward front and back surface) and because photons experience back and forth. As a result, we may consider in a good approximation that $\overline{hit}_b$=$\overline{hit}_f$, noted $\overline{hit}$ thereafter.

We can link $\overline{hit}$ with $\overline{d}$. In 3D, $\overline{d} \approx 4 \times dz \times \overline{hit}$. This approximation is valid except when SA becomes important. In this case, $4 \times dz \times \overline{hit}$ underestimates $\overline{d}$ because isotropic dye emission is centered at $\pi/2$. Figure 3.21 shows the difference $4 \times dz \times \overline{hit} - \overline{d}$ and $\overline{abs}_{dye}$:

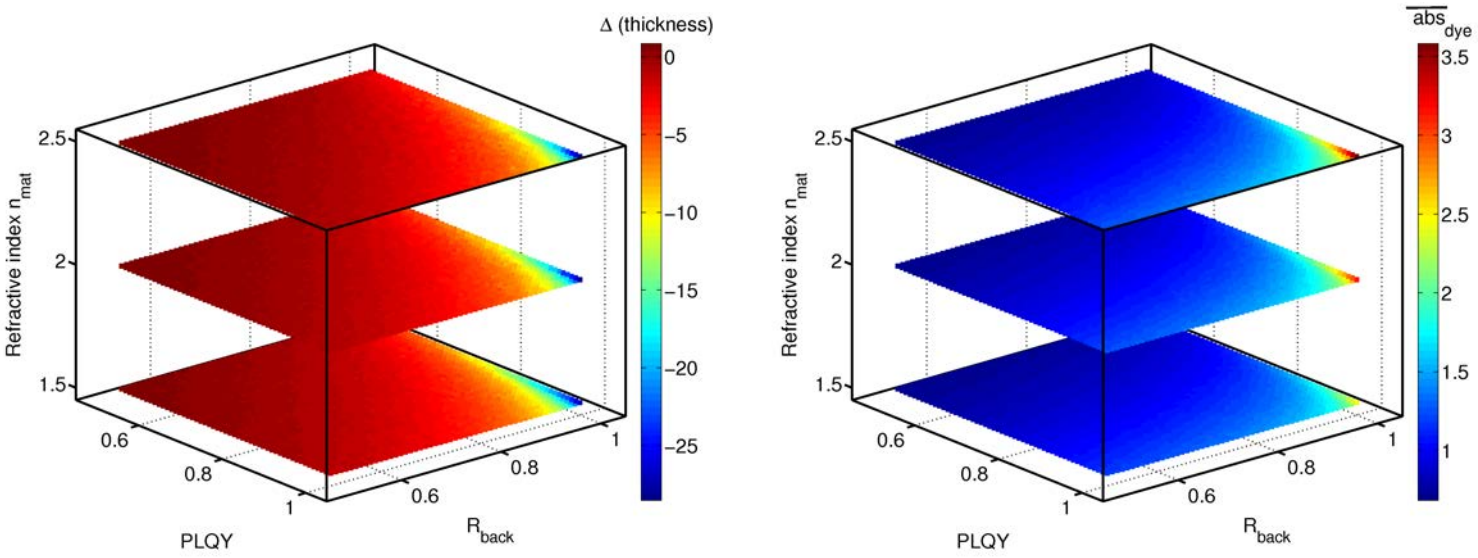

Figure 3.21: Left: $\Delta = \left(4 \times dz \times \overline{hit} - \overline{d}\right)/dz$ normalized in unit thickness. Right: $\overline{abs}_{dye}$ which illustrates the inverse correlation between Δ and SA.

Colorbar scale is extremely wide (from 0 to 25 thickness), but large error occurs only in a small range of LSC parameter, close to ideality. In realistic conditions, our approximation is reasonable.

Finally, can we express $\overline{abs}_{dye}$ as a function of $\overline{d}$? The answer is yes but assumptions must be taken.

We define $\widetilde{\alpha}_1$ as the averaged absorption coefficient taken away from emission range. This absorption coefficient will be used for the first absorption event. Thereafter, the absorption coefficient, which should be consider for self-absorption is the dye absorption coefficient in the emission range, weighted by the emission probability $\mathcal{P}_e$ (given by epdf (see section 2.2.2)). $\mathcal{P}_e(\lambda_0)d\lambda_0 = \int_{\lambda_0}^{\lambda_0+d\lambda_0} epdf(\lambda)d\lambda$. Thus $\widetilde{\alpha}_2 = \int_0^\infty \alpha_{dye}.\mathcal{P}_e(\lambda)H(\lambda)d\lambda$, H being the Heaviside function, equal to 1 when $e(\lambda) \neq 0$ and 0 elsewhere.

In the case of R305, $\widetilde{\alpha}_1 \approx 4.80\ cm^{-1}$ and $\widetilde{\alpha}_2 \approx 0.13\ cm^{-1}$. We can now express $\overline{abs}_{dye}$:

$$\overline{abs}_{dye}^{calc} = \begin{cases} \overline{d}.\widetilde{\alpha}_1 \text{ if } \overline{d} < \widetilde{\alpha}_1 \\ 1 + \left(\overline{d} - \dfrac{1}{\widetilde{\alpha}_1}\right).\widetilde{\alpha}_2 \text{ if } \overline{d} \geq \widetilde{\alpha}_1 \end{cases} \tag{3.12}$$

Figure 3.22 shows the difference between $\overline{abs}_{dye}$ and its approximation $\overline{abs}_{dye}^{calc} - \overline{abs}_{dye}$:

Again discrepancy is extremely high for ideal LSC system but greatly lowers when R_{back} is not ideal (maximum error drops to 2.5 when $R_{back} = 0.98$).

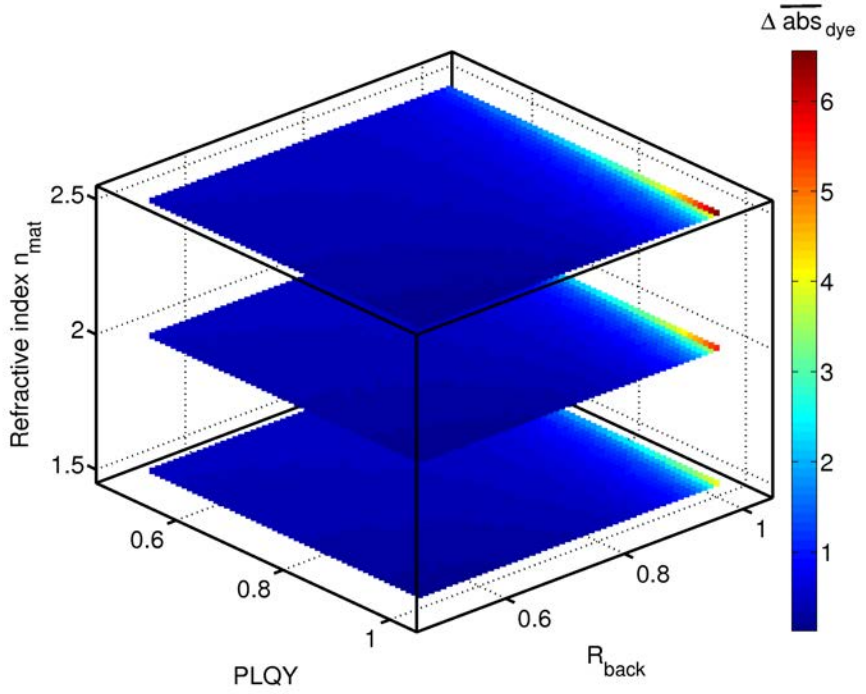

Figure 3.22: $\Delta = \overline{abs}_{dye}^{calc} - \overline{abs}_{dye}$ as a function of $PLQY$, R_{back} and n_{mat}

3.5 Big picture & LSC fundamental contradiction

We have shown that theoretical concentration factors higher than X1000 are achievable with a luminescent solar concentrator and an optical filter. The gap between theoretical limits and performances of state of the art LSC relies in the very high sensitivity of non idealities. An ideality discrepancy of 0.001 on crucial parameters can lead to a fall of 50% on the concentration factor. We have also shown that the loss mechanisms were not always additive and that their respective weights depended both on physical parameters and mean basic event occurrences (which can by expressed only by the mean traveled distance $\overline{d}$), making LSC a device with a strong intrication of loss channels. It can be schemed as shown below:

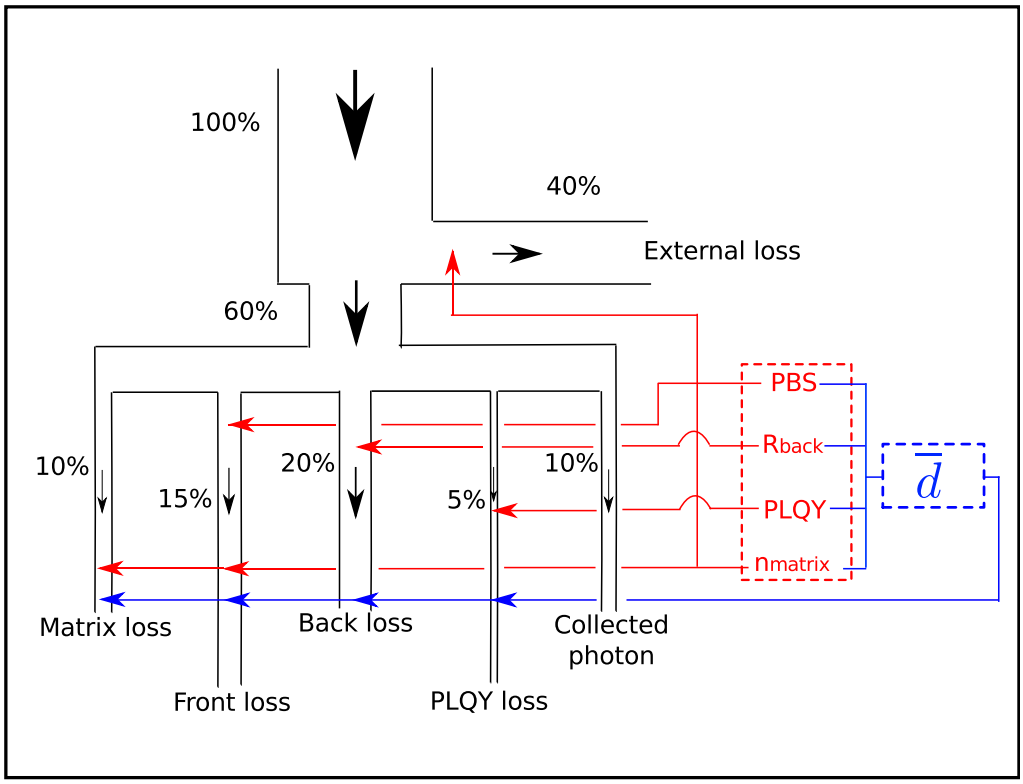

Figure 3.23: LSC loss channels scheme. Known physical parameters are represented in red. Each parameters is involved in specific loss(es), whereas the mean traveled distance (in blue) influences all internal loss channels

We have shown that the trends ruling the all ideal case are valid for realist case. Additionally, parameters sensitivity is greatly lowered when working at low geometrical gain. An important corollary is that there is no need use close-to-ideal parameters at low geometrical gain because of the low improvement they may provide.

Dye/PV cell mismatch has also been studied. Deviation from the ideal matching is not symmetrical: lower PV bandgap compared to dye emission is very prejudicial (short circuit current brutal drop). Conversely, higher bandgap is less damaging because the open circuit voltage shortfall is counterbalanced with the gain in short circuit current.

This theoretical study encourage to think that aside from ideal parameters, the dye emission bandwidth is a key factor if the LSC comprises a photonic band stop filter. Dye absorption threshold is also crucial because it heavily influences the self-absorption.

This study has also enabled to raise a contradiction. Having a high concentration factor requires a high geometrical gain, which in turn leads to a high mean traveled distance. Besides, a high mean traveled distance involves high loss and consequently reduces the optical efficiency and therefore ultimately reduces the concentration factor ($C = C_{geo}.\eta_{opt}$). As is often the case in Physics, a trade-off must be found. Sadly it ends up by a low geometrical gain (less than 10), as evidenced by all LSC results in the literature because this kind of system exhibit numerous loss channels. One way to go further is to add a PBS to shift this trade-off keeping η_{opt} constant while increasing C_{geo}.

This contradiction can be schemed as follows:

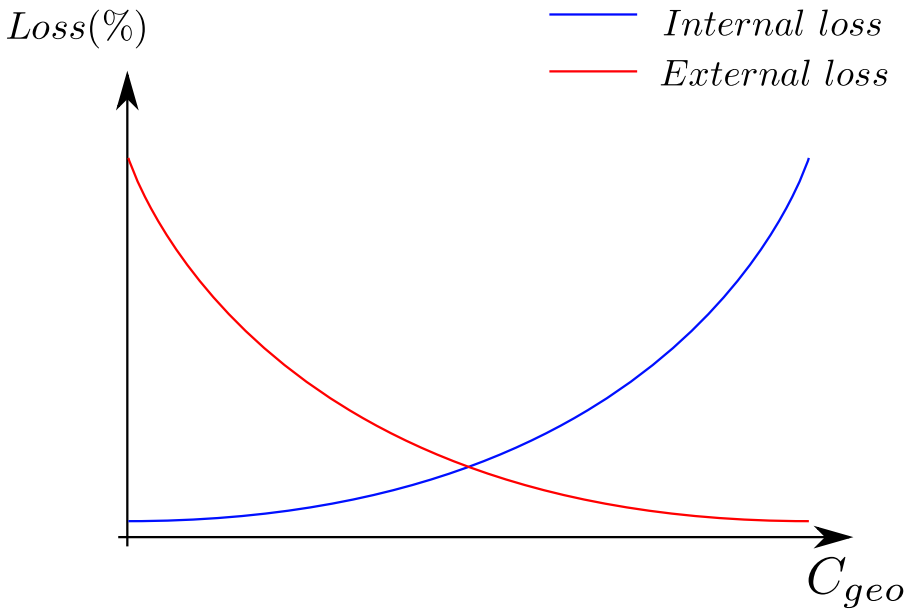

Figure 3.24: LSC fundamental contradiction scheme (only qualitative). Proportion of external and internal loss as a function of the geometrical gain.

Total loss contribution is coming from external loss and internal losses. Since the external loss is independent of C_{geo} and internal losses increase with C_{geo}, the trade-off on C_{geo} is of great importance. Improving LSC can be viewed as increasing C_{geo} threshold value to perform optimally. Before proposing an original way to circumvent this contradiction (chapters 5 and 6), experimental validation is required.

Chapter 4

CIGS-based micro solar cells coupled to Luminescent Solar Concentrator

Contents

This thesis has begun to answer, among others, this question: “Is LSC a viable solution to concentrate light on microcells array?”. This chapter aims at applying the knowledge described in precedent chapters to the special case of micro solar cells array. CIGS-based microcells array is a field in which more and more research teams are interested in, mainly because of their excellent behavior under concentration. The first part of this chapter presents why such microcells / LSC coupling is of interest. The next section deals with a prototype fabrication. This sample is characterized and results are compared to numerical calculations. Numerical inputs on the performance understanding are analyzed and improvements scheme are presented in the last section of this chapter.

4.1 Microcell array and LSC, a winning duo?

Light concentration on solar cell requires relatively small size solar cell to benefit from the concentrating effect (avoid resistive loss). Different examples of high concentration on $\sim mm^2$ PV cell area have already been published and commercialized. In 2010, Semprius demonstrates a X1000 concentration factor on 0.5 mm^2 cells array [80, 81] and two years later, X1100 was reached on 0.36 mm^2 [82].

This Concentration factor improvement is directly correlated to the lower PV cell area. Since resistive loss limits PV cell efficiency under concentration (fill factor drop), series resistance must be kept low to allow high concentration. Paire and co-workers [16] showed that reducing the PV area, especially going to micro size, improves heat dissipation and therefore these conditions are more suitable for working under concentration. This trend explains Semprius results. Nevertheless, PV cells (dual junction at 26% efficiency at 1 sun), its concentrator (Fresnel lens of 0.8 °acceptance angle) and the efficient sun tracker are expensive. Our study does not lie in this market segment because CIGS-based microcell arrays have the ambition to be a low-cost technology. Consequently, its concentration system has to be cheap not to jeopardize the low-cost potential.

The main interest of LSC lies in a 2π steradians acceptance angle as well as its low cost component. Additionally, the high acceptance angle avoids the use of expensive sun-tracker, strengthening the low cost aspect of LSC. Another big advantage of LSC is that no focusing is required (non imaging concentrator) and there is no alignment between cells and concentration optics, which is a huge asset knowing that the smaller the cells are, the more difficult the optical focusing will be. The technological steps to couple the solar cell array and its optics should also be inexpensive, that is why the "Bottom-Mounted LSC configuration" has been favored. Thus, LSC seems to have many advantages over its competitors, however on question remains: what about the LSC concentration factor? The real key figure is the concentration factor C achievable and therefore the electric output of the entire system CIGS micro-cell array & LSC.

4.2 Prototype fabrication & LSC-VMCA validation - Generation 1

The first step of the experimental work was to fabricate a microcell array / LSC prototype. Experimental measurements will be compared to LSC-VMCA for validation. CIGS microcell array prototype is produced by classical fabrication steps (IRDEP) and photolithography (LPN). More details on lithography can be found in appendix C.The photolithography mask comprises an array of 610×610 μm^2 squares with a period of 1610 μm (both x and y direction). This mask dimension leads to a geometrical gain of $C_{geo} = \left(\frac{1610}{610}\right)^2 \approx 7$.

4.2.1 Fabrication

4.2.1.1 Microcell array fabrication

The micro-cell array fabrication strategy was developed by M. Paire during her PhD thesis [83, 16]. We follow exactly the same fabrication steps. The first three steps are exactly those used to fabricate a standard CIGS cell (fig. 4.1). Others steps are dedicated to create micro-cells (fig. 4.2). The starting point is a soda-lime glass fig. 4.1a.

1. Deposition of a Mo layer on soda-lime glass (fig. 4.1b)

2. Co-evaporation of a $\sim 2.5\ \mu m$ thick CIGS absorber layer (fig. 4.1c) [84, 85]
3. Deposition of two 50 nm thick layers: CdS by chemical bath deposition (CBD) [86] and intrinsic ZnO:i by RF sputtering (fig. 4.1d-e)
4. Photolithographic process:
   (a) Resist layer (AZ2070 resist, AZ Electronics Materials) is spin-coated (Karl Süss CT62) at 4000 rpm (fig. 4.2b)
   (b) Exposition through the mask (365 - 435 nm light, through Karl Süss MJB mask aligner) during 5 seconds
   (c) Post-back at 105 °C during 3 minutes
   (d) Flood for 30 seconds (same light than in step (b))
   (e) Development (developer MF 26A) to reveal resist square block protecting the future active region of the device (fig. 4.2c)
5. Sputtering of 400 nm thick SiO_2 dielectric layer (Plassys MEB 400) (fig. 4.2d)
6. Evaporation of Ti/Ag 200 / 3000 Å(Plassys MEB 550SL) immediately followed by the next steps (fig. 4.2e)
7. Resist removal in acetone (fig. 4.2f)
8. Sputtering of ZnO:Al front contact (fig. 4.2g)

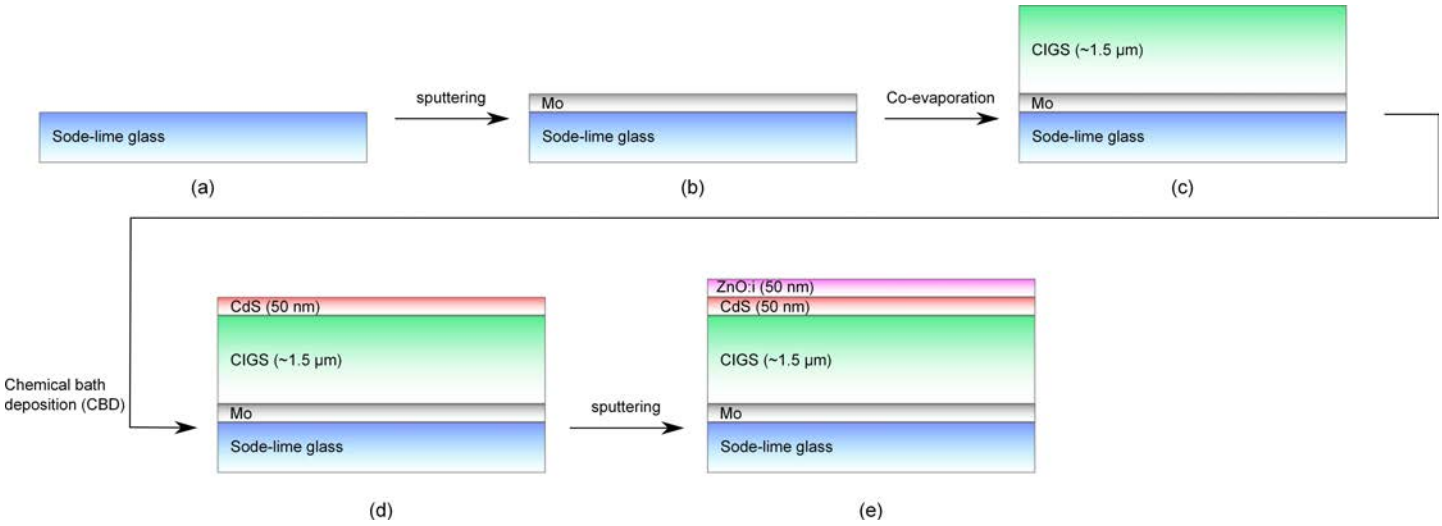

Figure 4.1: Standard CIGS cell process until ZnO:i layer

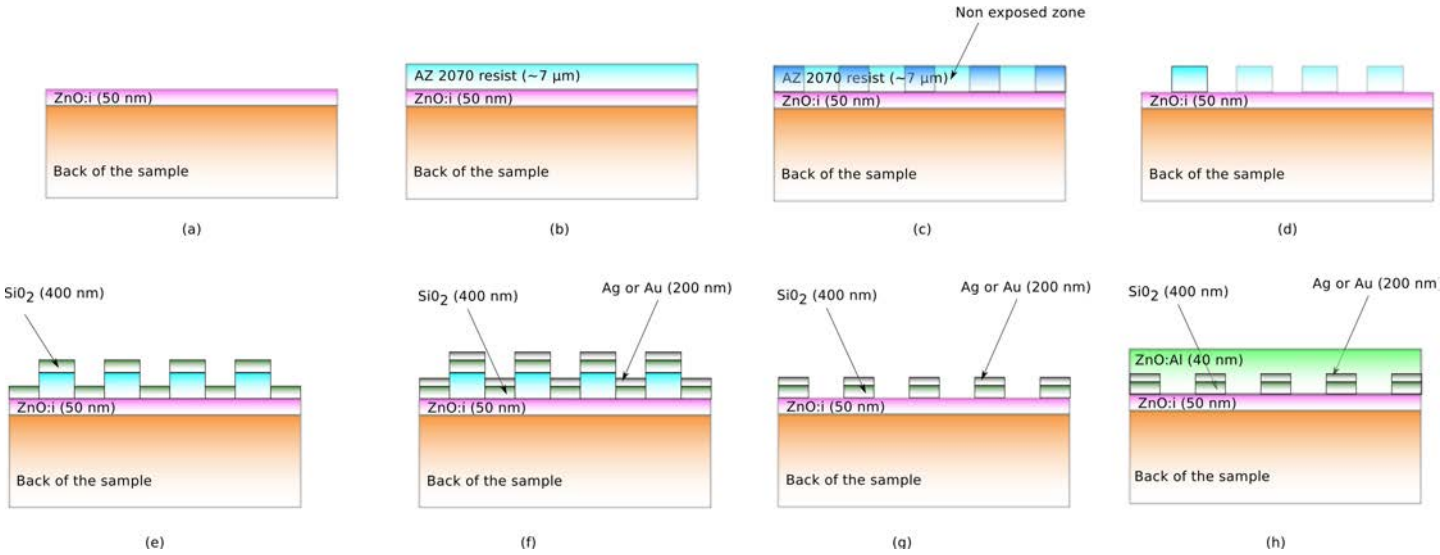

Figure 4.2: Process steps to define micro-cells

By construction, after all these steps the microcells are connected in parallel, as they share the same back and front contacts. Figure 4.3 shows a microcell SEM image of the CIGS microcell stack (FEG SEM Merlin VP Compact from Zeiss).

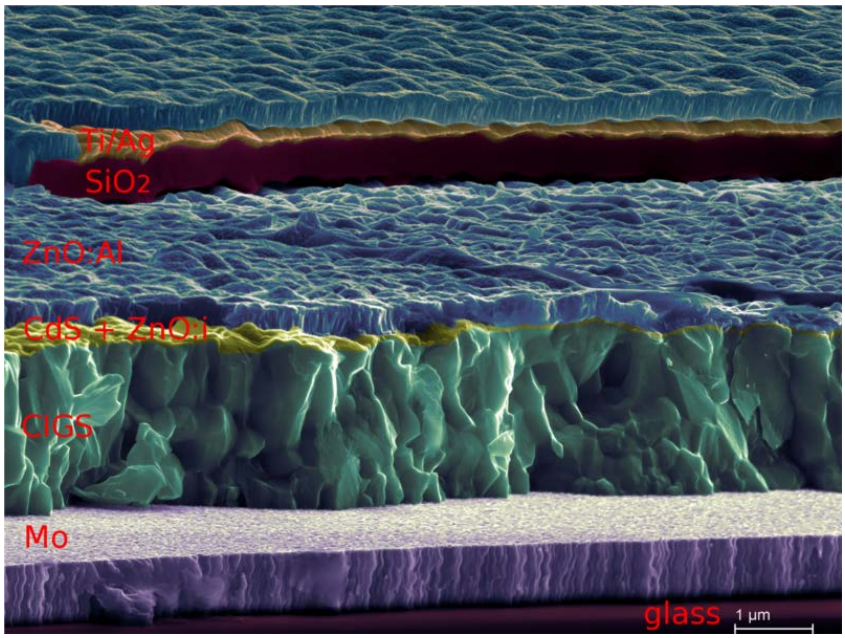

Figure 4.3: SEM image of an active micro-cell sample. Artificial colors. Forefront: active region (PV cell). Background: Non active region (reflector). In this image, the SiO_2 and Ag layers are visible which should not be the case because the ZnO:Al layer covers them totally (as in the extreme left part of the picture). The missing part of the ZnO:Al layer should have been broken during the sample cleavage.

The next task is to fabricate the doped-matrix.

4.2.1.2 LSC fabrication

The matrix choice should be driven by three main characteristics, its transparency, refractive index and capability to efficiently dissolve a dye. In a lesser extent the matrix stability is also a criteria to take into account. A common choice fulfilling these requirements is the Poly methyl methacrylate (PMMA).

PMMA is a polymer formed by the polymerization of MMA monomers. Both molecules are represented in fig. 4.4:

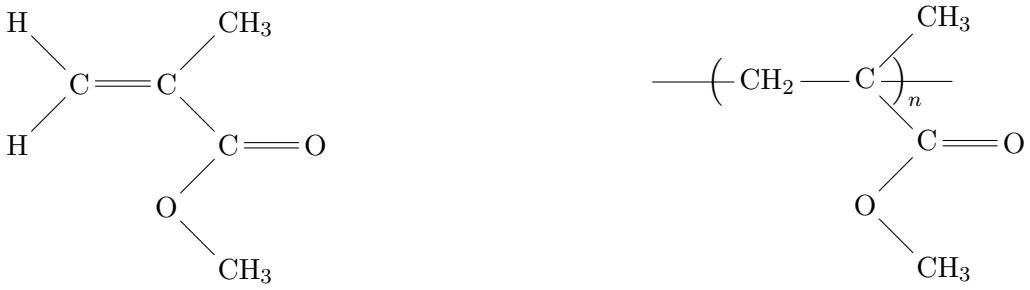

Figure 4.4: *Left*: Methyl methacrylate (MMA). *Right*: Poly methyl methacrylate (PMMA)

To prevent non desired polymerization, an inhibitor is added by the manufacturer. MMA forms PMMA by a free radical polymerization, meaning that the initiator should bring radicals to begin the chemical reaction. Radicals are not stable compounds whereas the initiator should be (to be able to stock it), so the initiator is a stable molecule able to split up in radicals. Two main paths can be used, either thermal or light induced activation. In the first case thermal energy dissociate the initiator, in the second case it is light, mainly UV. We used the thermal initiator azobisisobutyronitrile (AIBN). When heated up, AIBN forms a nitrogen molecules as well as two 2-cyanoprop-2-yl radicals (RC•) as shown below:

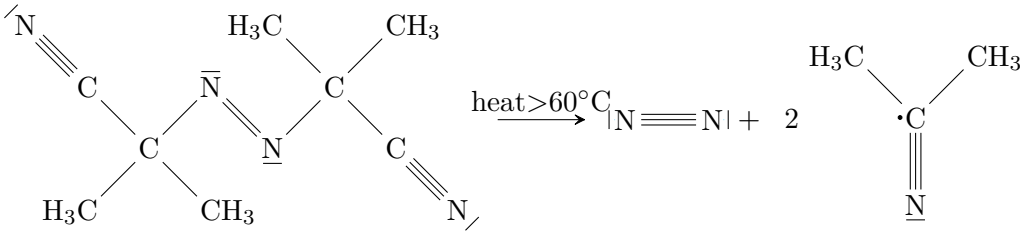

Figure 4.5: Lewis formula of AIBN and the resulting compounds after thermal dissociation. 60°C is a temperature at which polymerization is performed in roughly 18 hours.

The global reaction follows the four main steps of free radical polymerization described below [87]:

$$\textit{Initiation}\ \text{AIBN} \longrightarrow 2\ \text{RC}\bullet \tag{4.1a}$$

$$\textit{Transfer}\ \text{RC}\bullet + \text{MMA} \longrightarrow \text{RC} - \text{MMA}_1\bullet \tag{4.1b}$$

$$Propagation \begin{cases} \mathrm{RC-MMA_1\bullet + MMA} & \longrightarrow & \mathrm{RC-MMA_2\bullet} \\ \mathrm{RC-MMA_j\bullet + MMA} & \longrightarrow & \mathrm{RC-MMA_{j+1}\bullet} \\ \mathrm{RC-MMA_{n-1}\bullet + MMA} & \longrightarrow & \mathrm{RC-MMA_n\bullet}\ (1 \leq n \leq \infty) \end{cases} \tag{4.1c}$$

$$End \mathrm{RC-MMA_j\bullet + RC-MMA_k\bullet} \longrightarrow \begin{cases} \mathrm{RC-MMA_{j+k}}\ (recombination) \\ \mathrm{RC-MMA_j + RC-MMA_k}\ (dismut.) \end{cases} \tag{4.1d}$$

The polymerization being exothermic, the temperature must be controlled with a thermostat. In practice, the mixture is poured in a mold made by two glass sheets and a silicone seal (maintained by office-clip) and then heated up in a hot-water bath at temperature above 60 °C. The process steps are summarized and illustrated below:

1. PMMA powder (Aldrich 182230-500G) and MMA (Aldrich M55909-2L) are mixed in the ratio (PMMA 1 : MMA 9 in weight) at 60°C to ease the dissolution
2. Dye is added in the mixture according to the desired concentration (typically 100 ppm)
3. Mixture is allowed to cool until it reaches room temperature
4. AIBN is added in the mixture (0.08-0.1 % in weight)
5. The mixture is poured in the mold, then the mold is sealed
6. The mold is put in a hot-water bath at 80°C for 5 hours (or 60°C for 18 hours)
7. After polymerization, the geometrical shape is defined by a wire saw

Figure 4.6 illustrates steps 1-4, 5 and 7:

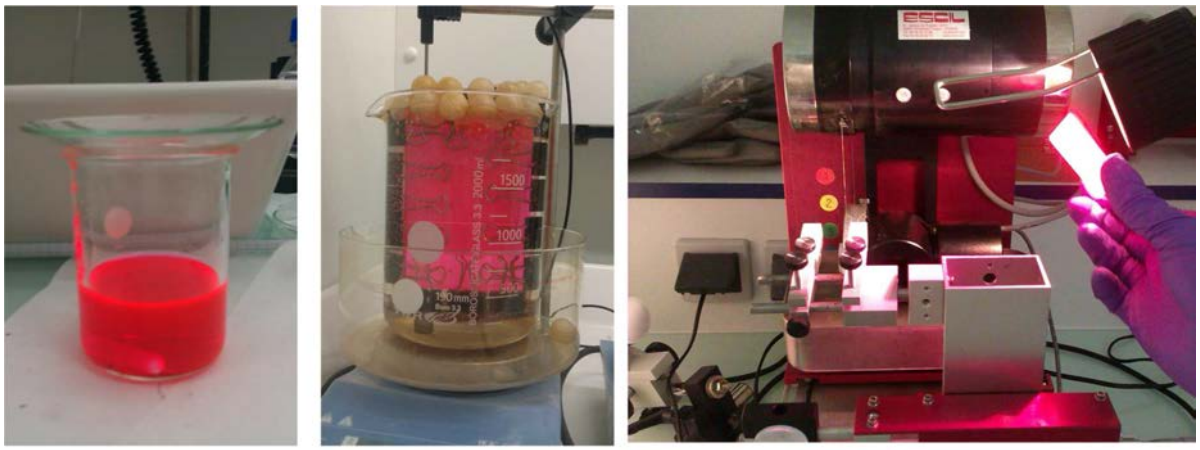

Figure 4.6: LSC fabrication process illustration. (a) Step 4: Mixture of PMMA + MMA + R305 + AIBN. (b) Step 5: Thermal polymerization in a sealed mold at 80°C in a hot-water bath. (c) Step 7: doped-PMMA plate cut by a wire saw.

After the polymerization, some bubbles are present on the matrix sheet edges. Before coupling the plate with micro-cell array, we have to cut the PMMA plate to obtain the same area than the matrix array. This is done using a wire saw (diamond wire saw, model W3242 from ESCIL).

This method ensures a sufficient PMMA quality. Yet, some improvements can be done. They were not applied in this work but are given as additional information. During the polymerization, viscosity increases progressively to the point where left monomers cannot react with unused AIBN. This effect, known as Trommsdorf effect [88], may be detrimental by reducing the sample transmittance. A way to circumvent this effect is to heat the sample above its glass-transition temperature (105 °C) in order to ease the mixing of unused monomers and radical. This may be done in a hot-air oven as shown in [89].

At this stage, the two parts (micro-cell array and doped-matrix) are ready to be coupled to form the LSC.

4.2.2 Coupling of generation 1 prototype

As a first step ethanol is used. Since CIGS is rough and micro-cell array is not flat (see fig. 4.1), putting directly the PMMA plate leads to air-gap between the active part of the micro-cell array and the doped-PMMA. This air-gap induces parasitic Fresnel reflection (between air / LSC and LSC / microcells) we want to avoid. As a consequence, ethanol role is mainly to fill all air-gap, therefore reducing Fresnel reflection. We have chosen ethanol for sake of simplicity, reversibility (do not attack PMMA) and electrical insulator properties.

4.2.2.1 Measurements

The device was then characterized with a solar simulator (Newport, class AAA). A photograph of the measure set-up is shown below:

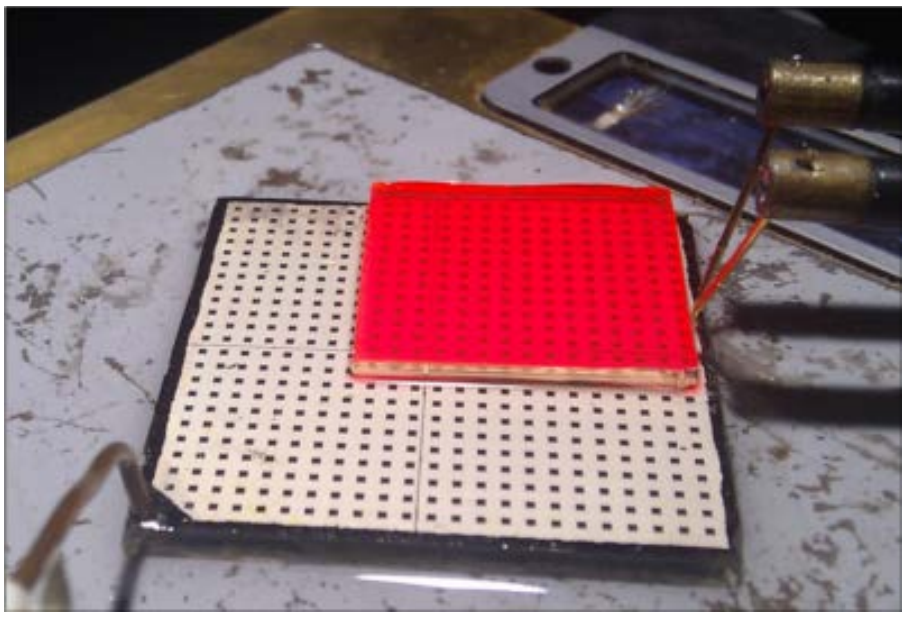

Figure 4.7: Picture of the CIGS array and LSC coupling under a solar simulator

The concentration factor C being proportional to the short circuit current, it is deduced from the ratio $C = \frac{J_{sc}^{LSC}}{J_{sc}^{bare}}$, with J_{sc}^{LSC} (J_{sc}^{bare}) the short circuit current of the sample with (without) the LSC respectively. The following configurations have been tested: No LSC (1), ethanol + LSC (2), ethanol + LSC + copper tape (3M) (3) and ethanol only (4). Results are summarized in table 4.1 and compared to the theoretical outcomes.

	Experimental configurations			
	no LSC	eth.+LSC	eth.+LSC+tape	eth.
J_{sc} (mA.cm^{-2})	17.71	20.54	21.37	22.06
ΔJ_{sc}	0	+2.83	+3.66	+4.35
$C^{exp}(\eta_{opt}(\%))$		1.16 (15.7)	1.21 (17.4)	1.25 (19.7)
$C^{calc}(\eta_{opt}(\%))$		1.24 (17.9)	1.75 (25.2)	1.47 (21.1)

Table 4.1: Experimental results of an unoptimized LSC-microcell array coupling. The last line of the table corresponds to the LSC-VMCA results.

Model inputs were the ones taken from experimental data available. When ethanol is used only as an optical coupler, it is not taken into consideration in the code since its refractive index is quite close to that of PMMA. The lateral dimensions were set to 2×2 cm^2 and thickness to 2 mm (0.5 mm for ethanol), refractive index of 1.5 for PMMA and 1.36 for ethanol case (4). The dye is R305, with a PLQY of 95 % at a concentration of 200 ppm. The back surface was considered lambertian and the reflection coefficient measured by a spectro-photommeter (Perkin-Elmer Lambda 900, see fig. 19 in appendix E). The tape reflection coefficient (considered specular) was measured and almost equal to 90% for $\lambda > 600$ nm. Since the tape does not recover totally the edges (see fig. 4.7), a 80 % wavelength-independent reflection coefficient was chosen. If a photon hits a solar cell, it is considered collected and no reflection coefficient at the interface cell / PMMA is considered. This assumption will be discussed in the next section. PV cell bandgap is 1.15 eV.

4.2.2.2 Discussion

4.2.2.3 Base-Line case

This first series of experiments shows that LSC concentration is not trivial because ethanol alone is sufficient to beat the use of LSC. All the concentration factors obtained are lower than the classical limit of $n^2 = 2.25$, which means in this case that LSC-induced losses are too important and counterbalance the dye benefits. This kind of result was qualitatively predictable, mainly because the back surface acts as a diffuse reflector (high surface roughness), making the waveguiding effect poorly efficient. The concentration factor in this case has two origins, the anti-reflection coating effect and only a diffusive concentration (thus limited to the classical limit).

Theoretical results corroborates (with a slight overestimate) the experience. Overestimation seams reasonable since no reflection coefficient between PV cell / PMMA interface is taken into consideration in LSC-VMCA. In addition, the real matrix surface may have some micro-defects (scratch, dust) damaging the TIR. The tape case is more overestimated than the others. A reflection coefficient of 40 % should be used to fit the experimental data.

To have a better understanding of the prototype performance, we look at LSC-VMCA outputs. Efforts will be focused on configuration (2). Throughout this chapter, this configuration will be called base-line 1 (BL I). The goal is to identify respective weight of loss mechanisms to develop strategies to improve performances. Results are shown in fig. 4.8:

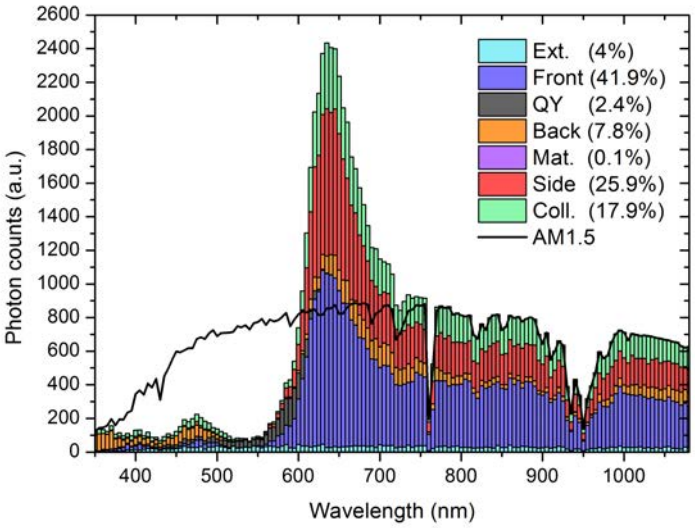

Figure 4.8: Simulation of the photon outcome in the system (2) LSC+ethanol.

MBEOs	BL I (optimal)
$\overline{hit}_b$	1.31 (7)
$\overline{hit}_f$	1.00 (6)
$\overline{abs}_{dye}$	0.52 (0.33)
$\overline{d}(cm)$	0.95 (5.6)

Table 4.2: BL I statistical data

The three main loss causes in the BL I case are (in descending order) front loss, side loss and back loss. Other losses account for only 6.5%. Looking at MBEOs, their values are far from ideal. Ideal MBEOs values may be found by the following reasoning. Statistically and without loss, the mean number of "round-trips" between back and front surfaces should be $C_{geo} \approx 7$ to reach a solar cell. So $\overline{hit}_b$ should be close to $C_{geo} \approx 7$ and $\overline{hit}_f$ close to $C_{geo} - 1 \approx 6$. Ideally, self-absorption should be avoided, consequently only photons with wavelength absorbable by dye should be absorbed one time, which corresponds to $\frac{\int_0^{620} AM(\lambda d\lambda}{\int_0^{\lambda_{gap}} AM(\lambda d\lambda} = 0.33$ (there is almost no absorption for $\lambda > 620\, nm$). Neglecting absorption events, a round trip takes $2\times2\times dz$ cm (first factor 2 comes from a back and forth in itself, second factor 2 arises because photons evolve in 3D without being normal to the surface [78]). Thus in our case ideal $\overline{d} \approx 7 \times 2 \times 2 \times 0.2 = 5.6$ cm.

Having identified loss hierarchy, the next step is to analyze reasons behind these results to, in a second phase, propose improvements.

4.2.2.4 Lowering side loss

More than 26% loss is due to side escape. One improvement is to put a side reflector (done with copper tape experimentally), but another solution is simply to increase the LSC area. In the BL configuration, the mean distance $\overline{d}$ is only 0.95 cm, so photons entering the system far from the edges ($> 0.95\, cm$) have a low probability to be lost by side escape (low but non null, we are dealing with averaged number). Photons traveling in 3D, the critical distance from the

edges is even lower than 0.95 cm. Side loss and collected photons dependence is shown on fig. 4.9 and results for 1 m^2 LSC area (named configuration BL II) are shown in table 4.3.

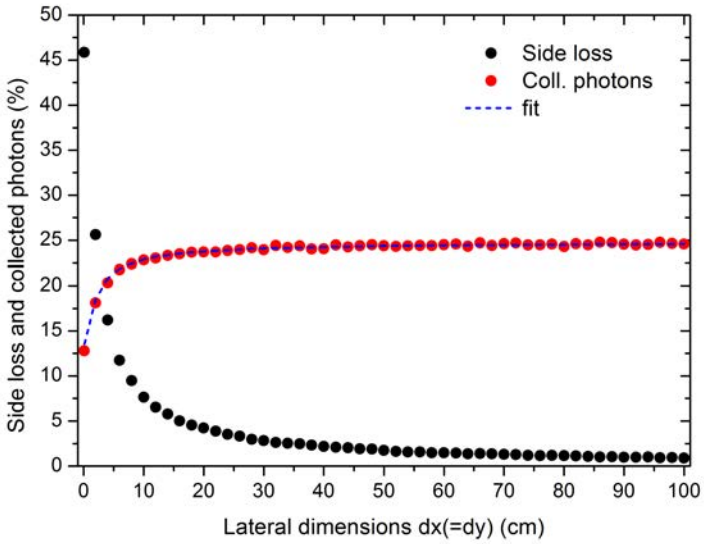

Figure 4.9: Size effect on a square LSC performances. The fit linking collected photons $\mathcal{C}oll$ and Side loss $\mathcal{L}_{side}$ is given by the formula: $\mathcal{C}oll(dx) = \mathcal{C}oll(\infty) * (1 + \mathcal{L}_{side}(\infty) - \mathcal{L}_{side}(dx))$

Loss repartition		**MBEOs**	
(cm)		$BL\ II (BL\ I)$	
Ext.	4.0	$\overline{hit}_b$	1.79 (1.31)
Front	57.1		
QY	2.9	$\overline{hit}_f$	1.51 (1.00)
Back	10.4		
Mat.	0.1	$\overline{abs}_{dye}$	0.58 (0.52)
Side	0.9		
Coll.	24.6	$\overline{d}$ (cm)	1.39 (0.95)
Total	100.0		

Table 4.3: BL II (area 1 m^2) LSC-VMCA result. BL I (area 4 cm^2) MBEOs are given in parenthesis for comparison

The fit is in good accordance with the numerical calculation of the collected photons, which means that the inter-correlation between $\mathcal{S}_{side}$ and all other loss channels is linear.

Visual influence of lateral dimension on side loss is given in fig. 4.10:

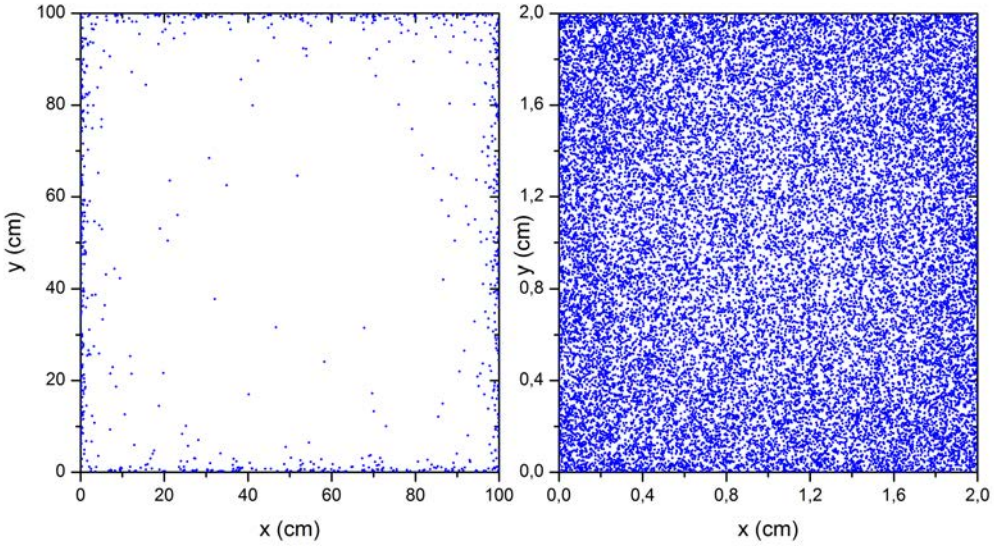

Figure 4.10: Side-escaped photon position when entering the LSC. Left: BL II area $1 \times 1\ m^2$, 0.91% side loss. Right: BL I area $2 \times 2\ cm^2$, 25.9% side loss

It is worth noting that $\overline{d}$ slightly increases (1.39 cm) because almost no photon are allowed to side-escape, which on average increases the mean pathlength.

We have shown that side loss is avoidable either by increasing the LSC area or by putting a reflector on the edges. Later in the document, we shall consider in our code $1 \times 1\ m^2$ area.

4.2.2.5 Back reflection schemes

Going further, one can think of increasing the reflector reflectivity but it won't drastically enhance the optical efficiency since only 10% of photons are absorbed by the reflector. In addition, it is hard to find better material than silver in the visible range except Bragg reflectors. Unfortunately, they are expensive and may be hard to fabricate since the CIGS substrate is rough. Another approach is to modify the reflection scheme using an air gap between silver and PMMA.

4.3 Air-gap LSC - Generation 2

4.3.1 Motivations

The advantages of air gap are double:

- Make the reflection becoming specular by TIR
- Reflection efficiency of 100 % if TIR

For photons with incidence angle larger than the critical angle (which is the same for both front and back surface), not only reflection is ideal but also specular. Neglecting self-absorption, the specular reflection on front and back surfaces ensures no front and back escape loss as long as photons have been emitted outside the escape cone. We have filed a patent on this concept on march 2014. An illustration of the air gap interest is shown in fig. 4.11.

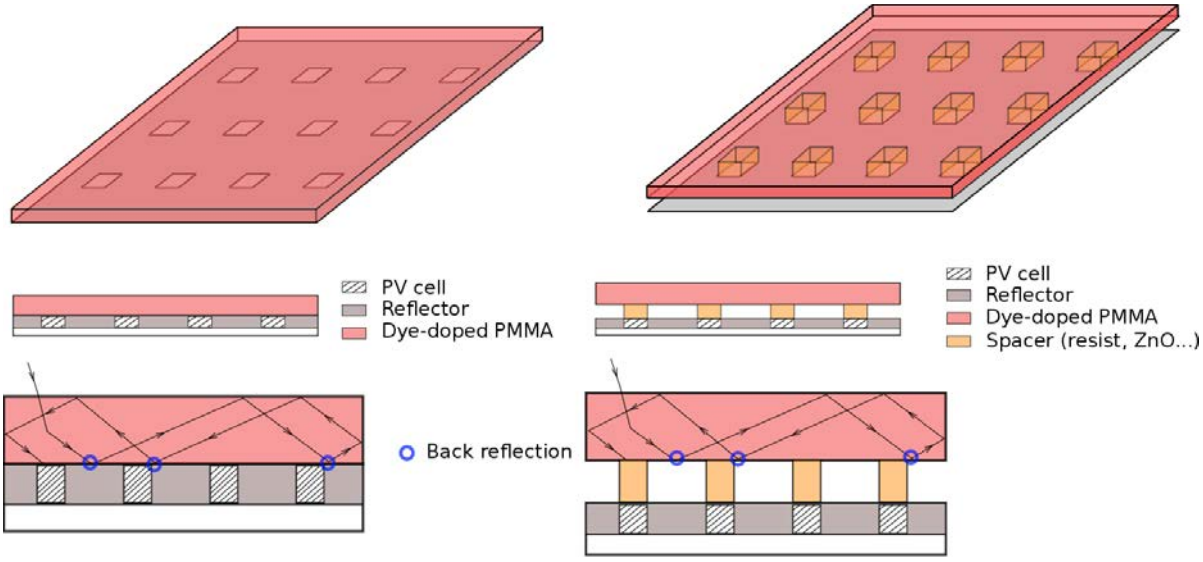

Figure 4.11: Schematic of the BM configuration with (right) and without (left) an air gap. Top: 3D view. Middle: Cross section view. Bottom Illustration with one ray

Applying an air gap (new configuration BL-III), back loss are reduced as expected but overall performance is not increased.

Loss repartition (%)		**MBEOs**	
$BL-III (BL-II)$		$BL-III$ $(BL-II)$	
Ext.	4.0 (4.0)	$\overline{hit}_b$	1.75 (1.79)
Front	62.2 (57.1)		
QY	2.9 (2.9)	$\overline{hit}_f$	1.53 (1.51)
Back	5.4 (10.4)		
Mat.	0.1 (0.1)	$\overline{abs}_{dye}$	0.60 (0.58)
Side	1.5 (0.9)		
Coll.	23.9 (24.6)	$\overline{d}$ (cm)	1.68 (1.39)
Total	100.0		

Table 4.4: BL III LSC-VMCA result

This behaviour can be explained as follows. The 5% improvement on the back surface is fully transferred to front loss and overall performances slightly decrease because the better waveguiding (angle conservation) induces more side loss than in BL-II. Thus, the increase of the mean back reflection coefficient is obviously a good point but the potential angle conservation advantage is not translated in the performances. This is also corroborated with the mean number of front reflection: lower than 2. This value is low, which does not enable to exploit the full potential of the air gap.

A high photon mean free path (and therefore a higher number of front reflection possibilities) makes the angle conservation more crucial. What appears in this section as a (low) degradation will therefore be an improvement. Following this reasoning, improvements may be found in tuning the LSC geometry (via C_{geo}).

4.3.1.1 Geometrical effects

In order to reach the classical thermodynamic limit of n^2, one has to increase the geometrical gain of the LSC as well as optimize the dye concentration. Figure fig. 4.12 shows the LSC performance of two configurations, one without dye (falling within the classical limit), and the BL-III with ideal $PLQY$ and R_{back} as well as periodic boundary conditions.

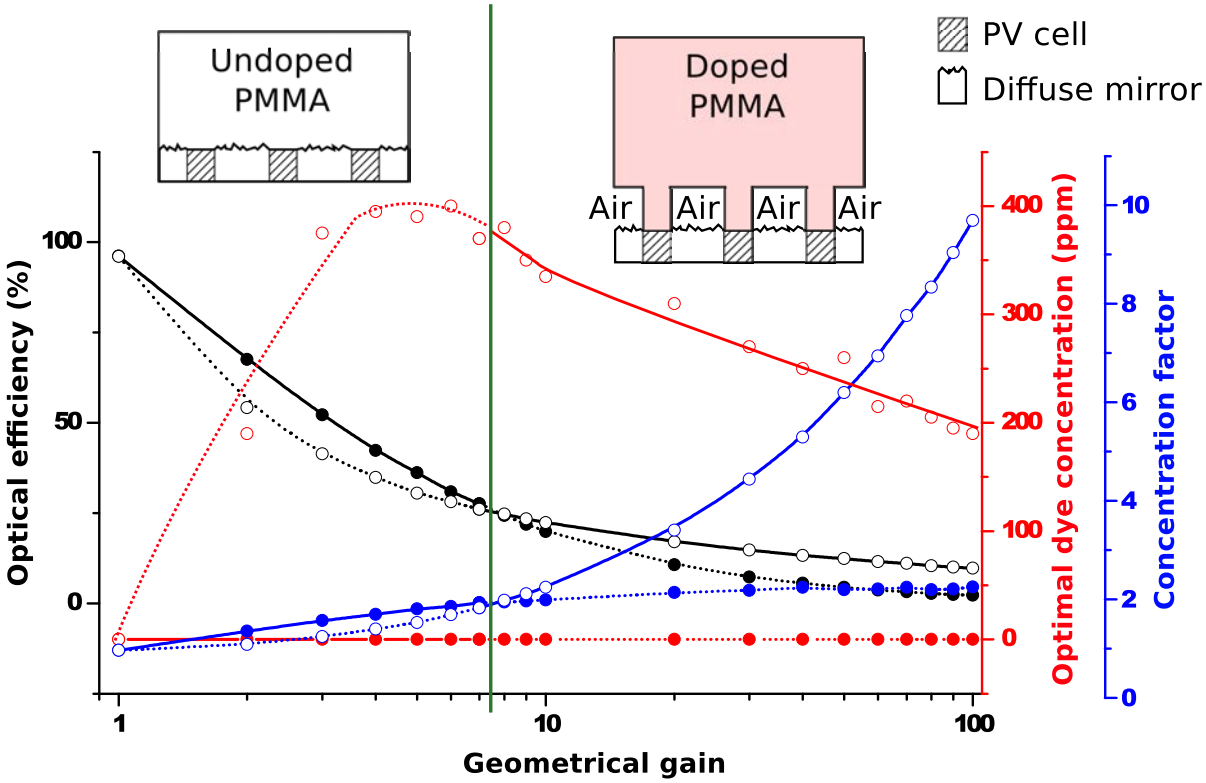

Figure 4.12: Concentration factor (blue), optical efficiency (black) and optimal concentration (red) versus the geometrical gain for two configurations: microcell array + undoped-PMMA (plain circles) or microcell array + doped-PMMA with an air gap (BL-III, empty circles). Green line at $C_{geo}^{th} = 7.3$ separates two regimes. If $C_{geo} < C_{geo}^{th}$: undoped PMMA configuration is more favorable whereas $C_{geo} > C_{geo}^{th}$ promotes the use of a dye and an air-gap. To perform optimally at a given geometrical gain, one must follow the solid lines.

Figure 4.12 exhibits two zones, delimited at $C_{geo}^{th} = 7.3$, when C and η_{opt} cross for the two configurations. For C_{geo} lower than C_{geo}^{th}, dye inherent losses (PLQY, escape-cone emitted photon) compensates its benefits. In the extreme case of $C_{geo} = 1$ trivially the dye induces only a degradation. Reversely, for $C_{geo} > C_{geo}^{th}$, effects of both dye and improved waveguiding (due to the air gap) become visible and the classical limit can be beaten. C_{geo}^{th} value is valid only for these specific conditions: dye, reflection coefficient or matrix change would lead to a different value.

The next section is devoted to the air gap LSC configuration.

4.3.2 Pillar-induced loss

Figure 4.12 has been done under several assumptions. In this paragraph we want to refine our model, in particular we question the perfect optical coupling PMMA plate - micro-pillar - PV cell. LSC-VMCA being not designed to deal with micro-pillar loss, we use a commercial ray-trace code Zemax (from Radiant Zemax). With Zemax, S. Jutteau (PhD student at IRDEP) and I have modeled one micro-pillar ($n_{pillar} = 1.6$), sandwiched between a plate of 1.5 refractive index and a PV cell. The situation is illustrated in fig. 4.13:

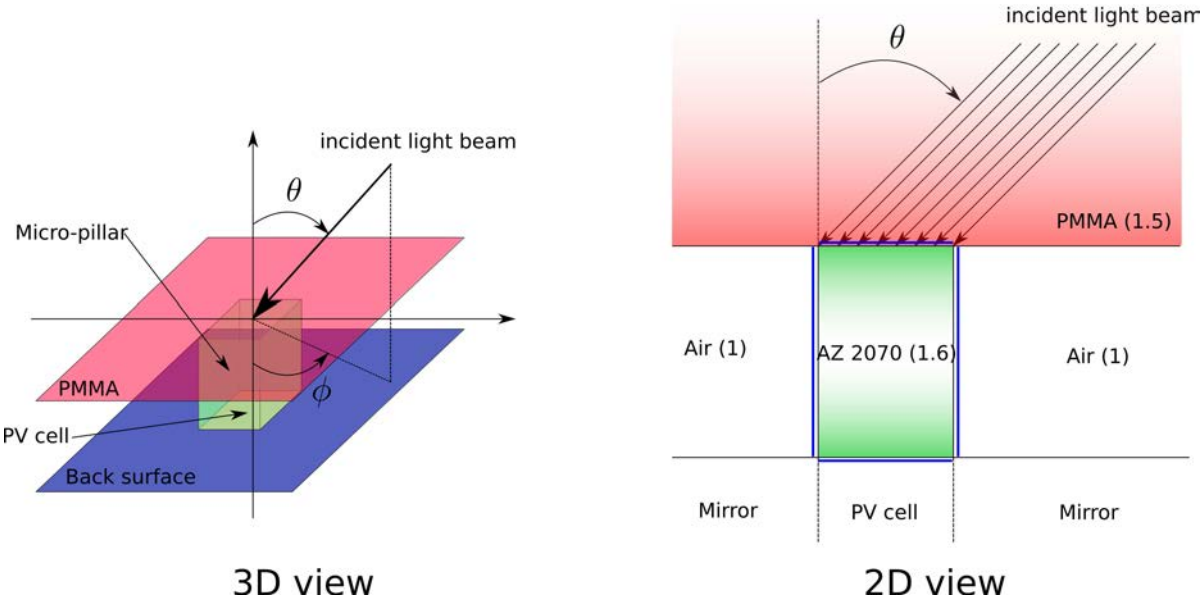

Figure 4.13: Scheme of Zemax calculation. 10^6 unpolarized light beams are sent in a $n_{PMMA} = 1.5$ medium toward the micro-pillar top with homogenous spatial distribution. Detectors (thick blue lines) count photons which may be escaped through pillar edges $\mathcal{N}_{side}$, reflected toward PMMA $\mathcal{N}_{refl.}$ or absorbed by the PV cell $\mathcal{N}_{PV}$ (ie. transmitted from micro-pillar to ZnO:Al)

The idea is to find averaged (over θ and ϕ) probabilities $\overline{\mathcal{N}}_{side}$, $\overline{\mathcal{N}}_{refl.}$ and $\overline{\mathcal{N}}_{PV}$ to be injected in LSC-VMCA.

Zemax calculations are done for $0° < \theta < 88°$ and $0° < \phi < 45°$ for square pillars and $\phi = 0$ for cylindric pillars (ϕ independent). For each couple (θ, ϕ), we obtain from Zemax 3 values ($\mathcal{N}_{side}(\theta,\phi)$, $\mathcal{N}_{refl.}(\theta,\phi)$ and $\mathcal{N}_{PV}(\theta,\phi)$). Then these values are averaged over θ and ϕ, weighted by the dye isotropic distribution D_θ and D_ϕ (given in section 2.2.2):

$$\begin{cases} \overline{\mathcal{N}}_{PV} &= \sum_\theta \left(\sum_\phi \mathcal{N}_{PV}(\theta,\phi) \cdot \mathrm{D}_\phi \right) \cdot \mathrm{D}_\theta \\ \overline{\mathcal{N}}_{side} &= \sum_\theta \left(\sum_\phi \mathcal{N}_{side}(\theta,\phi) \cdot \mathrm{D}_\phi \right) \cdot \mathrm{D}_\theta \\ \overline{\mathcal{N}}_{refl.} &= \sum_\theta \left(\sum_\phi \mathcal{N}_{refl.}(\theta,\phi) \cdot \mathrm{D}_\phi \right) \cdot \mathrm{D}_\theta \end{cases}$$

We analyzed four different pillars: two cylindrical pillars of 50 and 140 μm diameter and two square pillars of 50 and 140 μm side. Pillar height is set to 6 μm. After averaging over ϕ (only for square cases), the three probabilities are plotted against θ and then averaged over θ taking into account non uniform θ distribution. This is shown in fig. 4.14:

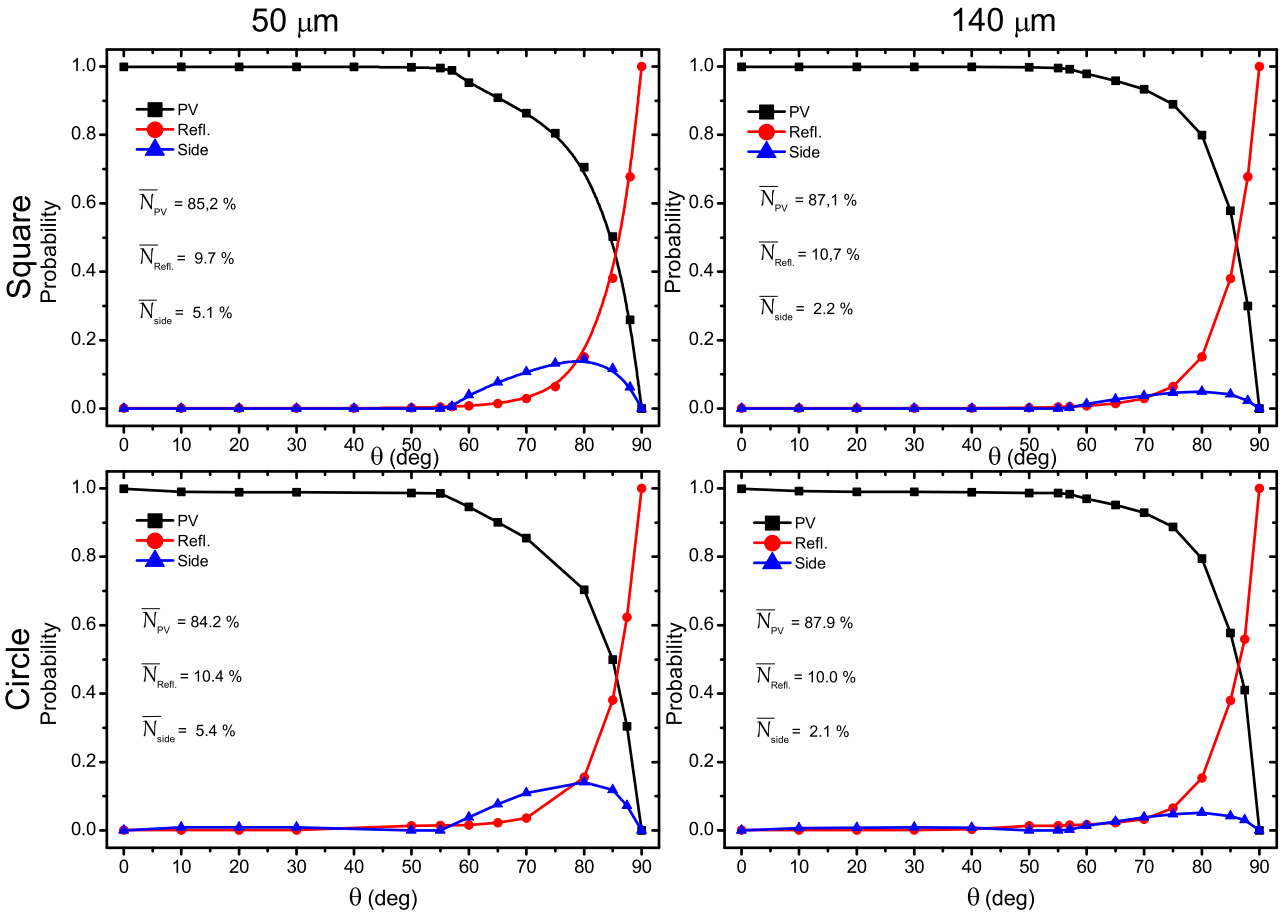

Figure 4.14: Evaluation of pillar shape (square base 1st row, circle base 2nd row) and size (50 μm 1st column, 140 μm 2nd column) on the optical coupling efficiency. Plots represent the proportion of photon reaching the PV cell (black), escaping through pillar side (blue) and reflected (red) against θ (after integration over ϕ). For each plot, averaged numbers $\overline{\mathcal{N}}_{PV}$, $\overline{\mathcal{N}}_{side}$ and $\overline{\mathcal{N}}_{Refl.}$ are given after integration over θ (weighted by isotropic distribution)

Better PV absorption occurs for high lateral size, reducing pillar-side escape. Indeed, high size keeping the same height reduces the ratio side / front area leading to less side-pillar escape. The shape influence is not so critical and either square or circle base pillar can be used. It is worth noting that pilar-side escaped photons are not lost, they might be reflected by the silver reflector. In LSC-VMCA, we will assume that pillar-side escape is considered as reflected. Taking into account the pillar induced loss, as well as realistic $PLQY$, R_{back}, fig. 4.12 becomes:

Figure 4.15 shows that realistic back reflector and dye quantum yield lead to a slight drop in performances compared to PLQY=1 and R_{back}=1. Conversely, side loss are very detrimental for a small device of 16 cm^2 area. Yet, this corresponds to laboratory samples size and experimental devices should be compared to dash curves

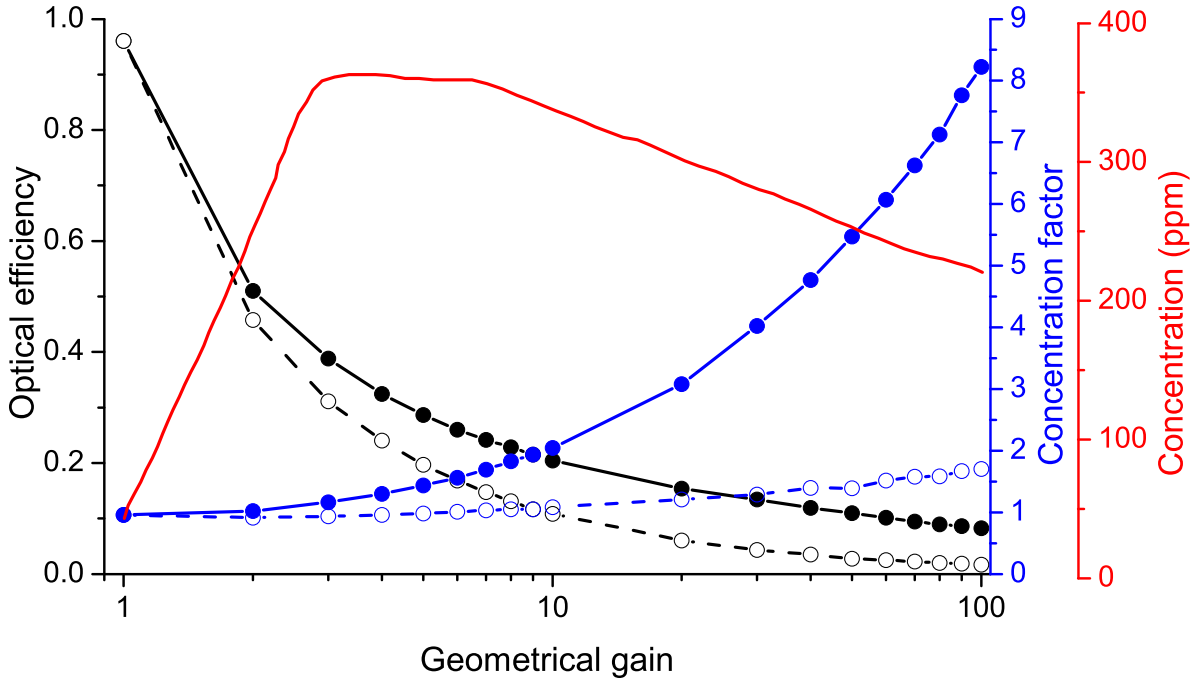

Figure 4.15: LSC + airgap modeling. Optical efficiency (black), concentration factor (blue) and dye concentration (red) are given as a function of the geometrical gain. Plain curves do not take side loss into account (periodic boundary conditions). Dash lines and open symbols consider side loss, for a device dimension of $4 \times 4\ cm^2$

The next step is to fabricate this LSC.

4.3.3 Fabrication

BL-III configuration requires to fabricate micro-pillars with the following requirements:

1. Same lateral dimension than the PV micro-cell
2. Thickness higher than few microns
3. Transparent
4. Refractive index between n_{PMMA} and $n_{ZnO:Al}$
5. Good alignment micro-cells / micro-pillars

The pillars on micro-cells must be aligned and ideally of the same lateral size (point 1). This will be dealt with using UV lithography. The micro-pillars act as a spacer enabling to create the air gap. In order to have TIR, one must avoid sub-wavelength optical effects, and consequently the air gap height (= pillar thickness) should be larger than the wavelength. We work on the visible spectrum extended to the near-infrared (depending on the absorber bandgap) around 1 μm. Thus a pillar height thicker than 5 microns will be considered as fulfilling the point 2

of the requirements. Point 3 is trivial since any absorbed photons in the micro-pillar will be lost for the solar cell. Yet the pillar being thin, the constraint on its absorption coefficient is weak. Point 4 is related to optical coupling between PMMA and PV cell. The addition of an additional layer is an opportunity to reduce reflection if the refractive index is between $n_{mat} \approx 1.5$ and $n_{ZnO:Al} \approx 2$.

Given the above, we choose the resist AZ nLOF 2070 negative resist from Microchemicals [90]. We have fabricated 3 photolithography masks of square cells with 3 different geometrical gains 5, 10 and 50. Cells period is always 1000 μm consequently square side are 447, 316 and 141 μm respectively. Pillar-side loss analyze was not completed when these masks have been designed, that is why they have square cells and not circular cells.

We begin with making micro-pillars on a soda-lime glass to check height and shape of micro-pillars. Process steps are:

- μ-pillar total area of 4×4 cm^2 in a sample of 5×5 cm^2. An array of 40×40 μ-pillars (square shape $\approx 140 \times 140$ μm^2) is fabricated on a glass substrate
- AZ 2070 spin coating at 3000 rpm, 3000 rpm/s, 30" on a MA6 from Züss Microtech
  1. Soft-baking at 105°C for 3'
  2. 30" UV exposure
  3. 1'25" development in AZ 826 MIF (microchemical) + 1' rinse in deionized water
  4. Post-exposure baking 105°C for 3'
- Profil measurements with a Dektak 6M Stylus Profiler (contact profilometer)

Figure 4.16 illustrates the process steps, how the sample has been analyzed and 5×5 pillar (line 5, column 5 pillar) profil:

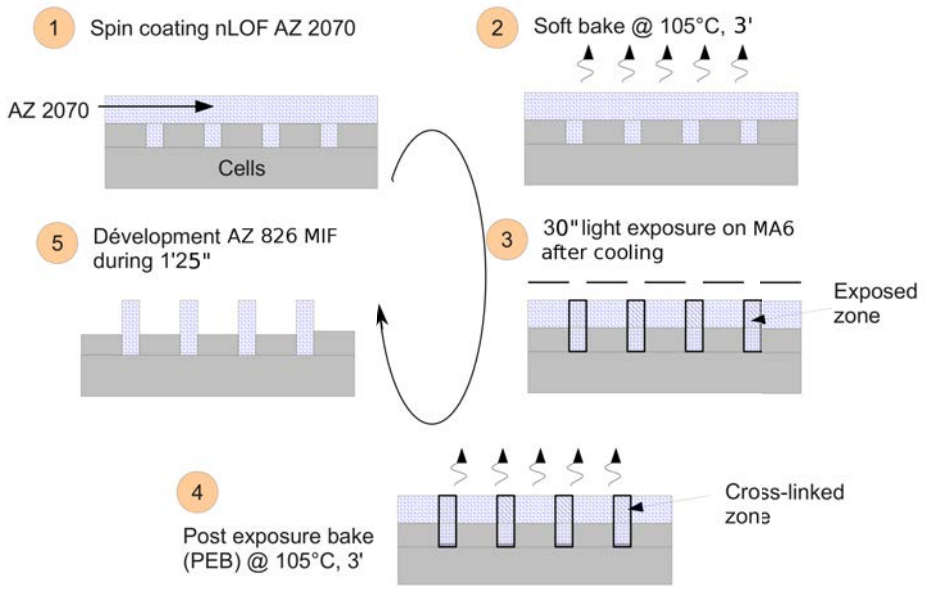

(a)

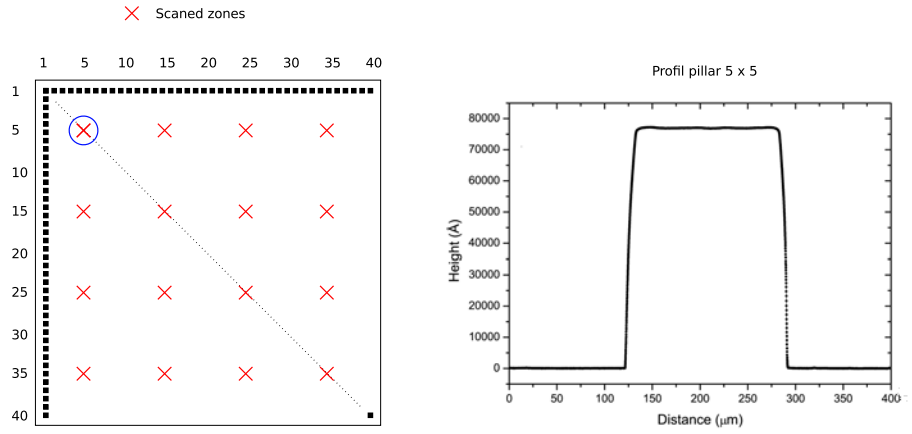

(b)

Figure 4.16: (a) Micro-pillars process steps. Numbers represent line and column numbering. (b) Schematic of a sample fabricated with $C_{geo} = 50$ mask and profil measurement on the line 5, column 5 pillar. These tests were done on a glass substrate and no on microcell substrate. The procedure is still the same.

Mean pillars height is 7.69 μm and mean pillar roughness is 440 Å.

These results are satisfying, so we move to micro-cell substrate made with the three masks. Alignment micro-cells / micro-pillars is done with MA6 from Züss Microtech. Figure 4.17 shows an optical microscope (Nikon, Eclipse) image of micro-pillar / micro-cell alignments (at $C_{geo} = 50$):

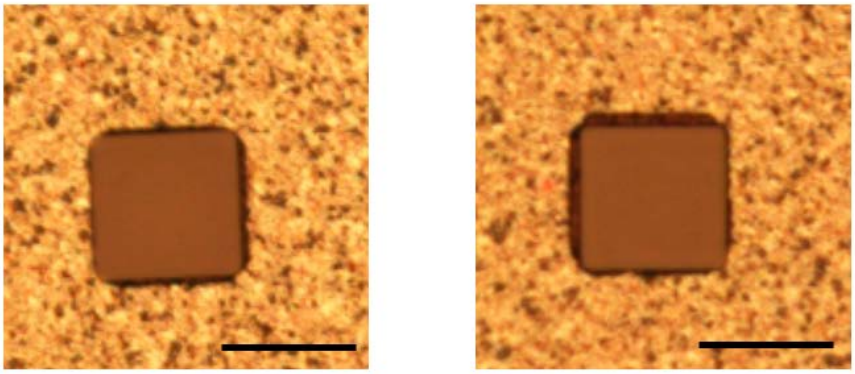

Figure 4.17: Optical microscope images of two micro-pillar / microcell alignment at $C_{geo} = 50$. Scale bar: 150 μm

Alignment is correct but not perfect. Aside from experimenter error, photolithography masks were made in plastic, which makes alignment procedures more challenging than conventional glass masks.

After checking alignment, profiles have been measured. For the 3 masks, pillar heights range from 7.0 to 7.5 μm (slightly lower than with soda-lime substrate) but roughness (peak-to-valley) has increased, in different proportions according to the mask :

- $C_{geo} = 5 \rightarrow$ roughness 320 nm
- $C_{geo} = 10 \rightarrow$ roughness 250 nm
- $C_{geo} = 50 \rightarrow$ roughness 150 nm

Pillar thickness dispersion (500 nm) added with roughness (320 nm) may create height difference of 820 nm between two pillars. It can jeopardize the optical coupling creating unwanted air gaps between “small” pillars and the LSC plate. Moreover, LSC plate + microcell array parallelism is not guaranteed.

Pillar shape differences between soda-lime glass substrate and microcell array is attributed to the non planarity of microcell substrate as shown in fig. 4.18:

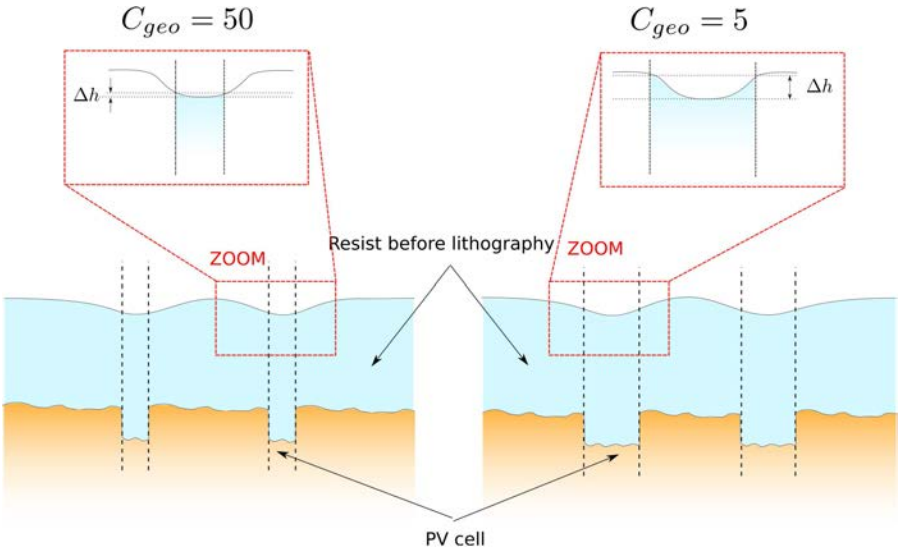

Figure 4.18: Scheme of pillar roughness induced by micro-cell array non planarity

Schematically, pillar top has a "flat V-shape". The higher is the microcell area, the higher will be the thickness difference Δh between center and pillar edges. Yet, looking for high geometrical gain tends to minimize this effect. Nevertheless, an optical coupling solution must be found to reduce pillar height non-uniformity.

We propose the a coupling via a buffer resist layer. This is illustrated in fig. 4.19:

Figure 4.19: μ-pillar / LSC coupling. μ-pillar are softly put down on a LSC plate on which buffer resist has been spin-coated.

The role of the buffer resist is to "absorb" the pillar roughness and height inhomogeneity as well as providing mechanical adherence. The buffer resist is an homemade PMMA (from Microchemicals) and Methyl isobutyl ketone (MIBK) solvent mixture (50 $g.L^{-1}$), which is spin-coated at 2000 rpm, 3000 rpm/s during 5 seconds on the doped-PMMA plate. Concentration determines layer thickness and resist viscosity. 50 $g.L^{-1}$ enables to have appropriate thickness. After the spin coating, the two samples microcell arrays and [doped-PMMA + buffer resist] are put in contact. No annealing is done after the contact to prevent mechanical constraints. It results in a 1 μm thick buffer resist. The difficulty is that we have maximum 20 seconds between the spin-coating end and LSC plate / micro-cell array coupling. It corresponds to MIBK solvent evaporation. After that time, the resist becomes too stiff to act as a good optical coupler.

Preliminary tests are done on molybdenum-coated glass substrate. After some optimization on the coupling conditions we manage to obtain satisfactory coupling, as shown on fig. 4.20:

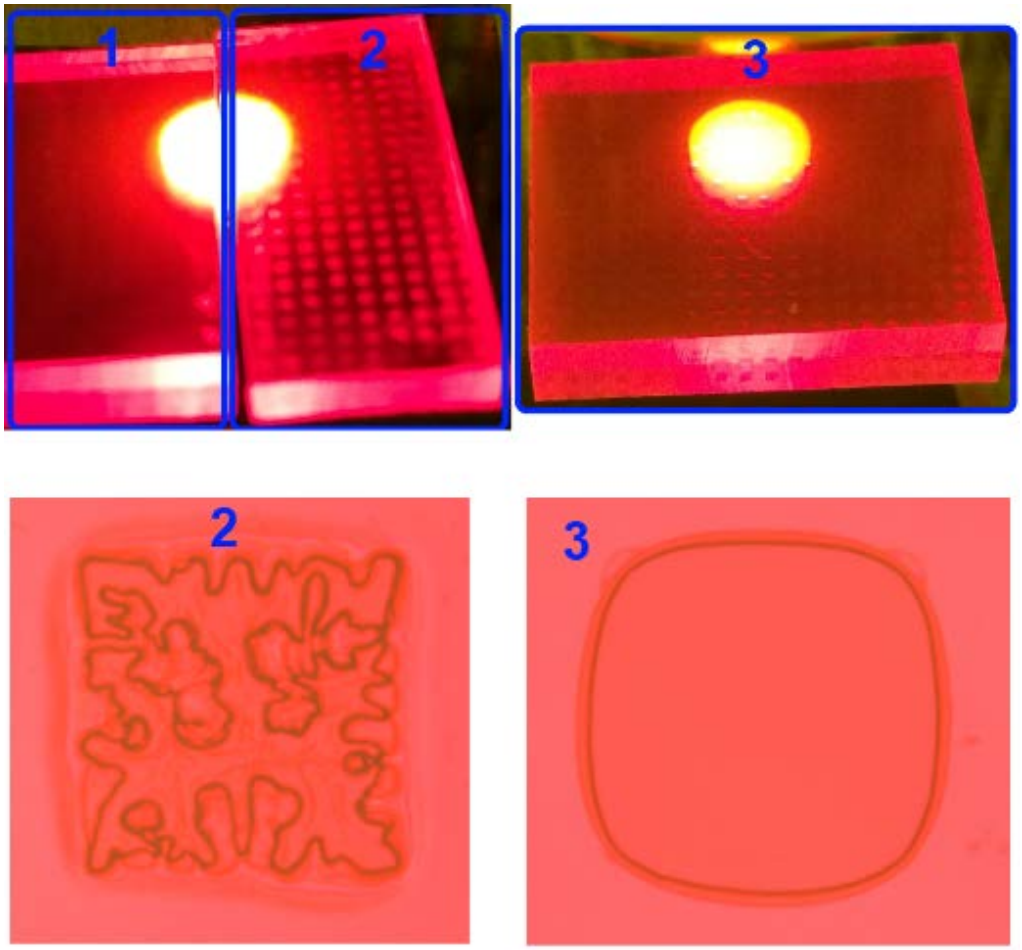

Figure 4.20: Visualization of the coupling LSC / micro-pillars. $C_{geo} = 50$ First row: photograph for three different configurations: 1. LSC is simply put on micro-pillars. 2. Unoptimized buffer layer between LSC and micropillars. 3. Optimized buffer layer between LSC and micropillars. Second row: Optical microscope image of one pillar: Left image corresponds to case 2 with unoptimized buffer layer. Right image corresponds to case 3 with optimized buffer layer. Pillar width is 150 μm

When no buffer layer is used (fig. 4.20(1)) , light is homogeneously distributed on the whole surface. Photograph suggests that optical properties on micro-pillars and around micro-pillars are identical. Light does not enter preferentially in micro-pillars and therefore the coupling is rather weak. On the other hand, using a buffer layer greatly improves the coupling, provided that no optical defect occurs on the pillars top surface. Optical coupling defects lead to undesired diffuse reflections on the micro-pillars top surface (fig. 4.20(2)). After optimization (mainly on the time between the spin-coating and the coupling and on pressure conditions), we may reach better coupling (fig. 4.20(3)). In this case, no reflection occurs on the top surface and light is allowed to enter the micro-pillars (which was not the case on fig. 4.20(1)). Micro-pillars evidence in this case lies on the micro-pillars side loss.

Micro-pillars fabrication on CIGS-based microcells arrays with three different geometrical gains have been fabricated as well as the LSC plate (200 ppm). Yet the coupling is under progress.

4.3.4 Measurements

The three samples being not finished, we have to wait before measurements. However, we have measured the short-circuit current after the microcell array completion ($J_{sc,0}$). Then we have measured again the short-circuit current after the micro-pillars fabrication ($J_{sc,1}$). When all samples will be fabricated, then we will measure again the short-circuit current to evaluate the light concentration ($J_{sc,2}$). To highlight the necessity of a proper LSC / microcells arrays coupling, we have measured the sample when the LSC plate is only put on the array ($J_{sc,2}$). When the coupling with the buffer resist will be done, we will measure again the short-circuit current to evaluate the light concentration ($J_{sc,3}$). Measurements are carried out with the same apparatus than in section 4.2.2.1.

Table 4.5 shows the results we have obtained:

Experimental measurements Gen 2 ($mA.cm^{-2}$)			
Process steps	$C_{geo} = 5$	$C_{geo} = 10$	$C_{geo} = 50$
Bare array ($J_{sc,0}$)	4.8	10.6	25.0
Bare array + pillars ($J_{sc,1}$)	4.8	9.6	24.0
Bare array + pillars + uncoupled LSC ($J_{sc,2}$)	3.72	7.43	19.37
Bare array + pillars + coupled LSC ($J_{sc,3}$)	6	12.5	28.43

Table 4.5: Experimental measurements on Gen 2 prototypes

The microcell arrays we have fabricated are very shunted and the short-circuit current is extremely low for $C_{geo} = 5$ and 10. Yet these cells act as a photodetector, which is satisfying for evaluate light concentration. Because this behavior was unexpected, we have checked (and confirm) that the short-circuit current was a linear function of the total light power. Adding micro-pillars has a week influence on J_{sc}. the slightly drop may be attributed to a possible small misalignment and the fact that the micro-pillars top surface is not perfectly flat ("V-shape").

Putting the LSC without a proper coupling is very prejudicial on performance. All samples exhibit $\sim$ 20% loss. It corresponds to PLQY, side and front losses which are not counterbalanced because of a bad optical coupling.

The pillar coupling is a key point to allow proper concentration. We report a photocurrent increase after LSC coupling, better than for first generation devices. Yet, the buffer layer dries rapidly after spin-coating, which leads to crack during the coupling, due to micro-pillars mechanical constraints. These cracks jeopardize total internal reflection and ultimately the overall performance. Some developments are currently done to increase pillars height in order to allow thicker buffer layer thickness to increase the drying time.

4.4 Opal filter on LSC - Generation 2

It appears clearly than good performances requires to tackle the front loss. Yet the front loss is the most delicate problem since the front surface must transmit as many photons as possible in the LSC but in the same time reflect as many photons inside the device as possible. The only difference between these two photons categories being their wavelength ranges (incoming

photon: full solar spectrum, inside LSC photon: dye absorption bandwidth). As introduced in section 2.1.4, a photonic band stop can be used at the front surface. Some attempts have been done during this thesis with the work of a trainee, Rémi Grapin and Mrs Anne-Laure Joudrier.

In a first approach and to demonstrate the concept feasibility, the opal silica structure was chosen. It is a well-known structure, easy to synthesize, composed of silica nanoparticles (low-cost materials, eco-friendly). It consists in stacked silica nanospheres forming a periodic face-centered cubic structure. As a consequence, the opal presents two kinds of areas: low and high refractive index. High refractive index areas act as scattering centers which may interfere with the incident light wave. The energy of the allowed modes splits, giving rise to a band structure which may comprise stop gaps (no states for photon are allowed). If the material is periodic in the three space directions, infinite and has no defect, then the stop gap can be complete (light propagation prevented in all directions, polarization-independent). Yet in reality, the opal is finite: there is no complete stop gap but we can hope that light propagation within the crystal may be greatly attenuated (pseudo stop gap).

Despite opal qualities already mentioned, its bandgap is tunable to the required wavelength and its optical properties are well adapted to the envisaged device.

The challenging points are to obtain monodisperse particles with the expected diameter and to realize homogeneous deposition on PMMA with the optical properties required.

4.4.1 Experimental

Silica nanoparticles syntheses are based on the Stöber method [91, 92, 93] which uses the hydrolysis and condensation of tetraethyl orthosilicate (TEOS). The starting solutions were TEOS (99,999%, Aldrich), absolute ethanol (99.8%, VWR), ammonia solution (32%, Merck), and deionised water. The reactants were used as purchased without further purification.

The nanoparticles diameter is determined by the well-known equations [92]:

$$\lambda_{111} = 2\sqrt{\frac{2}{3}}d.\sqrt{n_{eff}^2 - sin^2(\theta)} \tag{4.2}$$

$$n_{eff} = \sqrt{n_{air}^2\,(1 - f_{sphere}) + n_{SiO_2}^2 f_{sphere}} \tag{4.3}$$

with d the sphere diameter (nm), n_{air} the air refractive index, n_{SiO_2} the PBS refractive index ($n_{SiO_2} = 1.44$), f_{sphere} the volume fraction ($f_{sphere} = 0.74$ in our face-centered cubic structure), and θ the light incidence angle. In our case, with R305 dye, we want the opal filter reflect light on the emission spectrum, which starts from roughly 620 nm. Therefore the corresponding diameter is 280 nm.

Two solutions are needed: one containing ammonia (4.15 mL) and deionised water (0.85 mL), the other containing TEOS (0.5 mL) and ethanol (55 mL). The second solution is quickly added to the first under rapid stirring at 30°C (solution A). After about 3h, nanoparticles may be physically separated from the liquid phase and re-dispersed into deionised water or absolute ethanol.

The seeded-growth technique was also experimented, and in this case, after 3h, a solution B containing TEOS (1.132 mL) and ethanol (10 mL) is added drop by drop into the solution A, still under stirring and at 30°C. After about 2h under these reaction conditions, particles may be considered having their final sizes. This last step improves the monodispersity and the spheric shape of the particles, which is confirmed by SEM images (FEG-SEM Zeiss Merlin VP): under these conditions, spherical silica nanoparticles were obtained with an average diameter estimated at 280 nm (fig. 4.21). Moreover, these spheres have been spin-coated at room temperature (table-top SPIN150$^{\text{tm}}$ NNP processor) on a glass substrate, as shown in fig. 4.22

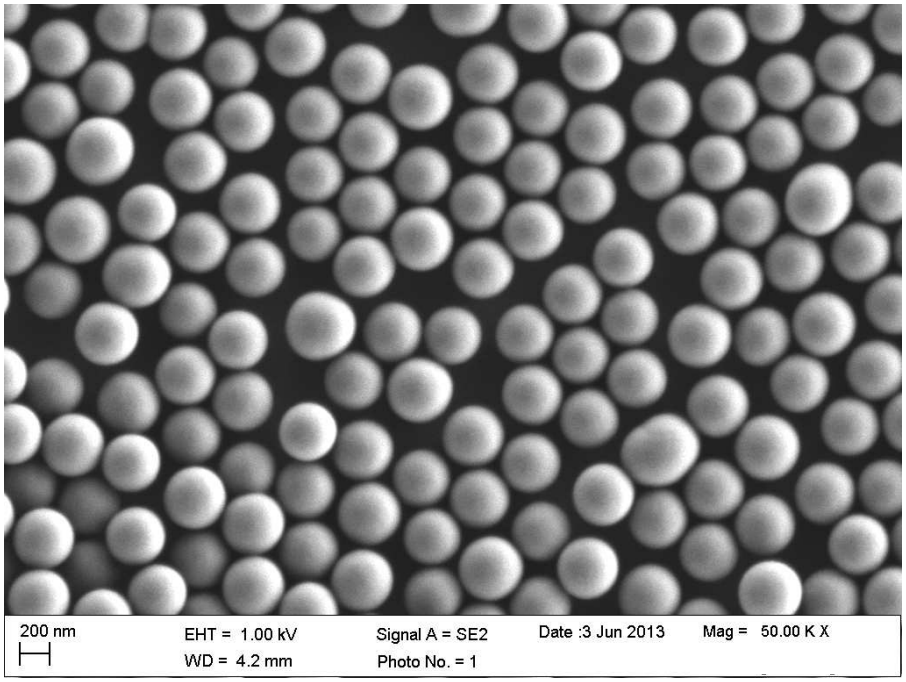

Figure 4.21: SEM image of silica nanospheres. Mean diameter: 280 nm

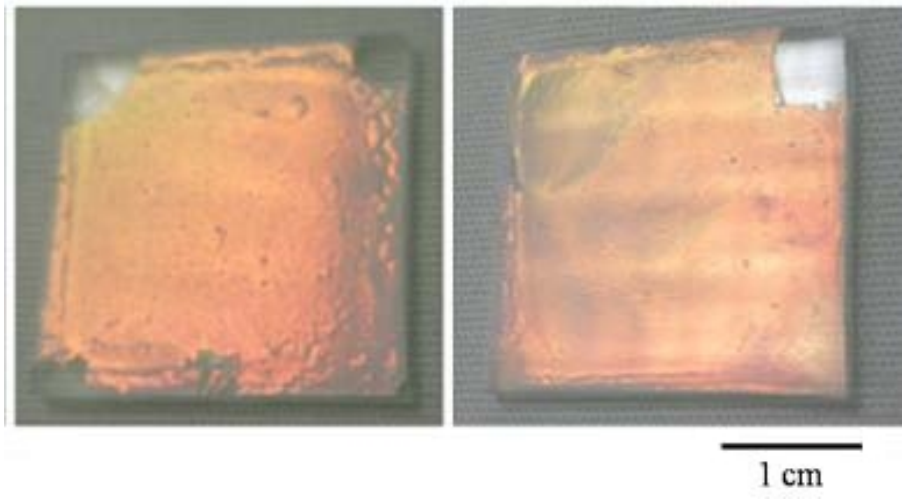

Figure 4.22: Nanoparticles deposited by spin-coating on glass substrates

The spin-coating process involves centrifugal forces for spreading the solution initially deposited at the center of a flat substrate. In this process, the key parameters are speed, viscosity, acceleration and duration. After a lot of parameters combinations, it seems that nanoparticles dispersed in absolute ethanol and deposited at 150 rpm and 100 rpm/s during 15 min allows to obtain a promising opal structure.

Natural sedimentation was also experimented as an alternative solution to synthesize PBS. But, this process was too long (minimum 5 days) and was not pursued. For the test samples, glass substrates are used, because of its good wettability properties and cleaning ease.

4.4.2 Optical characterization

The UV-Vis transmittance spectrum at a normal incidence of the opals shows that a photonic band-gap effect is observed around 620 nm, which results from Bragg diffraction due to the periodicity in the location of the nanoparticles fig. 4.23:

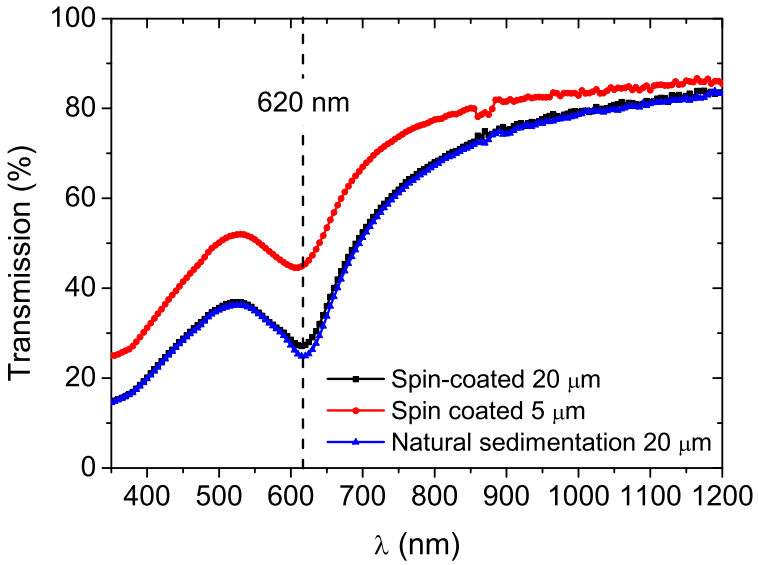

Figure 4.23: Transmission spectra of three different home-made samples: spin-coated samples with two different thicknesses (5 μm (red) and 20 μm (black)) and one by natural sedimentation (20 μm blue)

Three home-made samples were measured: two spin-coated samples (5 μm and 20 μm thick), and one deposited by natural sedimentation with a thickness of 20 μm. As expected, the fraction of transmitted light is more important in the case of the thinner layer. Nevertheless, the photonic bandgap is located at the same wavelength of about 620 nm for each sample. This transmission spectra is an evidence of a photonic bandgap and therefore a pseudo band stop existence. It proves that nanosphere monodispersity and piling up [94] are reasonable, even if they can be greatly improved. It has been also verified that no absorption occurred in our films, only reflection and transmission.

In a same way as on glass substrates, opals were deposited by spin-coating on LSC. Due to PMMA wettability, the nanoparticles organization is not as efficient as on glass. The deposition

parameters must be adapted: with 500 rpm and 500 rpm/s, during 30 seconds, photonic band stop effect was observed but only on small surfaces.

4.4.3 Conclusion & Perspectives

During this thesis we have begun to study opal as a photonic band stop filter. It was done in the frame of an internship at IRDEP for which I was one of the two supervisors. First silica nanosphere fabrication was tackle. Fabrication process was inspired from the literature and optimized to obtain the desired diameter, and consequently the desired bandgap. Then different deposition techniques have been tested. The two most promising techniques we have identified were spin coating and sedimentation. Then the opal films were characterized (morphology with SEM, optical transmission with a spectrophotometer).

Photonic band-stop effect have been identified. This promising result originates from both monodispersity and ordered stack. From SEM images, nanospheres stacking seems to be the most challenging issue, monodispersity being acceptable. Next steps will be to improve the nanospheres deposition, both on glass and on PMMA. Additionally, others structures can be studied, such as the inverse opal ("air nanospheres" surrounded by high index medium).

4.5 Big picture

This chapter was devoted to the LSC experimental part. We have successfully fabricated microcells arrays and LSC. To the best of our knowledge, this is the first time that CIGS-based microcells arrays are coupled to luminescent solar concentrator. Our first prototypes were unoptimized and were mainly used to compare experimental and modeling results. Despite their low concentration factors (best one 1.21), we have observed a good accordance between experimental and our numerical tool results.

Numerical results have enable to identify and quantify what were the devices limitations and lead us to propose some improvements. Aside of get rid of side loss by increasing the device size, we have considered to use an air gap in between solar cells. Numerical calculation showed that this configuration allows to half the back loss. Because this thesis seeks to deal with both theory and experimental, we have developed a process to put the air gap principle into action. Samples are not totally finished, that prevents us to finish our study. This kind of delay happens when technological process has to be developed from scratch, but we are confident that results will be very soon available.

We also have began to address the front loss issue, using an opal photonic band-stop filter. We have successfully fabricated monodisperse silica nanospheres with the desired diameter. The stacking to form an opal structure is under development. Yet sedimentation and spin-coating techniques have enable to demonstrate a band stop effect at the desired wavelength. this effect is not strong enough to improve LSC performance but first results are promising. Significant room for improvement in the opal stacking gives hope to get better results in the future.

Part I Conclusions

Thought the first part of this work, we have contributed to answer the question: Is luminescent Solar Concentrator a good match with CIGS-based microcells arrays? The literature survey has enabled to highlight the luminescent solar concentrator as a potential good candidate. Indeed, it theoretically combines numerous beneficial features for light concentration on microcells arrays:

- High concentration factor (medium - low concentration range)
- Both specular and diffuse light components concentrated
- No focal point
- Low-cost

Much of this part was committed to the theoretical study of luminescent solar concentration. We have developed a versatile numerical tool, based on Monte Carlo algorithm, to quantify each loss channels contribution, depending on the LSC parameters and geometry. It allows us to clearly explicit why there is such a gap between theoretical and experimental performances. On the one hand high theoretical concentration factor requires high geometrical gain, but on the other hand, high geometrical gain enhances existing loss mechanisms. It is apparent, therefore, that an ideal theoretical LSC which suffers only from front escape loss is less sensitive to high geometrical gain than an real LSC which experiences numerous loss channels (dye, reflector, matrix, front escape).

This fact leads us to search for innovative improvements. We developed an air gap configuration at the back surface that halves the back loss and improve the angle conservation in the LSC. We have also made some attempts to fabricate a photonic band stop filter in order to reduce the front loss. Although a stop-band effect has been measured, huge progress on the nanospheres stacking must be done to make this system viable.

To our knowledge, this work is the most advanced in some aspects of the LSC understanding, such as dye/solar cell mismatch effects, loss analysis via statistical data, related to the geometrical gain role.

Optical efficiency drop for large geometrical gain makes difficult to consider the medium concentrated photovoltaics market, even with improvements such as photonic band-stop or bottom airgap. The extremely high sensitivity to non-ideality explains why real devices performances are far from theoretical expectations. Yet, we think that luminescent solar concentrator is more likely suited to compete in the low concentrated photovoltaics ($<$ X10) market. Satisfying concentration factors have been achieved, with plenty room for improvements, not forgetting esthetics.

This study, in contributing to highlight the role of the geometrical gain, has been the starting point to a totally new concept emergence. The geometrical gain being a common denominator in all internal losses, it contributes to decreases the optical efficiency while in the same time it contributes to increase the concentration factor, which worth the geometrical gain times the optical efficiency. To circumvent this effect, we had the idea of introducing a nano photovoltaic cell embedded in an optical nano-antenna. This kind of device has an optical absorption cross section which can be larger than its metallurgical area, which means that a geometrical gain can be introduced (to a certain extent) without reducing the optical efficiency. That is the subject of the second part of this manuscript.

Part II

Nanophotonic-based concentration

Chapter 5

Nano-antenna for PV applications

Contents

The first part of this chapter focuses on our motivations to implement Metal-Insulator-Metal nano-antenna as well as a spectral convertor. The second part is dedicated to a general review of solutions to reduce PV absorber thickness in which nano-antenna can be considered as the ultimate step. Finally the last part will be dedicated to the modeling. The different existing solutions will be reviewed and the code we are using (RMCA) will be described.

5.1 Nano-antenna and spectral convertor coupling

In this section we explain exactly why we think this coupling can be a very efficient solution. We won't use the term LSC to refer to the doped matrix but to the spectral convertor instead. Indeed, we will see that the doped matrix main role is not to trap and guide light to PV cell but to modify the photon wavelength. Yet, matrix trapping by total internal reflection is an original feature for resonators, which are usually in contact with air. We will investigate (section 6.1.2.4) if matrix trapping can improve the resonator efficiency.

From the LSC point of view, as written in the conclusion of chapter 4, high concentration requires both high optical efficiency (η_{opt}) and high geometrical gain (C_{geo}). Sadly, the higher is C_{geo}, the lower is η_{opt} (because the probability of reaching solar cell is lower), so the mean free path is higher and finally losses increase. This is a fundamental limit which requires a

paradigm shift to be circumvented. To overcome this limitation, we have decided to explore the sub-wavelength scale in order to take advantage of sub-wavelength light properties. At this scale, light cannot be considered as a ray. If well designed, some structures will act as antenna and concentrate the electromagnetic fields. We will see that this concentration is vertical (orthogonal to the surface), which allows to have an extremely thin absorber layer while having still a good absorption. Additionally, the concentration is also lateral (x & y-axis) due to the so-called funneling effect [95].

Thus, the feature of nano-antenna which motivates most their use in an LSC-like system is that the optical antenna cross section is larger than its area. If now the antenna are localized in such a way that the cross sections overlap (or adjacent), then the total surface will have the same optical response even though antenna do not cover all the surface (giving rise to a geometrical gain without introducing related loss). Therefore, the optical response spatial independence ensures that η_{opt} is not correlated anymore to C_{geo} (until absorption cross-sections are too remote). The fundamental limit may be exceeded. This is depicted in the figure below:

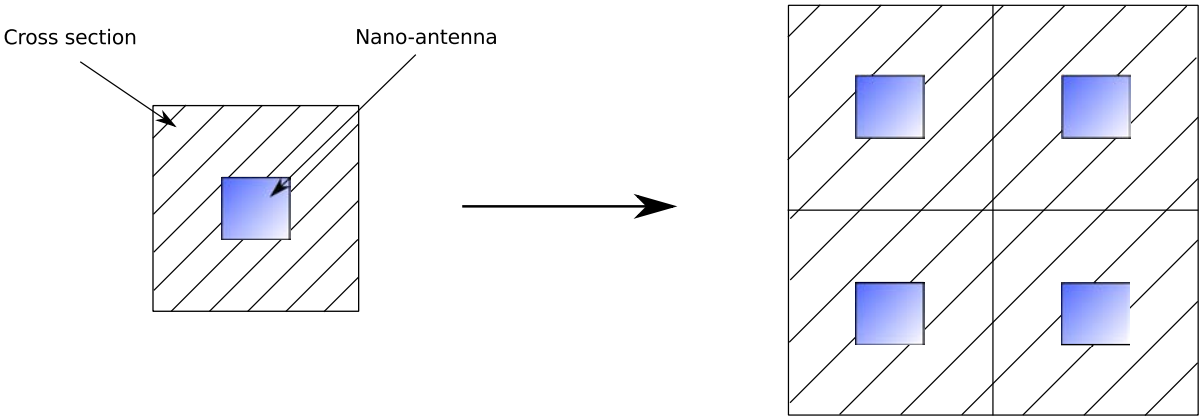

Figure 5.1: Qualitative scheme of the lateral concentration feature of nano-resonators. $Left$: one nano-resonator (blue) and its absorption cross-section (hatched). $Right$: nano-resonator patterning allowing homogenous optical response despite low coverage fraction.

Explanations given above can be viewed as the interest for the LSC community to explore sub-wavelength optics. Conversely, the breakthrough of this coupling is even easier to understand from the sub-wavelength optics point of view. Almost all structures in the literature able to concentrate the electric field at the nanoscale are resonant. Unfortunately, the more efficient the resonance (i.e. the higher the electric field confinement in the absorber layer), the thinner its bandwidth (the spectral region in which resonance occurs). Knowing that a PV cell operates on the full solar spectrum till the absorber bandgap, the resonator needs to be adapted to the solar spectrum which leads to design multi-resonant structures. Prior to this thesis, this strategy was adopted by every research teams working in PV nanophotonics [96, 97].

At this point, one can see the huge advantage that procures the spectral convertor: the solar spectrum is tuned to match the resonator thin spectral bandwidth absorption. Absorbing photons on a large bandwidth and re-emitting them on a thinner bandwidth at higher wavelength, the nano-antenna has to be efficient only on a thin spectral region, and consequently a mono-resonant antenna, tuned to the spectral convertor emission wavelength, may be as efficient as

multi-resonant devices without spectral convertor. Figure 5.2 illustrates the nano-resonator / spectral convertor coupling.

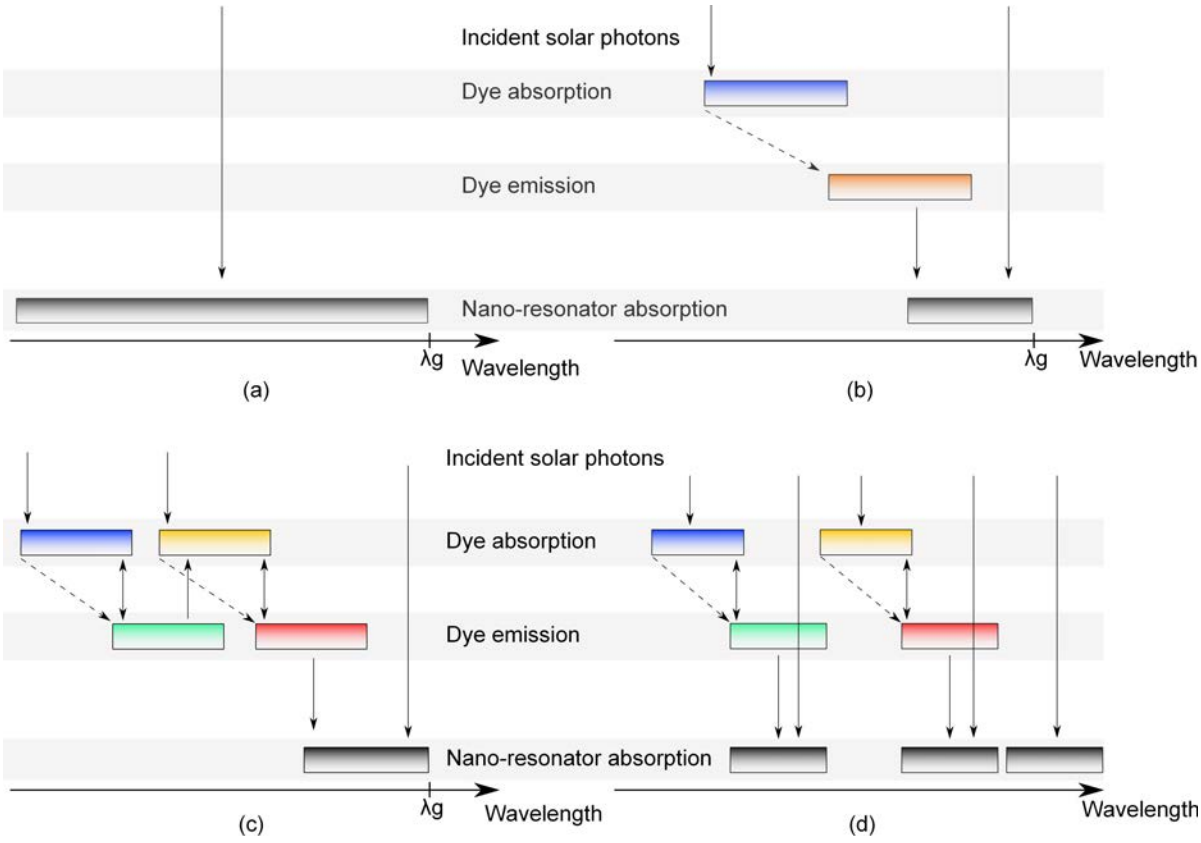

Figure 5.2: Illustration of the nano-resonator / spectral convertor coupling. The upper tinted area corresponds to dye absorption, the middle one to dye emission and the lower one to nano-resonator absorption. Dotted arrows illustrates the radiative dye emission, whereas the double arrow depicts self absorption (a). No spectral convertor, nano-resonator should be efficient on all the useful solar spectrum (multi-resonance mandatory). (b). One dye spectral convertor. (c) Two dyes spectral convertor. (d) Two dyes spectral convertor associated with two tuned resonator plus a last one. In configurations (b), (c) and (d), nano-resonator bandwidth is smaller than in (a).

Obviously when no spectral concentrator is used, the nano-resonator must be efficient on all the solar spectrum bandwidth (fig. 5.2a). With a simple one dye spectral convertor (fig. 5.2b), the nano-resonator should be efficient only close to the absorber bandgap (from the beginning of dye emission to the bandgap). Nevertheless a dye has generally an absorption bandwidth lower than 200-300 nm, and must be highly concentrated to absorb efficiently on all its absorption spectrum. As a consequence, the use of only one dye is generally not optimal. Figure 5.2c depicts a two dyes cascade spectral converter. Using two dyes release the constraint on the dye concentration and enables to cover a larger spectral bandwidth. Figure 5.2d pushes the concept to use different nano-resonators adapted to the dye, in order to extract the highest voltage as possible. Because these resonators are connected in parallel, the overall system acts like a multi-junction solar cell. More details on this aspects will be given in the perspectives of chapter 6.

This concept has consequently numerous advantages. Being mono-resonant, the nano-resonator design constraints are released since a high absorption is only expected on a thin bandwidth. A second advantage is that reflection on nano-antenna is not necessarily a loss because reflection at the top surface of the spectral convertor may happen. In this thesis, we will call this effect photon recycling (not to be confused with photon recycling in semiconductors). The corollary of photon recycling is that diffraction also may not be a loss, and consequently one can hope to increase the nano-antenna array period to save more material and improve concentration, without loosing too many photons. This will be shown in the next chapter. A more subtle consequence of the mono-resonance is that the SC volume can be reduced (see section 5.3.2.1).

5.2 Strategies to improve light absorption in a PV absorber

Reducing absorber thickness is becoming one of the main trend in photovoltaics research. The first reason is economic. As an example in silicon-based PV technology, even if Si is the third most abundant material in the Earth crust, material cost represents $\approx 40\%$ of the total cost of a c-Si PV module because of the high Si purity. An interesting mean of reducing this cost is to reduce the amount of silicon used in the module while keeping the same conversion efficiency. Doing so, it may be conceivable to use less pure material in a thin device. Moreover, c-Si share in the PV market regularly shrinks since 2000s compared to other PV technologies such as CdTe or Cu(In,Ga)Se_2 (thin films technologies) or organic photovoltaics (OPV). Many of these emerging technologies require expensive and/or scarce materials (Tellurium for CdTe, Indium for Cu(In,Ga)Se_2) leading to the need of raw material saving to drop the costs and avoid material shortage. Another important reason is that the carrier collection length and impurity recombination are reduced when the active layer is thinner, which converges to a better conversion efficiency. Finally, since light concentration induces resistive loss, lowering PV size lowers the resistive loss. Thus there are multiple reasons to reduce the PV absorber thickness, and significant efforts have been made to do so.

Reducing the active layer thickness is not drawback-free and compromises the optical absorption which in turn decreases the PV cell short-circuit current. When geometrical optics is valid, the proportion of absorbed light intensity on a one way path follows Beer-Lambert Law:

$$I(d) = I_0\,(1 - exp(-\alpha.d)) \tag{5.1}$$

Where $\frac{I}{I_0}$ is the ratio between the absorbed flux and the incident flux, α is the absorption coefficient of the absorber material and d the absorber thickness. From this law we see that to capture 95% of the photons, the thickness needs to be kept higher than $\frac{3}{\alpha}$. As a consequence, enhancing the optical path length is mandatory to keep a thick optical thickness despite a thin physical thickness. As described later in this section, at sub-wavelength scale, absorption enhancement will rely on local permittivity change.

We will now introduce light path enhancement through a back surface reflector. Although efficient, this approach cannot exceed the classical limit of light concentration and is not conceivable for nanodevices. That is why other light concentration means will also be reviewed, from periodic light trapping structures and nanowires to plasmonic-enhanced photovoltaic devices.

5.2.1 Back surface reflector and classical limit

The simplest way to increase the optical path length is to put a reflective layer at the back of the solar cell. If the reflector is specular, the path length will be at least doubled. Additionally, the active layer acts as a waveguide due to the back reflector and front reflection, which ultimately increases the light path length as the incident wave coupled to waveguide modes. To improve reflection, gratings can be used to create a specular back reflector. A Bragg reflector is a 1D stack of several dielectric layers of alternating materials of different refractive indexes. Interferences occurring inside the Bragg reflector can be either constructive or destructive (according to the wavelength) leading to high transmission or reflection [98]. Being strongly sensitive to the wavelength and the incidence angle, using Bragg reflectors makes the device more complex but can be used for some thin film solar cell to reflect the narrow spectrum range (wavelength close to the bandgap) not absorbed in one way path.

Lambertian reflector can also be used to enhance the light path length inside the absorber material. As a reminder a reflector is said Lambertian if the light is reflected along all directions with the same intensity. First works on Lambertian scattering were conducted by Yablonovitch group [99] as well as Goetzberger group [100]. They demonstrated that a Lambertian reflector of ideal reflection coefficient localized at the bottom of the absorber layer leads to an absorption enhancement of $4n^2$, n being the refractive index of the absorber material [101, 65]. It can be still very efficient, leading to X50 increase in silicon.

A 40% broad-band photo-current enhancement for a thin-film photovoltaic cell has been reported [102]. It was obtained by modifying the photon density of state with specifically designed dielectric mirrors. An increase of electric power conversion of a factor 4.3 due to light path enhancement was reported in [103] for an OPV cell. This result, commonly called the classical limit, is valid only if the system can be entirely described by geometrical optics.

Reflector needs to be rough (roughness higher than the wavelength) to be Lambertian. On the other hand, we are dealing with sub-wavelength devices. The two size domains do not overlap, which means that other ways of doing light trapping must be adopted.

Many other examples of light trapping techniques have appeared during the last decade taking advantage of the light property at the nanoscale. Nano-photonic gratings and photonic crystal were the first, followed by other concepts, such as nanowires or plasmonic-based light trapping. They are reviewed in the next three sections.

5.2.2 Nanophotonic light trapping grating and photonic crystal

2D and 3D gratings placed on (or below) the absorber layer have been proposed to perform nanophotonic light trapping. Mokkapati and Catchpole published a good review mainly focusing on these gratings [104]. The idea behind a nanophotonic grating of period smaller than the visible wavelength is to create a device in which the incident plane wave can be coupled to more diffraction modes in the absorber layer than in air. Indeed, the incoming plane wave can be coupled only to the fundamental (0^{th}) diffraction order in air whereas it can be coupled to numerous propagating diffraction modes inside the absorbing layer (for periods lower than the incident light wavelength). Thus, they provide a mean of enhancing the light path in a photovoltaic device. Different kind of gratings based on nanowell have also been developed [105] as well as different nanophotonic light harvesters [106].

A well known kind of grating is photonic crystals (PC). They can reflect light from any angle provided the wavelength and polarizations remain within the photonic bandgap [42]. A review on photonic crystals can be found in [107]. The photonic bandgap follows the same physics as the semi-conductor bandgap. Waves must oscillate according to the Bloch's theorem in a periodic medium. When they vary with a period proportional to the medium period, they concentrate their energy in the low and high refractive index medium, giving rise to a photonic bandgap. Furthermore, diffraction at highly oblique angle, like for usual gratings, is also valid for PC, enhancing light trapping. [98] compares PC light trapping to geometrical optics light trapping. Chutinan *et al.* [108] performed experimental calculations leading to a theoretical relative increase of 11.15% in the energy conversion in a 2 μm thick c-Si with a photonic crystal. Others research teams have showed enhanced absorption due to PC [109, 110]

5.2.3 Nano-wire-based light trapping

Nanowire-based devices are becoming more and more attractive as nanofabrication processes become more robust and better mastered. It paves the way toward nanodevices such as nanowires exhibiting interesting optical properties. It has been demonstrated by Garnett *et al.* [111] that ordered arrays of silicon nanowires increases the path length of incident solar radiation up to 73 times. More recently, Wallentin *et al.* [112] demonstrated 13.8% efficiency InP nanowires array exceeding ray optics limit.

The light trapping may come from a nanowire array grating effect or light guiding inside each nanowire. The second option is most likely according several authors [113, 114, 115] due to strong Fabry-Perot resonances inside the nanowire and better performances of aperiodic over periodic nanowires array of the same density. A review article on Si nanowires can be found here [116]. A work on InP nanowire design [117] shows that one can obtain optimal absorption with only 38% active material usage compared to a flat layer benefiting from both near-field enhancement and anti-reflection effect. OPV nanowires have also been reported [118].

5.2.4 Plasmonics-based light trapping

Plasmonics deals with metallic nanostructures exhibiting surface plasmons which, may ultimately lead to light concentration inside a thin absorber layer. Several fields in physics can benefit from plasmonics such as optical microscopy, photodetectors, modulators, thermal emitters and photovoltaics. More details can be found in the review of Schuller *et al.* [119] and Stockman [120]. As described by Atwater and Polman [121] and Pillai *et al.* [122], two main different ways of using plasmonic properties with photovoltaics have been investigated. The first one is light scattering from metal nanoparticles and the second one is the near field enhancement.

The first studies on photovoltaic devices with plasmonic effects were published in 1995 [123, 124], followed by Stuart and Hall [125, 126]. They demonstrate an order of magnitude enhancement in the photocurrent for light at 800 nm by taking advantage of metallic beads-induced light scattering. Latter, Pala *et al.* [127] defined some rules to design plasmonic resonators and to favor light concentration by coupling to waveguide modes and near-field light concentration by localized surface plasmon-resonances. They showed a theoretical 43% short-circuit current enhancement using metallic gratings at the top surface.

The second approach is to take advantage of a near-field enhancement in the absorber layer in the vicinity of metallic nanoparticles. First publications related to this effect were linked

to organic photovoltaics (OPV). The diffusion length of OPV is small (few tens of nanometers) compared to inorganic PV. Thus, reducing absorber thickness while keeping high optical absorption is of particular interest in this field. An interesting review is dedicated to light trapping nanostructures in OPV [128]. Barry P. Rand *et al.* [129] showed that more than a 10 fold light intensity enhancement on a wide spectral range [500 – 800 nm] was achievable. Rourke *et al.* [130] showed integrated enhancement of 22% in short circuit current under 1 Sun illumination on an OPV cell with a slot grating structure. Other research teams have also worked on this subject, both on organic or inorganic solar cells [131, 132].

5.2.5 Conclusions

We have seen that the classical back reflector does not allow to exceed a concentration factor of $4n^2$ and is not feasible below the wavelength size. Others strategies have been considered far, as illustrated in fig. 5.3:

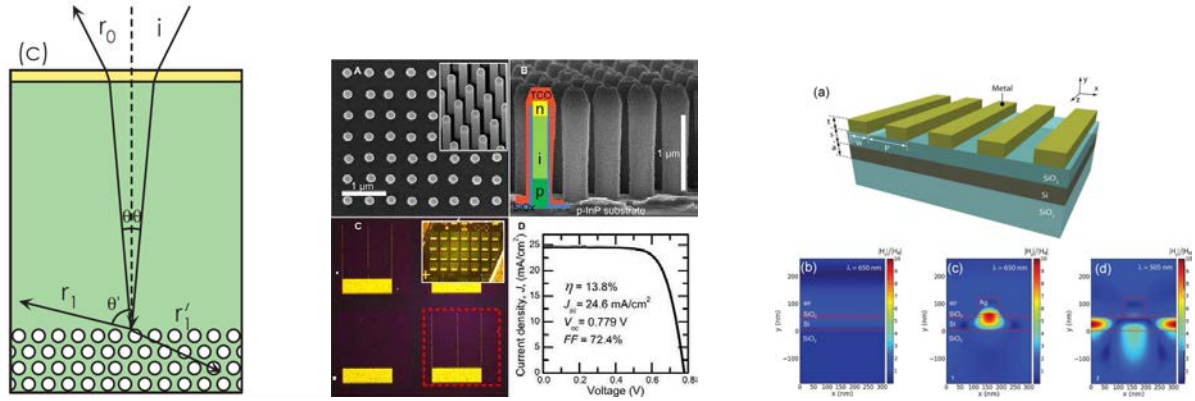

(a) (b) (c)

Figure 5.3: Illustration taken from the literature of light concentration with (a) photonic crystal [98], (b) nanowires [112] and (c) plasmonic / near-field effect [127]

There is no metal in photonic crystals, which makes the electrode design more challenging, compared to the solution we have chosen (MIM structure, see section 5.3). Conversely, we will see that metal is a loss cause in our device which does not exist in photonic crystal. An other photonic crystal feature is their higher quality factor compared to MIM. This is still due to metal loss in MIM which reduces the quality factor. The positive effect of a lower quality factor is that the resonance spectral bandwidth is larger, which makes MIM structures more appropriate in photovoltaics (large solar spectrum).

Nanowires in photovoltaics is a prospective research area which has numerous advantages. Nanowire growth (1D) exhibits less defects than film growth (3D). This is mainly due to the fact that a one dimension growth is constrained in only one direction, and therefore enables to "absorb" defects, at the price of orientation shift for example. Another big advantage is the possibility to produce radial junctions. In a radial junction, the space charge region is not close to the structure metallurgical limits (full of defects), which may greatly reduce non radiative recombination. Moreover, the local growth (bottom up approach) is much more satisfying when raw material saving is one main objective.

As explained in the next section, we have chosen to work on optical nano-antenna based on MIM geometry. This is a top down approach which involves etching. A pragmatic reason is that etching was mastered before this thesis and does not require too much development.

5.3 Optical nano-antenna based on Metal-Insulator-Metal geometry

5.3.1 Description

The structure we decided to study is an InP-based Metal-Insulator-Metal (MIM) structure (schematically illustrated in fig. 5.4). Through this work, MIM refers to the metallurgical aspect of the resonator (two metal layers, one dielectric layer in-between) and not to the MIM resonance mode [133].

MIM structures were first studied for the design of optical filter [134, 135]. However, their optical properties [136] in terms of light collection in small volumes are particularly interesting for designing efficient thin PV cells. More specifically, they may exhibit at resonance almost perfect absorption, over a very wide angular range (typically between -70 and +70 degrees) for cavity volumes (inside the dielectric layer) as small as $\frac{\lambda^3}{1000}$ [137].

A MIM structure can be used in photovoltaics if the "I" layer is replaced by a semiconductor absorber layer. It can be seen as a photovoltaic cell embedded in a nano-antenna, in which the metallic parts of the antenna play also the role of electrodes. At optical frequencies, when free electrical charges are generated by doping or illumination, the dielectric constant of the semiconductor does not vary significantly (less than 1/1000). It behaves like a lossy dielectric material, which allows us to take advantage of the MIM optical properties to enhance light absorption. Having a junction in a MIM structures, it implies that a minimal thickness is required, which is not the case when only optical absorption is of interest, as in [137].

The resonant feature of these antennas, which will be detailed later in this chapter, means that their bandwidth is very small compared to the entire solar spectrum (typically a tenth of the resonant wavelength at half maximum). Asymmetric structures dedicated to the production of photovoltaic cells have been reported in several publications [96, 97]. They are based on the simultaneous presence of a plurality of resonances allowing a large part of the solar spectrum to be covered. Although very efficient, the dimensions of these structures are highly constrained due to the conditions that must be met to obtain multi-resonance in the solar spectrum with a given semiconductor.

Recently, efforts were made to describe MIM resonators by analogy with metamaterials [97], resulting in a simple model that can be used to tailor the MIM resonances and optimize the material reduction.

5.3.2 Resonance mechanisms in a MIM structure

Despite of their simple geometry, MIM structures exhibit resonances of multiple origins. This section reviews three of the main resonance mechanisms identified during this work, which are:

1. The Fabry-Perot resonance
2. The plasmon confined mode resonance

3. The guided-mode resonance

The goal of this review is also to identify which mechanism is the more interesting for us. While multi-resonant devices must integer resonances of different nature and therefore deal with their specificities, we only need one resonance: better to choose the most favorable mechanism.

Nevertheless I would like to mention that they are not the only resonance mechanisms. Fano resonance is also a phenomenon which may occur in nano-antenna devices. More information may be found in [138, 120].

5.3.2.1 Fabry-Perot resonance

The first resonance mechanism is the well known Fabry-Perot effect. Its origin is the same as the Fabry-Perot Interferometer: when photons travel through a cavity with two mirrors, constructive interference occur if the phase shift on a round-trip is $2m\pi$, with $m \in \mathbb{Z}^*$. This phase shift has three contributions: two from the reflection on each mirror Φ_b, Φ_f (b stands for back and f for front), and one from the propagation in the cavity medium (Φ_t):

$$\Phi_b + \Phi_f + \Phi_t = 2m\pi,\ m \in \mathbb{Z}^*, \text{with: } \begin{cases} \Phi_b &= phase(\frac{\overline{n}_m - \overline{n}_{SC}}{\overline{n}_m + \overline{n}_{SC}}) \\ \Phi_f &= \Phi_b \\ \Phi_t &= 2.k_z.t \end{cases} \tag{5.2}$$

$\overline{n}_m$ and $\overline{n}_{SC}$ are the complex refractive index of the metal and semiconductor respectively, k_z the wave vector in the z direction and t the cavity thickness. The factor 2 in ϕ_t comes from the round-trip in the cavity. From eq. (5.2), it can be seen that the Fabry-Perot resonance spectral position can be adjusted with the SC thickness (influencing Φ_t).

Because the top metal of thin thickness cannot be considered as infinite (contrary to the back reflector), the equation $\Phi_f = phase(\frac{\overline{n}_m - \overline{n}_{SC}}{\overline{n}_m + \overline{n}_{SC}})$ is not correct. A more accurate derivation can be found in appendix D.

At normal incidence, $k_z = Re(n)k_0 = Re(n).\frac{2\pi}{\lambda}$, which gives an explicit relation between the resonance wavelength and the cavity thickness:

$$\lambda_{res} = \frac{4\pi.Re(n).t}{2m\pi - \Phi_f - \Phi_b},\ m \in \mathbb{Z}^* \tag{5.3}$$

Expressing the two reflection phase shifts either by the approximate expression (eq. (5.2)) or the complete derivation appendix D, one can tune the resonator thickness to have the m$^{\text{th}}$ order Fabry-Perot resonance at the desired wavelength. This type of resonance is extremely interesting in MIM nano-resonator because a first order resonance is centered inside the cavity (corresponding to the intrinsic region), and also because its angular dependence is weak (because of a low k_x influence, see eq. (5.4)). Inclining the light beam by an angle θ is equivalent to defining a non null $k_x = k_0.\sin(\theta)$. Thus with an incidence angle, we have:

$$k_z = \sqrt{Re(n)^2.k_0^2 - k_x^2} = \sqrt{k_0^2(Re(n)^2 - \sin(\theta)^2)} \tag{5.4}$$

From eq. (5.4) the angular dependance is lower when the refractive index is high, which is the case in the semiconductor ($Re(n) \approx 3.5$). This feature may be of importance because the dye in the spectral converter emits photon isotropically. Thus, evidence of Fabry-Perot resonance will be:

1. Electrical field enhancement spatial position (1^{st} order: 1 maximum in the center of the cavity, 2^{nd} order, two maxima close to the cavity edges and so on)

2. Good angular tolerance

In a MIM structure, two kinds of Fabry-Perot resonances may exist: vertical and horizontal ones. In addition, because the top metal layer is structured, there are two resonances of each kind, resulting in four distinct Fabry-Perot resonances, as illustrated in fig. 5.4a. Consequently four absorption peaks exist (if they are not degenerated) which makes the device, by nature, multi-resonant. We will see that studying mono-resonant systems, we do not need so many resonance, which allows us to structure even the semiconductor as shown in fig. 5.4b.

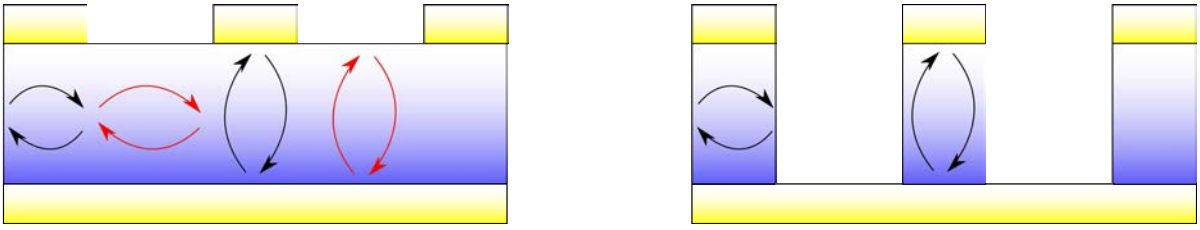

Figure 5.4: Fabry-Perot resonances. Red arrows, resonances between semiconductor and air. Black arrows, resonances between semiconductor and metal.

This observation makes the development of mono (instead of multi)-resonant structures even more appealing: semiconductor structuring may save material is growth is local.

5.3.2.2 Plasmonic resonance

Plasmonics is the study of the interaction between electromagnetic field and free electrons in a metal. A century old, this domain has been extensively studied since the 1990s with the emergence of new computational and fabrication methods. Plasmonics playing a minor role in this thesis because of the mono-resonant nature of the device we design, we will only describe its principle and how it takes part in our resonator performance. More information on plasmonics and PV can be found in [139, 121, 140, 122].

5.3.2.2.a Surface plasmon polaritons (SPP)

A SPP is an evanescent electromagnetic wave which propagates at the interface metal/dielectric (or metal/SC) and is coupled to free electron oscillations in the metal. A visual representation is given in fig. 5.5

SPPs are said to occur only at a metal/dielectric interface because they need a negative component of the real part of one of the two media dielectric constants, which is the case for metal. Nevertheless, even though uncommon, some non metallic materials also exhibit

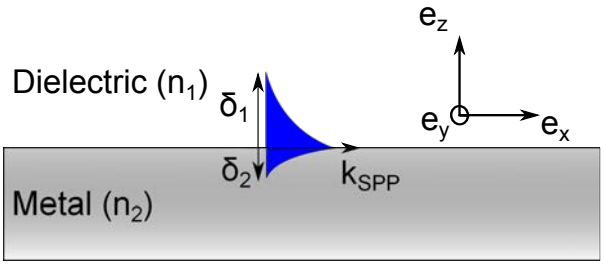

Figure 5.5: Surface plasmon polariton propagating at the interface dielectric/metal. δ_1 (δ_2) is the propagation length in the dielectric (metal) respectively.

this property, generally above NIR region (Indium Tin Oxide [141], Aluminium Zinc Oxide [142])and therefore can support SPP. A SPP is TM polarized, which will be very important in our structure design: this resonance mechanism won't appear in TE polarization. Indeed, a SPP is a charge oscillation perpendicular to the surface: only an electric field also perpendicular to the surface can lead to this charge oscillation, which is the case for TM polarization. For more details, see [134]. TM polarization means that the magnetic field $\mathbf{H}_i$ in the medium i is parallel at the interface metal/dielectric.

To understand the particular shape of the propagating SPP and also have some insight of the physics underlying SPP, one can express the SPP wave vector k_{SPP}, at the interface between two semi-infinite media, as a function of the dielectric permittivities ϵ_1 and ϵ_2 (magnetic permittivity $\mu_1 = \mu_2 = 1$):

$$k_{SPP} = \frac{k_0}{\sqrt{\frac{1}{\epsilon_1} + \frac{1}{\epsilon_2}}} = \frac{2\pi}{\lambda\sqrt{\frac{1}{\epsilon_1} + \frac{1}{\epsilon_2}}} \tag{5.5}$$

We can now express $\mathbf{H}_i$:

$$\mathbf{H_i} = H_{0,i} e^{j.(k_{SPP}.x + k_{z,i}.z - \omega.t)} \mathbf{u_y} \tag{5.6}$$

k_{SPP} is complex: $k_{SPP} = k'_{SPP} + j.k''_{SPP}$. The z component of the wave vector $k_{z,i}$ is linked with k_{SPP} as follows:

$$k_{z,i} = \sqrt{\epsilon_i.k_0^2 - k_{SPP}^2} = k'_{z,i} + j.k''_{z,i} \tag{5.7}$$

Finally one can express the magnetic field amplitude:

$$|H_{SPP,i}(x,z)| = H_{0,i} e^{-k''_{SPP}.x} e^{-k''_{z,i}.z} \tag{5.8}$$

Equation (5.8) shows that the magnetic field of a SPP is evanescent along x and z directions. The field decays exponentially during the propagation because of metal loss. We deduce from the previous equation the SPP propagation length Λ along the x axis and its confinement (SPP skin depth) in the two media δ_1 and δ_2:

$$\begin{cases} \Lambda & = & \frac{1}{|k''_{SPP}|} \\ \delta_i & = & \frac{1}{|k''_{z,i}|},\ i = 1\ or\ 2 \end{cases} \tag{5.9}$$

The skin depth in both media will monitor the loss in the metal part, which is a decreasing function of permittivity imaginary part [143]. It partly justifies our choice for metal: even though we do not especially seek after plasmonic resonance, we want to reduce potential loss and so we choose the metal with one of the lowest permittivity imaginary part in the visible range: silver. Some alkali metals are even better, such as potassium but they are too reactive with air and water to be used [144]. Yet gold is an excellent alternative to silver because of its stability (no oxidation/sulfurization).

5.3.2.2.b Plasmonic resonance coupling

We have seen in the previous section which physical parameters rule SPP: the imaginary part of the different media. In a MIM there are two metal layers on both sides, and consequently two SPP waves. If the SC thickness is thin enough, a coupling may occur. More precisely, there is a coupling when the thickness is thinner than the sum of the two skin depth in the SC. This coupling is illustrated in fig. 5.6:

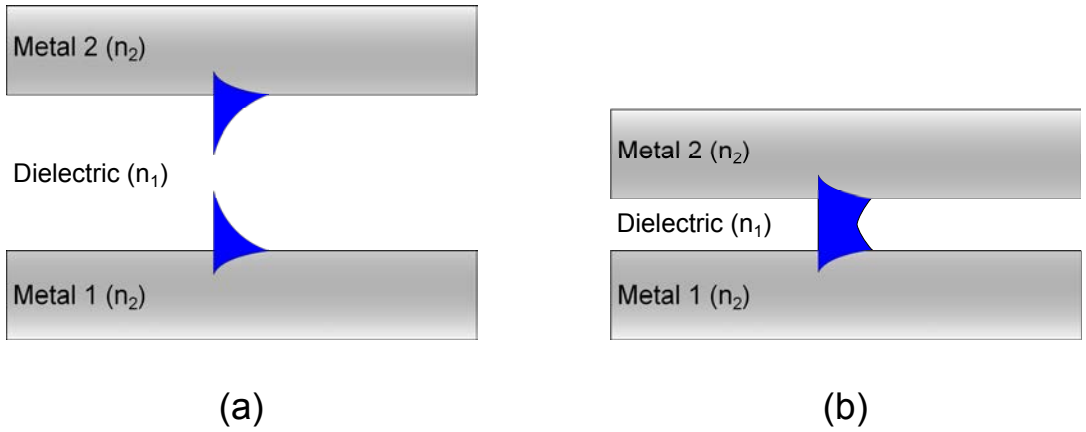

Figure 5.6: (a) Thick MIM structure: no SPP coupling. (b) Thin MIM structure: SPP coupling is possible

5.3.2.3 Guided-mode resonance

The nano-antenna has a grating structure (period p) which may supply an extra momentum ($\frac{2\pi}{p}$), allowing the coupling of incident light with a diffracted mode. Besides, the coupling depends also on the incident angle θ and the effective index of the wave-guided mode n_{eff} via the grating formula:

$$\frac{2\pi}{\lambda_{res}}.\mathcal{R}e(n_{eff}) = \left|\frac{2\pi}{\lambda_{res}} n_{inc} sin(\theta) + m.\frac{2\pi}{p}\right| \tag{5.10}$$

with m being the order of the waveguided mode and n_{inc} the real part of the incoming medium refractive index. This equation expresses the fact that the coupling must satisfy the conservation of the in-plane momentum. Guided mode resonances are very sensitive to θ which reduces their interest in the frame of this work. Indeed, in the small angle approximation, $\sin(\theta) \approx \theta$ which leads to:

$$\frac{\Delta\lambda_{res}}{\Delta\theta} \approx n_{inc}\frac{p}{m} \tag{5.11}$$

We will see in the next chapter that guided-mode resonance occurs in our resonator and how eq. (5.10) can be used to identify them.

The next section highlights the computational method we use to model these nano-structures.

5.4 Rigorous Maxwell Constitutive Approximation

Through all this manuscript, the code I use to model nano-resonator is based on the Rigorous Maxwell Constitutive Approximation (RMCA) method (except for few specific cases which will be mentioned later). This code has been written by Fabrice Pardo from LPN and Yaneck Gottesman from GET-INT-Evry, on the basis of Finite Equation Techniques adapted to 2D gratings.

RMCA simulations enable to design and analyze resonance mechanisms. The complex nature of resonance and resonance coupling in MIM does not allow to use analytical formulas and require numerical calculation. In this prospective work, I analyze only 2D structures (infinite in the y direction) for two reasons: it is simpler to analyze and faster to compute than 3D structures. Yet 2D configuration has some limits, including that the optical response is polarization dependent, which is not the case for 3D symmetric structures.

To catch how RMCA computes a 2D grating, we may divide the computation into 2 main steps:

1. Derive electromagnetic fields in each layer independently.
2. Take advantage of continuity relations with the S-matrix formalism

Electromagnetic fields can be expressed as a superposition of modes. Modal methods enable to find in each layer these modes. Then continuity relations helps to link these modes together to find the electromagnetic fields in the whole structure. A precise description of RMCA is given in appendix F.

5.5 Big picture

In this introductory chapter on nano-antenna for PV applications, we have shown that nano-antenna cross section is larger than its physical area, thereby contributing to light concentration. Even better, the low device height enables a 3D concentration. Yet a huge obstacle has to be overcome: nano-antenna are wavelength-dependent because absorption is based on resonance mechanisms. What is more problematic is that resonance bandwidth is spectrally thin

which is incompatible with the large solar spectrum. Instead of multi-resonant nano-antenna, we propose a mono-resonant approach in which a spectral convertor aims at down-shifting light to the mono-resonance bandwidth.

We have also reviewed the principal strategies to reduce PV cell thickness. From diffusive reflector limited to the classical limit of $4n^2$, extreme thickness reduction makes this approach not possible leading to new concepts such as nanowires, photonic crystals or nano-antennas.

Whether mono-resonant or not, nano-antenna present mainly three kind of resonance (Fabry-Perot, plasmonic, waveguided). We have described what were the physical principles behind these three mechanisms. In particular, Fabry-Perot resonances in nano-antenna are little dependent on the incidence angle, can be spatially localized only in the absorber reducing parasitic loss. For these two reasons our mono-resonant device will be built around a Fabry-Perot resonance.

The last part of this chapter was dedicated to the numerical calculation method which has been used. RMCA code has been described in detail. All the building blocks are now in place to properly design a mono-resonant concentrating system.

Chapter 6

Mono-Resonant Concentration Device (MRCD)

Contents

This chapter is dedicated to all the results we obtain in the realization of the coupling of a nano-resonator (equivalently nano-antenna) array and a spectral convertor. This concept has been patented [145]. This chapter is divided in 3 sections. The first one deals with optical properties modeling. It deals with resonance understanding, geometry screening and tracks for improvements. A second section is devoted to the clean room fabrication and the third one deals with electrical properties issue.

6.1 Optical design

The first issue we have to deal with is to have high optical absorption despite extremely thin thickness. That is why optical design will be the starting point of this chapter. In the meantime, our approach can be optimized if during the optical design, we take into consideration also the electrical properties. From this point of view, we choose the pin junction. The presence of a large intrinsic layer (compared to doped layers) allows to create a large region where the light

conversion takes place efficiently (low recombination loss). During this thesis, the pin junction consists in InP semiconductor. This material has been chosen for three reasons:

- InP has a direct bandgap well suited for photovoltaics
- InP is a III-V semiconductor with the lowest surface recombination velocity (as much as two orders of magnitude lower than that of GaAs [146])
- InP is a well known material at LPN

The pin junction will be sandwiched between 2 contact layers, themselves placed in-between two metal layers. Metal acts as electrode and participates to the resonance which may occur in the device. Contact layers improve the ohmic characteristic of the contact between the pin junction and the electrodes. The thickness of the different layers forming our resonator will consequently be of great importance, whether we deal with optical or electrical properties. These geometrical constraints must be accounted in our specifications.

Before the optimization process in itself, one has to clearly identify the goal which is aimed. We want to maximize the MRCD output performance, which means that all the losses must be considered (resonator and spectral convertor loss). For instance, in our case, reflection/diffraction is not entirely detrimental since the reflected/diffracted photons may be reflected by total internal reflection at the top surface and consequently may have another chance to be absorbed in the active layer. To overcome this difficulty, our analysis must couple the two correlated subsystems (resonator and LSC) to assess the overall performance.

6.1.1 Specifications

We will first look at 2D resonators (infinite y direction). Although the TE and TM responses are different, which is not the case in 3D for symmetrical structures, the calculation time is greatly reduced. We have identified 6 main specifications. The first two requirements concern the magnitude of absorption whereas the third one concerns the wavelength dependence. Absorption is $k.|\mathbf{E}|^2$ (k is the imaginary part of the refractive index and $\mathbf{E}$ the electric field), which means that a high absorption implies $|E|^2$ enhancement for a given material.

Good absorption for unpolarized light The resonator optical response is polarization dependent whereas incoming light is not polarized. Indeed, light can originates directly from the Sun, which is not polarized, or from a dye. Even if dye emission can be polarized, random dye orientation tends to produce, at the macroscopic scale, unpolarized emission.

Good absorption for a broad range of incidence angles This requirement is due to the fact that in the spectral convertor, photons are emitted isotropically by the dye. As a consequence, the device should ideally be able to absorb light whatever the incidence angle.

Good absorption for pertinent wavelength As explained before, the use of the dye allows to shrink the spectral range which will be "seen" by the resonator. Therefore, our device must be efficient only for these wavelengths: from dye emission spectral range till absorber bandgap. Conversely optical properties in the dye absorption spectral range are of little interest.

The three previous requirements unsure, if respected, good overall optical absorption. They are necessary but not sufficient conditions. In order to be useful, absorption must take place in a region where recombinations are minimized. This region is the space charge region, which is located in the intrinsic layer of the pin junction. This statement gives rise to other requirements:

Highly doped & thin contact layers To reduce as much as possible light absorption in these layers (highly recombinant), we want them as thin as possible. It will be set to 10nm throughout this work (thin and technologically feasible) Yet, it may jeopardize electrical properties by creating a depleted region at equilibrium and thereby prevent to fix the Fermi level. To struggle against that, we want these contact layers highly doped. However, a too high doping may reduce the tension of the device, as illustrated in fig. 6.1:

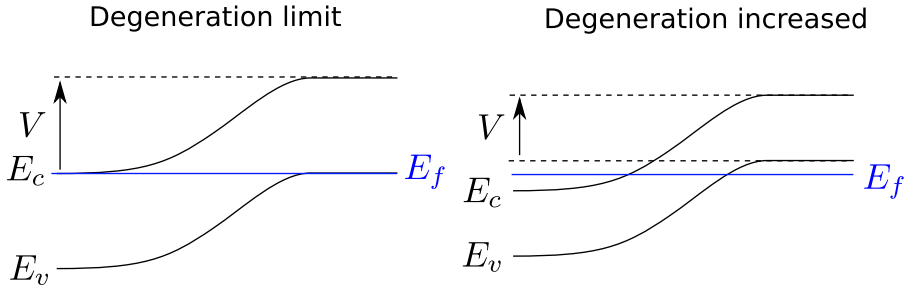

Figure 6.1: Illustration of the risk of a too high doping: Voltage which can be extracted from the device reduces if the semiconductor degeneration limit is exceeded

Advantageous trade-off on the intrinsic layer thickness The intrinsic layer thickness will be optimized to allow high absorption. Yet there is a minimal value threshold which can degrade electrical performance by increasing the tunnel current. However, PV cell works at high tension, which reduces the constraint on the tunnel current.

Lowest volume possible Aside material saving, low volume aims at reducing the dark current. Defects contributes to increase the dark current proportionally to the space charge region volume. We define one figure of merit: the mean thickness t_{mean}. It represents pin junction thickness times the coverage fraction. In 2D, $t_{mean} = t_{pin}.\frac{w}{p}$ (p is the period, w the resonator width and t_{pin} the pin junction thickness).

A trade off may be necessary between high optical absorption and low volume, especially when electrical properties are taken into account. One should be careful designing extremely thin MIM structure even if a very efficient electric field confinement is possible, mainly due to plasmonic resonances coupling. It may not be compatible with pn or pin junction. In addition, the very nature of plasmonic resonance implies non negligible metal absorption loss. These arguments drive us to consider a "thick" resonator $\sim$ 100 nm to be electrically compatible and to involve other resonance mechanisms leading to less parasitic absorption loss. To counterbalance a larger thickness, layer structuring is performed to end up with few tens nanometers mean thickness.

The next step is to acquire a numerical tool allowing to model the whole device.

6.1.2 Modeling: a multi-scale problem

6.1.2.1 Algorithmic

In order to model the complete system nano-antenna coupled to a spectral converter, we had to couple RMCA and LSC-VMCA. The philosophy of the coupling is that MRCD behaves as a LSC except that the optical response of the back surface does not depend on the geometry (x,y Cartesian coordinates) but rather on the photons wavelength and incidence angle. For a given λ and θ, the optical response given by RMCA comprises the absorption in each layer and the reflection. There is no transmission since the back metal of the antenna is thick enough to be considered as opaque. For this assumption to be true, the metal thickness must be several times higher than the skin depth. In practice the back metal will be 200 nm thick, which is largely sufficient in the visible range.

As a consequence, a complete calculation is done following this steps:

1. 8 nano-antenna absorption spectra given by RMCA:
   (a) 2 polarizations TE and TM.
   (b) 4 incidence angles 0, 20, 42 and 60°. This choice is not ideal but it enables reasonably fast calculation. The value of 42 °has been chosen instead of 40 °because it corresponds to the critical angle for an interface air/PMMA.
2. Absorption spectra averaged for unpolarized light: $A(\lambda)_{unpol.} = \frac{A(\lambda)_{TE}+A(\lambda)_{TM}}{2}$
3. Running LSC-VMCA: reflection at the back is treated in the code as follows:
   - if $0 \leq \theta < 20$ then the proper absorption spectrum is $\theta = 0°$
   - if $20 \leq \theta < 42$ then the proper absorption spectrum is $\theta = 20°$
   - if $42 \leq \theta < 60$ then the proper absorption spectrum is $\theta = 42°$
   - if $60 \leq \theta < 90$ then the proper absorption spectrum is $\theta = 60°$
   - Then the photon is treated with the chosen absorption spectrum at its wavelength.
   - If reflection/diffraction occurs, RMCA gives the reflection/diffraction angle which is used in LSC-VMCA

We have shown in the previous section how evolves the optical resonator response from a simple 3 layers resonator to a complete antenna structure. In this section we consider the problem reversely. We first find an optimized structure by multi-nested-loops on MRCD parameters, and then we analyze the different resonant mechanisms in the resonator. This approach can be applied because the resonator response calculation is parallelized on 8 cores and the vectorization of LSC-VMCA allows the treatment of 10^5 photons in less than 2 seconds. The entire calculation lasts between 1 and 5 minutes (depending mostly on the period (mesh size)) for a 8 cores Z600 HP computer. The following table 6.1 shows the different parameters which can be tuned:

Material optical constants we have used can be found in appendix G. Because we want to fabricate the device we model, some parameters which normally can be tuned are fixed according the material we have (PMMA, R305). Some materials are also set: Silver for reflector, InGaAs for contacts. Silver is known to be the best metal in the visible range. It can rise problems due to sulfurization and oxydation, but we will show in section 6.2 that these issues

	Parameter	Tuning	Value & Justification
Antenna	Materials	*fixed*	Metal Ag, contact InGaAs, pin InP
	top Ag thickness	*fixed*	15 nm (better trade-off found)
	InGaAs thickness	*fixed*	10 nm (see section 6.1.1)
	InP thickness	*varied*	from 50 to 100 nm
	Period	*varied*	from 150 to 1500 nm
	Width	*varied*	from 80 to 300 nm
Matrix	Refractive index	*fixed*	n=1.5 close to n_{PMMA}
	Dimensions	*fixed*	infinite , $\mathcal{L}_{loss}$ avoidable (see section 4.2.2.4)
Dye	Nature	*fixed*	R305, used for experiments
	PLQY	*fixed*	0.95, not tunable
	Concentration	*fixed*	200 ppm

Table 6.1: Parameters which can be tuned in the optical design. We vary simultaneously the width, period and InP thickness. After that, the dye concentration is optimized. It would have been too time consuming to optimize these four parameters together.

can be easily avoided and results on gold will also be shown. We have decided to focus on the thickness, width and period of the nano-antenna. Dye concentration optimization is done afterwards.

In our calculation, beside a constant PMMA refractive index of 1.5, we consider this material ideal (no permittivity imaginary part). In the visible range this hypothesis seems reasonable. However the matrix is dye doped, so there is a strong absorption until 600 nm, wavelength at which the dye absorption coefficient is nearly null. Non zero imaginary part of the PMMA will strongly modify the resonances. Yet two arguments to justify our assumption can be invoked:

1. Absorption occurs in the spectral range which is not interesting in our case since almost no photon at these wavelengths will be allowed to reach the resonator (dye absorption highly probable). Therefore a mistake is made but without huge consequences.

2. We can perfectly imagine a PMMA matrix divided in two parts. The top part being dye-doped, whereas the bottom part, in contact with the resonator, non-doped. If the product doped-layer thickness times the dye concentration is the same in the two cases, then the spectral convertor behavior may be equivalent. Doing that, the bottom part is not doped which solve the dye-absorption issue in our numerical calculation

The algorithmic being presented, the next section deals with the comprehensive (bottom-up) approach.

6.1.2.2 Comprehensive approach

6.1.2.2.a Results

One way of designing the resonator is to identify what resonance mechanism we favour and at which wavelength. Then we start from the simplest MIM structure, then we modify it end-up with the final device. The dye R305, used in the spectral convertor, has an emission peak at 650 nm. Moreover, we want good optical absorption in the intrinsic layer, that is to say we want the resonance in the middle of the resonator. Therefore first order Fabry-Perot resonance at 650 nm is well suited (see section 5.3.2.1). The simplest MIM structure is a PMMA/Ag/InP/Ag non-structured stack. Top silver layer thickness is fix to 15 nm. Using eq. (5.2) and the correction described in appendix D, analytical formula and RMCA show that InP thickness should be 44 nm. Results are shown in fig. 6.2:

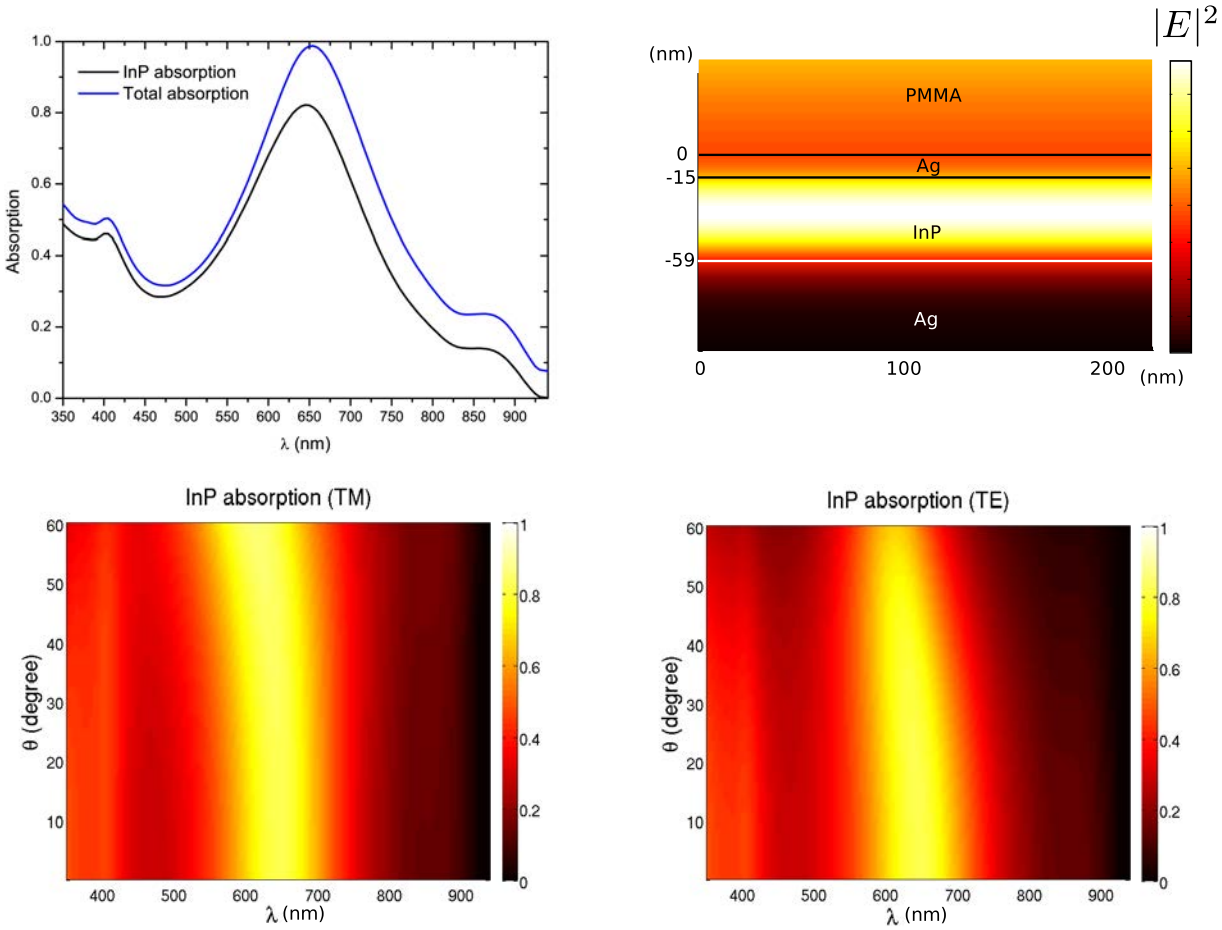

Figure 6.2: Simplest MIM structure. Absorption is maximized at 650 nm (top left) and located in the middle of the InP layer (top right). InP absorption angular dependence is shown in the two bottom figure (left TM, right TE). Good angle independency is an other evidence of Fabry-Perot resonance (cf. eq. (5.4))

Figure 6.2 top left shows that Fabry-Perot resonance allows perfect total absorption at 650 nm (80% in the InP). For comparison, InP absorption coefficient at $\lambda = 650\ nm$ is $5.7.10^{-3}\ nm^{-1}$, which leads to $e^{-44\times5.7.10^{-3}} = 0.22$ absorption. The resonance mechanism is a Fabry-Perot,

as evidenced by the others plots displayed in fig. 6.2: $|E|^2$ enhancement in the middle of pin junction and good angular tolerance.

It is worth noting that 44 nm thickness is very thin. Fabricating a pin junction in only 44 nm seems not the best solution from the point of view of electrical performances. Yet we can continue and structure the top silver layer. We choose a period of 200 nm (small enough to avoid diffraction issue) and a width of 100 nm. Doing that, the symmetry is broken which makes the system polarization dependent, even at normal incidence (fig. 6.3):

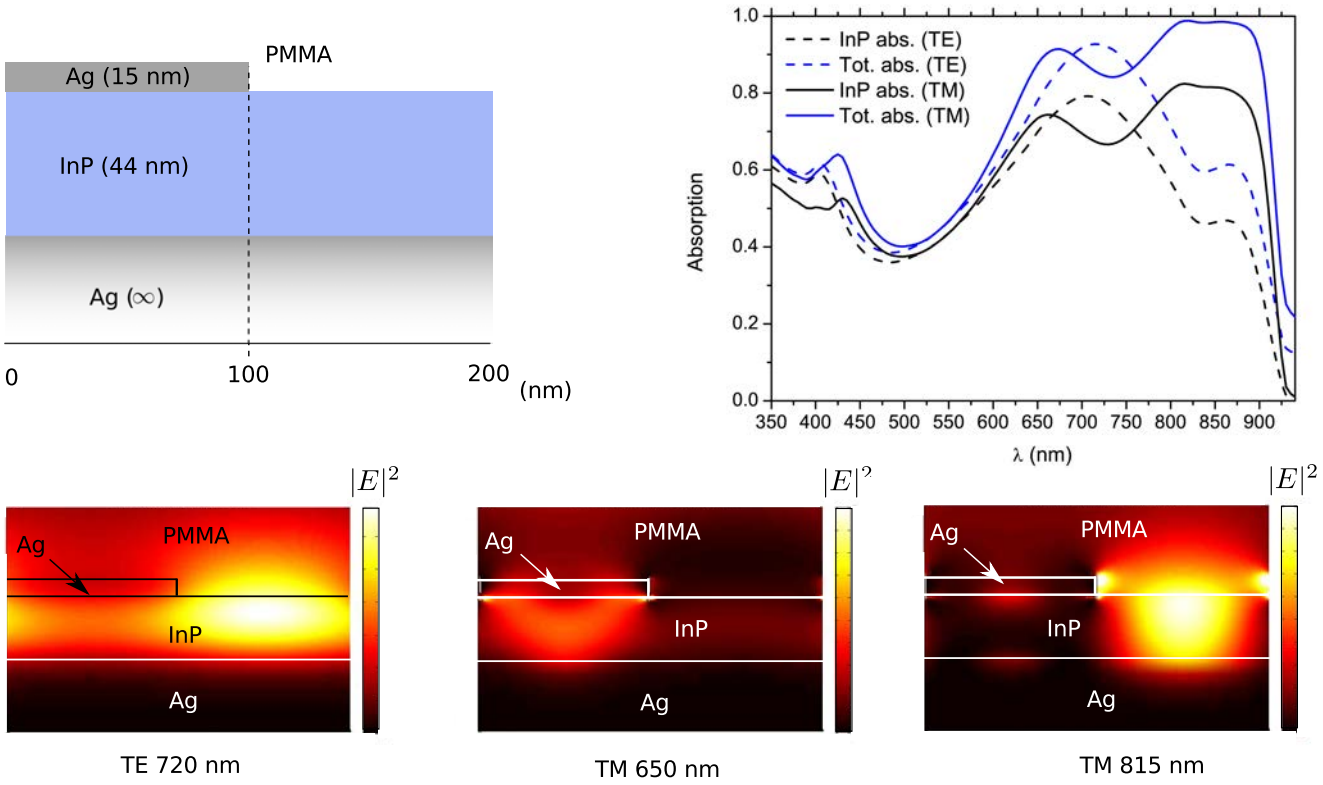

Figure 6.3: MIM structure, top metal structured. Top left, device scheme and dimension. Top right: absorption in TE (dash line) and TM (solid line). Bottom (from left to right): $|E|^2$ field map in TE at 720 nm, in TM at 650 nm and in TM at 815 nm.

Absorption spectrum is greatly modified by structuring the silver. The former Fabry-Perot resonance at 650 nm still exist in TM but two other peaks (815 and 860 nm) have appeared. The 815 nm resonance can be attributed to a vertical Fabry-Perot resonance in the stack PMMA/InP/Ag (cf. fig. 6.3 bottom right). The 860 nm resonance seems to be the same resonance that at 815 nm which has been red shifted due to a higher InP refractive index (see appendix G).

TE resonance at 720 nm cannot be easily interpreted as a Fabry-Perot occurring in the stack Ag/InP/Ag or PMMA/InP/Ag. Actually it seems to be a mix of these two resonances. An elegant way to interpret this resonance is to do an analogy with metamaterials [147]. It consists in assuming that the electromagnetic field does not "see" the structuring layer but on

homogeneous layer with an averaged dielectric constant. To be valid, this analogy requires that the fields do not vary on a period, which is a good approximation in TE at 720 nm (fig. 6.3 bottom left). The homogenous metamaterial dielectric constant is $\epsilon_{meta} = \frac{w\epsilon_{Ag}+(p-w)\epsilon_{PMMA}}{p}$ (w is the silver width, p the period). Absorption spectrum for the structured and metamaterial device is shown in fig. 6.4:

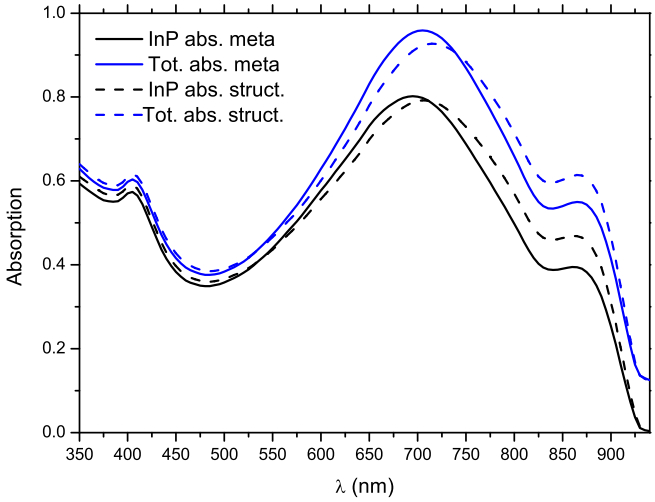

Figure 6.4: Absorption spectrum comparison between a structured device and the metamaterial analogy, in TE.

Figure 6.4 suggest that the metamaterial analogy is valid in this case, which justifies the hybrid TE resonance. We can go further and structure the InP layer (fig. 6.5).

Absorption spectrum begins to be heavily modified if compared to the first structure. Resonance in TE is blue shifted at 585 nm. The same metamaterial analogy can be used. The mean semiconductor dielectric constant is lowered due to PMMA, which blue shifts the resonance. $|E|^2$ field map (fig. 6.5 bottom left) suggests that the resonance mechanism is still a first order Fabry-Perot resonance.

TM response is also modified. Resonances at 815 and 860 nm have disappeared, which is consistent with the fact that no vertical PMMA/InP/Ag Fabry-Perot resonance can exist in structuring the InP. Yet, resonance occurring et 650 nm still exist but cannot be considered as a pure Fabry-Perot resonance, as suggested by (fig. 6.5 bottom right). Different resonance mechanism co-exist, which gives rise to complex resonances.

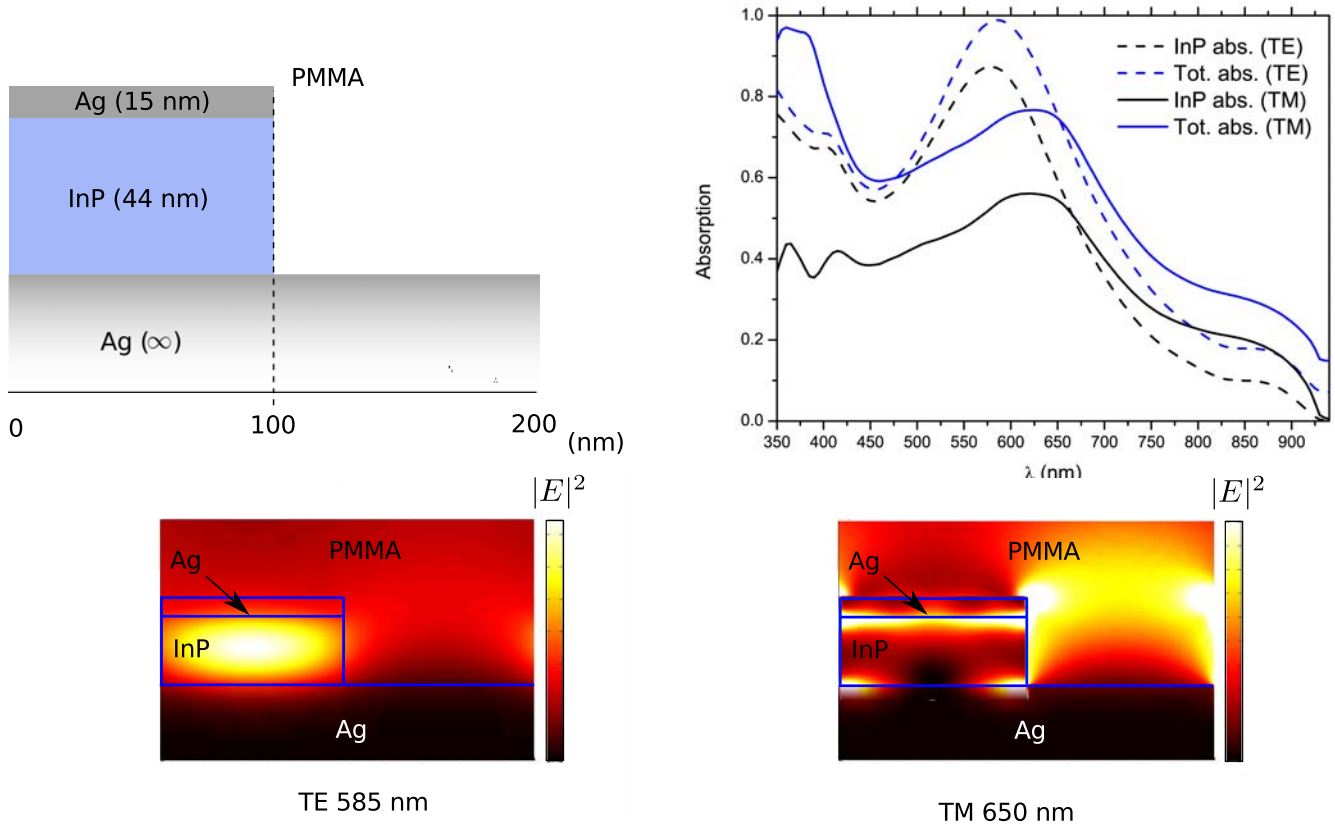

Figure 6.5: MIM structure, top metal and pin junction structured. Top left, device scheme and dimension. Top right: absorption in TE (dash line) and TM (solid line). Bottom left (right): $|E|^2$ field map in TE at 585 nm (in TM at 650 nm) respectively.

Next step is to add InGaAs contact layers. We assume that 10 nm thickness for each contact layer is reasonable, regarding the discussion we had on the contact layer thickness (see section 6.1.1). To keep the total semiconductor thickness at 44 nm, InP thickness is reduced to 24 nm. Figure 6.6 shows the device scheme and the absorption spectrum:

InGaAs contact layers have only a small influence on the total absorption (both TE and TM). This is due to the fact that InP and InGaAs dielectric constants are close to each other. Conversely, InP absorption dropped because resonances were not located in the middle of the pin junction but also on the semiconductor/metal interfaces.

6.1.2.2.b Discussion

If we summarize the comprehensive approach, we started from the simplest MIM structure to a nanostructured device with contact layers. Absorption spectrum has been modified throughout the structuring process. Unpolarized absorption spectra for the first and the last structure is shown in fig. 6.7:

Figure 6.7 highlights the degradation in the absorption spectrum. As a comparison, bare InP absorption is also represented. Solid (dash) red line should be compared to solid (dash) black lines respectively (in keeping in mind that the coverage fraction is 50% for the structured

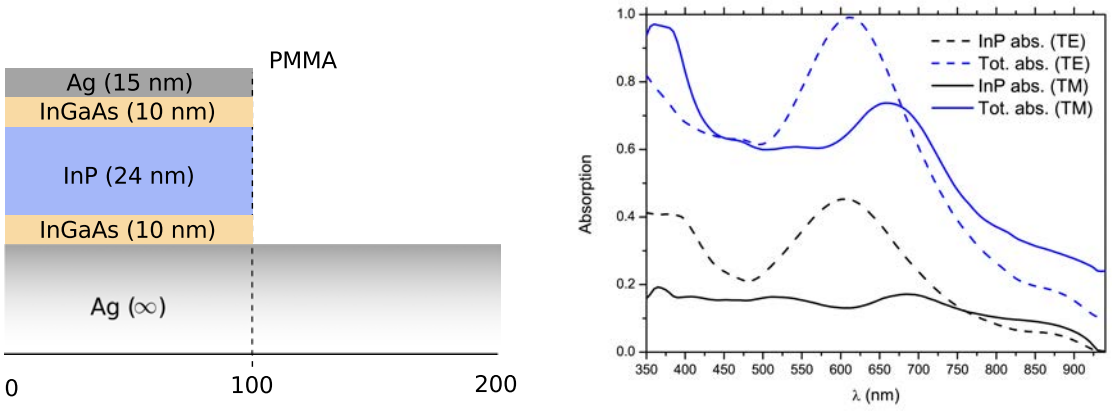

Figure 6.6: MIM structure, top metal and pin junction, InGaAs contact structured. *Left*: device scheme and dimension. *Right*: absorption in TE (dash line) and TM (solid line).

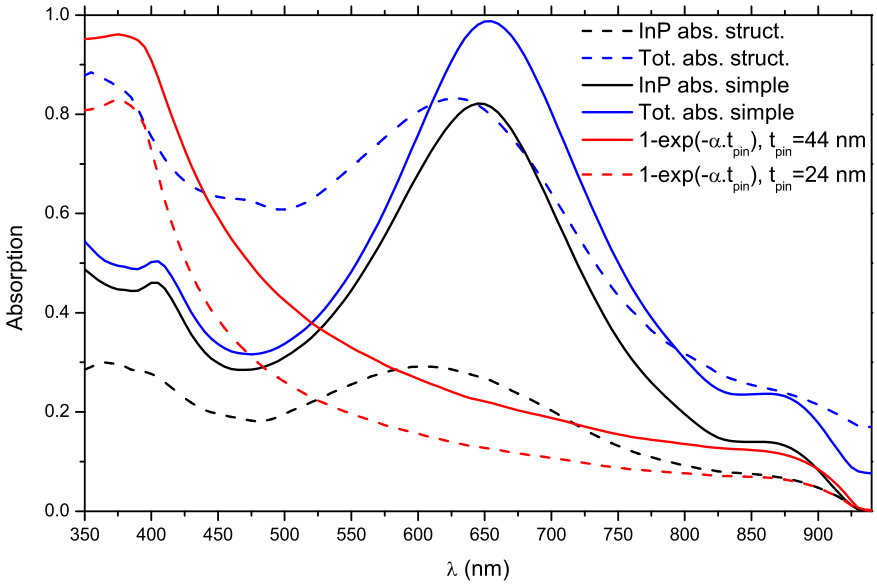

Figure 6.7: Unpolarized absorption spectrum for the simplest structure (solid lines) and the final structure (dash lines). Blue color is total absorption whereas black is for InP absorption. Red lines represent a bare InP layer absorption of thickness 44 / 24 nm (solid / dash lines respectively). It is calculated with the following equation $Abs = 1 - exp(-\frac{4\pi k}{\lambda}.t_{pin})$ (k is the imaginary part of the refractive index)

device). The simplest structure was good in term of optical absorption in the pin junction, but not electrically compatible. We have seen that structuring was not beneficial. Additionally, it leads to 24 nm thick pin junction, which is not electrically compatible.

On can argue that it would have been possible to tune the width and the period. If period is kept below the wavelength, changing p and w changes $\epsilon_{meta} = \frac{w\epsilon_{Ag}+(p-w)\epsilon_{PMMA}}{p}$. We can therefore expect a resonance blue (red) shift by increasing (decreasing) w in TE. TM response is harder to anticipate because it seems to be a mix of different mechanisms.

The comprehensive approach is adapted to the resonance understanding but not to optimization. This is why we use a second approach in this thesis, based on statistics.

6.1.2.3 Statistical approach

6.1.2.3.a Global optimization & a particular case

In this section, we model different resonator geometries, and we use LSC-VMCA for each geometry. We will then select the more interesting structure and then we will analyze the resonance mechanisms. The fixed parameters are described in table 3.3 and results are shown in fig. 6.8.

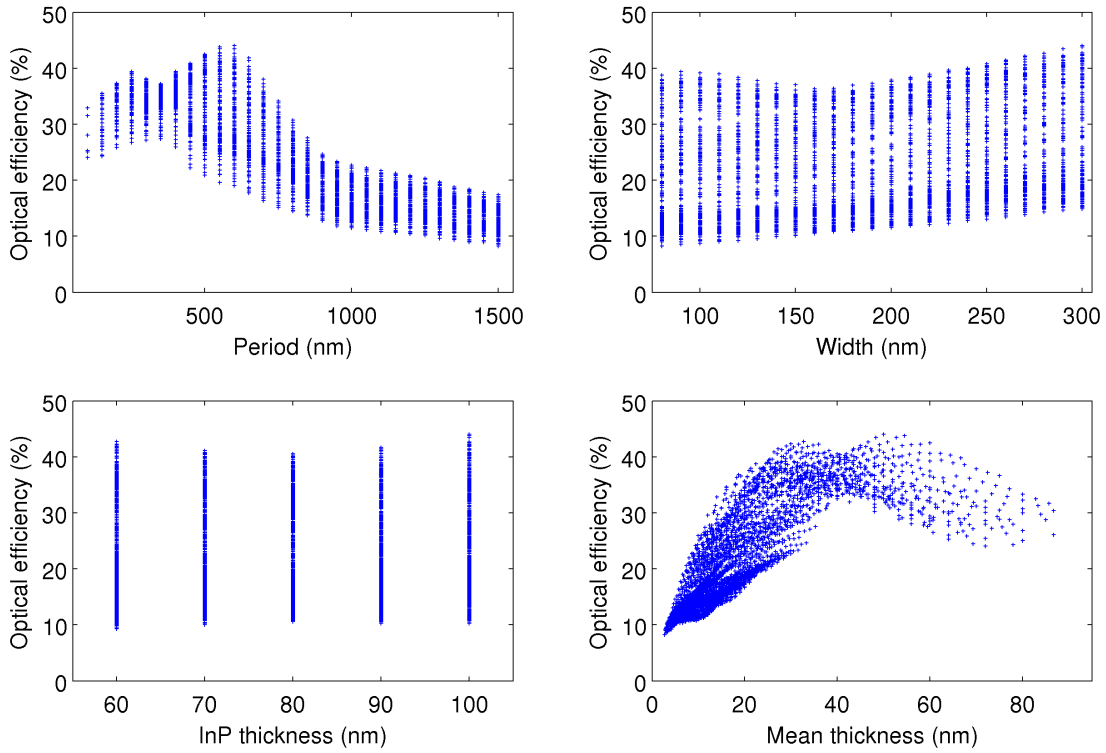

Figure 6.8: Nano-antenna optical efficiency versus geometrical parameters (period p, width w, InP thickness t_{InP} and the mean thickness t_{mean}).

Before looking in more detail at a particular example, some general comments can be given. Optical efficiency as high as 44 % can be obtained with a mean thickness of 50 nm. Furthermore, efficiency higher than 35 % are not rare and can be obtained for all parameter values except the period which must be lower than 700 nm.

What is surprising is that the InP thickness does not seem crucial, which can be counter-intuitive looking at chapter 5. Indeed we design the device to have a Fabry-Perot resonance which is very sensitive to the thickness. The tolerance on the thickness can be explained knowing that the dye spectral bandwidth emission is rather large which leads to an increased tolerance on the Fabry-Perot spectral position.

In this configuration, the photon recycling is not as efficient as expected, as attested by the decreased optical efficiency at higher period. Diffraction occurs if the period is larger than $\frac{\lambda}{n_{pmma}}$. In our case, photons with wavelength higher than 600 nm and lower than 940 nm can be absorbed by the nano-antenna active layer. Roughly, it gives an average wavelength of 770 nm which gives a diffraction threshold of $\lambda_{diff}^{th} \approx \frac{770}{1.5} = 513$ nm. It is in good accordance with the best structure ($\eta_0 = 44.04\%$) period of $p_0 = 550$ nm (with a calculation step of 50 nm).

We will focus our analysis on the following resonator geometry: $t_{InP} = 70$ nm, $w = 80$ nm, $p = 300$ nm. Despite a slightly lower optical efficiency of 37.8 % (against 44.04 % for the best structure), the mean thickness is lower than 20 nm (against 50 nm). Figure 6.9 shows the results associated to this structure:

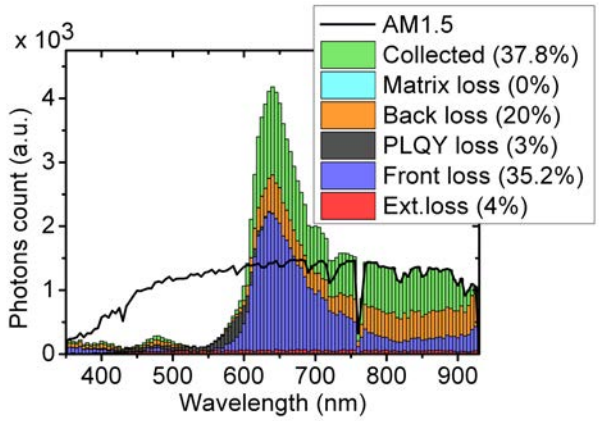

Figure 6.9: Overall performance of a MRCD with $t_{InP} = 70$ nm, $w = 80$ nm, $p = 300$ nm and others parameters listed in table 3.3. AM 1.5 is the standard solar spectrum. "Collected" represents the proportion of photon absorbed in the pin junction. Matrix (PLQY) losses correspond to photon proportion lost in the spectral convertor by matrix absorption (non radiative dye deexcitation) respectively. Back loss is the proportion of photon absorbed either in the contact or metal layers. Ext. loss is the proportion of photon which were reflected before entering the device (Fresnel reflection) and Front loss represent the proportion of photons which escaped through the front surface

Performances are limited mainly by front and back (antenna absorption in contact or metal layers) losses. To understand why we obtained these performances and why front and back losses are preponderant, further analysis on the resonator in itself will be carried out (section 6.1.2.3.b). Before that and as a comparison, on may wonder if:

- Is structuring advantageous? Does it compensate the additional technological efforts?
- Is the dye beneficial?

To answer these questions, calculations have been made in the alternative configurations suggested by these interrogations. They are summarized with associated results in table 6.2:

The previous table illustrates the interest of the simultaneous use of a structured resonator and a spectrum converter. Structuring the resonator always surpasses the non structured configuration, with and without dye. This assessment is not so surprising since the starting configuration was optimized.

Alternative configurations comparison			
(in %)	Structured	Non structured	
	$t_{pin} = 70$	$t_{pin} = 70\ nm$	$t_{pin} = 18.7\ nm$
Dye (200 ppm)	37.8	29.7	26.8
No dye	35	28.7	23.5

Table 6.2: Proportion of collected photons for different configurations. Column "non structuring / $t_{pin} = 70\ nm$" allows to compare the optimized configuration and the same one with less technologial steps. Conversely, column "non structuring / $t_{pin} = 18.7\ nm$" allows to compare the optimized configuration and a non structured configuration with the same amount of semiconductor.

The use of the dye is more questionable because the non dye structured configuration reached 35% collection efficiency (4% Ext. loss, 27.2% Back loss and 33.8% Front loss). In this case, PLQY losses canceled out but more surprising is lower front loss than in the optimized configuration with the dye (whereas reflection coefficient is higher at low wavelength (see fig. 6.10). This is partly due to the fact that after a dye absorption / radiative re-emission event, around 25% of these photons are emitted in the escape cone (dye isotropic emission and interface of refractive indexes 1.5 and 1) and therefore exit the spectral convertor without reaching the resonator. This "automatic" front loss concerns 25% of dye absorbed photons, which themselves represent $\frac{\int_0^{\lambda_g}(1-exp(-\alpha_{dye}(\lambda).dz).AM1.5(\lambda)d\lambda}{\int_0^{\lambda_g} AM1.5(\lambda)d\lambda} \sim \frac{\int_0^{600} AM1.5(\lambda)d\lambda}{\int_0^{\lambda_g} AM1.5(\lambda)d\lambda} = 35\%$ of the total number of photons (α_{dye} is the dye absorption coefficient, dz the spectral convertor thickness, λ_g InP bandgap and $AM1.5$ the solar spectrum). Thus, if a dye is used, there is an automatic $\sim 0.35 \times 0.25 = 8.8\%$ front loss (assuming no non radiative emission loss).
The automatic front loss plus the fact that the dye is effective on only 35% of the total number of photon explain why there is little difference between dye and no dye structured configuration. Yet, adding a dye in a matrix is not a costly technological effort and, more importantly, the dye is not optimized for this application and this semiconductor bandgap, which allows to be optimistic as for improvements.

6.1.2.3.b Antenna analysis

The first data we need is absorption spectra for the TE, TM and unpolarized light. This is shown in fig. 6.10.

In both polarizations, the absorption in the active layer (InP) is higher at long wavelength, which contributes to explain why this structure was among the best ones. The spectral convertor avoid short wavelength light to reach the resonator, that is why bad InP absorption for low wavelength is not detrimental. This is confirmed by fig. 6.9 which shows almost no loss at $\lambda < 600\ nm$. TM polarization brings huge absorption losses, mainly contributing to the overall back loss in fig. 6.9, whereas TE polarization is far more efficient. To understand why, one need to understand which resonant mechanisms give rise to the three peaks in TE and TM.

Electric field mapping at resonant wavelengths are shown in fig. 6.11.

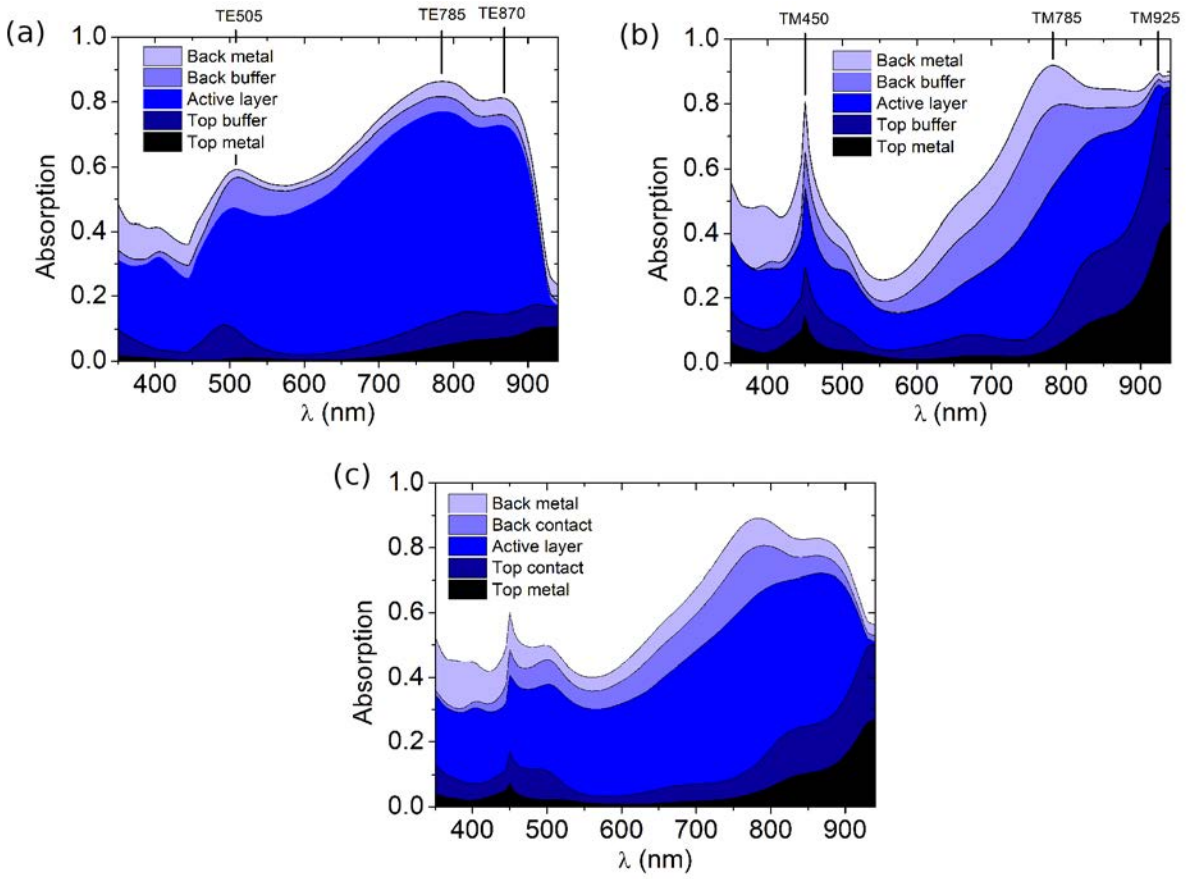

Figure 6.10: Optical response of an optimized resonator

Because PMMA is considered not absorbing for wavelength higher than 600 nm, there is no absorption loss due to PMMA and consequently the presence of an electric field in this medium is not an issue. In TE, $|E|^2$ enhancement is around X15, which is below the classical limit ($4n_{mat}^2$) but sufficient enough to allow good absorption.

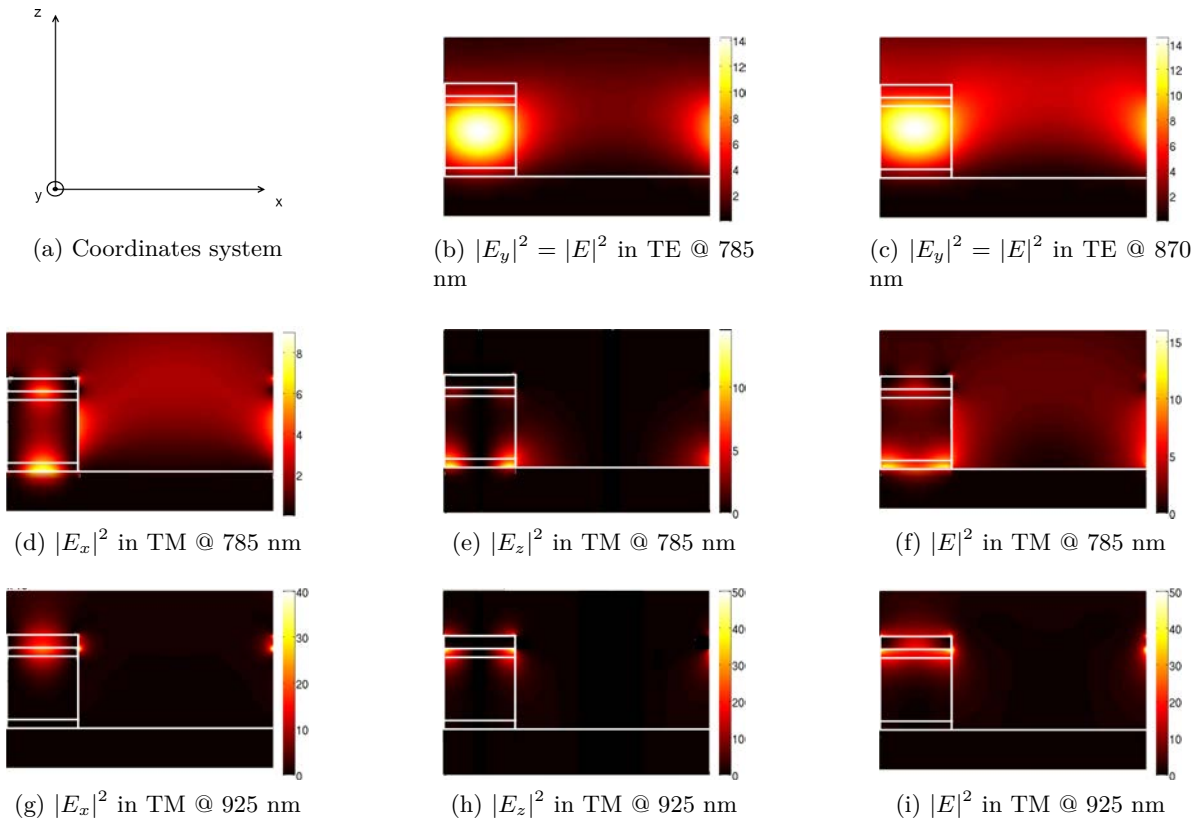

(a) Coordinates system

(b) $|E_y|^2 = |E|^2$ in TE @ 785 nm

(c) $|E_y|^2 = |E|^2$ in TE @ 870 nm

(d) $|E_x|^2$ in TM @ 785 nm

(e) $|E_z|^2$ in TM @ 785 nm

(f) $|E|^2$ in TM @ 785 nm

(g) $|E_x|^2$ in TM @ 925 nm

(h) $|E_z|^2$ in TM @ 925 nm

(i) $|E|^2$ in TM @ 925 nm

Figure 6.11: Electric field map for TE785, TE870, TM785 and TM925. First row: TE resonance at 785 and 870 nm. Second row: TM resonance at 785 nm. Third row: TM resonance at 925 nm. Colormap scale is arbitrary

We also plot, for both polarization, the total absorption versus the wavelength and incidence angle, shown in fig. 6.12:

Figures 6.12a and 6.12b show an absorption which does not depend on the incidence angle for TE785 and TE870. As explained in section 5.3.2.1, it suggests a Fabry-Perot resonance mechanism.

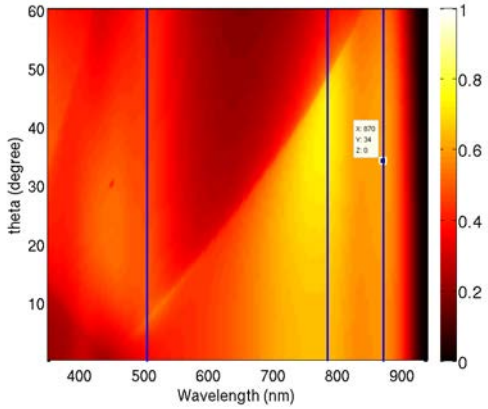

(a) Angle variation, TE, InP abs.

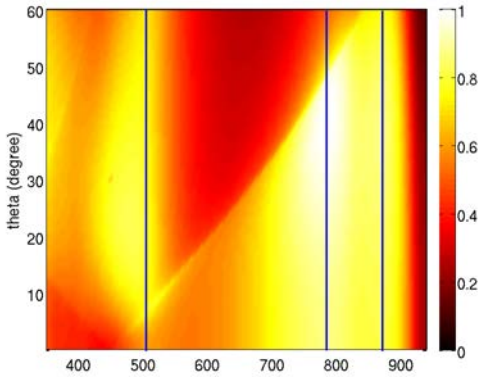

(b) Angle variation, TE, total abs.

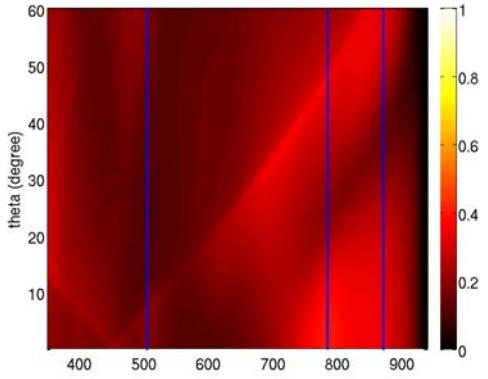

(c) Angle variation, TM, InP abs.

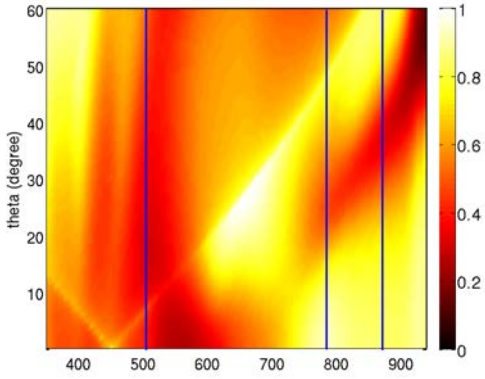

(d) Angle variation, TM, total abs.

Figure 6.12: Wavelength and angular dependence on InP / total absorption (first / second column respectively). The first (second) row deals with TE (TM) polarization respectively.

TE resonances:

The two field maps figs. 6.11b and 6.11c exhibits an $|E|^2$ enhancement well centered in the resonator (x and z). This suggest a first order Fabry-Perot resonance, corroborated by figs. 6.12a and 6.12b. The fact that the same behavior occurs for two wavelengths only separated by 100 nm comes from the real part of InP refractive index which is 10 % higher at 870 than 785 nm (see appendix E). These two resonances are mainly responsible for the good performances of this MRCD.

TM resonances:

TM450 is very sharp, which is typical for waveguided mode. To verify this assertion, we use the grating formula eq. (5.10) defined in chapter 5 and we plot the absorption dependence versus period and wavelength at 0° incidence angle (fig. 6.13):

Equation (5.10) for $\theta = 0°$, $n_{eff} = 1.5$ and m=1 fits well the narrow absorption enhancement, we can therefore conclude that TM450 corresponds to a first order waveguided mode in the PMMA.

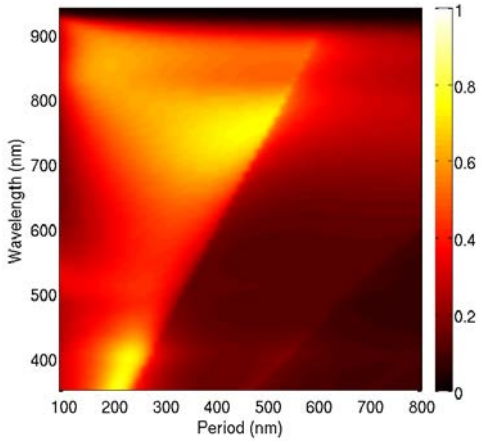

(a) Period variation, TE, InP abs.

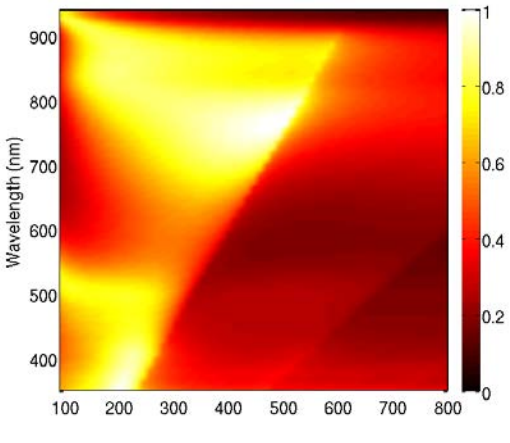

(b) Period variation, TE, total abs.

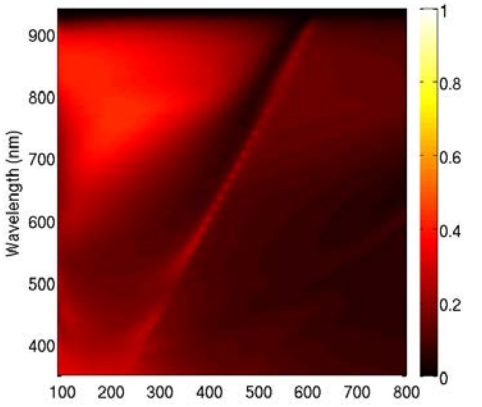

(c) Period variation, TM, InP abs.

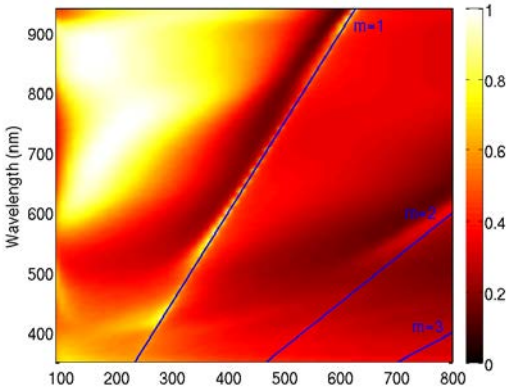

(d) Period variation, TM, total abs.

Figure 6.13: Wavelength and period dependence on InP / total absorption (first / second column respectively). The first (second) row deals with TE (TM) polarization respectively. The blue lines correspond to eq. (5.10) for $\theta = 0°$, $n_{eff} = 1.5$ and m=1,2 and 3.

TM785 and TM925 exhibit high absorption loss in contact and metal layer. Indeed $|E|^2$ of figs. 6.11f and 6.11i shows an enhancement at the interface between metal and contact, which is typical of plasmonic resonance. Contrary to TM925, resonance TM785 exhibit some electrical field inside the resonator (mixed mode), which allows some field enhancement in the InP layer. It is worth noting that metal and contact absorption (high $|E|^2$ in these layers) are considered as loss. It is fully valid for metal, but is questionable for contact layers since the resonator thickness may be lower than the diffusion length. Nevertheless, this assumption has been made to counterbalance the fact that InP absorption is a gain, without distinguishing doped and intrinsic layers.

The mechanisms underlying the resonance peaks have been studied. It is worth clarifying that only a first order Fabry-Perot resonance, perfectly matching the dye emission, is sought. The MRCD showed above is definitely not ideal for two main reasons. First, the dye emission is really large and does not match InP bandgap. Since the antenna must be tuned according the dye emission, the MRCD must have a good optical behavior on a too large spectral region.

Finding a dye with a thinner emission spectrum (such as Quantum Dots) and still a good quantum efficiency would help to have better performances. Second, we have too much loss for the TM polarization, due to plasmonic resonances. In an hypothetical case in which TM polarization does not exist, we may wonder what could have been the device performances. Integrated results are displayed below:

Unpolarized and TE polarized comparison						
(in %)	Collected	Matrix loss	Back loss	PLQY loss	Front loss	Ext. loss
TE polarized	48.8	0	15.5	3	28.7	4
TM polarized	24.4	0	43.5	3	25.1	4
unpolarized	37.8	0	20	3	35.2	4

Table 6.3: Loss repartition compared for TE and unpolarized light

In TE polarization only, back loss is reduced ($\sim 22\%$ relative drop) because the electric field enhancement is far from metal/contact interface. Front loss reflection is also reduced ($\sim 19\%$ relative drop). This arises from a lower reflection coefficient in TE for $600\ nm < \lambda < 700\ nm$ (see fig. 6.10). As a consequence, collected photons is increased (11 absolute percent). In TM, more than 4 photons over 10 are lost by metal or contact absorption (back loss).

After having investigated the MRCD performances, and before proposing improvement strategies, one may wonder what is the size and material robustness.

6.1.2.3.c Size and material robustness

A legitimate question is the size sensibility. Indeed, when comes the fabrication time, it is likely that the resonator lateral size will be different from the one used in the model. A too high sensitivity may jeopardize the entire process, so we have varied the width (and period) by ± 10 nm around 80 (and 300 nm) respectively. The value of 10 nm seems reasonable since this resolution is common for electronic beam lithography. Results are shown in fig. 6.14

The sensitivity is acceptable since the worst case leads to an optical efficiency drop of 36.4 %. During the fabrication, the period is generally very close to the expected value because electron lithography has the necessary resolution. Conversely, the width depends on the etching conditions which can give less precise geometrical definition.

Another concern may come from the metal choice. If silver is the best metal in the visible range (low absorption, high reflectivity), it raises oxydation/sulfurization issue. It mainly concerns the top metal layer since the back reflector is deposited in vacuum atmosphere and recovered by a Ti/Al bilayer, preventing any silver degradation. Nevertheless, we have simulated the same MRCD replacing the top silver layer by a gold layer of same thickness. We obtained only 1 absolute % loss with gold instead of silver (because their dielectric constants are close on the spectral range 600 - 940 nm). Our system is therefore not sensitive to metal material between gold and silver, which means that both metals can be used for a prototype.

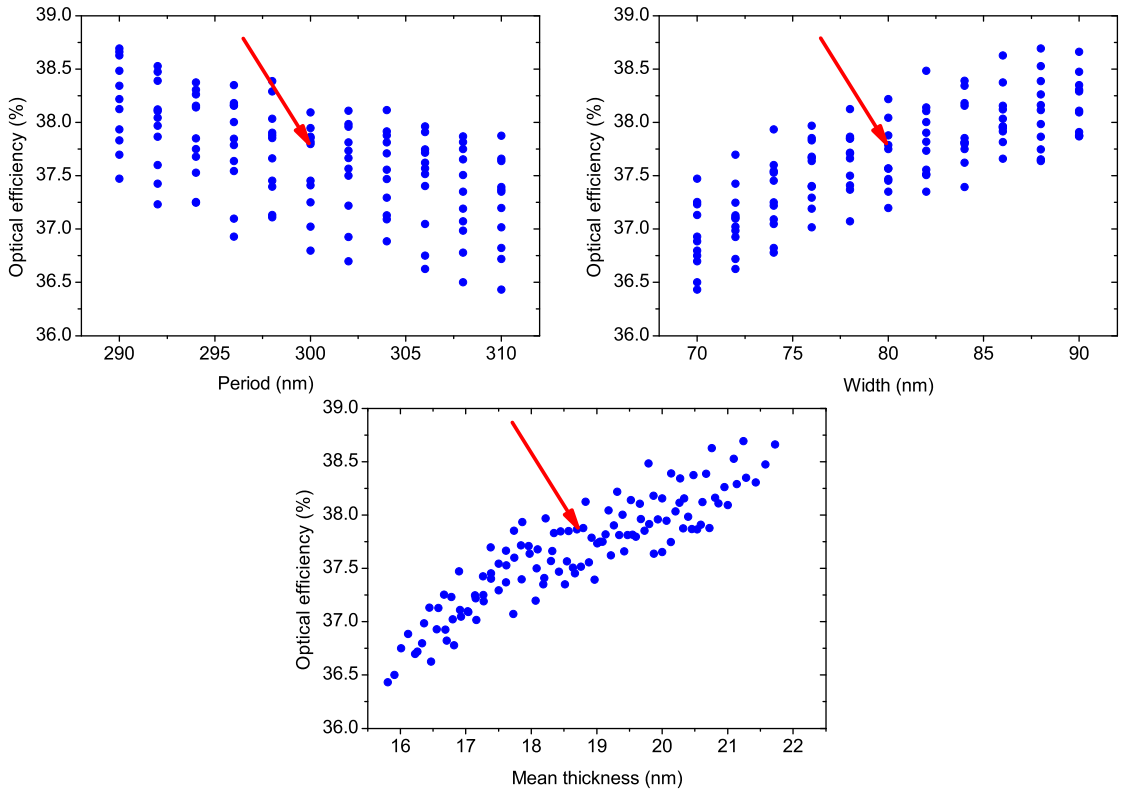

Figure 6.14: Geometrical robustness evaluation. Optical efficiency for $t_{InP} = 70$ nm, $w \in [70 - 90]$ nm, $p \in [290 - 310]$ against period (top left), width (top right) and mean thickness (bottom). Red arrow corresponds to $w = 80$ nm, $p = 300$ nm

6.1.2.4 Photon recycling

Before going further, let us have a look at the photon recycling due to front reflection at the spectral converter top surface. In order to quantify this effect, we have calculated the reflection and InP absorption for incidence angle between 0 and 90°. Results are shown below:

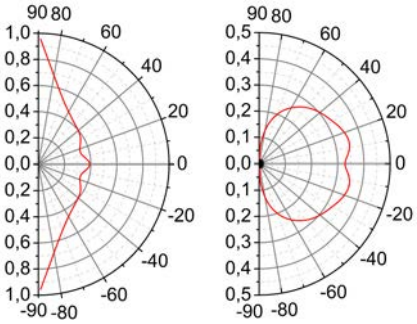

Figure 6.15: *Left*: Nano-resonator reflection for various angles. *Right*: Nano-resonator absorption in InP layer for various angles.

Interestingly, the InP layer absorption never exceed 35% (value reached for $10 < \theta < 20$ and $-20 < \theta < -10$ whereas the total absorption for this structure is 37.8%. When the InP absorption and reflection are weighted over the angular distribution of the isotropic dye

emission (distributed according to $acos(2\xi - 1)$, see section 2.2.2), we obtain a 22.9% mean InP absorption (equivalently $\overline{\eta_{opt}}$), 51.6% mean reflection ($\overline{\mathcal{R}}$) and consequently 25.5% absorption loss ($\overline{\mathcal{A}}$). Thus, the photon recycling ($\eta_{recycling}$) has, in this case, an efficiency described by the following equation:

$$\overline{\eta_{opt}^{ar}} = \overline{\eta_{opt}^{nr}} + \overline{\mathcal{R}^{nr}}\eta_{recycling}\left(\overline{\eta_{opt}^{nr}} + \overline{\mathcal{R}^{nr}}\eta_{recycling}\left(\overline{\eta_{opt}^{nr}} + \cdots\right)\right) = \frac{\overline{\eta_{opt}^{nr}}}{1 - \overline{\mathcal{R}^{nr}}\eta_{recycling}} \tag{6.1}$$

With ar refering to "after recycling"and nr for "no recycling". We can therefore calculate $\eta_{recycling} = \frac{1}{\mathcal{R}^{nr}}\left(1 - \frac{\overline{\eta_{opt}^{nr}}}{\overline{\eta_{opt}^{ar}}}\right) \approx 76.4\ \%$. This is an approximate result since it does not take into account self-absorption and more generally all losses occurring in the spectral convertor. Finally we compare 76.4 % with the maximum possible photon recycling efficiency, obtained with the convolution of the Fresnel reflection coefficient ($R_{\text{Fresnel}}^{\text{matrix}\to\text{air}}$, see section 2.1.2) and the isotropic distribution. We obtain a maximum efficiency of 77%, which is very close of $\eta_{recycling}$. We can therefore conclude that photon recycling operates at its maximum efficiency. A straightforward idea of improvement, linked with the fact that the main loss mechanism is the front loss (see fig. 6.9), would be to increase the matrix refractive index. This will be developed, among others ways of improving, in the next section.

6.1.3 MRCD improvements

This section aims at exploring some ideas to increase the optical efficiency of the system presented in the previous paragraphs.

6.1.3.1 Reducing back loss: contacts removal

The choice of InGaAs has been made to have an ohmic contact. Unfortunately its 0.75 eV bandgap allows absorption we consider as loss. This choice is consequently a bias towards electrical performance to the detriment of optics. The opposite choice can be done, which gives at least an upper limit of the MRCD performance at this specific geometry. As a consequence, the same optimization than in section 6.1.2.3 has been done without InGaAs contact layers. The two differences are the width step of 20 nm instead of 10 nm (because of calculation time) and the InP thickness, shifted 20 nm thicker to compensate InGaAs layer absence (fig. 6.16).

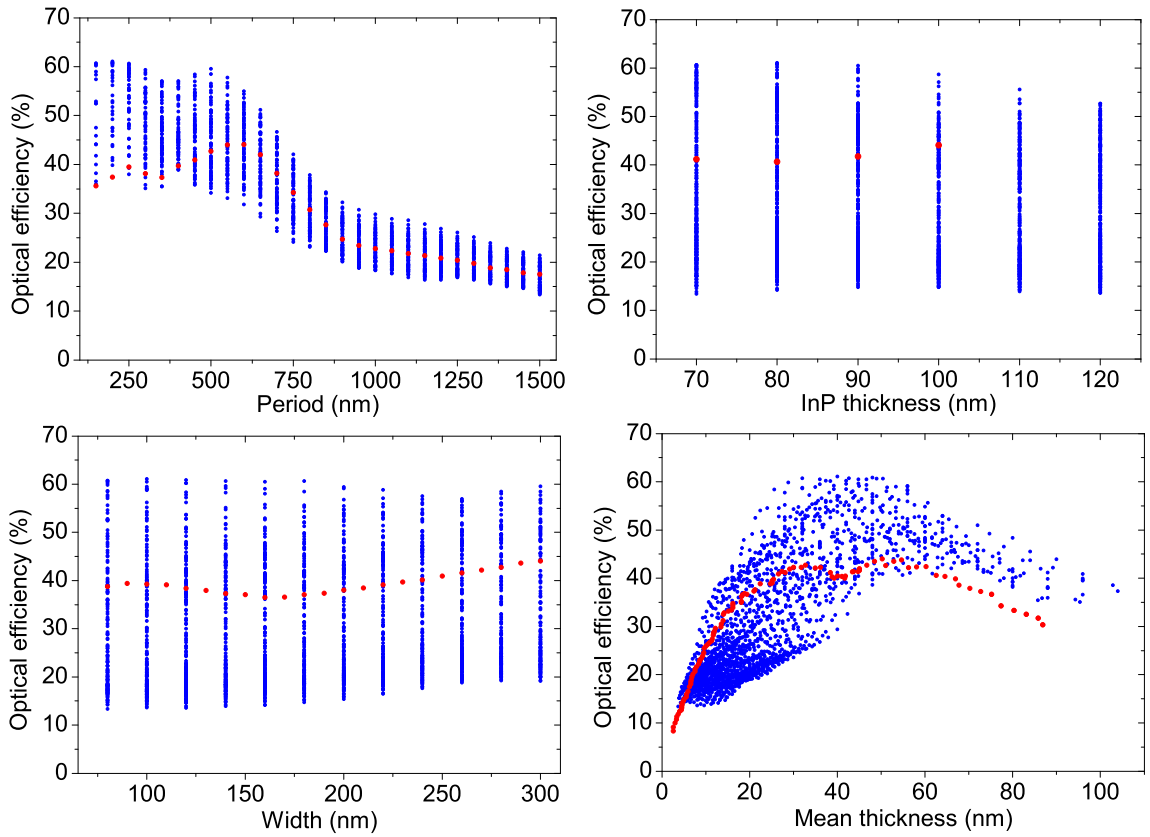

Figure 6.16: MRCD optimization without InGaAs contacts. Optical efficiency is plotted against period (top left), InP thickness (top right), width (bottom left) and mean thickness (bottom right). As a guide for the eyes, red dots represent the best optical efficiency obtained for the configuration of fig. 6.9 (no improvement)

Best structures exceed 60 % with a plateau starting at 30 nm mean thickness. This good result originates mainly for a better TM response with plasmonic resonance less damaging. Note that absorption in the doped layer may not be totally efficient, so in practice 60% optical efficiency may be slightly overestimated.

6.1.3.2 Reducing front (ext.) loss: High matrix refractive index (anti-reflection coating)

The second proposal of increasing the refractive index aims at improving the photon recycling by reducing the escape cone. Doing so, the escape cone is shifted from $asin(1/1.5) = 41.8°$ to $asin(1/2.5) = 23.6°$. Figure 6.17 shows the optical efficiency of the MRCD with 10 nm thick InGaAs contacts (same structure than described in section 6.1.2.3)

Optical efficiency is globally decreased compared to the same situation with n=1.5 (red dots in fig. 6.17). The main contributing factor is the Fresnel reflection loss ($\mathcal{L}_{ext}$) which has been greatly increased, from around 4% to 18.4% (Fresnel reflection between air ($n_{air} = 1$ and $n_{mat} = 2.5$). Anti-reflection coating (ARC) would be very beneficial in this situation.

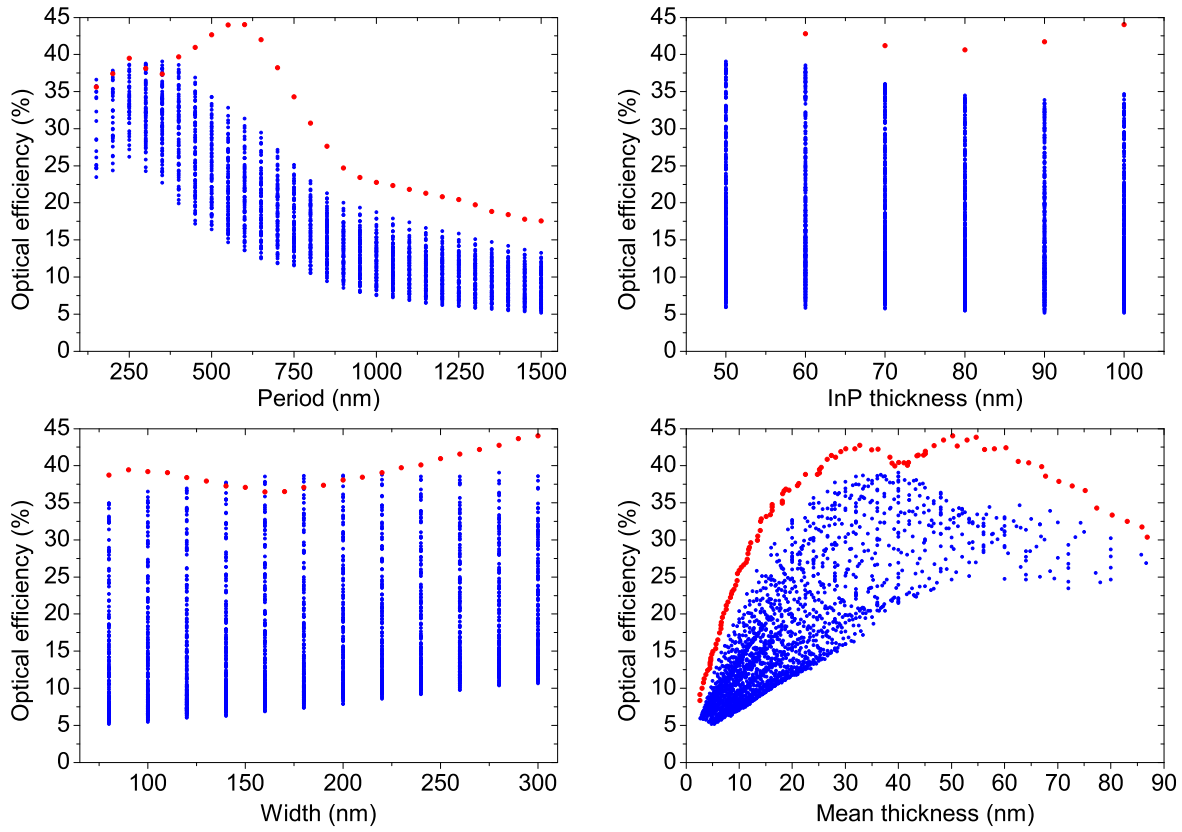

Figure 6.17: MRCD optimization with matrix refractive index of 2.5 and with InGaAs contacts. Parameters variation: $t_{InP} \in [50-100]$ nm, $w \in [80-300]$ nm and $p \in [150-1500]$ nm. As a guide for the eyes, red dots represent the best optical efficiency obtained for the configuration of fig. 6.9 (no improvement)

Assuming a perfect anti-reflection coating, the new optical efficiency can be deduced by a simple cross-product:

$$\eta_{opt}^{ARC} = \frac{\eta_{opt}^{no\ ARC} \times 100}{100 - \mathcal{L}_{ext}} \tag{6.2}$$

Equation (6.2) is justified because external loss are independent of λ. For the best structure at $\approx 39\%$, ARC would lead to $\frac{39\times100}{100-18.4} = 48.0$ %

If we now take a closer look to the photon recycling, we plot the optical efficiency as a function of the period, and compare it to the $n_{mat} = 1.5$ case (see fig. 6.8 upper left). As a guide for the eyes, the equation $\eta = \eta_{max}.\frac{p_{max}}{p}$ is also plotted. Indeed, from the most efficient structure with an optical efficiency η_{max} and a period p_{max}, it may be assumed that an increase of p can lead to a optical efficiency drop of $\frac{p_{max}}{p}$ (considering the antenna resonances do not depend on p and the loss of efficiency corresponds to a too high distance between resonators with respect to their cross section). This is a rough approximate which may only be viewed as a guide for the eyes.

Photon recycling is better with $n_{mat} = 2.5$, as suggested by the fact that the red line is not a maximum for fig. 6.18 (left), contrary to fig. 6.18 (right). Interestingly, antenna cross section is

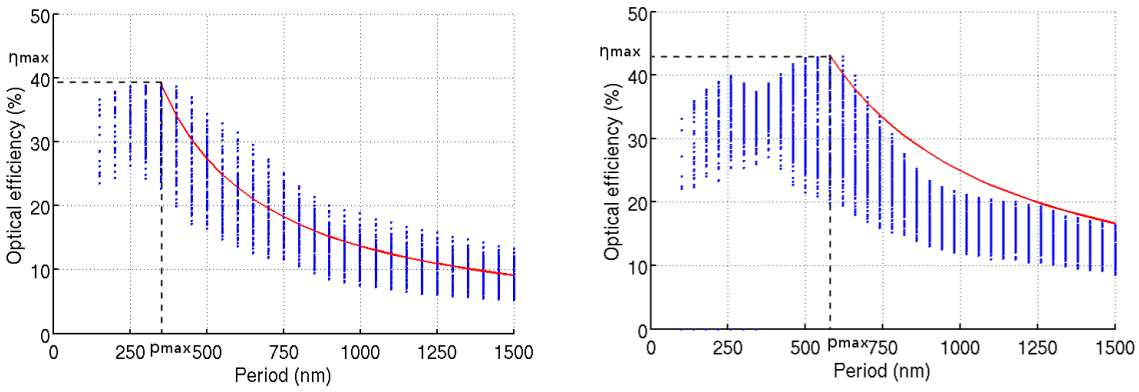

Figure 6.18: Comparison of photon recycling with $n_{mat} = 2.5$ (left) or 1.5 (right). No anti-reflection coating. The red curve is: $\eta = \eta_{max}.\frac{p_{max}}{p}$, $for\ p \in [p_{max} - 1500]$

reduced for a higher refractive index ($\approx \frac{\lambda}{n_{mat}}$). That explains why p_{max} is lower for $n_{mat} = 2.5$. This is not beneficial from the point of view of material saving. We can finally try to combine the a high refractive index with no contact antenna.

6.1.3.3 Combining high refractive index, no contact layers and ARC

If we remove contact layers, choose a matrix of refractive index of 2.5 and add a perfect anti-reflection coating, obtain the following results:

Figure 6.19 shows that a structure can reach 66.8% optical efficiency (best optical efficiency without optimization: 44.04 %) for a mean thickness lower than 50 nm. If we look at the best structure with a mean thickness of 18.7 nm, we reach 46.5 % (to be compared to 37.8 % in fig. 6.9).

High refractive index improves performance but in the meantime increases the mean thickness, by reducing the antenna cross section ($\propto 1/n_{mat}$). Implementation of this alternative is therefore questionable if a priority is the material saving. However, removing contacts and anti-reflection coating are always beneficial, but one has to keep in mind that we have made the assumption than light absorption was efficient in InP, without distinguishing doped and intrinsic layers.

The best structure ($t_{InP} = 70$ nm, $w = 160$ nm, $p = 250$ nm) is detailed in fig. 6.20:

66.8 % optical efficiency is obtained because external loss has been removed with an anti-reflective coating, back loss has been limited by removing the contacts and front loss has also been limited by increasing the refractive index and therefore by reducing the escape cone.

6.1.3.4 Summary

The two points the previous sections aim to address were:

1. How to increase the optical efficiency when there is no InGaAs contact layer
2. How is improved the photon recycling when the matrix refractive index increases.

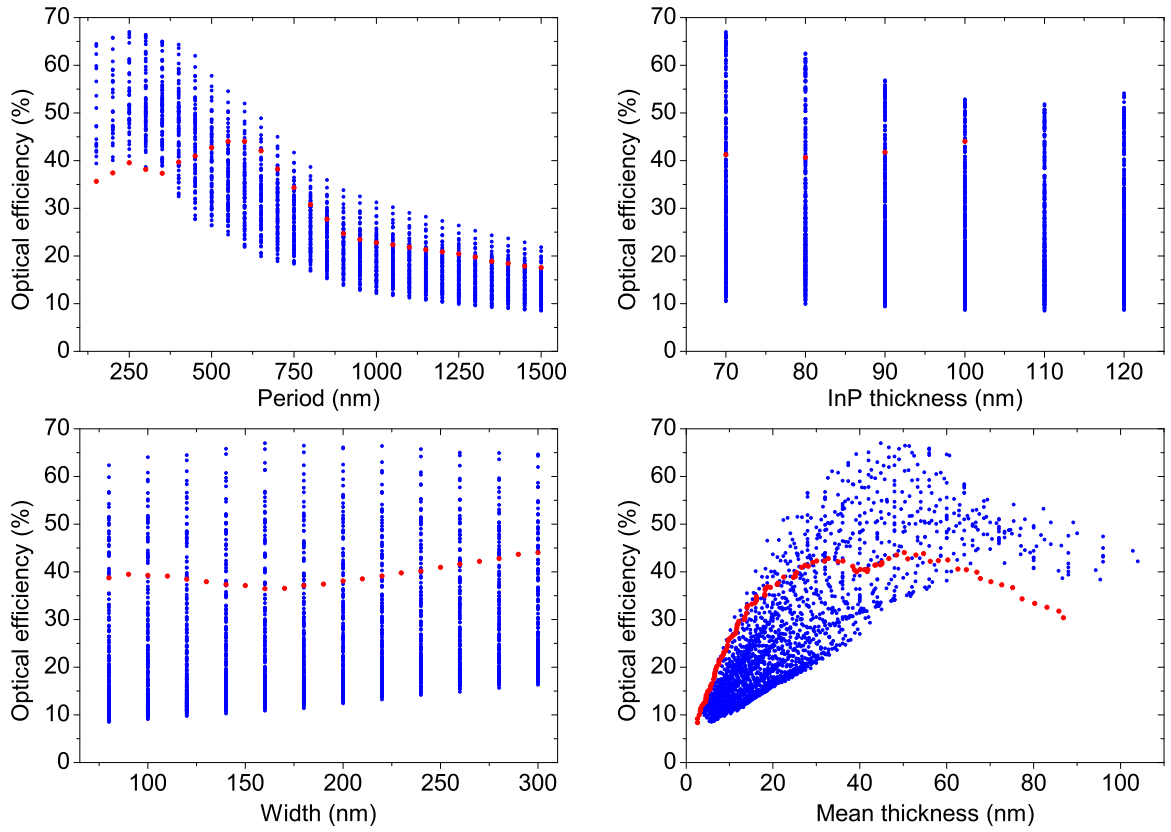

Figure 6.19: MRCD optimization combining no contact layers, matrix refractive index 2.5 and perfect anti-reflection coating. As a guide for the eyes, red dots represent the best optical efficiency obtained for the configuration of fig. 6.9 (no improvement)

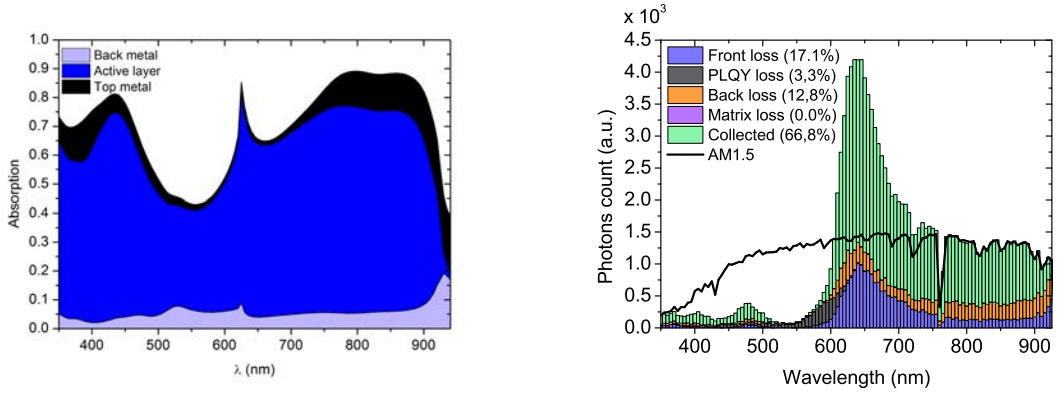

(a) Stacked unpolarized absorption

(b) Overall performance

Figure 6.20: Results for a MRCD ($t_{InP} = 70$ nm, $w = 160$ nm, $p = 250$ nm) with no InGaAs contact, refractive index of 2.5 and antireflective coating. Left: unpolarized absorption of the antenna. Right: overall performance.

To highlight the change in the photon recycling, we represent on fig. 6.21 (x-axis: period, y-axis: optical efficiency) the best optical efficiencies for the four configurations (with or without InGaAs contact and with $n_{mat} = 1.5$ or 2.5 (plus ARC)):

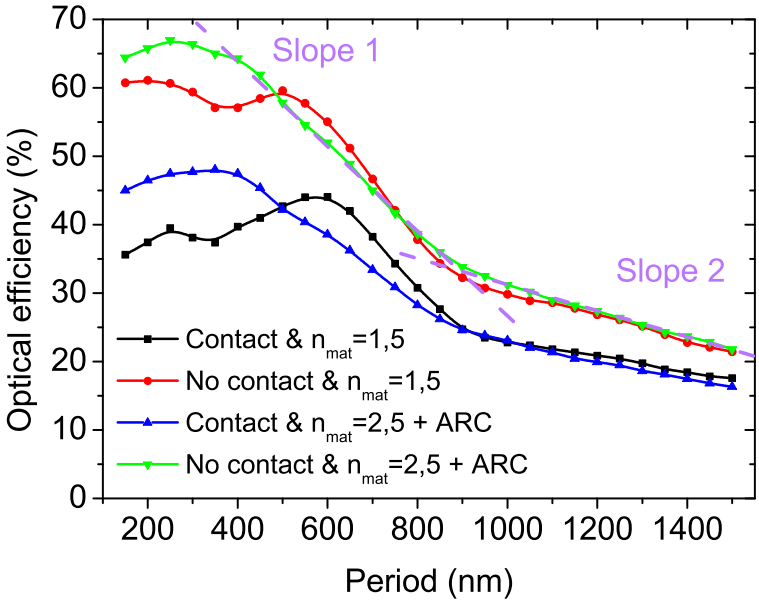

Figure 6.21: Best optical efficiencies as a function of the period. The two purple lines illustrates the two slopes characterizing the fall of the optical efficiency.

Optical efficiency drop is characterized by two slopes (purple lines in fig. 6.21) which seems to be strongly correlated to the refractive index. For each configuration, we summarize in table 6.4 the pertinent information to quantify the optical efficiency behaviour:

Optical efficiency key values				
Configuration	η_{max} (%)	p_{max} (nm)	Slope 1 (η_{opt}/nm)	Slope 2 (η_{opt}/nm)
C & $n_{mat} = 1.5$	44.0	600	-0.072	-0.010
NC & $n_{mat} = 1.5$	59.6	500	-0.083	-0.017
C & $n_{mat} = 2.5$	48.0	350	-0.049	-0.012
NC & $n_{mat} = 2.5$	66.9	250	-0.064	-0.019

Table 6.4: Optical efficiency summary for each configuration vs. period. C (NC) are structures with (without) InGaAs contacts respectively. Slopes 1 and 2 are represented in fig. 6.21

The absence of contacts enables to reach high optical efficiency at a lower period. In addition, optical efficiency drop is accentuated (slope 1 and 2). Regarding a high refractive index, it slightly increases the optical efficiency but drastically reduces the optimal period. Interestingly, optical efficiency drop is lowered is n_{mat} is high, which is attributed to a better photon recycling.

Slope 1 is more sensitive to the refractive index and contacts than slope 2. It suggests that slope 2 is only ruled by the coverage fraction (width / period)

Because the real figures of merit are the optical efficiency and the mean thickness, we can plot fig. 6.21 as a function of the mean thickness instead of the period (which was useful to understand how optical efficiency behaves). It is done in fig. 6.22:

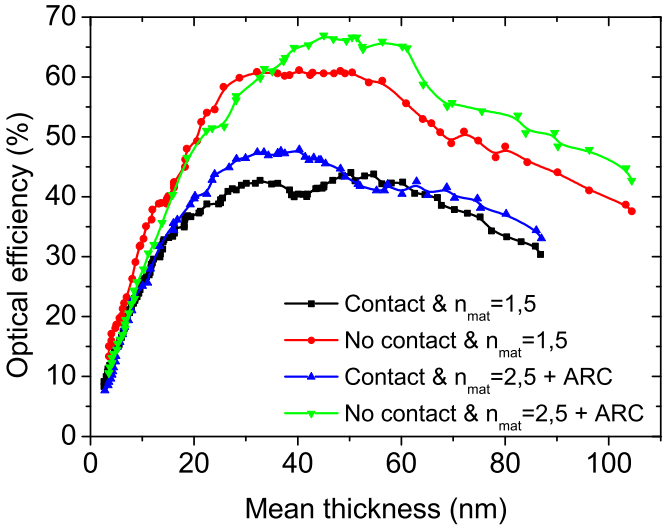

Figure 6.22: Optical efficiency summary for each configurations vs. mean thickness.

If efficiency is more important than material saving, then one has to choose no contact and $n_{mat} = 2.5$. Conversely, if material saving does matter, then considering no contact and $n_{mat} = 1.5$ can be interesting. Yet, we have to keep in mind that removing the contact is good for optical properties, and therefore will enhance the short-circuit current of the resonator, but it may rise electrical issue and therefore may decrease the open circuit voltage.

Finally, as a perspective on the nano-resonator design, one can think to have a low refractive index close to the nano-antenna (high capture cross section) and a high refractive index at the top of the structure to improve the photon recycling.

6.2 Fabrication

The fabrication process associated to MRCD was developed in the LPN clean room with the help of the technical team, especially Nathalie Bardou (electronic lithography) and Christophe Dupuis (global help). The fabrication process is illustrated in the case in which gold is used as metal contact and without InGaAs contact layers. The full process details can be found in appendix H. We would also emphasize the fact that despite numerous fabrication steps were already known before this work, it was not the case for all the steps (especially dry etching), which has required technological developments.

Epitaxial growth on metal is extremely challenging and no suitable solution was available during this thesis. Therefore the first step of the process is to report an epitaxial layer on a metal.

6.2.1 pin junction reported on pyrex

The report is the most challenging part of the process. The difficulty lies in the extremely thin thickness (around 100 nm) combined to the need of a perfect homogeneous adherence to the substrate and the total absence of dust. Thin thickness pin junction report does not tolerate high mechanical constraints (which may lead to pin junction damage during the substrate removal), that is why a low temperature technique is preferable. The solution we have chosen is the anodic bonding. This technique allows a strong electrostatic force to be applied between pyrex and metal, which is intrinsically homogenous and allows strong bonding. It has been first proposed in 1969 by Wallis and Pomerantz [148] and is illustrated in fig. 6.23:

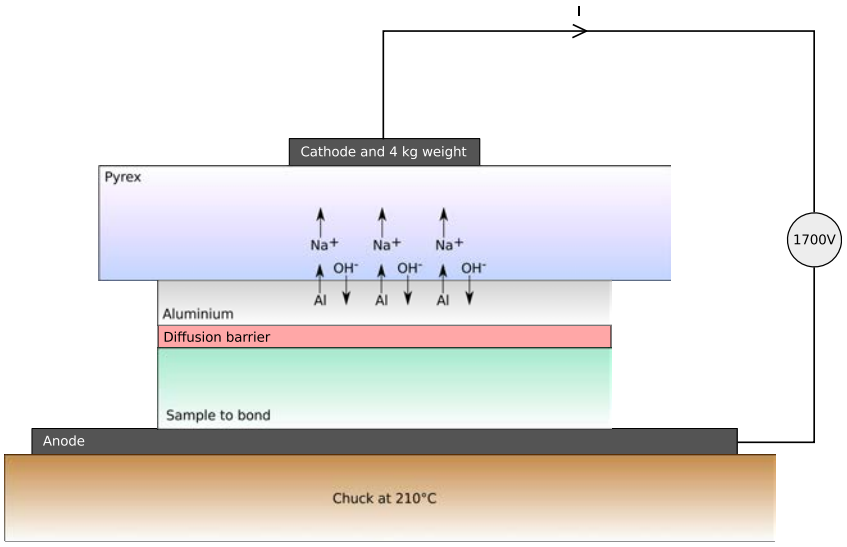

Figure 6.23: Principle of anodic bonding

It consists in an intimate bonding applying a high electrical potential (1700 V in our process) between pyrex and metal. The temperature should be both low to reduce mechanical constraints and high to improve ions mobility. A reasonable compromise is 210 °C. Due to the applied electrical field and high 210 °temperature, oxygen negative ion and sodium positive ion migrate in opposite directions. Oxygen ions are concentrated toward the aluminum interface, creating an intimate intermolecular bonding (covalent bond). Covalent bond is possible because the electrostatic force ($\propto 1/x$) allows to place the two surfaces to be bonded extremely close. A weight is applied on the samples to improve pyrex and aluminium proximity so that electrostatic force could take over. To ensure homogeneous bonding in all the sample surface, the top electrode is changed 3 times (from the smallest area to the biggest). During the bonding, the current flow is monitored and electrode change happens when the current has been divided by 2. The anionic (Na^+) current decreases because no Na^+ ions are injected, therefore an exponential decrease is expected.

Aluminium is a poor metal for nano-photonic applications. Gold or silver are better adapted. Moreover, a third Ti metal layer is added to avoid inter-diffusion, so a 3 metal stack is first evaporated Au / Ti / Al fig. 6.24 (a). Because we do not want apply 1700 volt across the pin junction (for obvious reasons), aluminium is also evaporated on the sample side and back surface fig. 6.24 (b). Then anodic bonding is done fig. 6.24 (c)

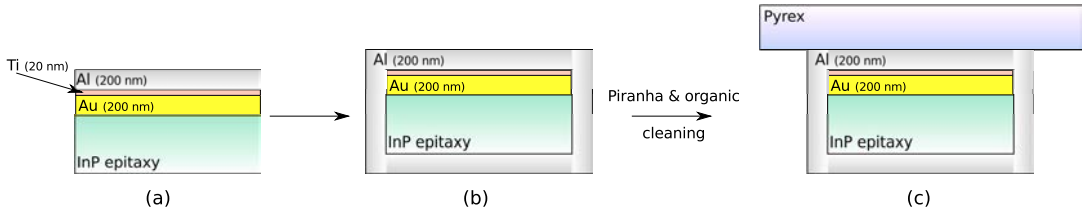

Figure 6.24: Principal process steps to report epitaxy on a pyrex substrate

6.2.2 Top metal patches preparation

At this step a metal has been deposited on the pin junction which is in-between gold mirror and the stack InGaAs stop layer / InP substrate / Al. From now the pyrex is our new substrate and the old one (InP substrate) must be removed (more precisely the stack Aluminium, substrate and stop layer)fig. 6.26 (b-d). It is worth noting that aluminium covering the InP substrate is the first layer to remove without damaging the aluminium layer bonded to pyrex (see appendix H for more details). During this process, side aluminium is removed naturally (200 nm width for more than 300 μm height Al). Nevertheless the substrate removal is not anisotropic (depending on crystallographic orientation, which explains we have two walls instead of four) and creates substrate "walls" we have to suppress in order to be able to spin-coat resist on the sample properly. This is done by a precision wire saw. The substrate "wall"problematic is showed in fig. 6.25.

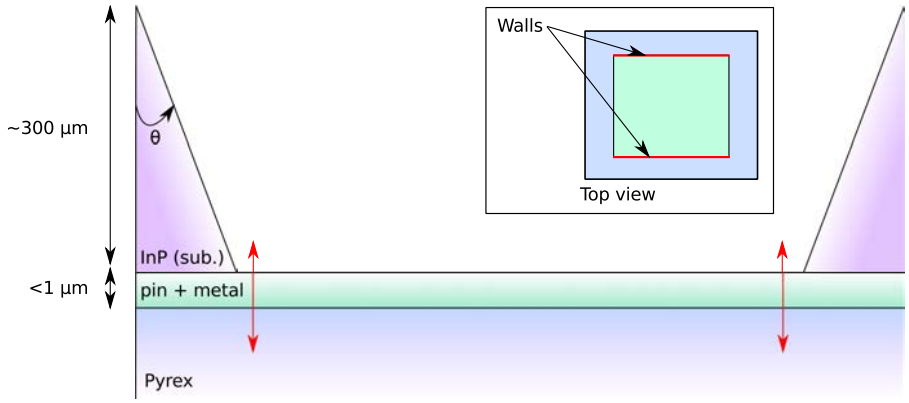

Figure 6.25: Illustration of substrate walls. θ is around 50°C (proportion not respected in the scheme). The red arrows correspond to the saw cut. The saw must enter the pyrex without cutting it entirely. Inset top view of the sample, illustrating that walls exist only on two edges

The next step is to prepare the sample for the electronic lithography. This should be done anticipating what will be the etching method used after the lithography. Indeed two kinds of solutions exist: wet and dry etching. We have chosen wet (chemical) etching for reasons which will be explained later. Similarly to the InP substrate etching, InP pin junction etching with HCl depends on the crystalline plans to be etched. When etching direction is (100), etching flanks will be almost vertical ($\theta \approx 87$ °). On the contrary, etching direction (010) gives rise to $\theta \approx 45$ °. If now etching directions are (110) or (-110), flanks will have 45°inclination. Thus, if we want to fabricate squared nanoresonators, it is best to be in (110) and (-110) orientations to have the same kind of etching on the square four sides. On the contrary, if a finger-like nanoresonator is desired ("semi-infinite" in the y-axis), then (100) orientation will be preferred for the 2 long sides (the 2 short sides matter little).

The next challenge is to be sure the lithography will be done along the good direction. A mismatch of few degrees will change totally the etching conditions. In the meantime, during electronic lithography, charges must be evacuated to have a fine resolution. Working on a substrate pyrex is not ideal. A gold line, exactly parallel to the direction (100) will be evaporated astride the back metal and the pyrex fig. 6.26 (e-e bis). Then the pyrex is cut along this line to ensure a good alignment fig. 6.26 (f-g).

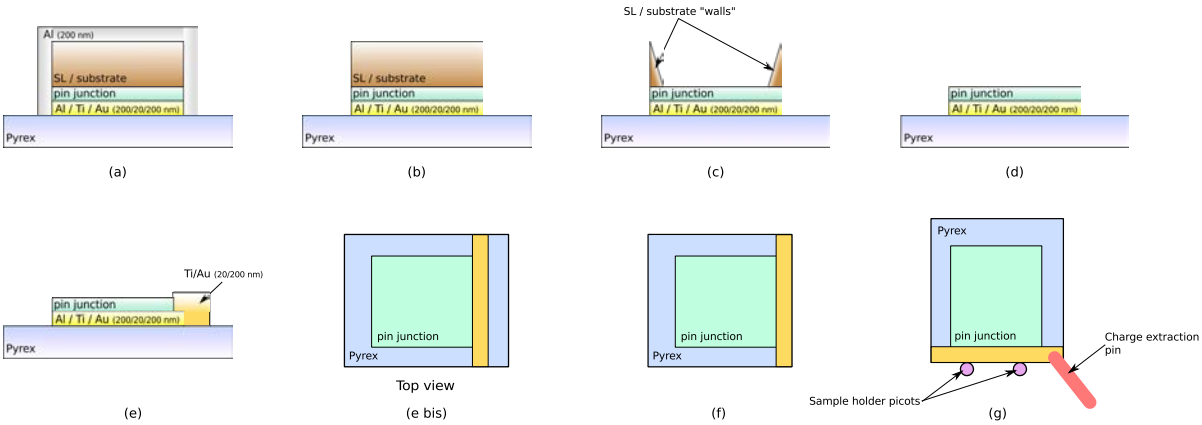

Figure 6.26: Overview of sample preparation to electronic lithography. (a) is the same than fig. 6.24 (c). (b) Al removal. (c) Substrate and Stop layer removal. (d) walls removal. (e) metal line evaporation parallel to plan (100), alignment done by photo-lithography. (e bis) the top view of (e). (f) pyrex cutting. (g) is a schematic of the sample and electronic lithography sample holder.

6.2.3 Top metal patches & etching

At this stage the electronic lithography resist can be spin-coated/annealed on the sample fig. 6.27 (a). The resist is PMMA A5 from Microchemicals. Electronic lithography is done either with a pattern at 0°(alignment (100)) or 45°(alignment (110) and (-110)) fig. 6.27 (b). Then the resist is developed, etching base cleaned (oxygen reactive ion etching) and InP surface deoxidized fig. 6.27 (c). Quickly after deoxidation metal is evaporated fig. 6.27(d) and a lift-off is done fig. 6.27 (e) to finish the top metal deposition process. InP pin junction is etched (HCl/H_3PO_4 1:99) to end up with the nano-antenna fig. 6.27 (f).

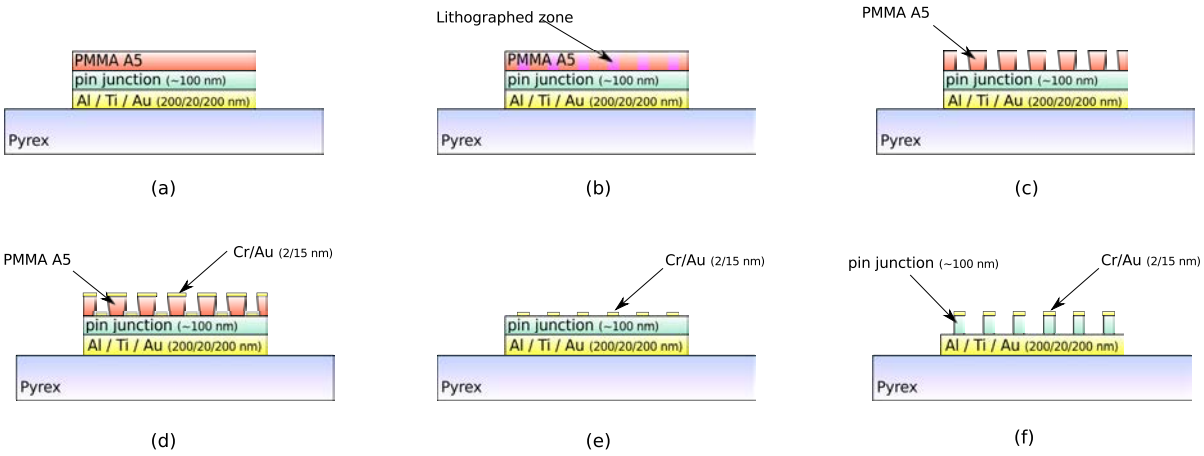

Figure 6.27: Overview of the metal patch deposition. (a) resist coating. (b) electronic lithography. (c) Development. (d) metallization. (e) Lift-off. (f) etching

6.2.4 Electrical connection

At the end of these steps, the sample has the proper geometry (if all fabrication steps have been successful) to act as a nano-resonator. Figure 6.28 illustrates how the sample looks like.

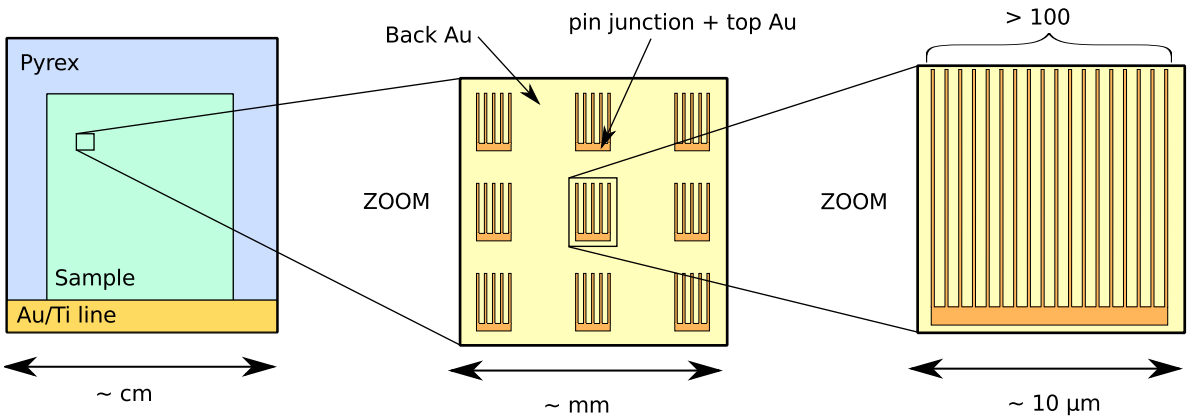

Figure 6.28: Sample top view before electrical connection

The final concern is the electrical contacts. The back metal is a common electrode for all resonators. In the case of ribbon resonator, a bus bar is fabricated to connect all individual resonators. This step is not an additional step, it simply requires an appropriate electronic lithography mask. Then the bus bar is connected to an electrical pad after array electrical isolation. Indeed different arrays may co-exist on the same sample (for example to test different geometries) and consequently each pad must be electrically independent. To do that, SiO_2 is sputtered on the all sample fig. 6.29 (a). Then the dielectric is selectively removed by photo-lithography from the resonator surface fig. 6.29 (b). Then most nano-resonator surface is protected by a resist by photo-lithography fig. 6.29 (c) prior to Cr/Au metallization. Finally a lift-off in acetone is performed to finish the entire process fig. 6.29 (d).

Experimentally, we manage to do nanoresonator arrays without the semiconductor etching step. It has been done with a geometry which is not adapted to visible light absorption because

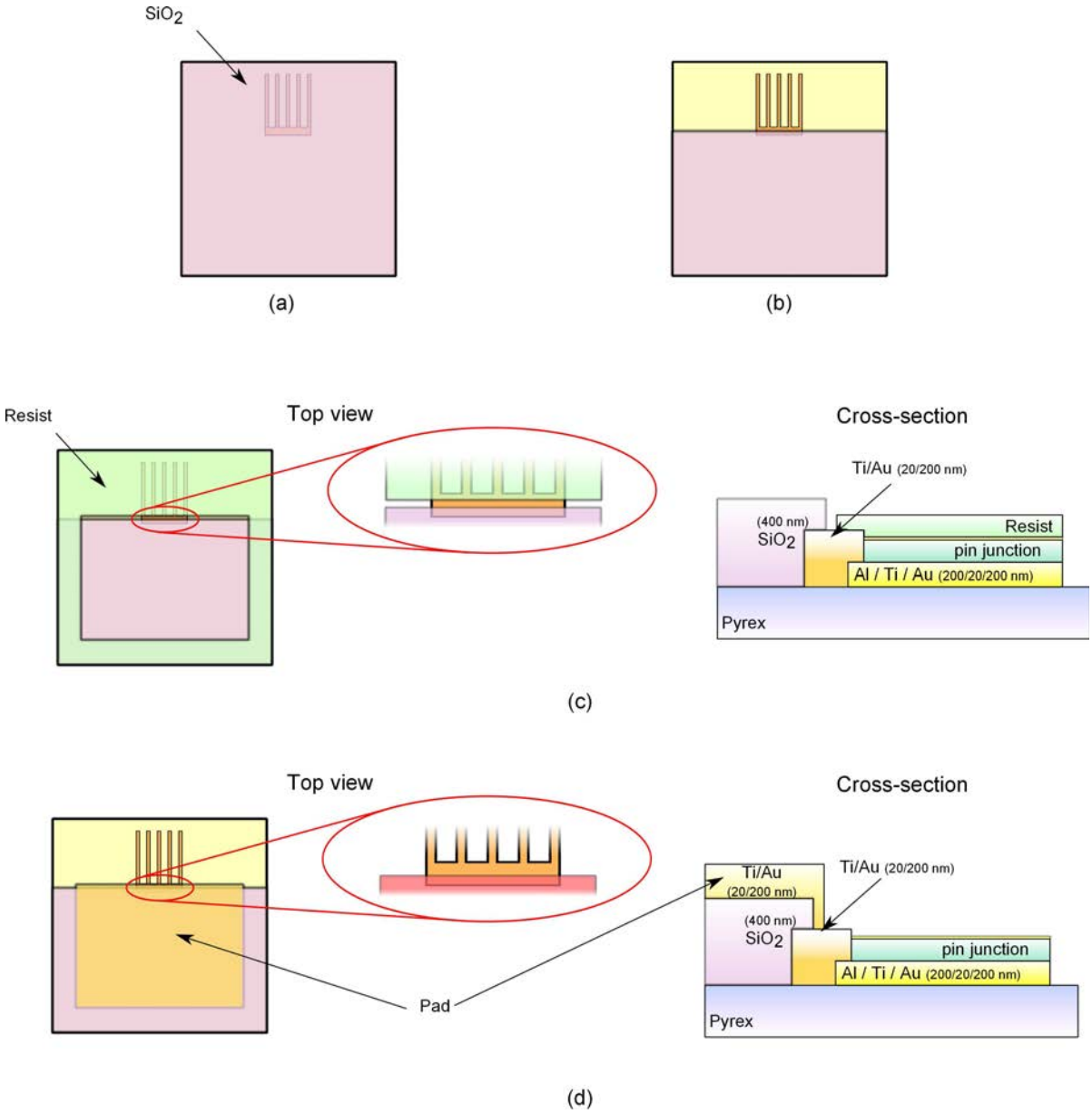

Figure 6.29: Electrical pads fabrication. (a) SiO_2 sputtering. (b) SiO_2 opening. (c) Nano-resonator protection. (d) Metal deposition followed by a lift-off.

at that time the numerical calculations had not been done. Figure 6.30 shows two SEM images of this sample.

Other sample with geometry identified in section 6.1.2.3.a is being processed at the time this manuscript is written.

One can object that no material is saved after etching. In our case we deal with InP and In is scarce. If a chemical etching is used, then In is in the beaker and can be re-used. Second, an obvious perspective in fabrication is the local growth, which can took inspiration from nanowire growth.

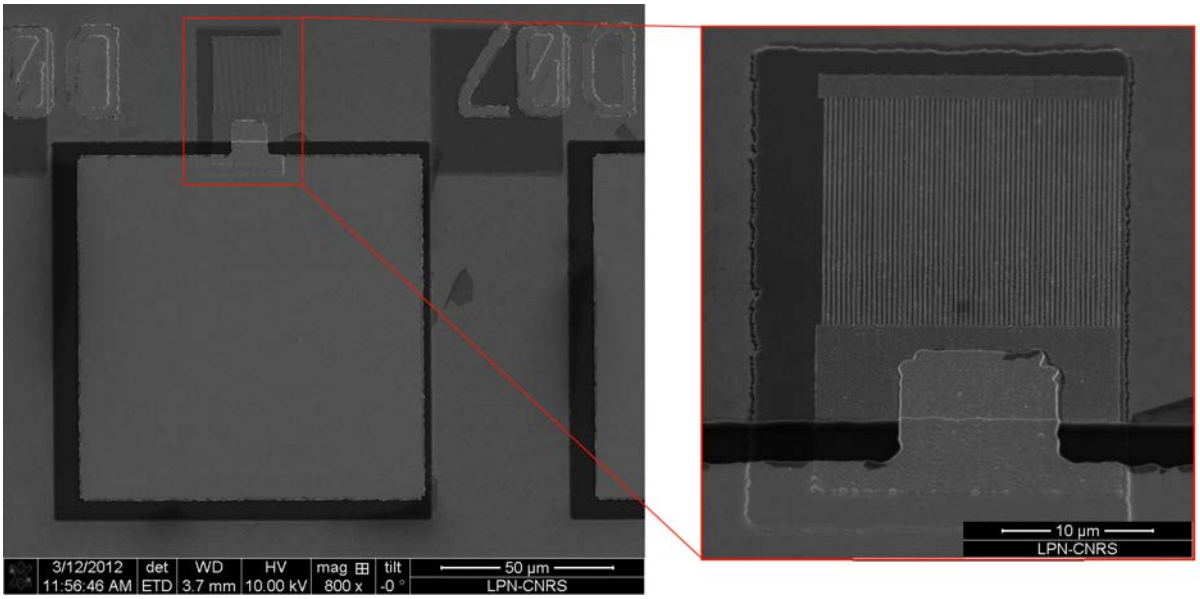

Figure 6.30: SEM images of a nanoresonator array. Left: global view of the array and its electrical pad. They are both isolated from others arrays. Right: Zoom on the resonator array.

6.3 Electrical performances

In the same time that the process has been developed, we have fabricated test samples to probe electrical properties of nano-diodes. More specifically we were interested in the dark current (diode saturation current).

In order to achieve high V_{oc}, the forward bias current must be low and consequently the recombination must be minimized. There are three main contributions influencing recombination:

1. Doping level: a high doping level ensures a minimization of the equilibrium carrier. That is why we have chosen epitaxy with a high doping concentration.

2. Diffusion length: a high diffusion length reduces recombination by allowing carrier to move fast from the junction. Unfortunately a high doping level tends to reduce the diffusion length. Nevertheless, the advantage of nano device is that the distance the charge carrier must cross is by definition very thin which reduces the diffusion length influence on recombination.

3. Passivating localized non radiative recombination source (SRH). Localized recombination source are to be avoided for trivial reasons. These sources may come from grain boundary (which are not present in epitaxy) and surface. The potential detrimental effect of surface being even worse when the ratio surface over volume is high. MRCD has a high ratio surface over volume, which can canceled out its advantages from the two previous items.

Thus, we decided to fabricate nano-diodes with different areas (but same thickness) to probe the geometry effect on the dark-current.

6.3.1 Nano-diode fabrication

The fabrication process, contrary to MRCD, does not require a substrate report because all electrical test will be done under dark condition and consequently the electrical field enhancement is in this case of little interest. Substrate report is replaced by back surface metallization (Cr/Au 20/200 nm) after deoxidation. The back surface will act as an electrode, knowing that the InP substrate is n-doped. To create the metal patches, the same process than in section 6.2.3 is used. Semiconductor etching is done in ICP (Inductively Coupled Plasma). It enables to have a directional etching. Etching depth was around 500 nm.

From that, we could have chosen to fabricate the electrical pad, as described in section 6.2.4. Indeed, conventional four-probes measurements requires at least 50x50 μm, which is far larger than our resonator surface. The problem of this strategy is that a bias is introduced with the pad and the connection "bridge". This bias may be prejudicial to the interpretation of electrical measurements, so we have opted for not continuing technological process but rather find a way of doing measurements directly on the nanodiodes.

The nanodiode matrix is showed on fig. 6.31 and two nanodiode SEM pictures are given in fig. 6.32:

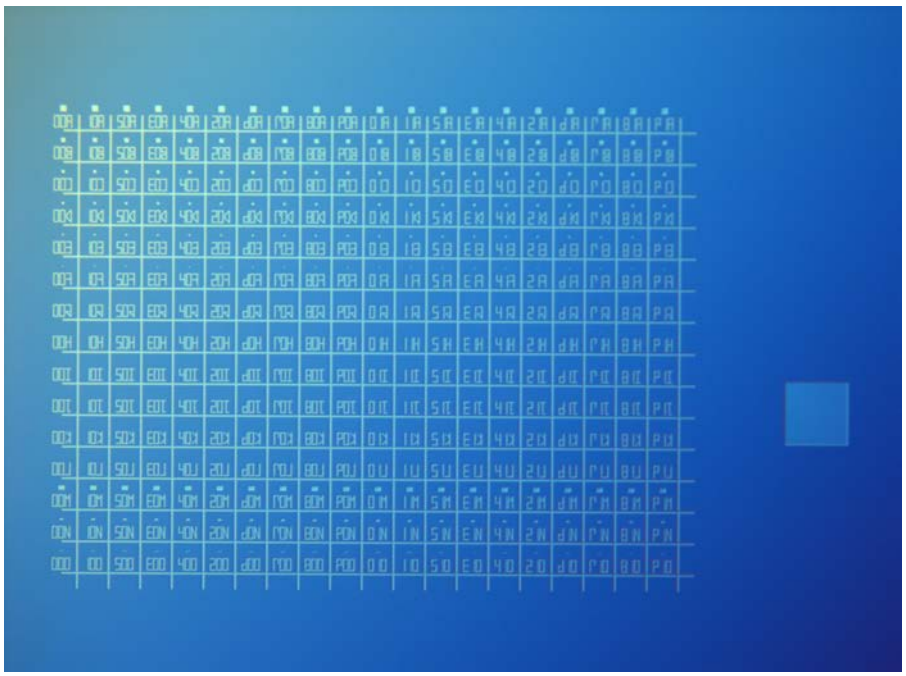

Figure 6.31: Optical microscope image of nano-diodes matrix: areas ranged from 10×10 μm^2 from 100×100 nm^2. The largest square to the right of the picture is 100×100 μm^2

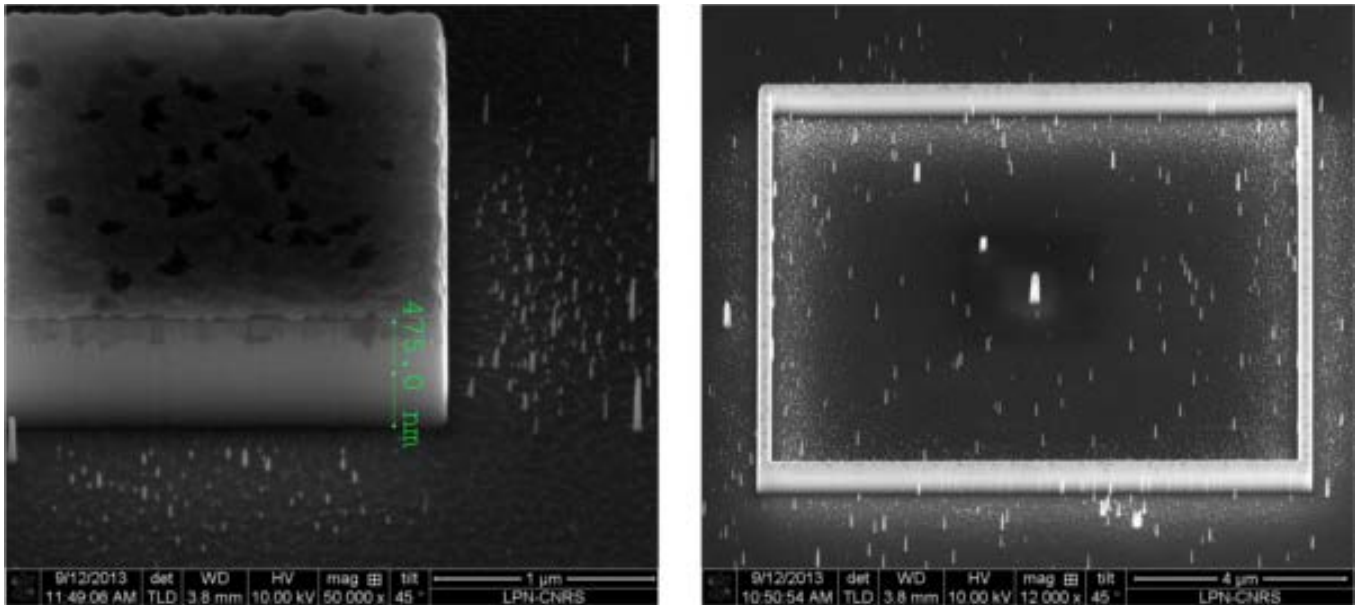

Figure 6.32: *Left:* $2 \times 2\ \mu m^2$ nanodiode. *Right:* $100 \times 100\ nm^2$ diode surrounded by a $1 \times 1\ \mu m^2$ square. Its role is to ease the diode spotting for electrical measurements

ICP etching produces numerous "micro-masking", which can be detrimental for the sample. Additionally, the gold patch on the nanodiode top is affected by the physical etching. This can be better viewed on fig. 6.33

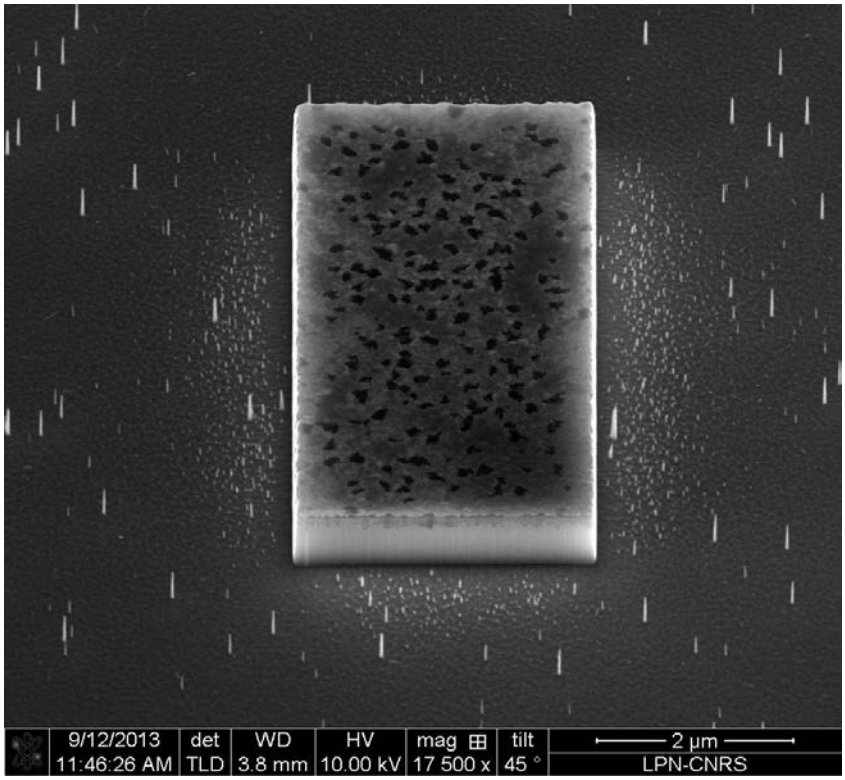

Figure 6.33: Rectangle nanodiode: top metal patch presents bright and dark regions which suggests metal alteration during etching

Dark and bright regions on metal is a clear evidence of metal degradation during ICP. As it will be shown in the next section, conductivity is modified, maybe because of alloy creation between gold and plasma atoms.

To perform electrical measurements, we used an Atomic Force Microscope (AFM), which has the suitable tip size to probe our nanodiodes.

6.3.2 Current-Voltage measurements by AFM-CP

A Conductive Probe AFM (AFM-CP) has been developed at LGEP. It consists in a classical AFM with a power system to apply a voltage and a source measure unit to measure the current. The tip material we used was p+ doped diamond tip. The back electrode is the sample holder in itself. We precise that the diodes which have been measured were not deoxidized prior measurements.

IV measurements should be done under dark conditions. The AFM sample holder is in a box which prevent external light to reach the diodes. The problem comes from the AFM laser used to monitor the tip displacement. The laser lights the head tip (whom reflection is record on a detector) but also the sample via light scattering. Because our AFM uses a red laser, our diodes are photo-sensible to the laser wavelength which disturb the dark condition. Yet, it was possible to shut down the laser for the measurement, which ensures satisfying dark condition.

To measure the metal conductivity, some resistance mappings have been done. Dark and bright contrast observed with a SEM is a consequence of surface metal alteration, as shown in fig. 6.34:

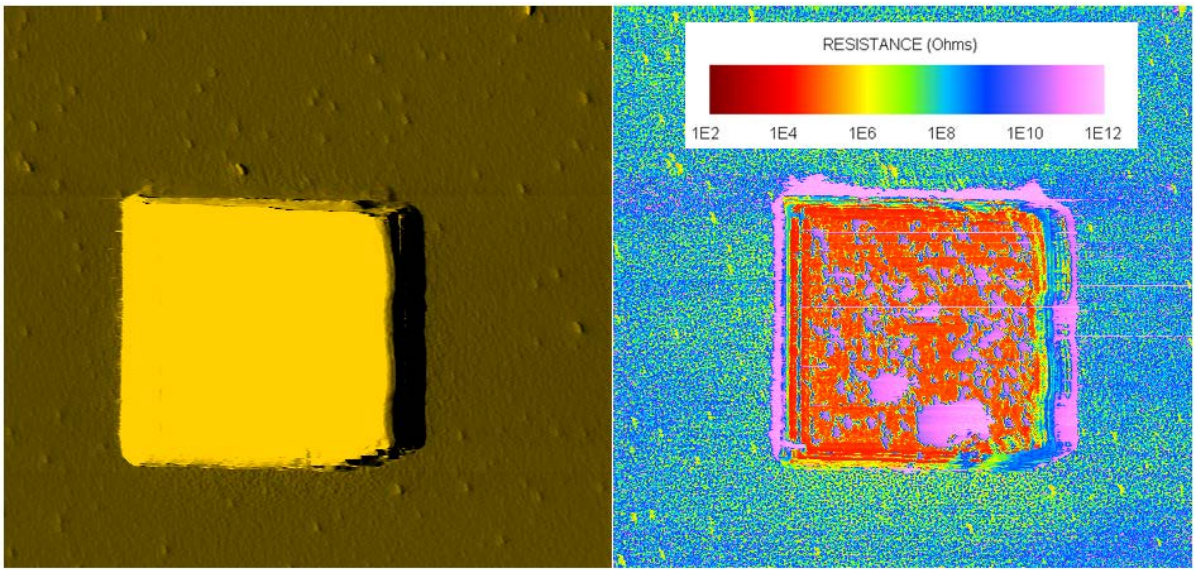

Figure 6.34: $3 \times 3\ \mu m^2$ nanodiode mapping. $Left$: topography. $Right$: resistance

The most conductive regions have still a resistance of around $10^4\ \Omega$. This is mainly due to the tip resistance, which was measured at $7\ k\Omega$. Lower resistance tips have been tested but the electrical contact was not satisfying.

Despite inhomogeneous metal surface, we manage to do some current-voltage measurements. Raw data are fitted with a two diodes model. The diodes ideality factors are set to 1 and 2 to be able to compare the saturation currents. One current-voltage measurement is shown in fig. 6.35:

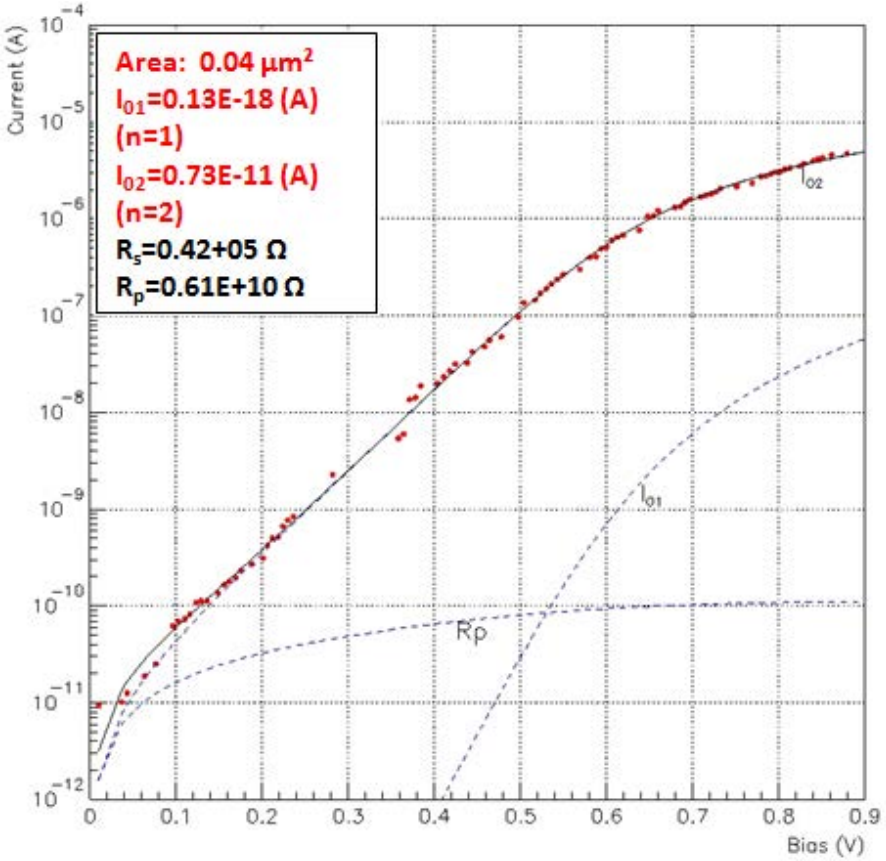

Figure 6.35: Current voltage measurement performed by Conductive Probe Atomic Force Microscope on a $200 \times 200\ nm^2$ nanodiode. The fit was done with a two diode model, setting the two ideality factors to 1 and 2

This nanodiode does not behave as an ideal diode. The fit suggests that an ideality factor of 2 better matches the experimental data, which can be interpreted as existence of SRH recombinations. Unfortunately, we did not manage to obtain reliable current-voltage measurements on different diodes. This is due to sample fabrication which was not optimal. A new nanodiodes sample has been fabricated and is being measured.

Despite partial results, we have found some surface recombination evidence. Even before obtaining these results, we have anticipated that passivation may be an issue, that is why we have worked on a passivation solution.

6.3.3 Passivation with polyphosphazen

The previous section shows without ambiguity that passivation and probably surface stabilization is required. Our strong collaboration with ILV and the need to find a time-stable

solution lead us to use polyphosphazen. The film formation is entirely done at ILV by Anne-Marie Goncalves and Christian Njel as well as the chemical interpretations. XPS and EDX characterization is also done at ILV by Muriel Bouttemy.

Polyphosphazen is a monolayer polymer formed by electrochemistry on a InP surface (n or p type) through Phosphorus-Nitrogen bonds in liquid ammonia NH_3 (see section 6.3.3.1). The monomer is $H_2N-P=NH$. Phosphorus comes from the InP surface whereas Nitrogen comes from ammonia. Figure 6.36 illustrates, at the atomic level, the polyphosphazen:

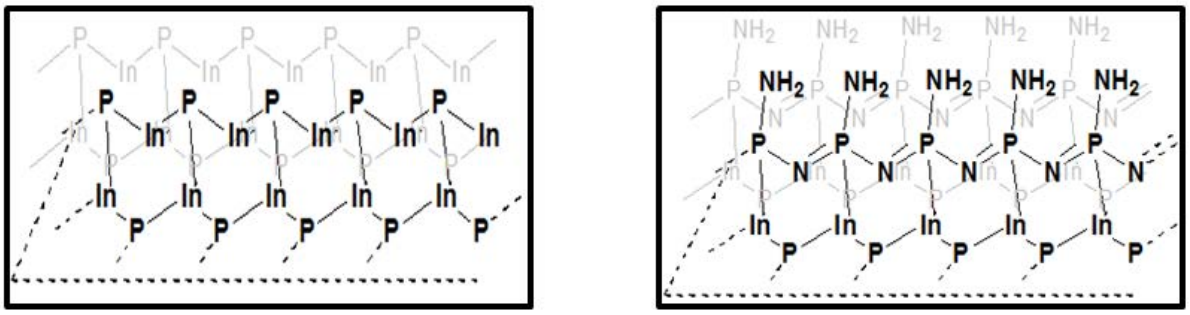

Figure 6.36: *Left:* (100) InP surface. *Right:* (100) InP surface with polyphosphazen. Reproduced from [149]

Before investigating polyphosphazen properties, let us mention the formation experimental conditions.

6.3.3.1 Polyphosphazen formation

There are different ways of forming polyphosphazen by electrochemical treatment in liquid ammonia [150, 151, 152, 153]. For a film growth on a (100) InP wafer, we have chosen a galvanostatic treatment which allows a better control of the charge crossing the interface. Galvanostatic treatment means constant current between a work electrode (n doped InP, anode) and a silver reference electrode. The preparation procedure is given below:

1. InP surface deoxidation with HCl 2M (2mol/L) because oxides are stable.
2. Deionised water rinse
3. N_2 drying
4. In liquid ammonia at -55 °C and NH_4Br (0.1 M):
   (a) Galvanostatic treatment at $I = 0.1\mu A$, corresponding to $1mC.cm^{-2}$ for 3600 s.
   (b) In-situ monitoring: Current-Voltage monitoring
   (c) Pure liquid NH_3 rinse for 1 hour
5. Deionised rinse
6. N_2 drying

Because a current flows through the sample during the film formation, the sample must be electrically connected. The rear surface is gold metalized (InP wafer is doped and consequently conductive). Then a gold wire is soldered to the rear surface with indium. Ammonia medium must be only in contact with InP surface and never metal part (if so it shunts the diode, no charges are allowed on the surface and no film formation occurs).

To avoid shunt, we use the following system:

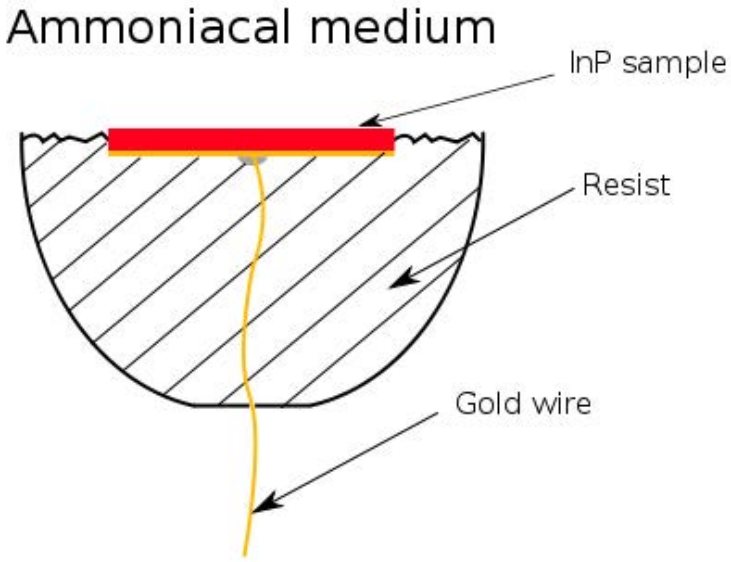

Figure 6.37: Schematic of the sample holder. A photograph of this system is showed in fig. 6.41

This system is compatible with -55°temperature and provides mechanical resistance. The sample is also illuminated with an optical fiber (see fig. 6.38). n-type semiconductor lighting enables to reduce the band bending by reducing the electrical field in the space charge region. Anodic treatment is therefore “softer”.

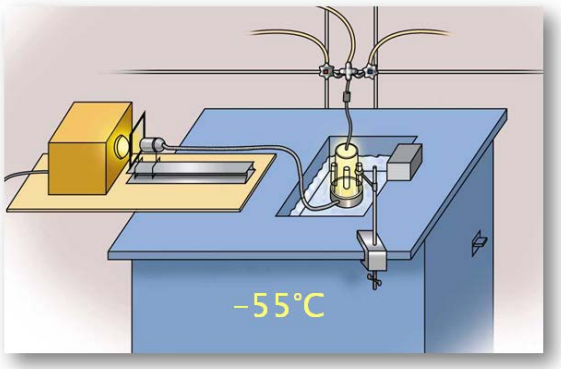

Figure 6.38: Schematic of the cell used to form the polyphosphazen [154]

6.3.3.2 Polyphosphazen characterization

To be sure that polyphosphazen forms an homogenous film on InP surface, different means are at our disposal.

6.3.3.2.a In-situ characterization

The polyphosphazen formation modifies the surface which in turn affects the InP surface potential. Because we use a three electrodes set-up, InP electric potential can be monitored with a silver reference electrode (SRE) (potential ESRE=+0.68 V/ENH). An example of obtained measurement is showed in fig. 6.39:

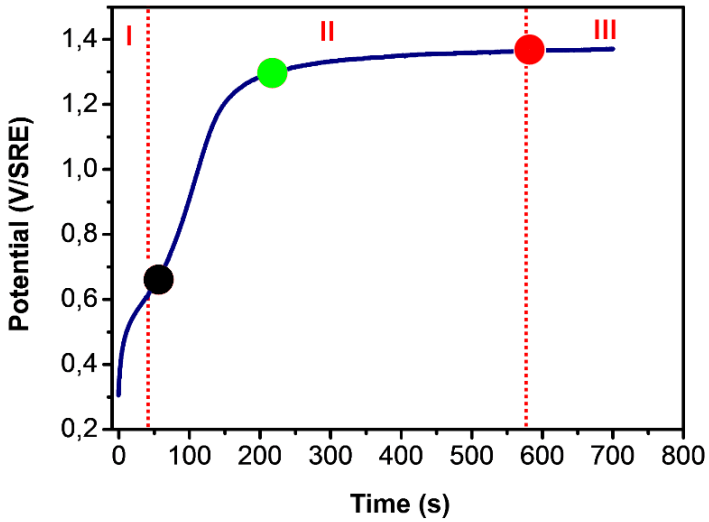

Figure 6.39: n-type (10^{18} cm^{-3}) InP surface potential monitored during the electrochemical treatment (current 0.1 μA) in liquid ammonia at -55°C under illumination.

The E(t) plot can be divided in three regions depicted in the figure above.

- **Zone I**: The first part of E(t) increases sharply (from +0.3 to +0.5 V/SRE). It corresponds to the beginning the transition between an equilibrium state with zero current (called open-circuit potential) to a new electrical potential determined by the 0.1 μA current. The second half plot slope (beginning at 40 seconds) is lower. It can be interpreted as a partial n-InP dissolution. This is corroborated by cyclic voltammetry [155].
- **Zone II**: Up to ≈ 200 seconds, E(t) rises abruptly (from +0.66 to +1.3 V/SRE). NH_3 partial adsorption/oxydation on InP surface may be the main reaction. Again this interpretation evidences can be found in [155]. After 200 seconds, the potential stabilizes (from +1.3 to +1.35 V/SRE). At the end, the film formation is total, which is confirmed by XPS measurements (see next section).
- **Zone III**: The potential does not evolve despite a constant current flow, which means that the surface modification is achieved. We presume that during this period NH_3 is oxidized in N_2 [149].

In-situ measurement is a first evidence of a good film formation but it requires more characterization.

6.3.3.2.b Others characterizations (XPS,EDX)

Energy-dispersive X-ray spectroscopy (EDX): EDX measurements are performed in a SEM. It can be used to probe the nitrogen composition of a surface treated by polyphosphazen. Because the only material containing nitrogen is polyphosphazen, it provides a qualitative evidence of film formation. Nitrogen cartography has been done and is shown below:

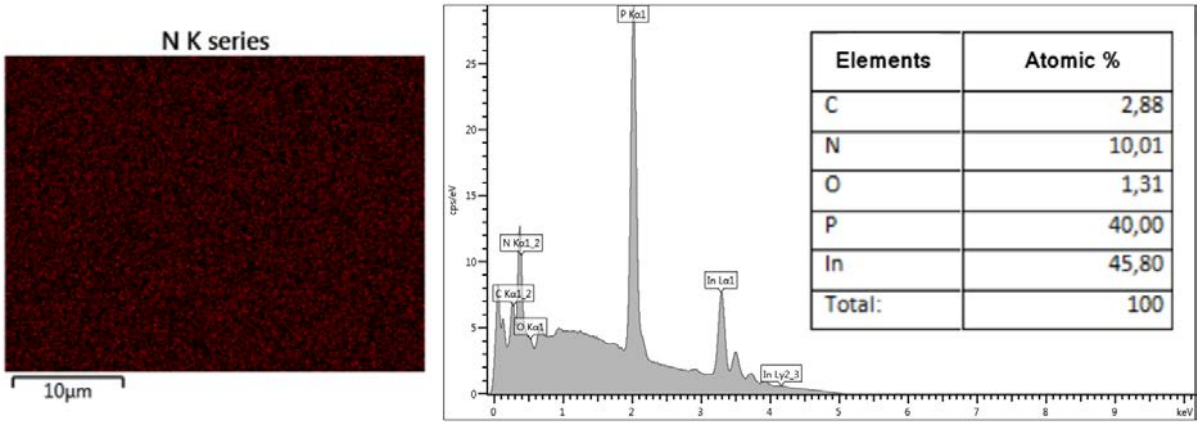

Elements	Atomic %
C	2,88
N	10,01
O	1,31
P	40,00
In	45,80
Total:	100

Figure 6.40: Left: Nitrogen cartography (red dots). Right: atomic percentage. N reaches 10 %

From this measurement nitrogen seems to be homogeneously distributed. The atomic ratio may be low but it is hard to exploit this value since EDX probes a volume of around 1 μm^3. A more quantitative characterization method is XPS.

X-Ray photo-electron spectrometry (XPS): Since XPS probes the sample within only few nanometers depth, it is well adapted to investigate surface chemical property. XPS gives access to atoms signatures we can exploit to deduce atomic ratios and conclude on the film coverage. We analyze In, P and N atoms. The XPS measurements were carried out in a AlKalpha (1486.5 eV) system from ThermoScientific, with a base pressure of 5.10^{-10} Torr, with a pass energy of 20 or 8 eV (resolution 0.2 eV). Energy levels of XPS were calibrated with Au single crystal. The spectra were processed using the VG Avantage Datasystem. We have done XPS analysis at different time during the polyphosphazen formation, identified by the three dots in fig. 6.39. Results are shown below as well as a photograph of the apparatus:

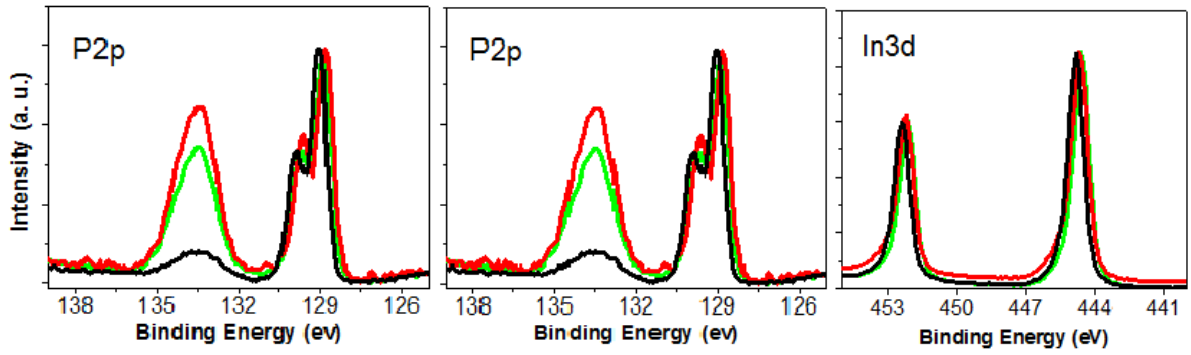

Figure 6.41: Binding energy of P, In and N atoms at the beginning (black 0.038 $mC.cm^{-2}$), middle (green 0.21 $mC.cm^{-2}$) and end (red 0.4 $mC.cm^{-2}$) of the electro-chemical treatment.

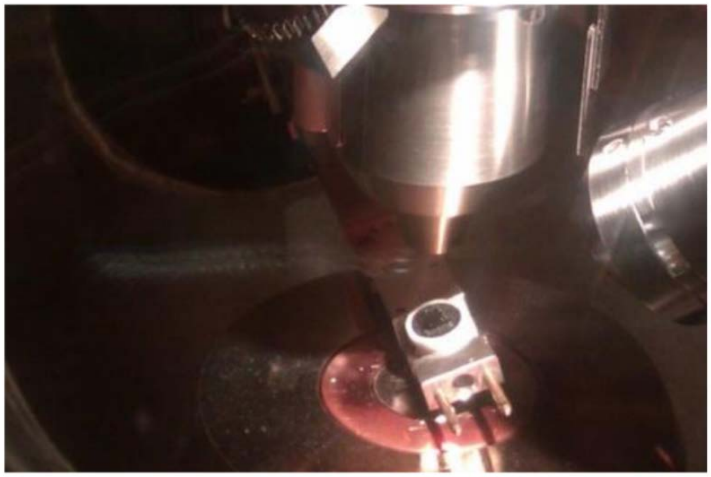

Figure 6.42: XPS chamber with one of our sample photograph

At the beginning of the film formation (black dot), there is almost no polyphosphazen and the polyphosphazen atoms signatures are weak. This is the case for Nitrogen which originates only from polyphosphazen, contrary to Indium which is not present in polyphosphazen. Phosphorus is both involved in polyphosphazen (polyphosphazen monomer contains one phosphorus atom) and InP. Thus one peak is weak (Polyphosphazen P) and the other one is intense (InP P). As expected during the film formation, indium signal does not evolve (not involved in the film formation), nitrogen signal increases and one phosphorus peak rises whereas the other one remains constant. From this data we extract atomic ratios as shown in fig. 6.43:

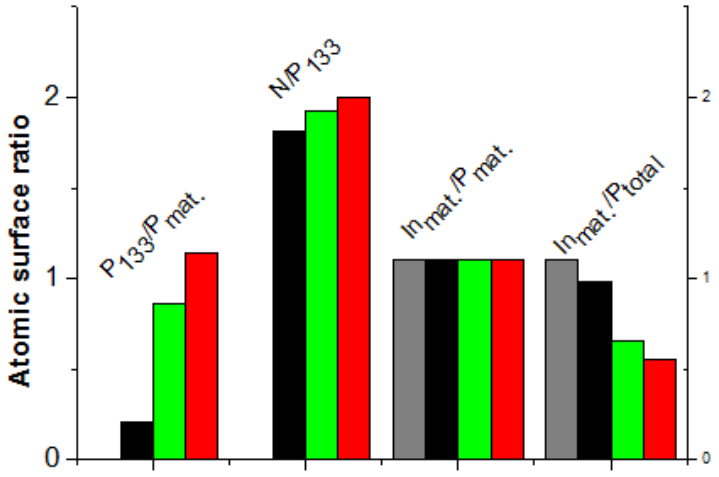

Figure 6.43: Atomic ratios during the film formation derived from XPS binding energy spectrum. Black corresponds to 0.038 $mC.cm^{-2}$), green to 0.21 $mC.cm^{-2}$ and red to 0.4 $mC.cm^{-2}$

The ratio P_{133}/P_{mat} should evolve from 0 to 1 after the film formation. Indeed there is one phosphorus atom in the polyphosphazen monomer for one phosphorus atom in the InP surface. There are two nitrogen atoms for one phosphorus atom in the polyphosphazen, so the ratio N/P_{133} should be around 2 (2 different chemical environments for nitrogen). InP is a binary compound of stoechiometry 1:1, so the atomic ratio In_{mat}/P_{mat} should be one throughout the entire process. Finally the ratio In_{mat}/P_{tot} should evolves from 1 ($P_{tot} = P_{mat}$) to 0.5 (2 P atoms (1 in the polyphosphazen, 1 in InP) against 1 In). The expected ratios meet the experiments which is another evidence of a good film coverage. The fact that we manage to detect without difficulty In and P matrix atoms at the end of the film formation is an other evidence of the extreme thin polyphosphazen thickness.

The atomic ratios have been measured on another sample one year after the chemical treatment: no change has been observed. This passivating technique is stable in time. Yet an important question remains: What is polyphosphazen influence on the surface recombination?

6.3.3.3 Polyphosphazen influence on surface recombination

6.3.3.3.a Luminescence measurements

The first characterization we have think of is the constant wave photoluminescence measurement (CW-PL). The samples (bare n-InP or polyphosphazen-n-InP, $10^{15}\ cm^{-3}$) are illuminated by a 532 nm monochromatic laser. This wavelength has been chosen because it is efficiently absorb by InP. Under illumination, electron-hole pairs are created (photo-carriers) in the SC bulk. The photo-carriers may diffuse in the material, according to the electron and hole mobility (μ_e and μ_h respectively), and will eventually recombine. Recombination may be radiative or not. The surface recombination being non radiative, recording the luminescence of the excited sample provides information on the surface passivation state. Indeed if CW-PL is done on two identical samples (except one is bare, the other has polyphosphazen) and if the luminescence intensity differs, one can conclude that the sample with less luminescence experiences more non radiative recombination which is likely due to a recombining surface.

Bare InP sample has been deoxidized (1 minute in deionized water, 2 minutes in HCl/H_2O (1:5) and 3 minutes rinse) and measured afterward (t=0). Then we have waited 8 hours and proceed to the same measure. The polyphosphazen-sample is also measured at t=0 and t=+8 h. PL is measured with an Horiba-Jobin Yvon LabRam HR apparatus in PL mode (hole size 200 μm, grating 150, objectives X10). This is shown in fig. 6.44

At t=0, the PL control sample peak is more intense ($\approx$ 20%) than the polyphosphazen sample, but after 8 hours, the polyphosphazen signal is unchanged whereas the control sample peak loses 60% intensity. After 8 hours, the polyphosphazen sample is roughly two times more intense than the bar sample. It means that polyphosphazen slightly degrades a clean freshly deoxidized surface (one should keep in mind that InP is the III-V semiconductor with the lowest surface recombination velocity), but stabilizes the surface which otherwise would have been oxidized. Knowing also that polyphosphazen has been demonstrated to be unmodified during one year, it is an excellent way to durably stabilize a InP surface.

In order to be more quantitative, TR-PL measurements have been made on the same samples, 24 hours after CW-PL. Experimental conditions are as follows: Excitation wavelength 450 nm to probe mainly the surface, objective X50 (aperture 0.8), three measurements averaged each

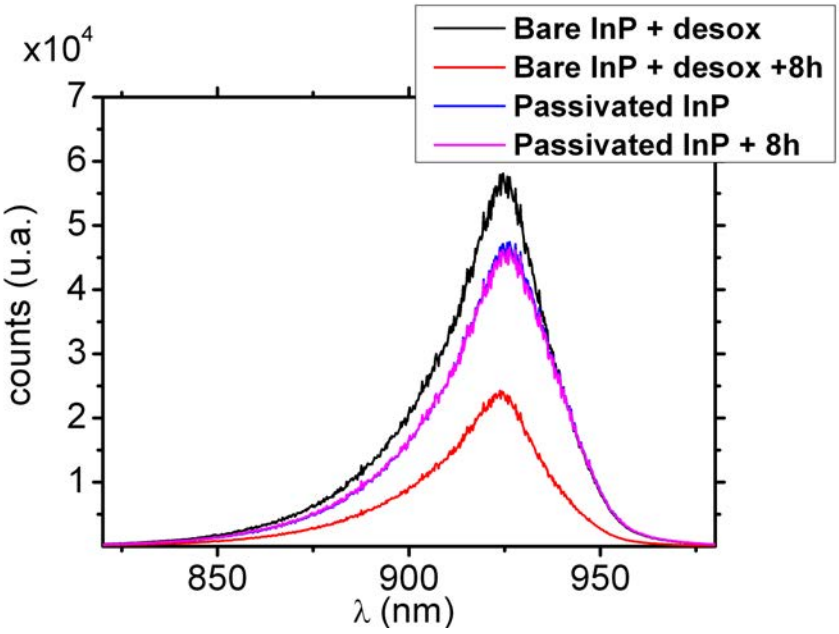

Figure 6.44: CW-PL on bare n-InP and polyphosphazen/n-InP 10^{15} cm^{-3}.

time. We used a Si-base detector and a laser frequency of 10 MHz. Results are shown in fig. 6.45:

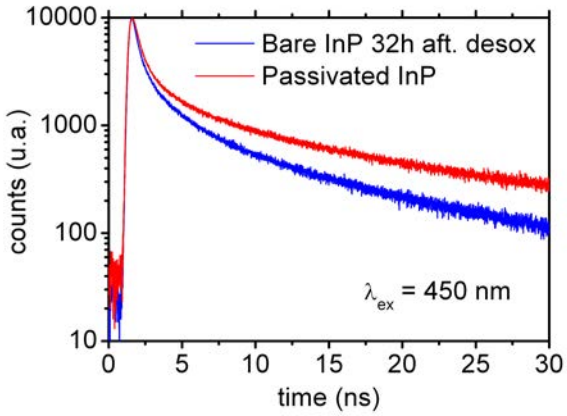

Figure 6.45: TR-PL on bare n-InP and polyphosphazen-n-InP 10^{15} cm^{-3}.

Samples	Lifetimes (ns)	
Bare	0.63	8.57
polyphosphazen	0.73	11.68

Table 6.5: TR-PL lifetimes deduced with a double exponential fit

The lifetimes increase on passivated sample, which is consistent with CW-PL measurements. As already said before, the important information is that polyphosphazen enables to stabilize in time InP surface, which ass the lowest surface recombination velocity of every III-V semiconductors

6.4 Big picture

This chapter gives a proof of concept of a InP-based nano-resonator and the spectral convertor coupling. inspired from the luminescent solar concentrator study, this coupling enables a 3D light concentration with few semiconductor material.

A significant effort has been made in theoretical calculations to quantify this coupling interests. To answer quantitatively this question, we have developed a new numerical tool, hybrid between nanophotonics and geometrical optics. This code allows us to directly model the whole device. We end up with a structure with around 38% optical efficiency in less than 20 nm mean absorber thickness. This is two orders of magnitude lower than thin films technologies, and more importantly this kind of structure should be electrically viable. To our knowledge, this is the first time a photovoltaic device combines both high optical efficiency, low semiconductor material and electrical compatibility. We have also proposed different improvements and analyze in more details unique feature of this device, such as matrix photon recycling. Best structures theoretically found so far may achieve around 68% optical efficiency in less than 45 nm mean InP thickness. 68% optical efficiency can lead to 18.9% conversion efficiency (using the same derivation than in section 3.3.3).

We also tackle fabrication issues in clean room. Elementary fabrication steps are mastered. A sample without the semiconductor etching has been produced

Efforts, divided in two parts, have also been done on the electrical behavior. First we have fabricated nano-diodes and made current-voltage measurements with an atomic probe force microscope. Second we have investigated InP surface passivation with a polyphosphazen polymer film.

Perspectives are numerous. Lot of preliminary tasks have been carried out, but the full device has not been produced yet: this is the number one perspective. Another perspective concerns the nano-resonator design. According our results, the best device should have low refractive index (n) medium surrounding the resonator (larger cross section $\propto \frac{\lambda}{n}$) and a high refractive index at the top surface to increase photon recycling. Transition between the two index should be as smooth as possible to avoid internal Fresnel reflection. Although very challenging to fabricate, this should be the ideal design.

Another perspective is to do 3D devices. In addition to possibly make the device polarization independent, it allows to save more material and increase the lateral concentration factor.

As in part I, the use of a better adapted dye would definitely improve the overall performance. Here, "better" means a dye emission spectrum which matches InP bandgap as well as a thinner bandwidth. A thin resonance bandwidth is important to be able to spectrally concentrate photons on the most efficient resonance.

Finally, one can think to use different resonator with different absorber materials in order to make a multijunction solar cells.

Part II Conclusions

In this part, we have investigated the possibility of optical nano-antennas integration in a luminescent solar concentrator. This new concept has been first imagined to improve the luminescent solar concentrator performance. The idea was to use photovoltaic nanocells array which has an optical absorption cross section larger than its metallurgical area.

To model this new device, a new numerical tool was required in order to take into account simultaneously the spectral convertor (classical optics) and the nano-resonators array (sub-wavelength optics). To meet our needs, we have coupled the Monte Carlo algorithm developed during this thesis to a Maxwell equations solver. We have then modeled different geometries to end up with a device which reached an overall 37.8 % optical efficiency, with a semiconductor material of less than 20 nm per area unit and a geometry which has been designed to get a pin junction and good electrical contact.

Different improvements have also been proposed, to reach almost 67% optical efficiency, which corresponds to 18.9 % conversion efficiency.

This thesis seeking to deal not only with modeling and theory, we have identified the main barriers to overcome to successfully fabricate such a device. All the fabrication steps are individually mastered and fabrication results obtained so far are very encouraging.

Moreover, we also endeavour to anticipate passivating issue. Preliminary current-voltage measurements on individual nanodiodes by conductive probe atomic force microscope suggest that passivation may be important. It is for this reason that an original passivation technique has been investigated. We manage to form a polyphosphazen film on a structured InP substrate. We have shown with photoluminescence measurements that the polyphosphazen slightly reduces the luminescence peak but it manages to stabilize the surface for a duration longer than one year. Knowing that InP is known for its low surface recombination velocity but in the same time is likely to oxidize and therefore may loss its low surface recombination velocity, the use of polyphosphazen is also very promising.

Thus, the mono-resonant concentrator device spadework has been done, which augurs well for the future of this concept.

General conclusions & Perspectives

Main results of this thesis

Throughout this thesis, we studied light concentration on micro/nano solar cell. The first part was dedicated to evaluate the feasibility of concentrate light onto CIGS-based microcells array with a luminescent solar concentrator. Indeed we have seen that photovoltaics plays an ever-growing role in the energy mix and that this dynamic can last in reducing the ratio cost / efficiency. In this regard, thin films technologies (such as CIGS solar cell) combined with light concentration is promising. On one side thin films are low cost solar cells with high throughput while on the other side efficiency can be enhanced and material saved with light concentration. The literature overview has shown that luminescent solar concentrator has the potential to combine high concentration factor, low cost (in avoiding expensive sun tracking system) and good compatibility with micrometer solar cell size.

We have developed a numerical tool to model luminescent solar concentrator working in bottom mounted configuration (solar cells pave the back surface), which is the most suitable configuration for microcells array coupling. Our algorithm was then used to study LSC from a theoretical point of view. The first important result is the contribution to explain the huge difference between theoretical and real devices. LSC appears as extremely dependent of non ideality (as an example photoluminescence quantum yield value of 0.998 instead of 1 halves the concentration factor) and, in a lesser extent, to dye / solar cell mismatch. We also proposed an original way of analyzing LSC with statistical data we call mean basic event occurrence. It enables to have more physical insight on this concentration system and to describe the concentrator with equations involving known LSC parameters and only one unknown variable with a strong physical meaning.

To the best of our knowledge, this is the first attempt of concentration on CIGS-based microcells. Microcells arrays have been successfully coupled to luminescent solar concentrator. The first unoptimized prototype performances were in accordance with our modelling but rather low. Yet the first concentration on CIGS-based microcell array with luminescent solar concentrator have been achieved. With the help of numerical calculation, some improvement routes have been proposed and applied, such as optical micro-pillar coupling between microcell array and luminescent solar concentrator. Our best result has been a concentration factor of 1.21 on an unoptimized prototype and results on an airgap prototype are expected soon.

Both theoretical and experimental results converge to identify a luminescent solar concentrator limits. Photon mean free path must be maximized (which reflects that photon exhibits low loss) while in the same time loss mechanisms are all the more important that the mean free path is high. Additionally, high geometrical gain is mandatory to hope to reach high con-

centration factor but conversely it enhances losses. The part two of this work was the study of an original strategy to bypass this limitation.

We have studied the completely new concept of nanocells array (acting as a photovoltaic cell and as an antenna) coupled to a spectral convertor, which is one of the luminescent solar concentrator feature. This system was called Mono-Resonant Concentration Device. The ideas were double. The absorption cross section being larger than the nanocell area, such a device naturally exhibits a geometrical gain which does not enhance luminescent solar concentrator loss. This is due to an homogenous optical response of the system back surface despite non unity nanocell coverage fraction. The other advantage is that the nanocells array is illuminated by "monochromatic" light (at least by a narrowed solar spectrum due to the dye). This enables to consider mono-resonant systems, which can compete with more classical multi-resonant system.

We have studied Mono-Resonant Concentration Device with a nanostructured epitaxial InP pin junction. It is worth noting that our study is not limited to this material and can be extended to every other existing material. According to our simulations, we obtained a record geometry enabling to reach 37.8 % optical efficiency. Going further, improvements have been proposed, which have lead us to a device of 66.8% optical efficiency and consequently 18.9 % conversion efficiency. These results have been obtained theoretically in taking into consideration loss in the luminescent solar concentrator, the two light polarizations and the angle dependence of the nano-resonators. To find the optimal devices, different geometries (thickness, width, period) have been screened, but substantial efforts have also been made to understand the physics underlying these results.

Experimental approach has not been forgotten. Fabrication was one of the most time-consuming part of this work. Elementary fabrication steps in clean room to create nano-antenna array have been identified and mastered. Despite having demonstrated the technological feasibility, the high number of elementary steps makes the overall fabrication extremely challenging.

In parallel of Mono-Resonant Concentration Device fabrication, we also begin to address InP passivation issue. Individual nanodiodes have been fabricated and electrically characterized, in collaboration with the Laboratoire de Génie Electrique de Paris. Conductive-probe atomic force microscope has been used to obtain current-tension characteristics which suggest possible surface recombination. Nano-structured devices have a larger developed area which accentuates surface recombination. In parternship with the Institut Lavoisier de Versailles, they have successfully formed a mono-atomic polyphosphazen passivating layer. Both constant wave and time-resolved photoluminescence lead to the conclusion that polyphosphazen stabilizes the nanostructured InP surface over at least one year.

Perspectives

Being relatively broad, this work has numerous perspectives. One the first part of this work, the main way of improvement is to work on the dye. Aside from the Stokes shift, the emission spectral width is of a great importance and must be minimized. If used with a photonic band stop, it enables to reduce the PBS reflection spectral range which in turn reduces external loss and increases the proportion of photon absorbed by the dye. Indeed, the spectral range between the solar cell bandgap and the dye absorption tail is not absorbed by the dye and consequently does not contributes to good performances. This spectral range being equal

to the emission spectral range (plus a possible mismatch), narrowing the emission spectral bandwidth is beneficial.

Another perspective is to use fluorescent molecules emitting at higher wavelength (near infrared) while having a high photoluminescence quantum yield. Indeed the ideal bandgap for a monojunction solar is around 900 nm, which should be in accordance with the dye spectral emission.

The first two perspectives were about the dye, which is of great importance although it is not the only improvement track. As discussed in chapter 3, improvement on photonic band stop fabrication may play a major role in improving the LSC (in relation with a thinner dye emission range). Another more prospective track we can mention is non isotropic dye which emits light in preferential directions, where solar cells are located.

Regarding the second part of this work, there are also numerous perspectives. The obvious one is to accomplish the first attempt at combining both nanoantenna array and LSC. We have studied only 2D nano-resonator while 3D systems seem promising, in term of both material consumption and polarization-independence if the structure is symmetric. Beyond the proof of concept, this system may have an industrial potential only if the nano-structuration is the result of a bottom-up approach, possibly inspired from nanowires fabrication.

Résumé en Français

Introduction

Bien que considérée comme nouvelle, l'étude de l'énergie photovoltaïque remonte au tout début du XIX$^{\text{ème}}$ siècle. La première batterie électrochimique est présentée par Volta à Napoléon en 1800, suivi 39 ans plus tard par la découverte de l'effet photovoltaïque à proprement parlé par Becquerel. La première démonstration « mondiale » de l'énergie solaire a lieu dans les années 1860. Un peu plus de 100 ans plus tard aura lieu en 1973 la conférence séminale de l'UNESCO sur le rôle du Soleil comme source d'Energie pour l'Homme. Pratiquement inconnu du grand public il y a à peine 20 ans, le photovoltaïque est devenu un acteur majeur du paysage énergétique mondial.

Déjà rentable dans certaines parties du globe, le photovoltaïque continu à gagner du terrain. Malgré cela, des incertitudes demeurent et des efforts significatifs doivent être fait pour en améliorer l'efficacité, les coûts, la durabilité et l'acceptabilité sociale.

Parmi les pistes envisagées, la concentration de la lumière sur une cellule photovoltaïque (photovoltaïque concentré) a le potentiel de combiner à la fois une meilleure efficacité, un moindre coût et une meilleure durabilité. Par sa nature même, une cellule solaire fonctionnant sous flux concentré est de faible dimension. Plus sa surface est faible, meilleur en sera l'effet de la concentration. Dans ce cadre, cette thèse explore la possibilité de concentrer la lumière solaire sur des cellules photovoltaïques pas plus larges que quelques centaines de microns. L'originalité de ce travail est double. D'une part nous étudions le couplage de deux domaines du photovoltaïque, les microcellules et le concentrateur fluorescent. D'autre part, nous poussons la logique de miniaturisation à l'extrême en proposant un nouveau concept de cellule photovoltaïque, à l'interface entre le concentrateur fluorescent et la nanophotonique.

Cette thèse est organisée en deux parties et six chapitres. Le chapitre 1 place ce travail dans un contexte plus général. Le contexte énergétique, et en particulier photovoltaïque est abordé. Les principes physiques généraux d'une cellule solaire sont exposés ainsi que les techniques de concentration optique.

Le première partie comprend les chapitres 2, 3 et 4. Cette partie est dédiée à l'étude du concentrateur fluorescent et des microcellules. Le chapitre 2 traite de la description d'un concentrateur fluorescent ainsi que la description du code de calcul développé pendant cette thèse. Le chapitre 3 a pour but l'étude fine du concentrateur fluorescent en traitant de la physique sous-jacente au fonctionnement du concentrateur. L'étude théorique des mécanismes de perte est effectuée via le code de calcul décrit au chapitre précédent. Enfin, le chapitre 4 est une contribution expérimentale traitant du couplage microcellule / concentrateur fluorescent. Cette partie

souligne, parmi bien d'autre choses, l'intérêt potentiel de disposer d'un dispositif photovoltaïque présentant une surface efficace d'absorption plus grande que sa surface métallurgique. La deuxième partie aborde cette problématique.

La seconde partie comprend les chapitres 5 et 6. Nous y proposons un nouveau concept de dispositif photovoltaïque tirant avantage des propriétés de la lumière à l'échelle sub-longueur d'onde lui permettant d'agir aussi comme une nano-antenne. Le chapitre 5 illustre le fort intérêt qu'il y aurait à coupler le concentrateur fluorescent à une nano-antenne. Ensuite, les stratégies de piégeage de la lumière sont exposées afin de motiver notre choix d'utiliser une structure de type Metal-Isolant-Metal. Le chapitre 6 décrit comment un tel dispositif est conçu, d'un point de vue à la fois théorique et expérimental. Outre l'aspect modélisation, la fabrication est abordée ainsi que nos réalisations expérimentales.

Nous proposons ici un résumé des résultats marquants de ce travail, l'ensemble des éléments pouvant être trouvés dans la version anglaise du manuscrit.

Le photovoltaïque, une des réponses au défi énergétique

Nous vivons une époque où la prise de conscience de l'influence délétère des activités humaines sur notre environnement est grandissante. En particulier nos sources d'énergie posent question, tant au niveau de leur durabilité que de leur impact environnemental. Par ailleurs, la consommation d'énergie à l'échelle mondiale a atteint plus de 25 PWh en 2012 [3] et ne cesse de croître. Il convient donc d'augmenter notre production d'énergie tout en nuisant le moins possible à l'environnement. C'est dans ce contexte que le photovoltaïque trouve sa place dans le paysage énergétique mondial.

La puissance installée photovoltaïque a atteint 136.7 GW en 2013, contre moins de 0.1 GW en 2000 [5]. Néanmoins, le secteur du photovoltaïque connait une forte restructuration, entrainant la faillite de nombreuses entreprises du secteur, des tarifs d'aide instables etc. D'après l'Agence Internationale de l'Energie (IEA), un des leviers principaux pour redresser le secteur réside dans la baisse des coûts. La concentration optique est une des voies explorées pour répondre à ce défi.

L'intérêt de la concentration est double. Cela permet d'une part d'économiser les matériaux rares et onéreux de la cellule en réduisant sa taille d'un facteur C_{geo} (nommé gain géométrique). Le facteur de concentration C étant le produit du gain géométrique et de l'efficacité optique du système (η_{opt}). Le second intérêt est l'augmentation du rendement d'une cellule solaire avec le facteur de concentration de manière logarithmique. Ce dernier point n'est vrai que si les pertes résistives induites par la concentration sont limitées, ce qui est le cas avec des microcellules [16].

Dans l'optique d'une technologie bas coût, les microcellules seront fabriquées sur des couches minces à base de Cu(In,Ga)Se_2 (CIGS). Il convient donc de trouver un système de concentration qui soit lui aussi à faible coût, et qui en même temps concentre le plus possible. Le concentrateur fluorescent (LSC) est à ce titre un candidat sérieux. D'une part c'est un système non imageant qui ne nécessite pas de focalisation de la lumière, ce qui est d'autant plus difficile que la cellule est petite. D'autre part, le LSC peut, théoriquement, permettre d'atteindre des facteurs de concentration pouvant dépasser X1000 [39].

La première partie, intitulée « Concentration par un concentrateur fluorescent », traite de la viabilité d'un tel système de concentration sur microcellules.

Les bases du concentrateur fluorescent

Le concentrateur fluorescent peut être vu comme une cavité qui piège la lumière jusqu'à ce que celle-ci atteigne une cellule photovoltaïque. Cette cavité est généralement constituée d'une plaque de plastique (PMMA généralement) dopée par un luminophore. Par soucis de simplicité d'implémentation avec des microcellules, nous étudions la configuration dite de « montage arrière », c'est à dire que le réseau de microcellules est placé sur la face arrière du LSC. Ceci est décrit par la figure 1, qui par ailleurs illustre les différents mécanismes de perte à l'œuvre dans un LSC.

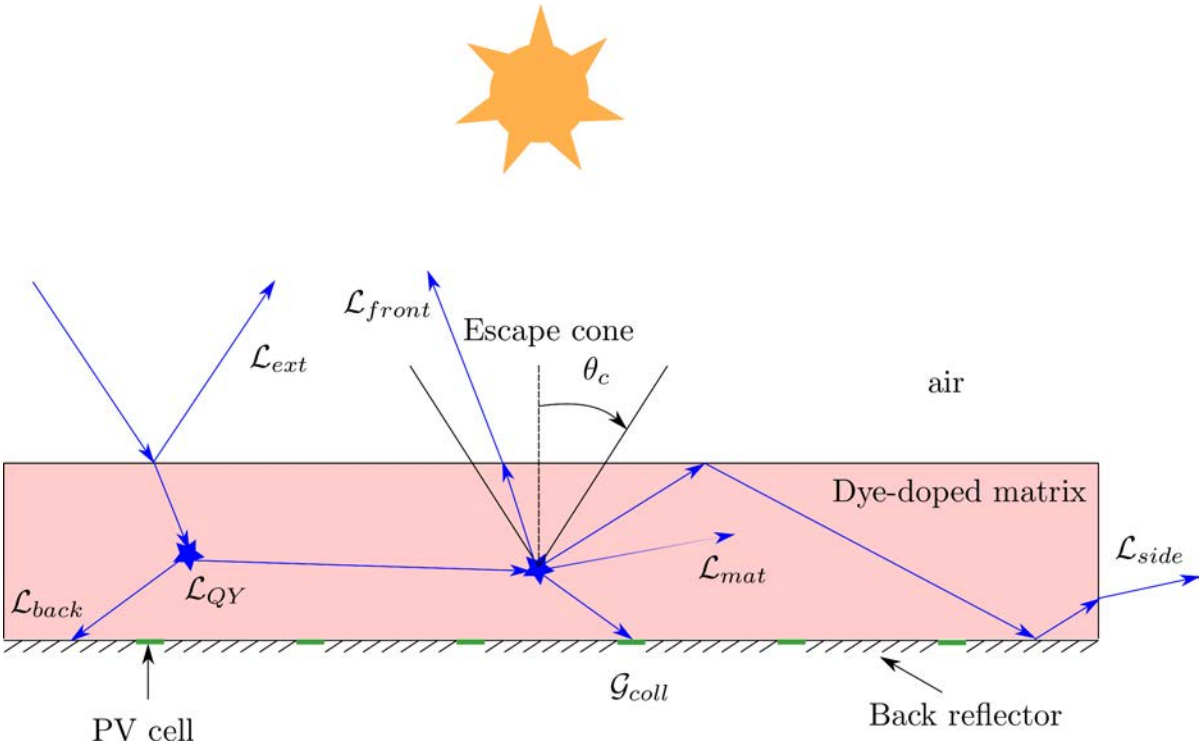

FIGURE 1 – Schéma d'un LSC en configuration « montage arrière » et des mécanismes de pertes associés. Perte externe $\mathcal{L}_{ext}$. Pertes internes : Désexcitation non radiative $\mathcal{L}_{QY}$, non piégeage en face avant $\mathcal{L}_{front}$, Absorption par la matrice hôte $\mathcal{L}_{mat}$, Absorption par le réflecteur arrière $\mathcal{L}_{back}$, Perte latérale $\mathcal{L}_{side}$, Photons collectés $\mathcal{G}_{coll}$.

Idéalement, les bonnes performances d'un LSC résultent d'un bon piégeage latéral ($\mathcal{L}_{side}$) et en face arrière, entre les cellules ($\mathcal{L}_{back}$). Le piégeage en face avant ($\mathcal{L}_{front}$) s'effectuant soit par réflexion interne totale, soit par l'ajout d'un filtre photonique coupe-bande (PBS) qui réfléchit les longueurs d'onde d'émission du colorant. Outre le piégeage, un maximum de lumière doit pouvoir rentrer dans le concentrateur ($\mathcal{L}_{ext}$), la matrice hôte ne doit pas absorber ($\mathcal{L}_{mat}$) et le colorant doit ré-émettre les photons absorbés de manière radiative ($\mathcal{L}_{QY}$).

Dans un LSC, le rôle du colorant est donc double. D'une part il absorbe puis ré-émet la lumière de manière isotrope, permettant la réflexion interne totale en face avant. D'autre part,

la limite de concentration d'un système diffusant, parfois nommée limite de Yablonovitch [99], de $4n^2$ (n étant l'indice de réfraction du milieu considéré) peut être dépassée dans le cas d'un LSC. D'un point de vue thermodynamique, le changement de couleur opéré par le colorant, et donc la perte d'énergie du photon, entraine la création d'entropie qui permet de briser la conservation de l'étendue à l'origine de la limite de Yablonovitch. Dans le cas d'un système à deux niveaux (le photon est absorbé à une énergie ν_1 et émis à une énergie $\nu_2 \leq \nu_1$), la limite thermodynamique du facteur devient proportionnelle à $\exp \frac{h(\nu_1-\nu_2)}{kT}$ [51].

Le code de calcul nommé Vectorized Monte Carlo Algorithm (VMCA) utilisé dans ce travail a été développé au laboratoire tout au long de la thèse. L'algorithme utilisé, codé sur Matlab®, est de type Monte Carlo. Il permet de calculer quelle est la répartition spectrale des photons concentrés et associés aux différents mécanismes de perte. En outre, la mémoire des évènements subis par chaque photon est conservée afin d'obtenir des données statistiques.

Physique des LSC

Un LSC théorique idéal est d'abord étudié afin de déterminer la limite théorique maximale. Ce type d'étude a déjà été fait précédemment mais permet d'une part de tester la validité du code, et aussi sera le point de départ d'une étude plus poussée sur la tolérance aux non idéalités de ce système. La figure 2 décrit le colorant idéal utilisé ainsi que l'efficacité et le facteur de concentration du système idéal.

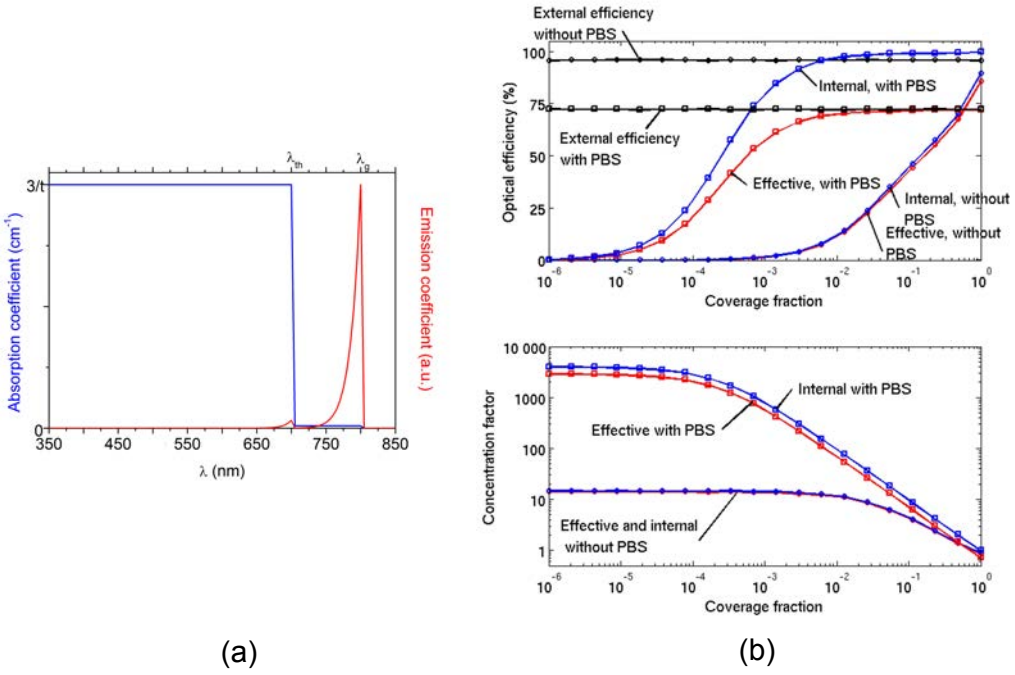

FIGURE 2 – (a) Colorant idéal utilisé. (b) Influence du taux de couverture f ($f = \frac{1}{C_{geo}}$) sur l'efficacité optique (haut) et le facteur de concentration (bas), pour un système idéal, avec ou sans PBS. Les graphes bleus prennent en compte uniquement les pertes internes alors que les rouges les pertes effectives (à la fois interne et externe).

Le facteur de concentration peut atteindre X3000 pour un faible taux de couverture f si un PBS est utilisé. Néanmoins, un système n'étant jamais idéal, il est pertinent de s'interroger

sur sa tolérance aux non-idéalités des paramètres physiques. L'étude a porté sur le coefficient d'absorption de la matrice hôte α_{mat}, les coefficients de réflexion du miroir arrière et du PBS (R_{back} et R_{PBS} respectivement) et le rendement quantique de photoluminescence du colorant $PLQY$. La figure 3 résume les résultats trouvés :

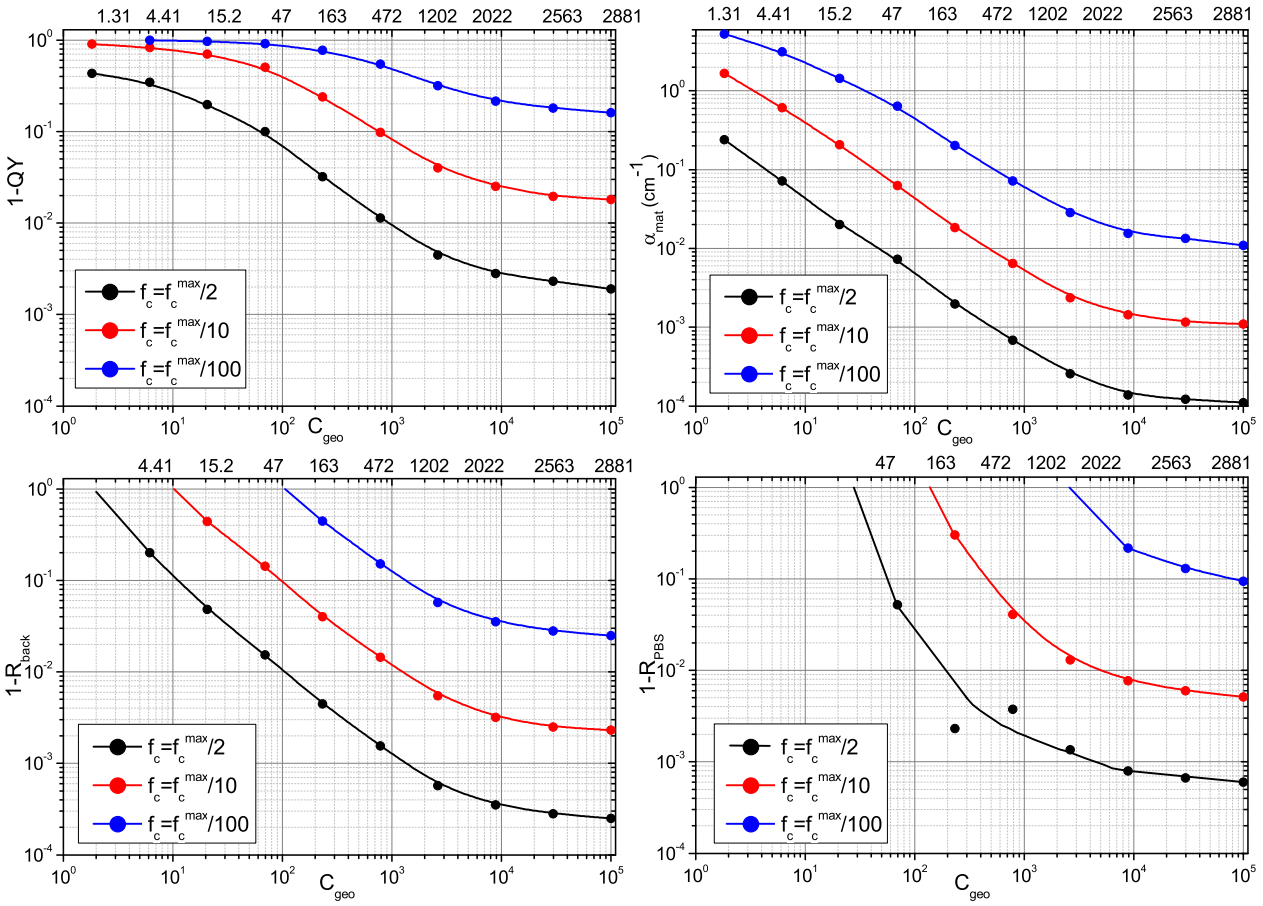

FIGURE 3 – Influence de R_{back}, R_{PBS}, $PLQY$ et α_{mat} sur le facteur de concentration. En ordonnée est affichée l'écart à l'idéalité. L'axe des abscisses supérieur représente le facteur de concentration maximal pour un gain géométrique donné. L'écart à l'idéalité nécessaire pour diviser le facteur de concentration maximal par un facteur 2, 10 ou 100 est donné par les courbes noires, rouges et bleues respectivement

Un facteur de concentration élevé ne peut exister qu'à gain géométrique élevé. Or la sensibilité aux non idéalités est d'autant plus forte que C_{geo} est important. Ainsi, un écart à l'idéalité de l'ordre de 10^{-2} peut entrainer une baisse de 90% du facteur de concentration théorique maximal pour de grands gains géométriques. Cela contribue à expliquer l'écart colossal entre les performances théoriques et les performances expérimentales. C'est aussi la raison qui explique qu'en pratique, les gains géométriques utilisés sont très faibles (< 10). Les augmenter reviendrait à engendrer trop de pertes.

Le désaccord entre le colorant et la bande interdite de la cellule solaire a aussi été étudié de manière théorique, comme montré par l'image 4 :

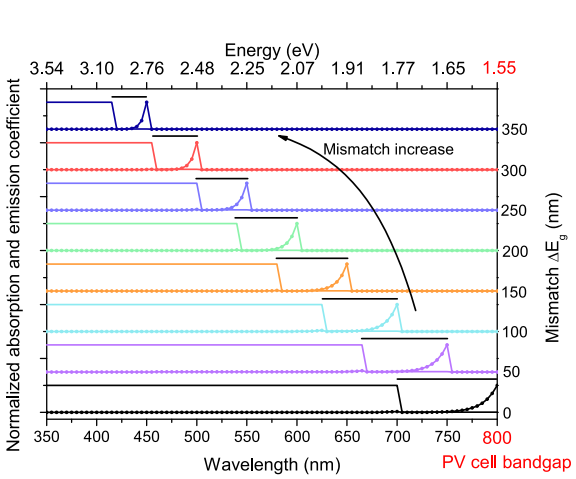

(a) Coefficient d'absorption et d'émission du colorant. Les lignes noires représentent le domaine de réflexion spectral du PBS

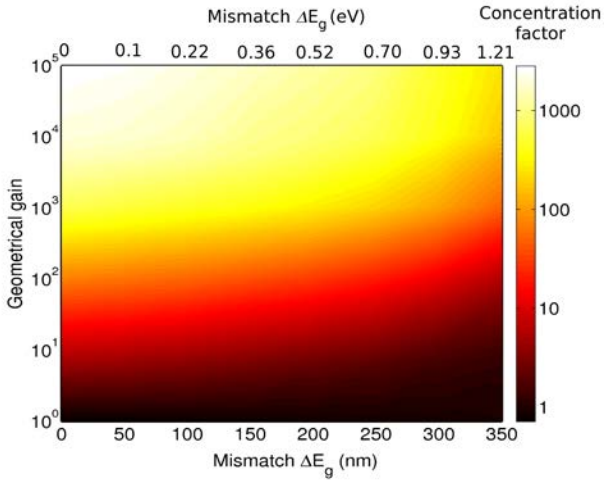

(b) Facteur de concentration en fonction du désaccord colorant/cellule et du gain géométrique.

FIGURE 4 – Effet du désaccord colorant/cellule. Le Stokes Shift est constant et vaut 0.2 eV

Bien que fortement dépendant du gain géométrique, le désaccord colorant/cellule solaire contribue aussi à diminuer fortement le facteur de concentration.

Fort de ces éléments, un système réaliste est enfin simulé. Le colorant idéal est remplacé par un colorant commercial, le PBS idéal est remplacé par un spectre de réflexion d'opale et les autres paramètres tels que le coefficient d'absorption de la matrice, le rendement quantique de luminescence, ou le coefficient de réflexion du miroir arrière ont des valeurs plus réalistes (10^{-3} cm^{-1}, 0.95 et 0.97 respectivement). Les résultats sont donnés dans la figure 5 :

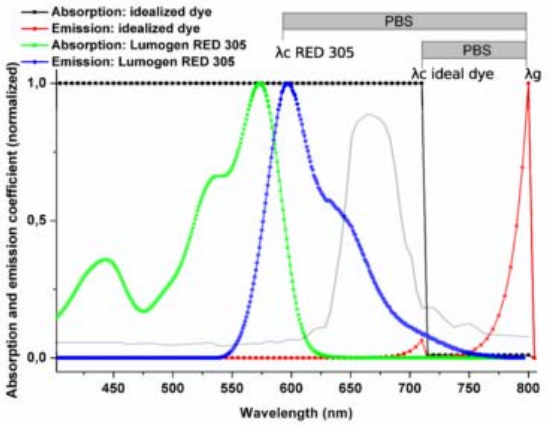

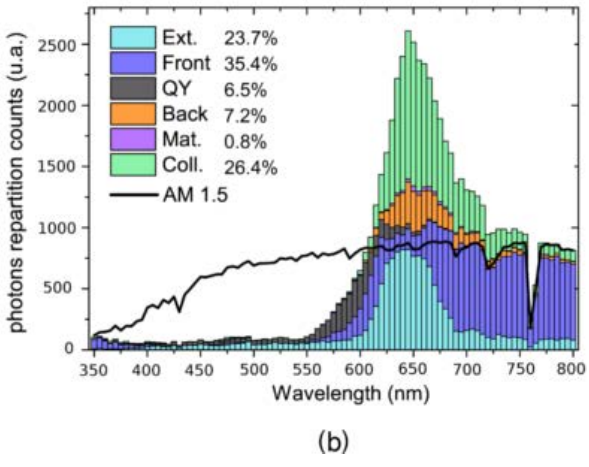

FIGURE 5 – (a) Spectres d'absorption et d'émission du colorant commercial et du colorant idéal (à titre de comparaison). Le spectre de réflexion de l'opale est aussi indiqué en gris. (b) Répartition spectrale des photons selon les différents mécanismes de perte. Le gain géométrique utilisé est de 10.

Le facteur de concentration de 2.64 est bien éloigné des valeurs théoriques dépassant X1000. Bien que non optimisé, cette simulation illustre bien la problématique des LSC et de leur grande dépendance aux non idéalités, qui sont multiples et de forte amplitude dans un système réaliste. Néanmoins, les tendances mises en évidence dans le cas idéal se retrouvent dans un cas plus réaliste, bien que généralement de moins forte amplitude. La sensibilité des LSC aux non-idéalités est fortement réduite aux faibles gains géométriques. Un corollaire important est qu'il n'est pas nécessaire de rechercher des paramètres extrêmement proches de l'idéalité aux faibles gains géométriques compte-tenu du faible bénéfice que cela procurerait.

Microcellules solaires à base de CIGS couplées au concentrateur fluorescent

Nous avons fabriqué des microcellules CIGS à l'aide d'un procédé standard [83, 16]. De même le LSC est fabriqué par polymérisation radicalaire de MMA. Le dopage s'effectue en dissolvant le colorant dans la solution de monomère avant le début de la polymérisation.

La première génération de dispositif consiste à coupler directement le LSC au réseau de microcellules via de l'éthanol, comme le montre la photographie 6 :

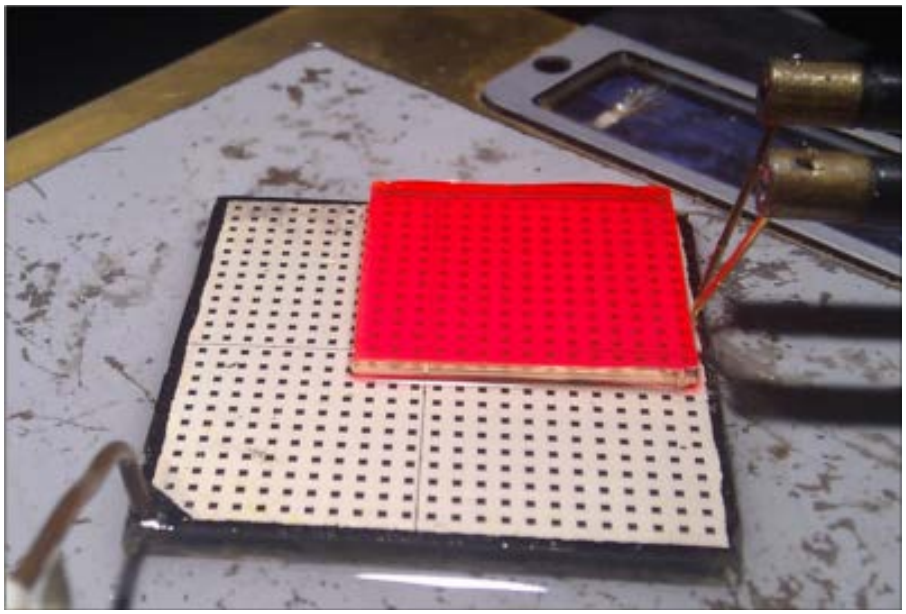

FIGURE 6 – Image d'un réseau de microcellules (610 x 610 μm^2) couplé à un LSC. L'échantillon est mesuré sur un simulateur solaire

Pour un gain géométrique de 7, le facteur de concentration mesuré expérimentalement est faible : C=1.21 (+3.66 $mA.cm^{-2}$). Dans cette configuration non optimisée, le gain provient plutôt de l'effet anti-reflet procuré par le PMMA d'indice 1.5.

La modélisation de ce LSC, en bon accord avec les mesures expérimentales, permet de mettre en évidence différentes pistes d'amélioration. L'augmentation de la surface réduit par exemple les pertes latérales. Le CIGS étant rugueux, l'argent que l'on dépose en guise de réflecteur arrière l'est lui aussi ce qui rend la réflexion diffusive. Nous proposons donc une nouvelle configuration

permettant de créer un gap d'air entre le LSC et le miroir arrière. Ceci ouvre la possibilité d'une réflexion totale interne en face arrière, qui est non seulement spéculaire mais efficace à 100 %. Cette nouvelle configuration est illustrée par le schéma 7 :

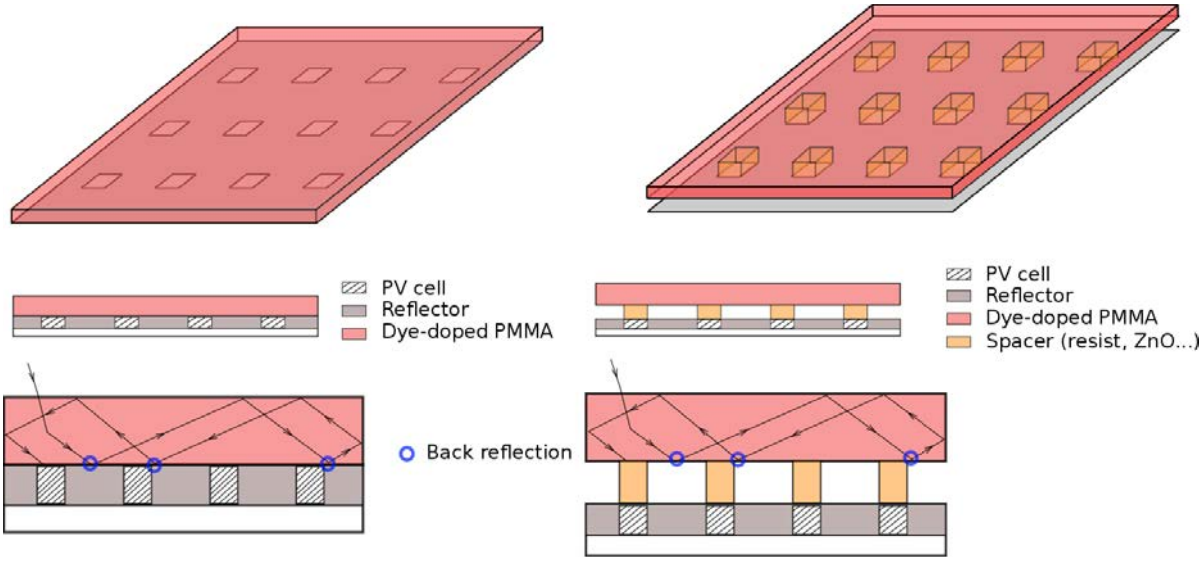

FIGURE 7 – Schéma d'un LSC avec (droite) ou sans (gauche) le gap d'air

Le gap d'air est créé en fabriquant des micropiliers transparents en résine par lithographie UV sur chaque microcellule. L'influence des micropiliers sur le couplage optique est modélisée. Les résultats sont montrés par l'image 8.

Un gain net de courant de court-circuit a été mesuré pour 3 échantillons de gains géométriques 5, 10 et 50 (+24%, +18%, +14% respectivement). Ces résultats sont prometteurs et peuvent être grandement améliorés par une amélioration du procédé de fabrication. En effet, la couche tampon permettant le bon couplage optique entre les piliers et le LSC sèche trop rapidement, ce qui engendre des contraintes mécaniques lors du couplage. En conséquence de quoi de multiples petites craquelures se créent, gênant ainsi la réflexion interne totale et par voie de conséquence les performances finales.

Des travaux préliminaires ont aussi été effectués sur les opales, une des structures qui présentent des propriétés optiques coupe-bande, intéressantes pour créer un PBS. Des nanosphères de silice monodisperses ont été fabriquées pour former une opale, à savoir un empilement cubique-face centré. Un gain de réflexion de 20% à la longueur d'onde de résonance a été mesuré.

Nano-antenne pour applications photovoltaïques

Dans le cas du LSC, l'augmentation du gain géométrique induit nécessairement une perte d'efficacité optique. L'idée de la deuxième partie de ce travail est de s'affranchir de cette limitation. Pour ce faire, il faut quitter l'optique géométrique et exploiter les propriétés de la lumière à l'échelle sub-longueur d'onde. A cette échelle, il est possible de concevoir un dispositif dont la section efficace d'absorption est plus grande que sa surface métallurgique. Dès lors, on voit bien qu'on peut rendre peu dépendant l'efficacité optique du gain géométrique.

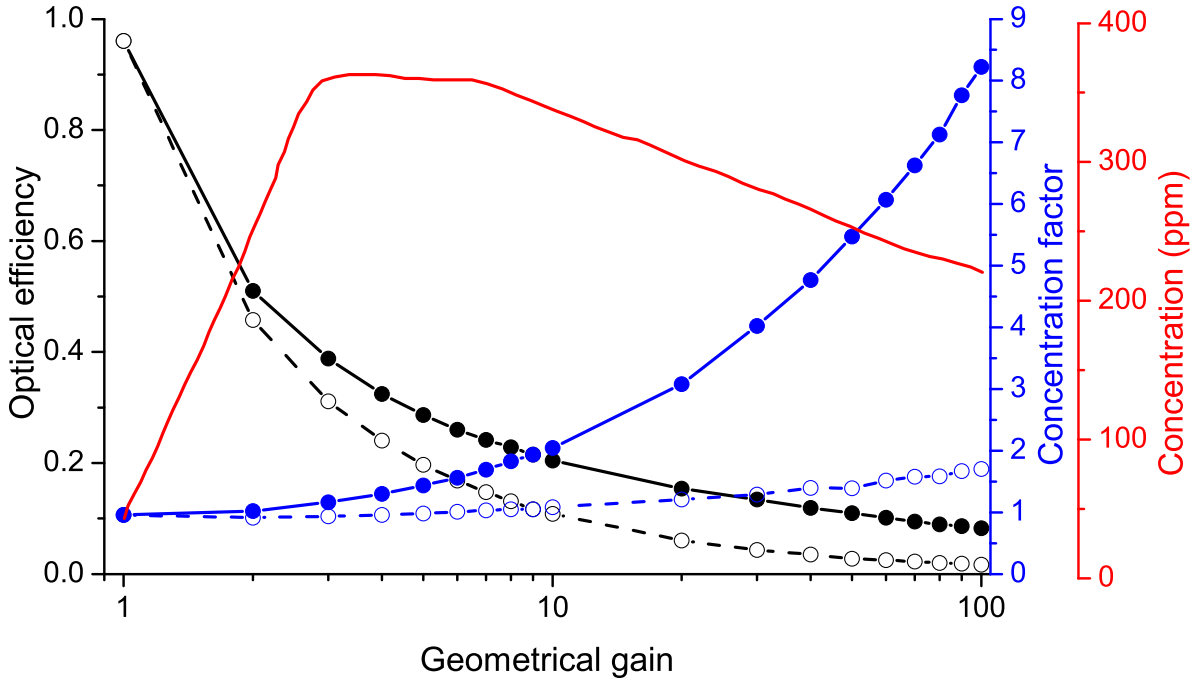

FIGURE 8 – Résultat de simulation d'un LSC avec gap d'air. η_{opt} (noir), le facteur de concentration (bleu) et la concentration optimale en colorant (rouge) sont donnés en fonction de C_{geo}. En traits pleins sont représentés les calculs ne prenant pas en compte les pertes latérales. Les tirets prennent en comptent les pertes latérales pour un échantillon de surface $4 \times 4\ cm^2$

Bien que répondant à notre problématique, les dispositifs exploitant l'optique sub-longueur d'onde présente un inconvénient majeur : leur dimension « nanoscopique ». Se pose alors la question de l'absorption de la lumière dans un faible volume. Ce chapitre donne des éléments sur l'état de l'art du piégeage optique.

Le réflecteur Lambertien est ici à proscrire car il nécessite une rugosité supérieure à la longueur d'onde, ce qui est incompatible avec les dispositifs sub-longueur d'onde. Différentes stratégies sont passées en revue, comme les réseaux, les nanofils, les cristaux photonique, la plasmonique. Nous avons choisi de travailler sur les nano-antennes optiques, basées sur une structure de type Metal-Isolant-Metal (MIM), dans laquelle l'isolant est remplacé par une jonction pin permettant d'apporter l'aspect photovoltaïque à ce résonateur.

Il s'agit donc de designer des nano-antennes photovoltaïques. Ce sont des dispositifs résonants, à savoir qu'ils présentent une grande efficacité d'absorption uniquement à la résonance, qui elle même présente une plage spectrale généralement bien plus faible que le spectre solaire utile. Cela constitue une des fortes originalités de ce travail : au lieu de créer un dispositif présentant de multiples résonances pour absorber efficacement le spectre solaire, nous présentons ici un dispositif présentant une seule résonance utile ; le reste du spectre solaire étant converti par le convertisseur spectral à la longueur d'onde de résonance du résonateur. Le dernier chapitre regroupe tous les résultats, théoriques et expérimentaux à ce sujet.

Dispositif de concentration mono-résonant (MRCD)

Un MRCD se schématise comme suit :

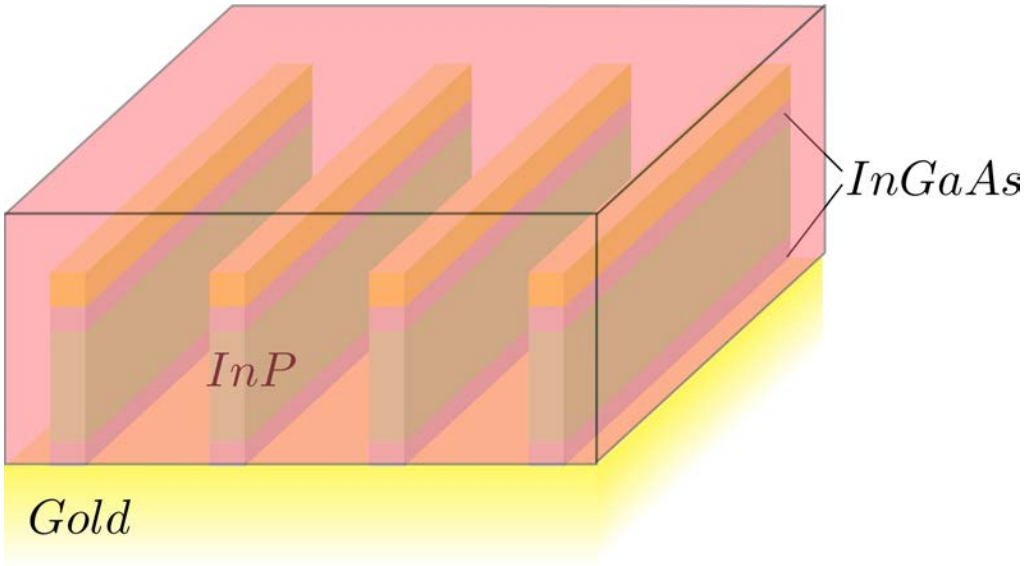

Figure 9 – Schéma d'un dispositif de concentration mono-résonant.

Nous avons cherché les paramètres géométriques permettant d'obtenir le meilleur compromis efficacité optique / volume pour des systèmes 2D (direction y infinie). Pour se faire, nous avons utilisé un code de calcul multi-échelle. La partie optique sub-longueur d'onde est gérée par un code de résolution d'équations de Maxwell (RMCA) alors que la partie optique géométrique dans le convertisseur spectral est gérée par le code utilisé dans la première partie de ce travail. Nous avons d'abord discuté l'approche dite « compréhensive », qui s'est révélée intéressante du point de vue de la compréhension des résonances, mais difficile à utiliser pour trouver la meilleure structure, compte tenu de la complexité de la structure. Nous avons donc utilisé une approche plus statistique, consistant à simuler plusieurs milliers de structures, comme le montre la figure 10

Une efficacité optique de 44% est calculée pour une épaisseur moyenne de 50 nm. Un bon compromis étant le structure permettant d'atteindre 37.8% d'efficacité optique dans moins de 20 nm d'épaisseur moyenne. Ici, le fait de structurer l'échantillon permet d'obtenir des structures avec une épaisseur d'InP suffisamment importante pour faire tenir une jonction pin et donc espérer avoir une bonne séparation des photo-porteurs. De nombreuses pistes d'amélioration sont proposées, comme augmenter l'indice de la matrice en y ajoutant un anti-reflet, ou supprimer les couches de contact en InGaAs qui absorbent de manière non négligeable. La structure qui rassemble ces deux améliorations présente une efficacité optique de 66.8 % pour une épaisseur moyenne inférieure à 50 nm. La figure 11 montre son spectre d'absorption en lumière non polarisée ainsi que la répartition spectrale des photons :

Bien que théorique, ce type de structure présente donc un fort potentiel d'absorption dans des volumes très réduits. Nous avons aussi entrepris la fabrication de ce type de structure.

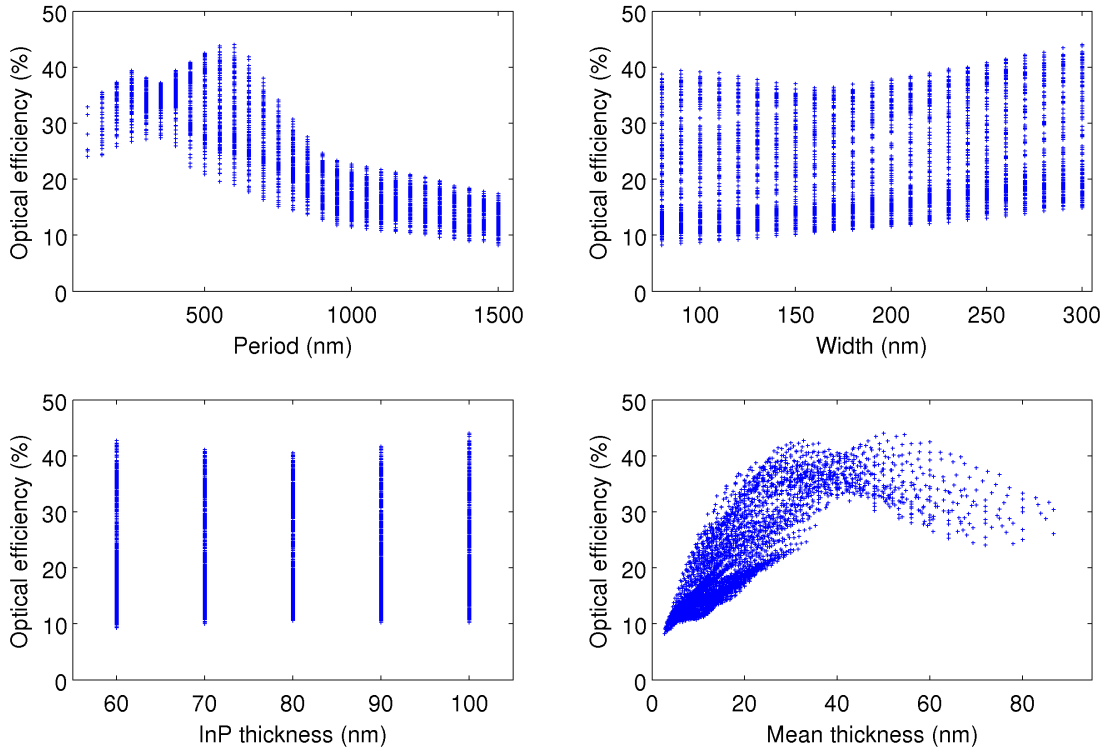

FIGURE 10 – Efficacité optique des nano-antennes en fonction de certains paramètres géométrique (période p, largeur w, épaisseur d'InP t et épaisseur moyenne t_{mean}).

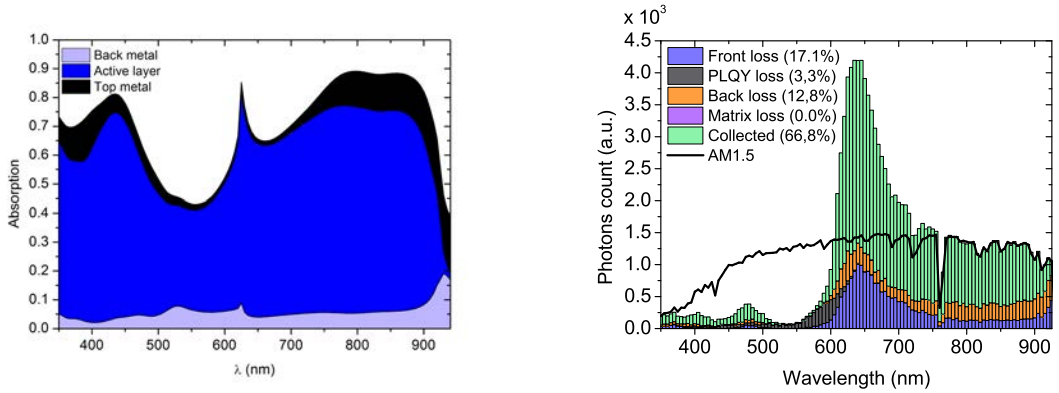

(a) Spectre d'absorption en lumière non polarisée

(b) Performance globale

FIGURE 11 – Résultat d'une structure MRCD ($t_{InP} = 70$ nm, $w = 160$ nm, $p = 250$ nm) sans contact en InGaAs, avec une matrice d'indice de réfraction de 2.5 et avec une couche anti-reflet idéale

Les principales difficultés de fabrication consistent en un report de substrat, une lithographie électronique sur un substrat isolant, et une gravure de semiconducteur avec de très faibles ouvertures. Le procédé de fabrication est maîtrisé, avec encore un effort de développement sur la gravure d'InP à faire pour obtenir une gravure anisotrope sans micro-masquage. L'image suivante illustre un dispositif :

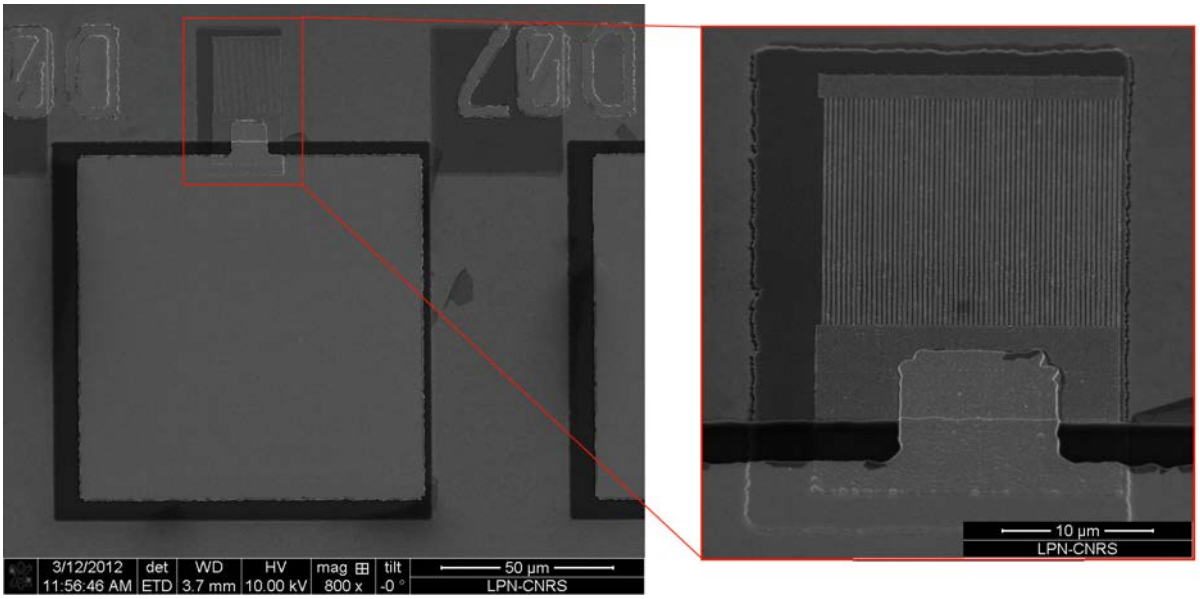

FIGURE 12 – Image MEB d'un réseau de nano-résonateur non gravé. Gauche : vue globale du réseau et du pad électrique. Droite : zoom sur le réseau.

Par ailleurs, des mesures électriques sur des nano-diodes isolées ont été faites par AFM à pointe conductrice. Elles montrent que les recombinaisons non-radiatives de type SRH sont les mécanismes dominants, comme l'illustre la figure 13. Ils sont principalement dus aux défauts créés à la surface de semi-conducteur lors de la gravure.

Cette observation nous a poussé à travailler la passivation de ces défauts. Nous avons donc étudié la formation d'un film de polyphosphazène [150, 151, 152, 153]. Formé par électrochimie ce film stabilise la surface d'un point de vue chimique (sur plus d'une année). Nous avons démontré par XPS que la surface de film était totalement couvrante. Par ailleurs, des mesures de photoluminescence, ont montré que la présence du film réduisait légèrement l'intensité du pic de photoluminescence, mais que celui-ci restait stable, ce qui n'est pas le cas d'une surface d'InP « nue ».

Nous avons donc montré par le calcul qu'un système mono-résonant pouvait être très efficient d'un point de vue optique, et que sa géométrie même était compatible avec la tenue d'une jonction photovoltaïque. Nous avons aussi entrepris sa fabrication et surmonté la plupart des barrières technologiques. En outre, l'aspect passivation a aussi été étudié, avec le polyphosphazène qui stabilise remarquablement la surface.

Conclusion générale

Le dénominateur commun de cette thèse était la concentration sans système de suivi de Soleil. L'aspect concentration spatiale a traité du concentrateur fluorescent couplé à des microcellules en CIGS. Dans ce cadre, un code de calcul a été développé pour étudier ce système d'un point de vue théorique. Il a été montré que le potentiel de concentration est très important, mais que la grande sensibilité aux non-idéalités expliquait l'écart significatif entre théorie et expérience. Cette thèse était l'occasion de quantifier et de hiérarchiser les différents mécanismes de pertes.

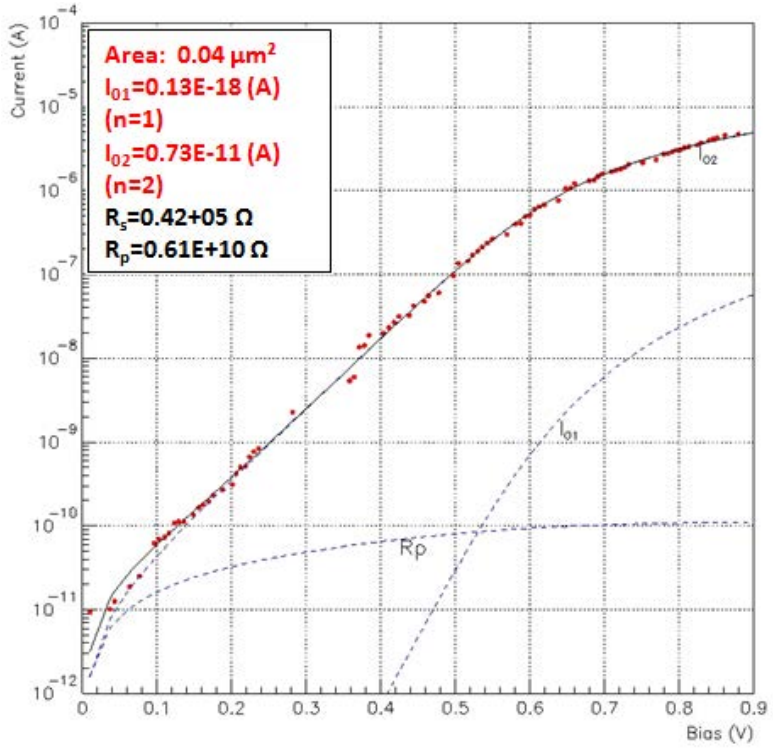

FIGURE 13 – Mesure courant-tension par AFM à pointe conductrice sur une nano-diode de surface $200 \times 200\ nm^2$. Le fit est obtenu par un modèle à deux diodes de facteurs d'idéalité fixés à 1 et 2.

Un formalisme nouveau, basé sur des données statistiques a été développé, reliant les différents mécanismes de pertes à des paramètres physiques « simples ».

Pour la première fois, de la concentration sur microcellules via un LSC a été effectué. Bien que modestes, les résultats obtenus sont très encourageants. Des pistes d'améliorations ont été proposées, et ce grâce à une excellente compréhension des mécanismes de perte issue des simulations numériques. Parmi elles, l'ajout d'un gap d'air ou la création d'opale ont été discutés et des réalisations expérimentales effectuées.

L'idée de conversion spectrale a aussi été appliquée aux nano-antennes optiques. Déjà bien connues pour leur capacité à concentrer la lumière dans une faible épaisseur, nous avons étudié leur couplage à un LSC. L'intérêt était double : d'une part cela permet d'utiliser un résonateur dit mono-résonant (MRCD), et d'autre part la possibilité de recyclage de photons était présente. Concept de rupture, la conversion spectrale a permis de trouver des structures permettant d'absorber efficacement la lumière (37.8%) dans moins de 20 nm d'épaisseur moyenne. Outre l'effort pour expliquer les raisons physiques derrière ce résultat, des pistes d'améliorations ont là aussi été proposés, permettant d'atteindre dans le cas le plus favorable près de 67% d'efficacité optique dans moins de 50 nm d'épaisseur moyenne.

En complément de l'aspect théorique, le procédé de fabrication d'un tel système a été développé. De nombreux verrous technologiques ont été résolus, rendant ce procédé réaliste et réalisable. Enfin, des collaborations nous ont permis d'étudier le comportement d'une nano-diode unique ou de traiter la passivation de l'InP, aspect important pour les propriétés électriques.

Ainsi l'aspect concentration spectral du LSC a pu être conjugué à l'aspect mono-résonant des nano-antennes optiques. De même les concentrations spatiale macroscopique des LSC et nanoscopique des nano-antennes ont été combinées avec succès. L'ensemble formant un concentrateur 3D efficace et prometteur pour une concentration des lumières directes et diffuses sans suivi du Soleil.

Bibliography

[1] A.E. Becquerel. Mémoire sur les effets électriques produits sous l'influence des rayons solaires. *Comptes rendus de l'Académie des Sciences*, 9:561–567, 1839.

[2] IPCC. *Climate Change 2013: The Physical Science Basis.* Cambridge University Press, 2013.

[3] U.S. Energy Information Administration. *Annual Energy Outlook 2014.* 2014.

[4] W. Paltz. Global renewable energy implementation to date. In *Renewable energies in the service of humanity : the current challenges and prospects by 2030 and 2050, avalaible at http://www.celluleenergie.cnrs.fr/spip.php?article174*, 2013.

[5] Global market outlook for photovotlaics 2013-2017, 2013.

[6] Germany: Record 40 percent solar weekend, 2012.

[7] C. Kittel. *Introduction to Solid State Physics, 6th edition.* Wiley, New York, 1986.

[8] H. Schlangenotto, H. Maeder, and W. Gerlach. Temperature dependence of the radiative recombination coefficient in silicon. *phys. stat. sol. (a)*, 21(1):357–367, 1974.

[9] W. Shockley and W. T. Read. Statistics of the recombinations of holes and electrons. *Phys. Rev.*, 87:835, 1952.

[10] R.N. Hall. Electron-hole recombination in germanium. *Phys. Rev.*, 87:387, 1952.

[11] A. Richter et al. Improved quantitative description of auger recombination in crystalline silicon. *Phys. Rev. B*, 86:165202, 2012.

[12] http://rredc.nrel.gov/solar/spectra/am1.5/.

[13] M.A. Green. Solar cell fill factors: General graph and empirical expressions. *Solid-State Electronics*, 24:788 – 789, 1981.

[14] G. Conibeer. Third-generation photovoltaics. *Materials today*, 10(11):42–50, 2007.

[15] http://www.nrel.gov/ncpv/images/efficiency_chart.jpg.

[16] M. Paire et al. Resistive and thermal scale effects for Cu(In, Ga)Se_2 polycrystalline thin film microcells under concentration. *Energy and environmental Science*, 4:1972, 2011.

[17] J. Chaves. *Introduction to Nonimaging Optics.* CRC Press, 2008.

[18] http://re.jrc.ec.europa.eu/pvgis/apps4/pvest.php.

[19] G. Zubi, J. L. Bernal-Agustın, and G. V. Fracastoro. High concentration photovoltaic systems applying III–V cells. *Renewable and Sustainable Energy Reviews*, 13:2645–2652, 2009.

[20] A. Lo and J. Arenberg. New architecture for space telescopes uses Fresnel lenses. *SPIE Newsroom*, 2006.

[21] E. M. Kritchman, A. A. Friesem, and G. Yekutieli. Highly concentrating Fresnel lenses. *Applied Optics*, 18(15):2688–2695, 1979.

[22] Photon international. market survey on concentrating PV, Nov. 2008, p.146.

[23] http://www.semprius.com/the-semprius-difference/cpv-technology.html.

[24] P.K. Sen, K. Ashutosh, K. Bhuwanesh, Z. Engineer, S. Hegde, and S. P. Daviesa. Linear fresnel mirror solar concentrator with tracking. *Procedia Engineering*, 56:613–618, 2013.

[25] http://www.generation-tv.com/portfolio/axiosun-numerisun/.

[26] SiliconCPV. Si-con^{tm} 120x medium concentration pv. Technical report.

[27] T Uematsu et al. Static concentrator photovoltaic module with prism array. *Solar Energy Materials and Solar Cells*, 67(1–4):415 – 423, 2001.

[28] G.R Whitfield, R.W Bentley, C.K Weatherby, A.C Hunt, H.-D Mohring, F.H Klotz, P Keuber, J.C Miñano, and E Alarte-Garvi. The development and testing of small concentrating PV systems. *Solar Energy*, 67(1–3):23 – 34, 1999.

[29] M. Morimoto and T. Maruyama. Static solar concentrator with vertical flat plate photovoltaic cells and switchable white/transparent bottom plate. *Solar Energy Materials and Solar Cells*, 87(1–4):299 – 309, 2005.

[30] W.H. Weber and J. Lambe. Luminescent greehouse collector for solar-radiation. *Applied Optics*, 15(10):2299–2300, 1976.

[31] A. Goetzberger and W. Greubel. Solar-energy conversion with fluorescent collectors. *Applied Physics*, 14(2):123–139, 1977.

[32] J.S. Batchelder, A.H. Zewail, and T. Cole. Luminescent solar concentrators. 1: Theory of operation and techniques for performance evaluation. *Applied Optics*, 18(18):3090–3110, 1979.

[33] P.P.C. Verbunt, C. Sanchez-Somolinos, D.J. Broer, and M.G. Debije. Anisotropic light emissions in luminescent solar concentrators–isotropic systems. *Optics Express*, 21(9):A485–A493, 2013.

[34] L. Pronneke, G.C. Glaser, and U. Rau. Simulations of geometry effects and loss mechanisms affecting the photon collection in photovoltaic fluorescent collectors. *EPJ Photovoltaics*, 3, 2012.

[35] K. Rurack and M. Spieles. Fluorescence quantum yields of a series of red and near-infrared dyes emitting at 600-1000 nm. *Analytical Chimistry*, 83(4):1232–1242, 2011.

[36] A. Zastrow. Physics and applications of fluorescent concentrators: a review. In *Optical Materials Technology for Energy Efficiency and Solar Energy Conversion XIII*, pages 534–547. International Society for Optics and Photonics, 1994.

[37] W.R.L. Thomas, J.M. Drake, and M.L. Lesiecki. Light transport in planar luminescent solar concentrators - the role of matrix losses. *Applied Optics*, 22(21):3440–3450, 1983.

[38] H Langhals, O Krotz, K Polborn, and P Mayer. A novel fluorescent dye with strong, anisotropic solid-state fluorescence, small stokes shift, and high photostability. *Angewandte Chemie-International Edition*, 44(16):2427–2428, 2005.

[39] U. Rau, F. Einsele, and G.C. Glaeser. Efficiency limits of photovoltaic fluorescent collectors. *Applied Physics Letters*, 87(17), 2005.

[40] E. Yablonovitch. Inhibited spontaneous emission in solid-state physics and electronics. *Physical Review Letters*, 58(20):2059–2062, 1987.

[41] J. Sajeev. Strong localization of photons certain disordered dielectric superlattices. *Physical Review Letters*, 58(23):2486–2489, 1987.

[42] J.D. Joannopoulos, S.G. Johnson, J.N. Winn, and R.D. Meade. *Photonic Crystals Molding the Flow of Light (second edition)*. Princeton University Press, 2008.

[43] B. G. Bovard. Rugate filter theory: an overview. *Applied Optics*, 32(28):5427–5442, 1993.

[44] J.C. Goldschmidt et al. Increasing the efficiency of fluorescent concentrator systems. *Solar Energy Materials and Solar Cells*, 93(2):176–182, 2009.

[45] J. Gutmann, J. Posdziech, M. Peters, B. Blaesi, L. Steidl, R. Zentel, H. Zappe, and J.C. Goldschmidt. Emission of rhodamine b in pmma opals for luminescent solar concentrators. In *SPIE Proceedings*, volume 8438, 2012.

[46] I. M. Peters. *Photonic concepts for solar cells*. PhD thesis, Faculty of mathematics Albert-Ludwigs-University Freiburg im Breisgau, 2009.

[47] P. Kittidachachan, L. Danos, T.J.J. Meyer, N. Alderman, and T. Markvart. Photon collection efficiency of fluorescent solar collectors. *Chimia*, 61(12):780–786, 2007.

[48] P. P. C. Verbunt et al. Controlling light emission in luminescent solar concentrators through use of dye molecules aligned in a planar manner by liquid crystals. *Advanced Functional Materials*, 19:2714–2719, 2009.

[49] C. L. Mulder et al. Dye alignment in luminescent solar concentrators: II. horizontal alignment for energy harvesting in linear polarizers. *Optics Express*, 18, 2010.

[50] S. McDowall, T. Butler, E. Bain, K. Scharnhorst, and D. Patrick. Comprehensive analysis of escape-cone losses from luminescent waveguides. *Applied Optics*, 52(6):1230–1239, 2013.

[51] Eli Yablonovitch. Thermodynamics of the fluorescent planar concentrator. *Journal of Optical Society of America*, 70(11):1362–1363, 1980.

[52] P.S. Friedman. Progress on the development of luminescent solar concentrators. *Proc. SPIE*, 248:98–104, 1980.

[53] V. Wittwer, W. Stahl, and A. Goetzberger. Fluorescent planar concentrators. *Sol. Energy Mater.*, 11(3):187–197, 1984.

[54] L. H. Slooff, E. E. Bende, A. R. Burgers, T. Budel, M. Pravettoni, R. P. Kenny, E. D. Dunlop, and A. Buechtemann. A luminescent solar concentrator with 7.1% power conversion efficiency. *PHYSICA STATUS SOLIDI-RAPID RESEARCH LETTERS*, 2(6):257–259, DEC 2008.

[55] L. Desmet, A.J M. Ras, D.K.G. de Boer, and M.G. Debije. Monocrystalline silicon photovoltaic luminescent solar concentrator with 4.2% power conversion efficiency. *Optics Letters*, 37(15):3087–3089, 2012.

[56] K. Barnham, J. L. Marques, J. Hassard, and P. O'Brien. Quantum-dot concentrator and thermodynamic model for the global redshift. *Applied Physics Letters*, 76:1197, 2000.

[57] A. Schuler, M. Python, M. Valle del Olmo, and E. de Chambrier. Quantum dot containing nanocomposite thin films for photoluminescent solar concentrators. *Solar Energy*, 81(9):1159 – 1165, 2007.

[58] S.M. Reda. Synthesis and optical properties of CdS quantum dots embedded in silica matrix thin films and their applications as luminescent solar concentrators. *Acta Materialia*, 56(2):259 – 264, 2008.

[59] S.J. Gallagher, B. Norton, and P.C. Eames. Quantum dot solar concentrators: Electrical conversion efficiencies and comparative concentrating factors of fabricated devices. *Solar Energy*, 81(6):813 – 821, 2007.

[60] J. Bomm et al. Fabrication and full characterization of state-of-the-art quantum dot luminescent solar concentrators. *Solar Energy Materials and Solar Cells*, 95(8, SI):2087–2094, 2011.

[61] R. Koole et al. On the incorporation mechanism of hydrophobic quantum dots in silica spheres by a reverse microemulsion method. *Chem. Mater.*, 20:2503–2512, 2008.

[62] M. G Hyldahl, S. T. Bailey, and B. P. Wittmershaus. Photo-stability and performance of CdSe/ZnS quantum dots in luminescent solar concentrators. *Solar Energy*, 83:566–573, 2009.

[63] U. Aeberhard, R. Vaxenburg, E. Lifshitz, and S. Tomic. Fluorescence of colloidal PbSe/PbS QDs in NIR luminescent solar concentrators. *Physical Chemistry Chemical Physics*, 14(47):16223–16228, 2012.

[64] F. Meinardi et al. Large-area luminescent solar concentrators based on "stokes-shift-engineered" nanocrystals in a mass-polymerized PMMA matrix. *Nature Photonics*, 8:392–399, 2014.

[65] M.G. Debije and P.P.C. Verbunt. Thirty years of luminescent solar concentrator research : Solar energy for the built environment. *Advanced Energy Materials*, 2012.

[66] W. van Sark. Luminescent solar concentrators - a low cost photovoltaics alternative. *Renewable Energy*, 49(SI):207–210, 2013.

[67] D.J. Farrell and M. Yoshida. Operating regimes for second generation luminescent solar concentrators. *Progress in Photovoltaics*, 20(1):93–99, J 2012.

[68] A. J. Chatten, K. W. J. Barnham, B. F. Buxton, N. J. Ekins-Daukes, and M. A. Malik. Quantum dot solar concentrators. *Semiconductors*, 38(8):909–917, 2004.

[69] A.J. Chatten et al. Thermodynamic modelling of luminescent solar concentrators. *Proceedings 31st IEEE Photovoltaic Specialists Conference and Exhibition*, 2005.

[70] M Kennedy et al. Thermodynamic modelling and ray-trace modelling of luminescent solar concentrators: a comparison of the two approaches. *EMRS proceedings*, 2008.

[71] J. Gutmann, M. Peters, B. Blaesi, M. Hermle, A. Gombert, H. Zappe, and J.C. Goldschmidt. Electromagnetic simulations of a photonic luminescent solar concentrator. *Optics Express*, 20(6):A157–A167, 2012.

[72] T. Rist, M. Hermle, and C. Goldschmidt. Monte Carlo simulation of complex fluorescent concentrator systems. *Proc. 26th EUPVSEC*, 2011.

[73] M. Carrascosa, S. Unamuno, and F. Agullolopez. Monte-Carlo simulation of the performance of PMMA luminescent solar collectors. *Applied Optics*, 22(20):3236–3241, 1983.

[74] S.W. Leow, C. Corrado, M. Osborn, M. Isaacson, G. Alers, and S.A. Carter. Analyzing luminescent solar concentrators with front-facing photovoltaic cells using weighted monte-Carlo ray tracing. *Journal of Applied Physics*, 113(21), 2013.

[75] G.C. Glaeser and U. Rau. Collection and conversion properties of photovoltaic fluorescent collectors with photonic band stop filters. *Proc. SPIE*, 6197, 2006.

[76] P Wurfel. The chemical potential of radiation. *Journal of Physics C: Solid State Physics*, 15(18):3967, 1982.

[77] Marius Peters, Jan Christoph Goldschmidt, Thomas Kirchartz, and Benedikt Blasi. The photonic light trap—improved light trapping in solar cells by angularly selective filters. *Solar Energy Materials & Solar Cells*, 93:1721–1727, 2009.

[78] E. Yablonovitch. Statistical ray optics. *J. Opt. Soc. Am.*, 72(7):899–907, 1981.

[79] Marius Peters et al. Spectrally-selective photonic structures for PV applications. *Energies*, 3:171–193, 2010.

[80] B. Furman et al. A high concentration photovoltaic module utilizing micro-transfer printing and surface mount technology. *Photovoltaic Specialists Conference (PVSC), 35th IEEE*, pages 000475 – 000480, 2010.

[81] R. Bukovnik et al. A micro transfert printed high efficiency flexible photovotlaic panel. *Photovoltaic Specialists Conference (PVSC) 37th IEEE*, pages 001543 – 001547, 2011.

[82] K. Ghosal, S. Burroughs, K. Heuser, D. Setz, and E. Garralaga-Rojas. Performance results from micro-cell based high concentration photovoltaic research development and demonstration systems. *Progress in Photovoltaics*, 21:1370–1376, 2010.

[83] M. Paire. *Cellules solaires à haut rendement en base dimensionnalité à base de matériaux chalcopyrites Cu(In,Ga)Se$_2$*. PhD thesis, Universite Pierre et Marie Curie (Paris VI), 2012.

[84] T. Klinkert, M. Jubault, F. Donsanti, and J.F. Guillemoles D. Lincot. Differential in-depth characterization of co-evaporated Cu(In,Ga)Se$_2$ thin films for solar cell applications. *Thin Solid Films*, 558:47–53, 2014.

[85] T. Klinkert, M. Jubault, F. Donsanti, D. Lincot, and J.F. Guillemoles. Ga gradients in Cu(In,Ga)Se_2: Formation, characterization, and consequences. *Journal of Renewable and Sustainable Energy*, 6:011403, 2014.

[86] N. Naghavi et al. Buffer layers and transparent conducting oxides for chalcopyrite Cu(In,Ga)(S,Se)$_2$ based thin film photovoltaics: present status and current developments. *Progress in Photovoltaics*, 18:411–433, 2010.

[87] G. Odian. *Principles of Polymerization (4th ed.)*. Wiley-Interscience, 2004.

[88] R. O. Ebewele. *Polymer Science and Technology*. CRC Press, 2000.

[89] L. R. Wilson. *Luminescent Solar Concentrators: A Study of Optical Properties, Re-absorption and Device Optimisation*. PhD thesis, Department of Mechanical Engineering School of Engineering & Physical Sciences Heriot-Watt University, 2010.

[90] Microchemicals. AZ nLOF 20xx negative resist. Technical report, AZ nLOF 20xx Negative Resist, 2005.

[91] W. Stöber, A. Fink, and E. Bohn. Controlled growth of monodisperse silica spheres in the micron size range. *J. Colloid and Interface Science*, 26:62, 1968.

[92] D.A.S. Razo et al. A version of stöber synthesis enabling the facile prediction of silica nanospheres size for the fabrication of opal photonic crystals. *J. Nanopart. Res.*, 10(7):1225, 2008.

[93] G. H. Bogush, M. A. Tracy, and C.F. Zukoski. Preparation of monnodisperse silica particles: control of size and mass fraction. *J. Non-Crystalline Solids*, 104:95, 1988.

[94] J. H. Zhang, P. Zhan, Z. L. Wang, W. Y. Zhang, and N. B. Ming. Preparation of monodisperse silica particles with controllable size and shape. *J. Mater. Res.*, 18(3):649, 2003.

[95] F. Pardo, P. Bouchon, R. Haïdar, and J.-L. Pelouard. Light funneling mechanism explained by magnetoelectric interference. *Physical Review Letters*, 107:093902, 2011.

[96] I. Massiot et al. Nanopatterned front contact for broadband absorption in ultra-thin amorphous silicon solar cells. *Applied Physics Letters*, 101:163901, 2012.

[97] I. Massiot et al. Multi-resonant absorption in ultra-thin silicon solar cells with metallic nanowires. *Optics Express*, 21(9):A372–A381, 2013.

[98] Peter Bermel, Chiyan Luo, Lirong Zeng, Lionel C. Kimerling, and John D. Joannopoulos. Improving thin-film crystalline silicon solar cell efficiencies with photonic crystals. *Optics Express*, 15(25):16986–17000, 2007.

[99] E. Yablonovitch and G.D. Cody. Intensity enhancement in textured optical sheets for solar cells. *IEEE Trans. Electron Devices*, 29:300, 1982.

[100] A. Goetzberger. Optical confinement in thin si solar cells by diffuse back reflectors. In *Proceedings of the 15th IEEE Photovoltaic Specialist Conference*, 1981.

[101] W. van Sark et al. Luminescent solar concentrators - a review of recent results. *Optics Express*, 16(26):21773–21792, 2008.

[102] Mukul Agrawal and Peter Peumans. Broadband optical absorption enhancement through coherent light trapping in thin-film photovoltaic cells. *Optics Express*, 16(8):5385–5396, 2008.

[103] Sven Ruehle, Shlomit Greenwald, Elad Koren, and Arie Zaban. Optical waveguide enhanced photovoltaics. *Optics Express*, 16(26):21801–21806, 2008.

[104] S. Mokkapati and K. R. Catchpole. Nanophotonic light trapping in solar cells. *Journal of Applied Physics*, 112(10), 2012.

[105] Siu-Fung Leung et al. Efficient photon capturing with ordered three-dimensional nanowell arrays. *Nano Letters*, 12, 2012.

[106] Jia Zhu, Ching-Mei Hsu, Zongfu Yu, Shanhui Fan, and Yi Cui. Nanodome solar cells with efficient light management and self-cleaning. *Nano Letters*, 10(6):1979–1984, 2010.

[107] R.M. De La Rue and C. Seassal. Photonic crystal devices: some basics and selected topics. *Laser & Photonics Reviews*, 6:564–587, 2012.

[108] Alongkarn Chutinan, Nazir P. Kherani, and Stefan Zukotynski. High-efficiency photonic crystal solar cell architecture. *Optics Express*, 17(11):8871–8878, 2009.

[109] V. Depauw et al. Micrometer-thin crystalline-silicon solar cells integrating numerically optimized 2-d photonic crystals. *IEEE Journal of Photovoltaics*, 4:215 – 223, 2014.

[110] R. Peretti et al. Modal approach for tailoring the absorption in a photonic crystal membrane. *Journal of Applied Physics*, 111, 2012.

[111] Erik Garnett and Peidong Yang. Light trapping in silicon nanowire solar cells. *Nano Letters*, 10(3):1082–1087, 2010.

[112] J. Wallentin et al. InP nanowire array solar cells achieving 13.8% efficiency by exceeding the ray optics limit. *Science*, 339:1057–1060, 2013.

[113] B.C.P. Sturmberg et al. Modal analysis of enhanced absorption in silicon nanowire arrays. *Optics Express*, 19(19):A1067–A1081, 2011.

[114] B.C.P. Sturmberg et al. Absorption enhancing proximity effects in aperiodic nanowire arrays. *Optics Express*, 21(22):A964–A969, 2013.

[115] M. Foldyna, L. Yu, S. Misra, and P. Roca i Cabarrocas. Using nanowires to enhance light trapping in solar cells. *SPIE Newsroom*, 2013.

[116] Kui-Qing Peng and Shuit-Tong Lee. Silicon nanowires for photovoltaic solar energy conversion. *Advanced Materials*, 23(2):198–215, 2011.

[117] Jan Kupec, Ralph L. Stoop, and Bernd Witzigmann. Light absorption and emission in nanowire array solar cells. *Optics Express*, 18(26):27589–27605, 2010.

[118] M. Law, L. E. Greene, J. C. Johnson, R. Saykally, and P. Yang. Nanowire dye-sensitized solar cells. *Nature materials*, 4:455–459, 2005.

[119] Jon A. Schuller et al. Plasmonics for extreme light concentration and manipulation. *Nature Materials*, 9(3):193–204, 2010.

[120] M.I. Stockman. Nanoplasmonics: past, present, and glimpse into future. *Optics Express*, 19(22):22029–22106, 2011.

[121] Harry A. Atwater and Albert Polman. Plasmonics for improved photovoltaic devices. *Nature Materials*, 9(3):205–213, 2010.

[122] S. Pillai and M. A. Green. Plasmonics for photovoltaic applications. *Solar Energy Materials and Solar Cells*, 94(9, SI):1481–1486, 2010.

[123] O. Stenzel, A. Stendal, K. Voigtsberger, and C. Vonborczyskowski. Enhancement of the photovoltaic conversion efficiency of copper phthalocyanine thin-film devices by incorporation of metal-clusters. *Solar Energy Materials and Solar Cells*, 37(3-4):337–348, 1995.

[124] T. Kume, S. Hayashi, H. Ohkuma, and K. Yamamoto. Enhancement of photoelectric conversion efficiency in copper phthalocyanine solar cell: white light excitation of surface plasmon polaritons. *Jpn. J. Appl. Phys*, 34:6448–6451, 1995.

[125] H.R. Stuart and D.G. Hall. Enhanced dipole-dipole interaction between elementary radiators near a surface. *Physical Review Letters*, 80(25):5663–5666, 1998.

[126] H. R. Stuart and D. G. Hall. Absorption enhancement in silicononinsulator waveguides using metal island films. *Applied Physics Letters*, 69:2327, 1996.

[127] Ragip A. Pala, Justin White, Edward Barnard, John Liu, and Mark L. Brongersma. Design of plasmonic thin-film solar cells with broadband absorption enhancements. *Advanced Materials*, 21(34):3504, 2009.

[128] Doo-Hyun Ko et al. Light-trapping nano-structures in organic photovoltaic cells. *Journal Of Material Chemistry*, 21(41):16293–16303, 2011.

[129] B.P. Rand, P. Peumans, and S.R. Forrest. Long-range absorption enhancement in organic tandem thin-film solar cells containing silver nanoclusters. *Journal of Applied Physics*, 96(12):7519–7526, 2004.

[130] D. Rourke, S. Ahn, D. Lu, J. v. de Lagemaat, N. Kopidakus, and W. Park. Combined optical and electrical modeling of plasmon-enhanced organic photovoltaic devices. *Renewable Energy and the Environment Congress*, 2013.

[131] Nathan C. Lindquist, Wade A. Luhman, Sang-Hyun Oh, and Russell J. Holmes. Plasmonic nanocavity arrays for enhanced efficiency in organic photovoltaic cells. *Applied Physics Letters*, 93(12), 2008.

[132] R. B. Konda et al. Surface plasmon excitation via Au nanoparticles in n-CdSe/p-Si heterojunction diodes. *Applied Physics Letters*, 91(19), 2007.

[133] M. Kuttge, J. Garcia de Abajo, and A. Polman. Ultrasmall mode volume plasmonic nanodisk resonators. *Nano Letters*, 10:1537–1541, 2010.

[134] S.A. Mayer. *Plasmonics: Fundamentals and Applications*. Springer, 2007.

[135] Kenneth Diest, Jennifer A. Dionne, Merrielle Spain, and Harry A. Atwater. Tunable color filters based on metal-insulator-metal resonators. *Nano Letters*, 9(7):2579–2583, 2009.

[136] L. Novotny and N. v. Hulst. Antennas for light. *Nature photonics*, 5:83–90, 2011.

[137] A. Cattoni et al. $\lambda^3/1000$ plasmonic nanocavities for biosensing fabricated by soft UV nanoimprint lithography. *Nano Letters*, 11:3557, 2011.

[138] U. Fano. Effects of configuration interaction on intensities and phase shifts. *Physical Review*, 124, 1961.

[139] D. Duche, P. Torchio, L. Escoubas, F. Monestier, J.-J Simon, F. Flory, and G. Mathian. Improving light absorption in organic solar cells by plasmonic contribution. *Solar Energy Materials and Solar Cells*, 93:1377–1382, 2009.

[140] M.A. Green and S. Pillai. Harnessing plasmonics for solar cells. *Nature Photonics*, 6(3):130–132, 2012.

[141] P.F. Robusto and R. Braunstein. Optical measurements of the surface plasmon of indium-tin oxide. *Phys. Status Solidi A - Appl. Res.*, 119:155 – 168, 1990.

[142] M. Hiramatsu, K. Imaeda, N. Horio, and M. Nawata. Transparent conducting ZnO thin films prepared by XeCl excimer laser ablation. *J. Vac. Sci. Technol. A*, 16:669–673, 1998.

[143] J M Pitarke, V M Silkin, E V Chulkov, and P M Echenique. Theory of surface plasmons and surface-plasmon polaritons. *Reports on Progress in Physics*, 70(1):1, 2007.

[144] P.R. West, S. Ishii, G. Naik, N. Emani, V.M. Shalaev, and A. Boltasseva. Searching for better plasmonic materials. *Laser Photonics Rev.*, 4(6):795–808, 2010.

[145] J.-L. Pelouard, F. Proise, M. Paire, J.F. Guillemoles, and D. Lincot. Composant photovoltaïque à fort rendement de conversion, 2012.

[146] H.C. Casey and E. Buehler. Evidence for low surface recombination velocity on n-type inp. *Applied Physics Letters*, 30:247–249, 1977.

[147] C. Koechlin, P. Bouchon, F. Pardo, J.-L. Pelouard, and R. Haidar. Analytical description of subwavelength plasmonic mim resonators and of their combination. *Optics Express*, 21(6):7025–7032, 2013.

[148] G. Wallis and D.I. Pomerantz. Field assisted glass-metal sealing. *Journal of Applied Physics*, 40:3946–3949, 1969.

[149] A.-M.Goncalves, N. Mezailles, C. Mathieu, P. Le Floch, and A. Etcheberry. Fully protective yet functionalizable monolayer on InP. *Chem. Mater.*, 22:3114–3120, 2010.

[150] A.-M. Gonçalves, O. Seitz, C. Mathieu, M. Herlem, and A. Etcheberry. First evidence of stable P–N bonds after anodic treatment of InP in liquid ammonia: A new III–V material passivation route. *Electrochem. Comm.*, 10/2:225, 2007.

[151] C. Njel, A-M. Goncalves, D. Aureau, D. Mercier, and A. Etcheberry. Evidence of phosphazene steps formation on InP by cyclic voltammetry studies and XPS analyses in liquid ammonia (-55°C). *ECS Trans.*, 53(6):93–98, 2013.

[152] A-M. Goncalves, C. Mathieu, M. Herlem, and A. Etcheberry. The pH response of the InP/ liquid ammonia interface at 223K: A pure nernstian behaviour. *Electrochimica Acta*, 55:7413–7418, 2010.

[153] A-M. Goncalves et al. An ARXPS study of the passivating layer formed on III-V surface by an innovative anodic treatment in liquid ammonia. *Surface and Interface Analysis*, 42:775–778, 2010.

[154] A.-M. Goncalves. *Influence des protons dans le mécanisme de réduction de l'oxygène sur électrodes semiconductrices III-V dans l'ammoniac liquide*. PhD thesis, Université Versailles Saint-Quentin, 1997.

[155] A.-M. Goncalves, C. Njel, C. Mathieu, D. Aureau, and A. Etcheberry. Phosphazene like film formation on inP in liquid ammonia (223 K). *Thin Solid Films*, 538:21–24, 2013.

[156] B. Portier, F. Pardo, P. Bouchon, R. Haïdar, and J.L. Pelouard. Fast modal method for crossed grating computation, combining finite formulation of Maxwell equations with polynomial approximated constitutive relations. *J. Opt. Soc. Am. A*, 30:573–581, 2013.

Appendix

A Cosine weighted hemisphere sampling

By definition a lambertian surface reflects equally into all directions. It requires a cosine distribution and as a consequence the lambertian reflector probability density function $pdf(\theta\varphi) = \frac{\cos\theta\sin\theta}{\pi}$. From $pdf(\theta\varphi)$ one can derive the marginal density function $pdf(\theta)$ and the conditional density function $pdf(\varphi \mid \theta) = \frac{pdf(\theta\varphi)}{pdf(\theta)}$. In our case it comes:

$$\begin{cases} pdf(\theta) & = & \displaystyle\int_0^{2\pi} \frac{\cos\theta}{\pi}\sin\theta d\varphi & = & 2\cos\theta\sin\theta \\ pdf(\varphi \mid \theta) & = & \dfrac{\cos\theta\sin\theta/\pi}{2\cos\theta\sin\theta} & = & \dfrac{1}{2\pi} \end{cases}$$

The cumulative distribution functions $cdf = \displaystyle\int_0^{\theta \text{ or } \varphi} pdf$, to whom ξ can be compared, can be derived:

$$\begin{cases} cdf(\theta) & = & \displaystyle 2\int_0^{\theta} \cos\theta'\sin\theta' d\theta' & = & 1-\cos^2\theta \\ cdf(\varphi \mid \theta) & = & \dfrac{\varphi}{2\pi} \end{cases}$$

The only thing left is inverse the last two equations which finally ends up with:

$$\begin{cases} \theta & = & \text{acos}(\sqrt{\xi_1}) \\ \varphi & = & 2\pi\xi_2 \end{cases}$$

B Other comparisons between numerical and semi-analytical loss channels

An opal is used as PBS (see fig. 3.17)

C Lithography

C.1 Photo-lithography

Photolithography is a patterning technique based on the use of the photosensitive resist. It enables to obtain patterning with resolution limited by the light wavelength. In classical lithography UV light around 350 nm (opposed to deep UV lithography), resolution of 1 μm is commonly achieved. Basically, a part of the resist is exposed to UV light whereas the remaining

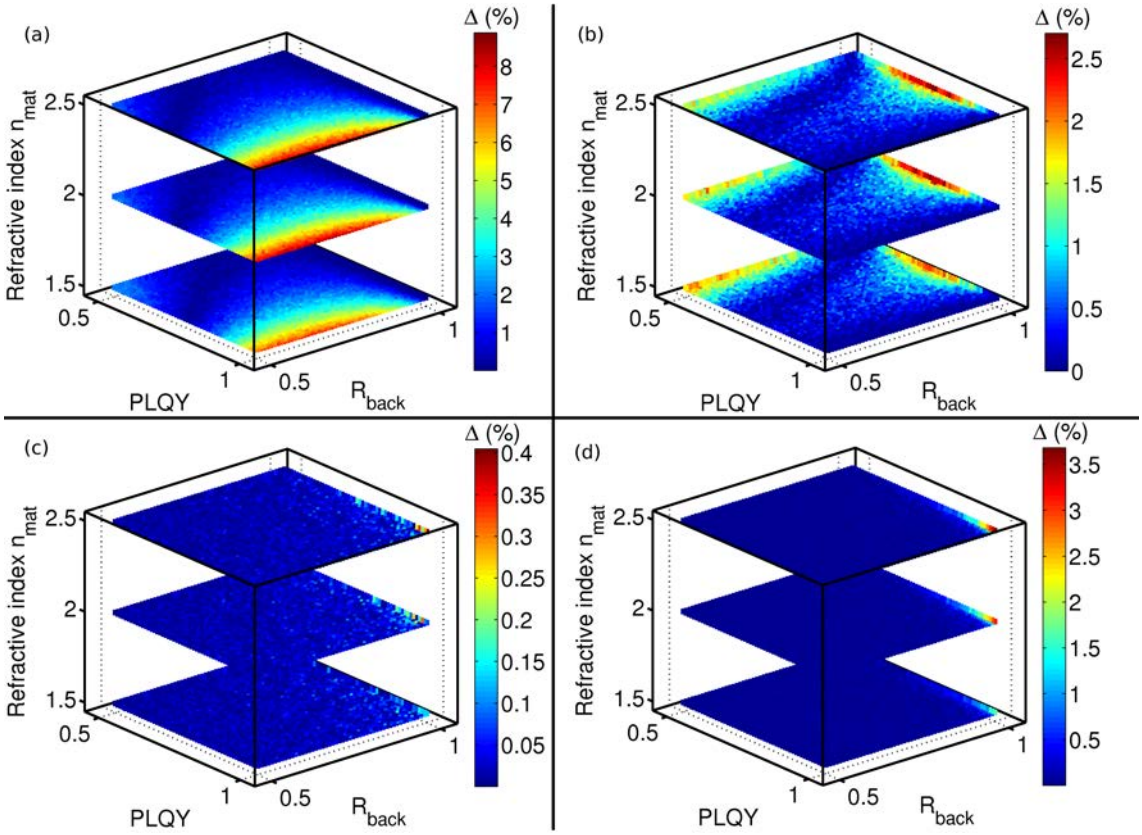

Figure 14: Comparison between numerical and semi-analytical loss channels derivations with PBS and at $C_{geo} = 100$. Colormap is in absolute percentage ($\Delta = |\mathcal{L}^{num} - \mathcal{L}^{ana}|$). (a) $\mathcal{L}_{back}$, (b) $\mathcal{L}_{QY}$, (c) $\mathcal{L}_{mat}$, (a) $\mathcal{G}_{coll}$.

part is shaded. It creates a solubility difference in a developer mixture, which allows the partial removal of the most soluble part. They are two kinds of photoresists: positive and negative and each resist comprises a photoactive compound (diazonaphtlhoquinone-sulphonates for AZ® resist) and a solvent (micture of phenol and formaldehyde for AZ® resist). Positive (negative) resists get more (less) soluble respectively in the developer after light exposure (fig. 17):

Spin-coating: The first step is to deposit homogeneously the resist. This is done by spin-coating. The main parameters to obtain the desired resist thickness is time, speed and acceleration.

Soft-bake: After coating, the resist film contains a remaining solvent concentration. The softbake reduces the remaining solvent content in order to:

- Avoid mask contamination and/or sticking to the mask
- Prevent popping or foaming of the resist by N_2 created during exposure
- Improve resist adhesion to the substrate

Soft-bake temperature is typically around 100 and 130 °C.

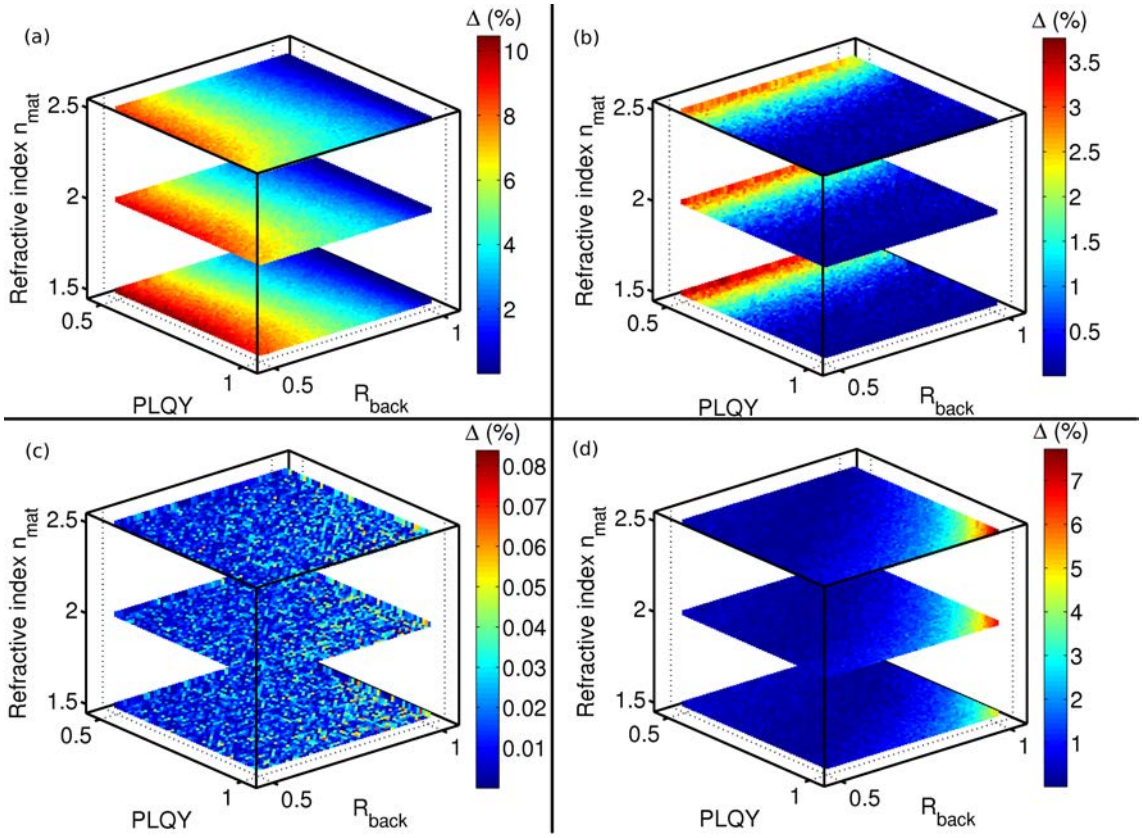

Figure 15: Comparison between numerical and semi-analytical loss channels derivations without PBS and at $C_{geo} = 5$. Colormap is in absolute percentage ($\Delta = |\mathcal{L}^{num} - \mathcal{L}^{ana}|$). (a) $\mathcal{L}_{back}$, (b) $\mathcal{L}_{QY}$, (c) $\mathcal{L}_{mat}$, (a) $\mathcal{G}_{coll}$.

Exposure: Exposure enables to activate the photoactive compound. The duration, light wavelength and mask / resist gap are of great importance. Light wavelength and duration rules the photoactive compound activation whereas resist / mask gap and light wavelength rules the resolution ($= \sqrt{\lambda \times gap}$).

Post exposure bake: Post exposure baking is required only for negative resist. It is essential for the cross-linking mechanism initiated during the exposure. Post-exposure bake temperature is typically around 100 and 130 °C.

Development: Developer selectively etches the most soluble part of the resist. The developer optimal concentration enables to have the better trade-off between etching rate and selectivity.

C.2 Electron-beam lithography

Electron beam lithography (or e-beam lithography) is based on the same principle than photolithography. The main difference is that this time electrons are used instead of photons, which greatly improves the resolution. Resolution up to few tens of nanometers can be routinely achieved. Resolution limits being mainly due to charge scattering in the resist. A side effect of this technique is the time consumption. While all the mask is lighted in photolithography, the electron canon must move for each pixel, which greatly enhanced the lithography duration, which can exceed hours, according the size of the patterning.

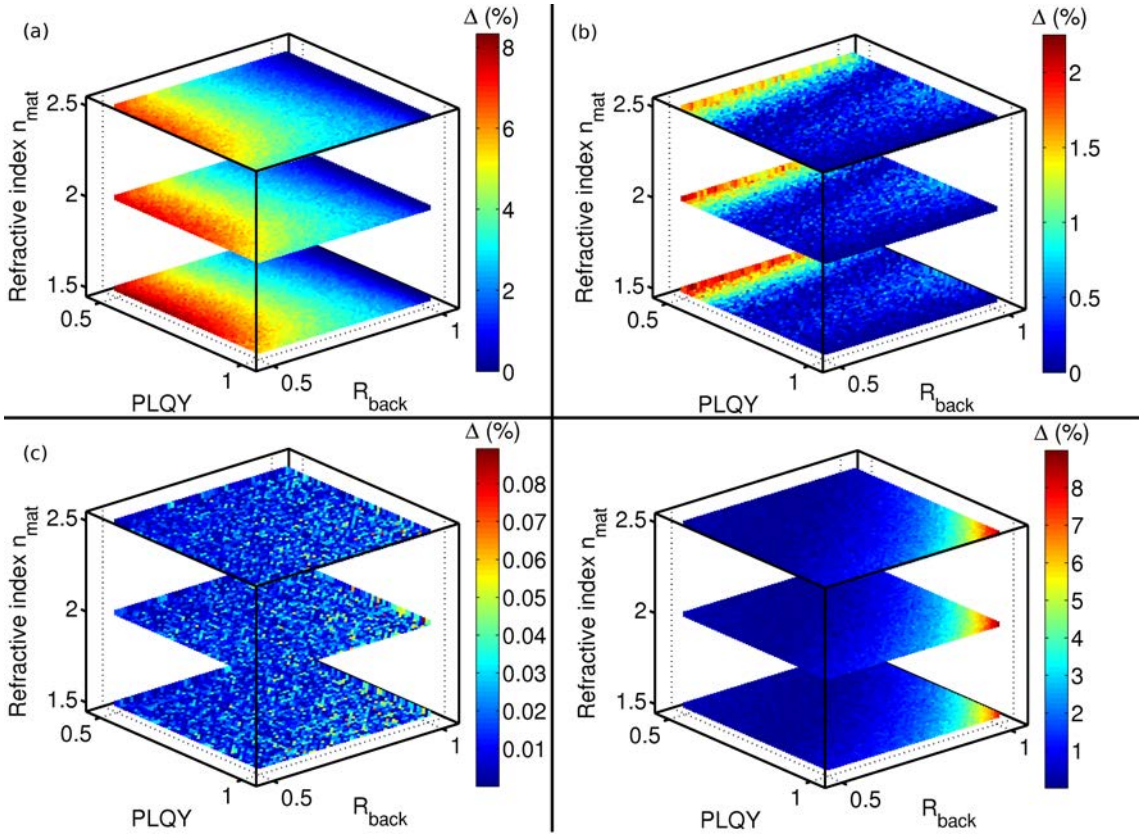

Figure 16: Comparison between numerical and semi-analytical loss channels derivations with PBS and at $C_{geo} = 5$. Colormap is in absolute percentage ($\Delta = |\mathcal{L}^{num} - \mathcal{L}^{ana}|$). (a) $\mathcal{L}_{back}$, (b) $\mathcal{L}_{QY}$, (c) $\mathcal{L}_{mat}$, (a) $\mathcal{G}_{coll.}$

Some additional concerns must be addressed before performing the lithgraphy, such as setting the electron dose (in $\mu C.cm^{-2}$) or take care about charge evacuation.

D Fabry-Perot correction induced by thin top metal layer

The stack semiconductor/Metal/external medium (PMMA or air) and the different reflection/propagation/transmission coefficient can be depicted as follows:

The global reflection coefficient is:

$$R_{top} = r_{dmd} + ((... + \overbrace{t_{dm}).p_m.r_{mam}.p_m.t_{md}.r_{mdm}}^{red\ loop} + \underbrace{t_{dm}).\overbrace{p_m.r_{mam}.p_m.t_{md}}^{red\ loop}}_{blue\ loop}$$

The "..."is a serie which leads to:

$$R_{top} = r_{dmd} + t_{dm}.\frac{1}{1 - p_m.r_{mam}.p_m.r_{mdm}}.p_m.r_{mam}.p_m.t_{md}$$

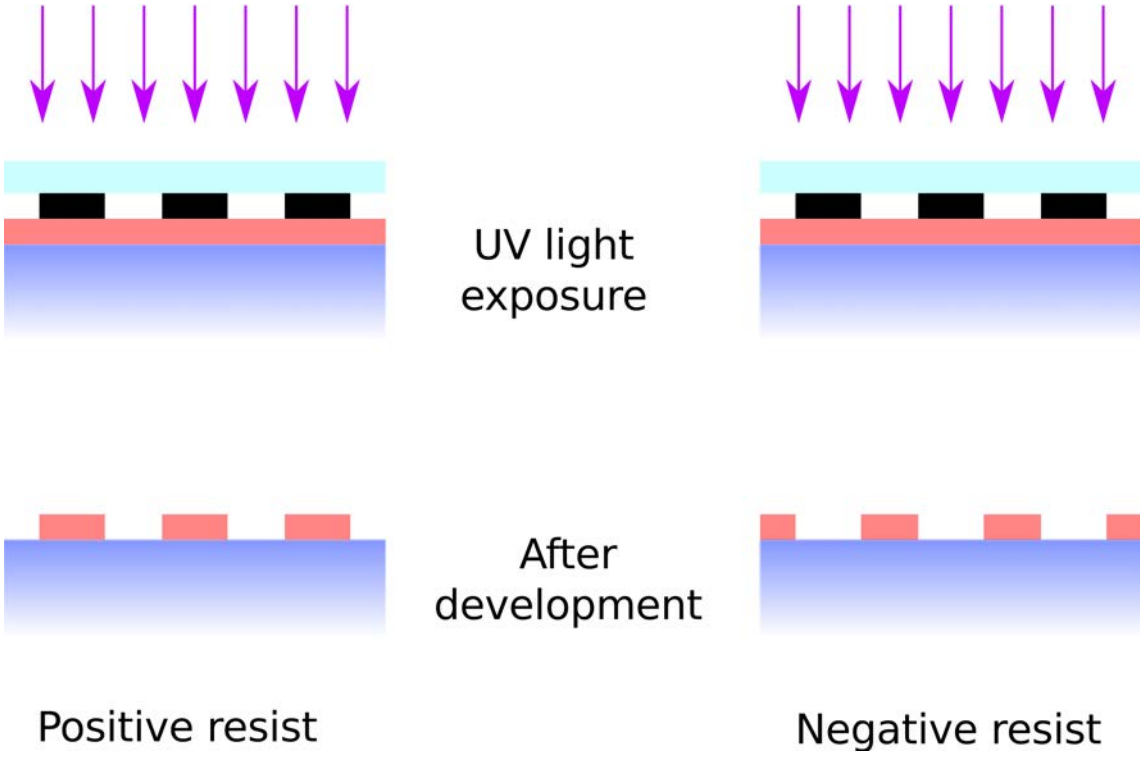

Figure 17: Illustration of positive (left) and negative resist (right). Dark blue represents the subtrate, red the resist. Positive resist forms the image of the mask whereas negative forms the negative image of the mask.

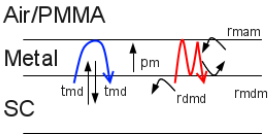

Figure 18: Schematic of the top part of resonator. r_{xyx}: reflection from medium x by the medium y (bounced back in x). Transmission coefficient t_{yx}: transmission from medium x to y. p_x: propagation in medium x. m is for metal, d for dielectric (semiconductor)

Knowing that $r_{mam} = \frac{n_m - n_a}{n_m + n_a}$, $r_{mdm} = \frac{n_m - n_d}{n_m + n_d} = -r_{dmd}$, $t_{md} = 1 + r_{dmd}$, $p_m = exp(i.\frac{2\pi}{\lambda} h_m.n_m)$, the global reflection can be written only as a function of material parameters (n_x is the complex refractive index of the medium x (d for semiconductor, m for metal, a for air or PMMA), h_m is the metal thickness)

E Ag/ZnO:Al stack reflection coefficient

F RMCA description

F.1 Prerequisites

We use a Cartesian coordinate system (z corresponds to vertical direction, x and y to lateral directions). Incident light is considered monochromatic. For sake of simplicity, we consider structures semi-infinite in the y-direction. This limitation can be overcome [156] but the code I used was running only in 2D. The structure is periDIc along the x-axis. Almost all the following

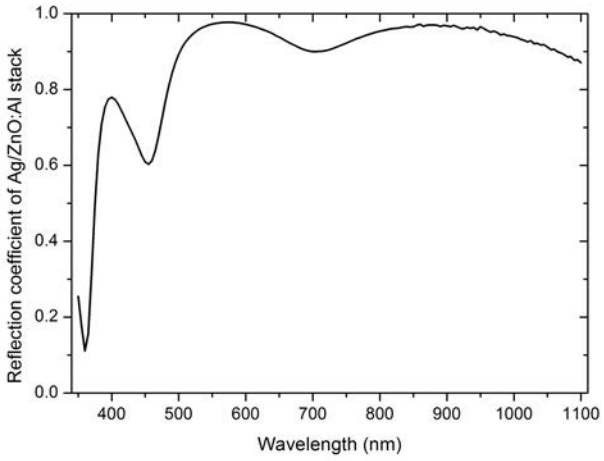

Figure 19: Reflection coefficient of a Ag:ZnO:Al measured by a Perkin Elmer lambda 900

presentation does not require this extra hypothesis, we will emphasize when necessary on the need of this periDIc condition. The structure we want to model is anisotropic and consists in different superposed layers (along the z direction). Each layer may comprise different materials (along the x direction).

Thus, in a given layer, the sample is invariant along the z direction. We use this property to describe electromagnetic fields as a superposition of modes, which makes RMCA a modal method.

F.2 Assess electromagnetic fields: RM in RMCA

The first step is to derive electromagnetic fields in one layer. To do so, we use the invariance property in the z-direction to describe an electromagnetic field F as a superposition of modes such as:

$$F(x) = \sum_j \left(a_j^+ f_j^+(x) e^{i.(k_z^{(j)}.z - \omega.t)} + a_j^- f_j^-(x) e^{-i.(k_z^{(j)}.z + \omega.t)} \right) \tag{3}$$

Equation (3) states that one mode is a combination of two plane waves propagating in both directions along the z-axis. Our problem is to derive these modes. We begin with the discrete Maxwell equations which are totally rigorous (no approximation at this stage).

$$\text{First group} \begin{cases} \nabla \cdot \mathbf{B} = 0 \\ \partial_t \mathbf{B} + \nabla \times \mathbf{E} = 0 \end{cases} \qquad \text{Second group} \begin{cases} \nabla \cdot \mathbf{D} = \rho = 0 \\ -\partial_t \mathbf{D} + \nabla \times \mathbf{H} = \mathbf{j} = 0 \end{cases} \tag{4}$$

B and E are the magnetic and electric fields (respectively) whereas H and D are respectively the magnetizing and displacement fields. ρ is the free charge density and $\mathbf{j}$ the free current density. These two physical quantities worth zero in our case.

The following concerns only the TM polarization. In TM, we focus on non zero fields components which are B_y, H_y, D_x, D_z, E_x, E_z. Note that in TE polarization, one has only to permute x and y.

All TM fields can be expressed as sums of functions $f(x).e^{ik_z.z-i\omega t}$, therefore the second equation of the second group (eq. (4)) gives:

$$i\omega D_x - iH_y k_z = 0 \tag{5a}$$

$$i\omega D_z - \partial_x H_y = 0 \tag{5b}$$

Equation (5)a enables to link D_x with H_y:

$$D_x = H_y \frac{k_z}{\omega} \tag{6}$$

The z component of $\mathbf{D}$ is given by eq. (5)b. Yet $\partial_x H_y$ is unknown, so an integration along a segment $[x_p - x_{p+1}]$ is needed:

$$i\omega \int_{x_p}^{x_{p+1}} D_z + \Delta H_y = 0 \tag{7}$$

Dividing by the segment length l, we finally obtain:

$$i\omega \langle D_z \rangle + \frac{1}{l}\Delta H_y = 0 \tag{8}$$

The second equation of the first group in 4 gives the third relation, after integration along a segment $[x_p - x_{p+1}]$:

$$\langle B_y \rangle - \langle E_x \rangle \frac{k_z}{\omega} = \frac{i}{\omega l}\Delta E_z \tag{9}$$

At this point our three equations include 3 mean field components on a segment : $\langle B_y \rangle$, $\langle E_x \rangle$ and $\langle D_z \rangle$, 3 sampled field components : D_x, H_y and E_z and the exact difference operator Δ. No approximation has been done to derive these relations. We may represent these three equations (eq. (6) and eq. (8) for group 2, eq. (9) for group 1 graphically):

It is worth noting that the mesh used for group 1 equation is not necessarily the same as for group 2 equations. We can easily define two others groups for TE with non zero field components. It should be noted that TE and TM group are totally independent and can be treated as such. The next step is to link the two groups, which means link:

- $\langle E_x \rangle \leftrightarrow D_x$
- $\langle B_y \rangle \leftrightarrow H_y$
- $\langle D_z \rangle \leftrightarrow E_z$

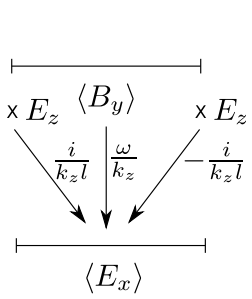

(a) Group 1

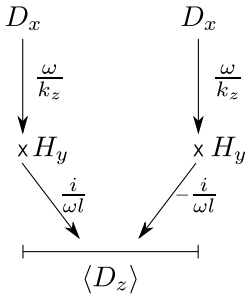

(b) Group 2

Figure 20: Graphical representation of the three equations derived from Maxwell equations

F.3 Assess electromagnetic fields: CA in RMCA

To link the two groups of equations, we use the constitutive equations:

$$\begin{cases} \dfrac{1}{\mu_0} B_y(x) = \mu_0 H_y(x) \\ \mu_0 c^2 D_x(x) = \epsilon_x(x) E_x(x) \\ \mu_0 c^2 D_z(x) = \epsilon_z(x) E_z(x) \end{cases} \tag{10}$$

Sadly field components expressions in constitutive equations are discrete values, whereas we need $\langle B_y \rangle$, $\langle E_x \rangle$ and $\langle D_z \rangle$. Consequently we need to do some approximations. We use an approximation which can be either simplistic or polynomial.

Simplistic approximation:

$$\begin{cases} \langle B_y \rangle \approx \mu_0 H_y \\ \langle E_x \rangle \approx \dfrac{\mu_0 c^2}{\epsilon} D_x \\ \langle E_z \rangle \approx \dfrac{\mu_0 c^2}{\epsilon} D_z \end{cases} \tag{11}$$

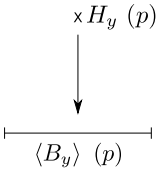

Figure 21: Graphical scheme of the simplistic approximation

In the simplistic approximation, we use only one value of H_y, D_x and D_z to approximate $\langle B_y \rangle$, $\langle E_x \rangle$ and $\langle E_z \rangle$ respectively. It is graphically depicted in fig. 21 for H_y and $\langle B_y \rangle$.

These polynoms are continuous at ϵ discontinuities. Code performance being mainly due to a proper description of epsilon discontinuities, using continuous polynoms is a great advantage.

Finally, the coupling between the two groups through constitutive approximations has been achieved, which is depicted in fig. 23:

The polynomial approximation evaluates H_y, D_x and E_z by a n degree polynom.

$$\begin{cases} H_y = \pi_y(x) \\ D_x = \pi_x(x) \\ E_z = \pi_z(x) \end{cases} \tag{12}$$

We use $n+1$ values of H_y, D_x and D_z to approximate $\langle B_y \rangle$, $\langle E_x \rangle$ and $\langle E_z \rangle$ respectively. It is depicted on the right for H_y and $\langle B_y \rangle$ and n=4 (yet all calculations have been done with n=13).

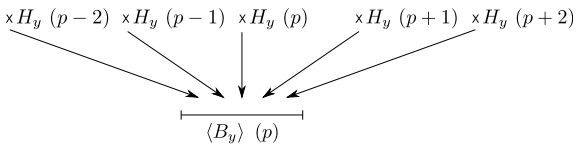

Figure 22: Graphical scheme of the polynomial approximation with $P = 4$. The scale is not exactly respected: the distance between two crosses must be the same that the segment $\langle B_y \rangle (p)$.

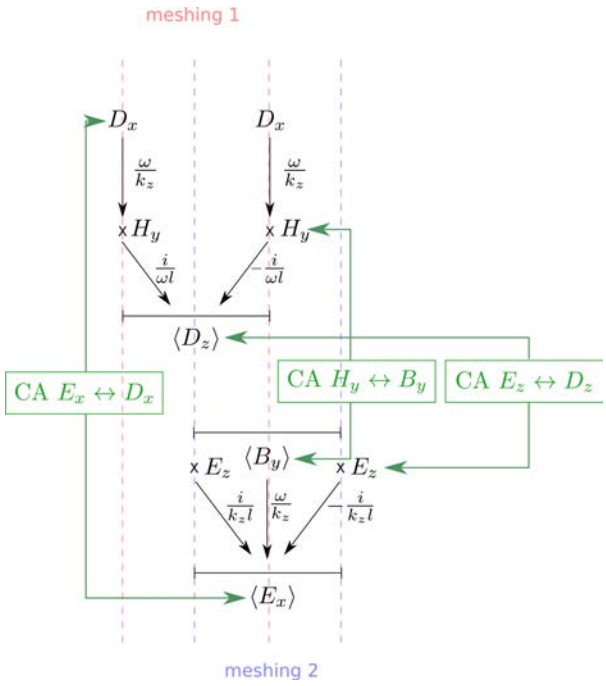

Figure 23: Rigorous Maxwell equations linked with Constitutive Approximation graphical illustration in the case of simplistic approximation. The clever way to mesh the structure is to shift one group mesh of half a segment length from the other group meshing

Constitutive equations can be written using matrices:

$$\begin{cases} [\![\frac{\langle E_x \rangle}{\mu_0 c^2}]\!] = [\![CA_x]\!][\![D_x]\!] \\ [\![\frac{\langle B_y \rangle}{\mu_0}]\!] = [\![CA_y]\!][\![H_y]\!] \\ [\![\frac{\langle E_z \rangle}{\mu_0 c^2}]\!] = [\![CA_z]\!][\![D_z]\!] \end{cases} \tag{13}$$

For a 4 degree polynom :$\pi(x) = \pi_0 + \pi_1 x + \pi_2 x^2 + \pi_3 x^3 + \pi_4 x^4$, we have the following matrix equation to evaluate $\langle B_y \rangle$ from H_y:

$$\begin{pmatrix} 1 & x_{-2} & x_{-2}^2 & x_{-2}^3 & x_{-2}^4 \\ 1 & x_{-1} & x_{-1}^2 & x_{-1}^3 & x_{-1}^4 \\ 1 & x_0 & x_0^2 & x_0^3 & x_0^4 \\ 1 & x_1 & x_1^2 & x_1^3 & x_1^4 \\ 1 & x_2 & x_2^2 & x_2^3 & x_2^4 \end{pmatrix} \times \begin{pmatrix} \pi_0 \\ \pi_1 \\ \pi_2 \\ \pi_3 \\ \pi_4 \end{pmatrix} = \begin{pmatrix} H_{(y,-2)} \\ H_{(y,-1)} \\ H_{(y,0)} \\ H_{(y,1)} \\ H_{(y,2)} \end{pmatrix}$$

Left matrix is known and depends only on the mesh. This matrix is inverted to find polynom coefficients. Mixing everything together, we end up with a secular equation with the unknown field component $[\![H_y]\!]$ only:

$$\left([\![CA_y]\!] + [\![\frac{c}{\omega l_1}]\!][\![\Delta]\!][\![CA_z]\!][\![\frac{c}{\omega l_2}]\!][\![\Delta]\!] \right) [\![H_y]\!] = \frac{k_z c}{\omega}^2 [\![CA_x]\!][\![H_y]\!] \tag{14}$$

This is an eigenvalue equation which can be solved optimally since matrices involved are sparse (contrary to Fourier Modal Method). At this point this is an infinite equation. Yet, the system is pseudo-periDIc ie. $f(x+d) = e^{i.\frac{2\pi}{\lambda_0}.sin(\theta).d}.f(x)$. A sparse matrix $[\![\Pi]\!]$ taking into account the pseudo-periDIcity is added in the secular equation to make this equation finite:

$$\left([\![CA_y]\!] + [\![\frac{c}{\omega l_1}]\!][\![\Delta]\!][\![CA_z]\!][\![\frac{c}{\omega l_2}]\!][\![\Delta]\!] \right) [\![\Pi]\!][\![H_y]\!] = \frac{k_z c}{\omega}^2 [\![CA_x]\!][\![\Pi]\!][\![H_y]\!] \tag{15}$$

For a N points mesh, we have N eigenvalues $(k_z^{(m)})^2$ and N eigenvectors $H_y^{(m)}(p)$ with $m = 1...N$, each field mode is then a superposition of $\pm\, k_z^{(m)}$ modes. As an example for H_y:

$$H_y(x_p) = \sum_{m=1}^{N} H^{(m)}(p).\left(a_-^m.e^{-i.k_z^{(m)}.z - i\omega t} + a_+^m.e^{i.k_z^{(m)}.z - i\omega t} \right) \tag{16}$$

At this point we know all the optical mode components in each layer. All that is left is to take advantage of continuity relations to solve the entire problem.

F.4 S-matrix formalism

The field components E_x, H_y, D_z and B_z are continuous (in TM) at the interfaces between two layers which enables to use continuity relations. They are treated using S-matrix formalism . Notations we used are defined as follows: S_{AA}^{α} is the S-matrix associated to a reflection from layer A to layer A at the interface α and S_{BA}^{α} and is S-matrix of the transmission from layer A to layer B at the interface α and so on. These matrices individually are thanks to field continuity.

Everything is known, we finally use the classical S-matrix computation to assess global reflection coefficient, illustrated in fig. 24 for 3 layers A,B,C, with A and C semi-infinite. The bottom layer, C in this case, can often be considered as semi-infinite. In this thesis it will always be a metal, thick enough (ie. thicker than few skin depths) to be electromagnetically semi-infinite.

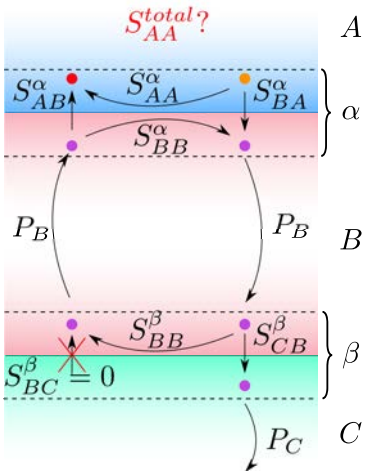

Figure 24: Feynman-like diagram of a 3 layers structure enabling to find the global reflection coefficient S_{AA}^{total} from elementary S-matrices. C being semi-infinite, there is no possibility to have a propagating wave going up from C to B.

Finding S_{AA}^{total} goes back to follow arrows, starting from the orange point to the red one. We obtain (must be read from right to left):

$$S_{AA}^{total} = S_{AA}^{\alpha} + \underbrace{S_{AB}^{\alpha} P_B S_{BB}^{\beta} P_B S_{BA}^{\alpha}}_{1loop} + \underbrace{S_{AB}^{\alpha} P_B S_{BB}^{\beta} P_B S_{BB}^{\alpha} P_B S_{BB}^{\beta} P_B S_{BA}^{\alpha}}_{2loops} + \cdots$$

$$S_{AA}^{total} = S_{AA}^{\alpha} + S_{AB}^{\alpha} \left(1 + P_B S_{BB}^{\beta} P_B S_{BB}^{\alpha} + \left(P_B S_{BB}^{\beta} P_B S_{BB}^{\alpha}\right)^2 + \cdots\right) P_B S_{BB}^{\beta} P_B S_{BA}^{\alpha}$$

$$S_{AA}^{total} = S_{AA}^{\alpha} + S_{AB}^{\alpha} \left(1 - P_B S_{BB}^{\beta} P_B S_{BB}^{\alpha}\right)^{-1} P_B S_{BB}^{\beta} P_B S_{BA}^{\alpha} \tag{17}$$

Finally, the entire problem is solved. The problem has been subdivided in horizontal regions (layer), eigen modes have been found using Maxwell and constitutive equations in each layer. Coupling between the different layers is done using continuity relations. Diffraction efficiency of the structure and total electromagnetic field are derived using the S-matrix formalism.

G Optical indexes

Silver (Ag)

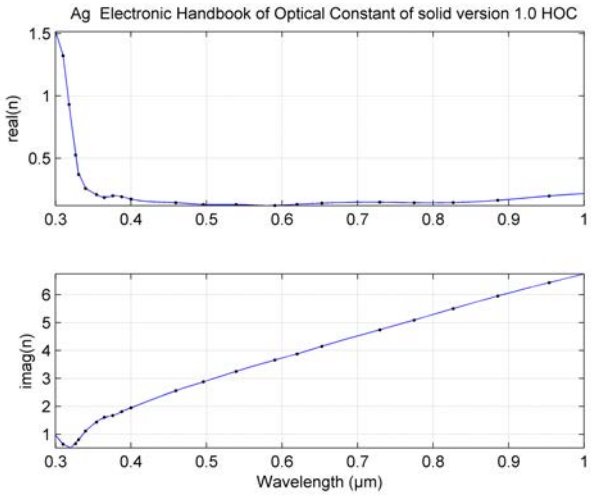

Figure 25: Optical constants of Ag

Gold (Au)

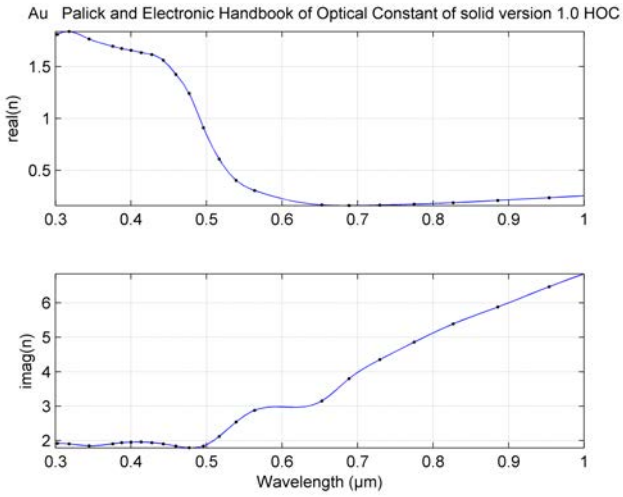

Figure 26: Optical constants of Au

Aluminium (Al)

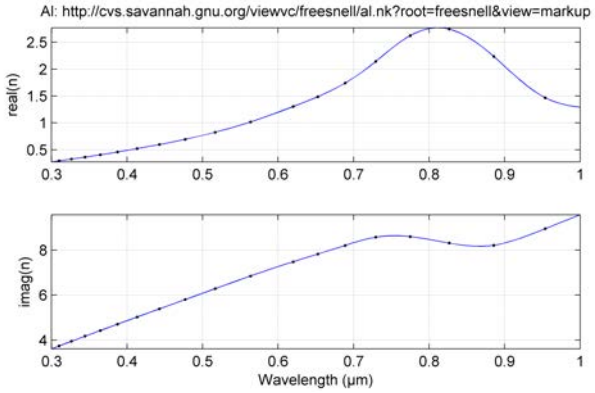

Figure 27: Optical constants of Al

Indium phosphide (InP)

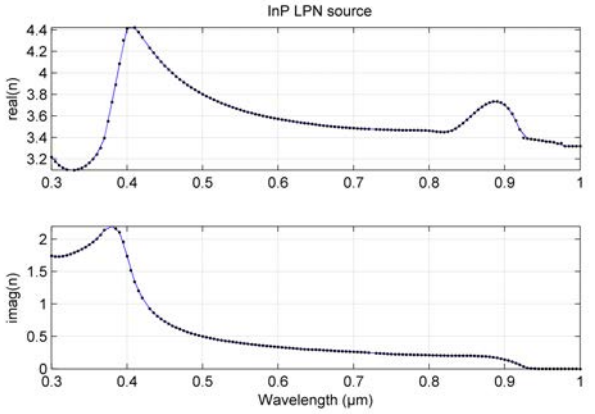

Figure 28: Optical constants of InP

InP-lattice matched Indium Gallium Arsenide (InGaAs)

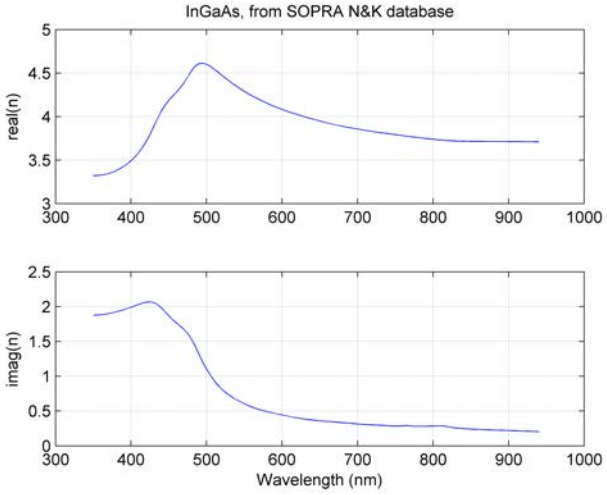

Figure 29: Optical constants of InGaAs

H Process fabrication of nano-resonator

H.1 pin junction reported on pyrex

Epitaxy is schemed on the figure on the right.
InP being crystaline, the epitaxy wafer is cleaved along the **natural** crystal axes [100] and [010]. The sample area is around 1 cm^2. InGaAs layer is a stop layer which will be usefull for the substrate removal.

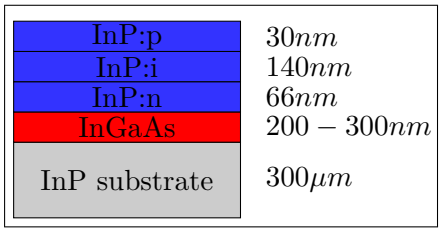

H.1.1 Deoxidation

Goal: Remove the native InP oxide
Method:

- Rinse in DI for 1'
- Sample in a mixture HCl/H_2O : 20/80 (volume) from a 37% HCl bottle (equivalent 2 M) for 2'
- Rinse in DI for 3'
- Dry with nitrogen gun (dry is always done by a nitrogen gun, therefore it will not be precised again throughout the rest of this manuscript)

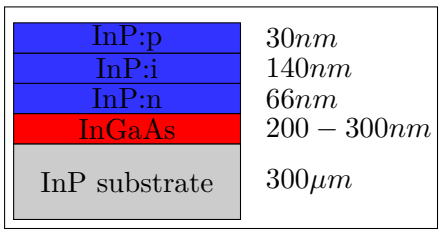

H.1.2 Front face metalization

Goal: Deposit the back mirror layer. Aluminium is required for the anodic bonding. Titanium is a buffer layer to avoid inter diffusion between aluminium and gold.
Method:

- Metalization with a Plassys MEB 550 SL evaporator. Thicknesses are (Al 200 nm / Ti 20 nm / Au 200 nm)

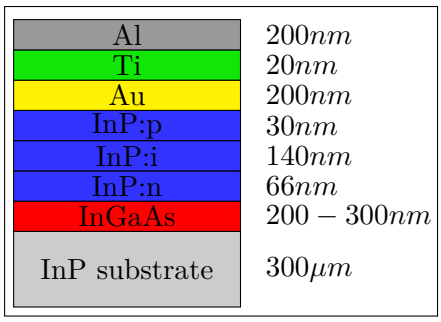

H.1.3 Front face protection

Goal: Protect the metalized face during the other process steps until the anodic bonding
Method:

- Resist AZ nLof 52-14 (microchemicals) Spin-coated (3000 rpm, 4000 rpm/s, 30")
- Annealing 127.5 °C for 1'

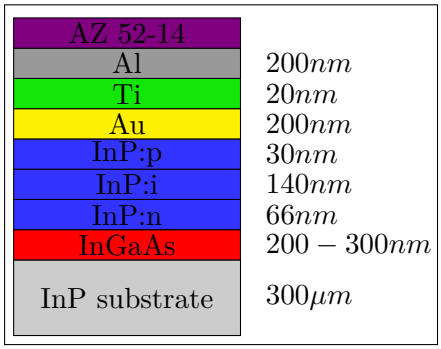

H.1.4 Back and side metalization

Goal: during the anDIc bonding there will be 1700 Volts between the front and back surface. To avoid damaging the pin junction, one has to metalize also the side and back part of the sample to avoid the current flowing in the pin.
Method: 200 nm Al with the Plassys MEB 550 SL evaporator.

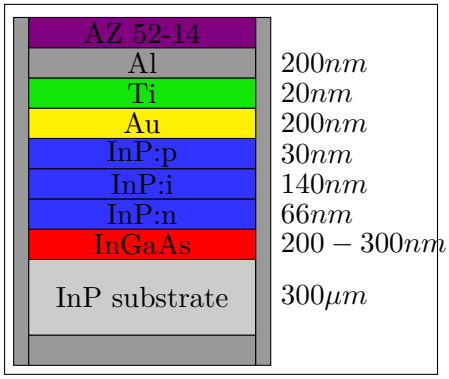

H.1.5 Pyrex and sample cleaning

Goal: Pyrex and sample surface must be extremely clean during the bonding.
Method:

- Remove the protective resist on the aluminium surface (see appendix H.1)
- Sample and pyrex in a mixture H_2SO_4/H_2O_2 (2:1 in weight) for 2'. (remove surface crystallographic defects, inclusion)
- Rinse in DI for 15'
- Organic rinse (under a laboratory fume hood **class 100**): sample and pyrex should be successively rinsed for 2' in:
  - Trichloroethylene at 90°C
  - Aceton
  - Isopropanol
- Dry

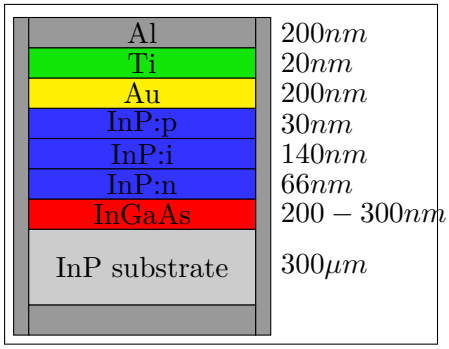

- Heat pyrex and sample at 90°C for 1' to be sure all the solvents have been evaporated

H.1.6 Anodic bonding

Goal: Bond the epitaxy on its new pyrex substrate
Method:

- Under a laboratory fume hood, put the epitaxy and pyrex samples between the two electrodes, as shown below:

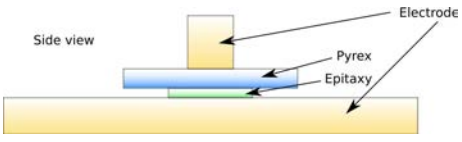

- Bring the samples and electrodes on the heating chuck at 210 °C.
- Apply 1700 Volt

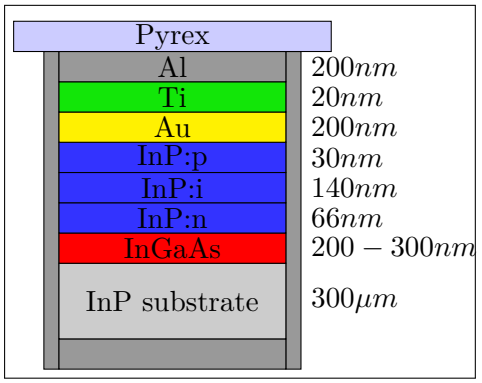

- Monitor the current
- In around 20', current must have been divided by 2. At this point, remove voltage a change electrode with a larger one. The same operation is repeated and a third largest electrode is used.
- Bonding is now finished.

H.2 pin junction strip

H.2.1 Wax deposition

Goal: Side "shielding" to protect pin junction from etching
Method:

- Wax heating at 80 °C
- Put wax on the pyrex close to the edges. Wax will cover semiconductor edges by capillary action without shading device area.
- Allow sample cooling to harden the wax

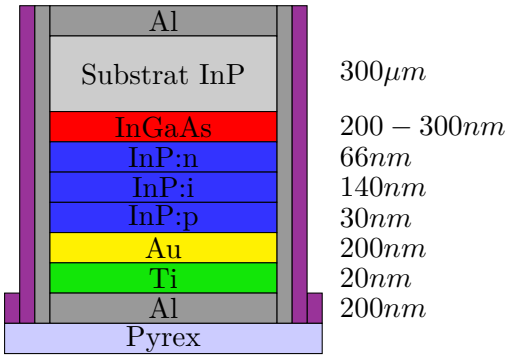

H.2.2 Al etching

Goal: Remove Aluminium
Method:

- Sample in NaOH (10g NaOH / 500 mL DI) for 4'
- Rinse in DI for 4' and dry

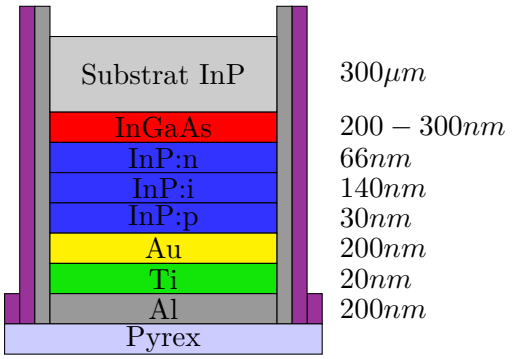

H.2.3 InP substrate etching

Goal: Remove InP substrate
Method:

- Sample in HCl (@ 37.5 %) until gassing stops (around 30')
- Rinse in ODI for 10' and dry

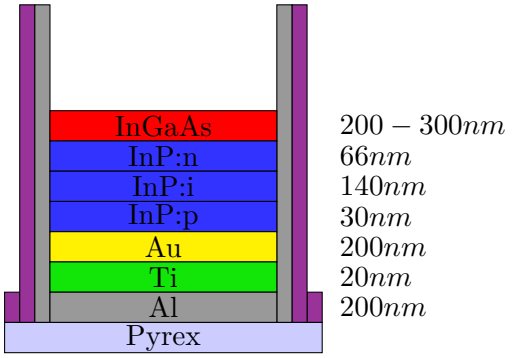

H.2.4 Stop layer etching

Goal: Remove InGaAs stop layer layer
Method:

- Mixture in a mixture H_3PO_4 : H_2O_2 : H_2O (3:1:40 in volume) for 1'
- Rinse 2' and dry

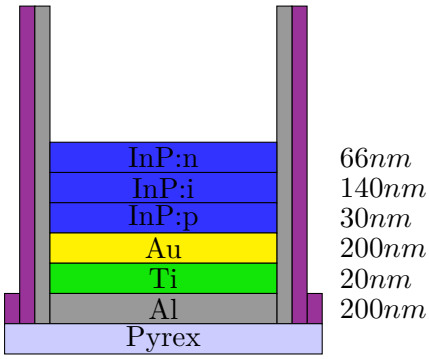

H.2.5 Wax removal

Goal: Substrate etching is finished, therefore wax can be removed
Method:

- Prepare 4 beakers, 2 with trichloroethylene at 80-90 °C, 1 aceton, 1 isopropanol
- Soak the sample in the first trichloroethylene beaker until was is not visible
- Soak in the second trichloroethylene beaker for 1'
- Soak in aceton for 2'
- Soak in isopropanol for 2' and dry

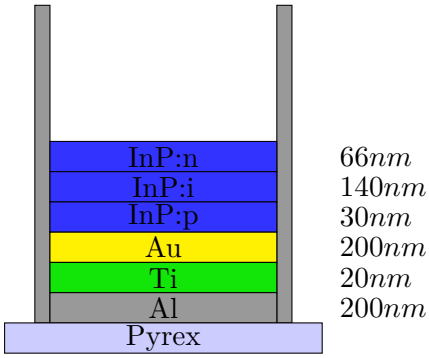

H.3 Remove InP "walls"

H.3.1 Front face covering with resist

Goal: Protect the front face
Method:

- AZ 52-14 spin-coating (see appendix H.1)

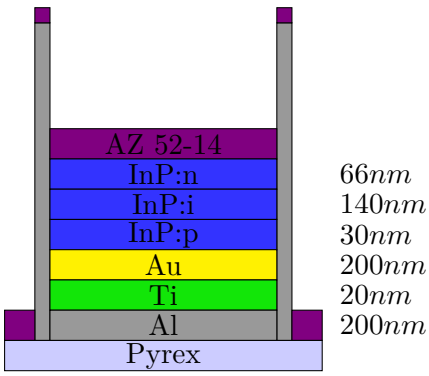

H.3.2 InP wall sawing

Goal: Remove InP walls. They arise because the chemical InP etching is isotropic, which leads to non etched crystallographic planes. Wall height is close to substrate thickness, which prevent lithography if they are not removed
Method:

- Wheel saw cutting
- The cut should enter the pyrex but not too deeply (see blue arrows). Here the aim is to disengage InP walls from the device to allow their removal in scratching.

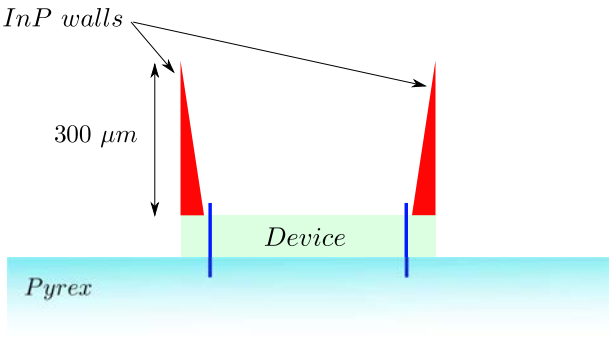

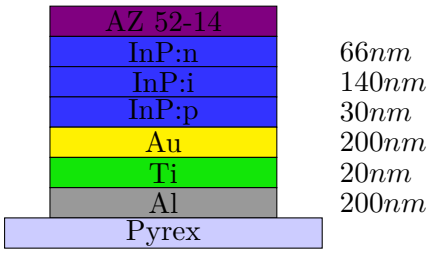

H.4 Sample alignment and charge extraction improvement

H.4.1 Resist removal

Goal: AZ 52-14 is not necessary
Method:

- Soak in aceton (see appendix H.1)

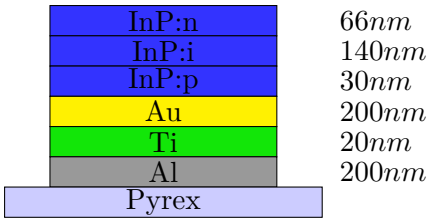

H.4.2 Optical lithography for sample opening

Goal: Cover the sample with resist except where the charge extraction will take place
Method:

- Resist AZ 52-14 spin-coated (2000 rpm, 4000 rpm/s, 30")
- Annealing 2'
- Optical lithography 5"
- Annealing at 128 °C for 2'
- Flood for 30"
- Development MIF 726 for 1'05"
- Post-baking 2' to remove solvent resist to promote resist adhesion

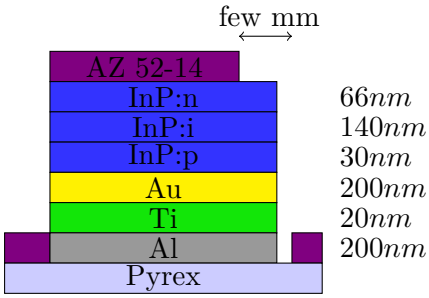

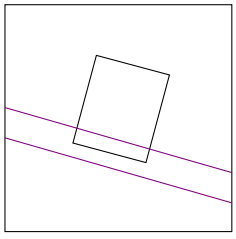

H.4.3 InP etching

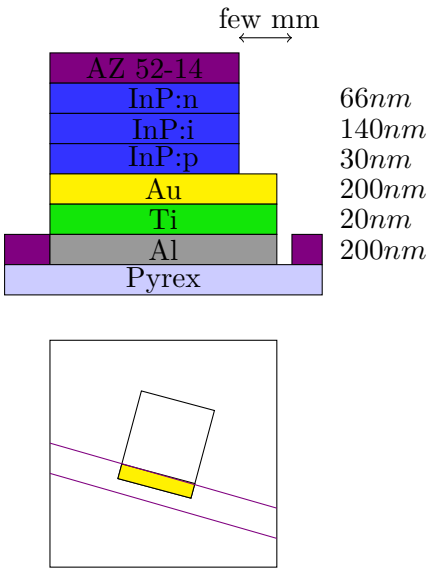

Goal: Strip semiconductor
Method:

- sample in a mixture H_3PO_4 : HCl (4:1 in volume) to remove HCl (30")
- Rinse in DI for 1' and dry

H.4.4 Metalization

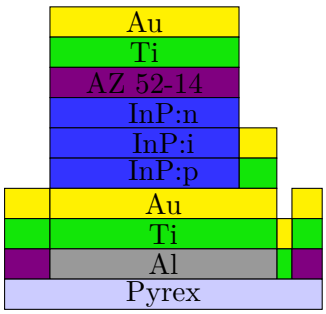

Goal: Create a gold line, parallel to the sample, in-between the active device and pyrex
Method:

- Metalization Ti/Au (300/3000 A)

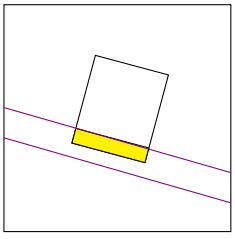

H.4.5 Lift-off

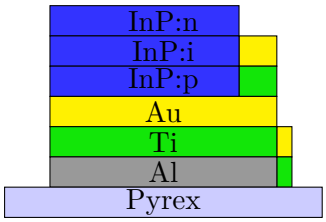

Goal: Resist removal
Method:

- Soak the sample in aceton (until resist is dissolved)

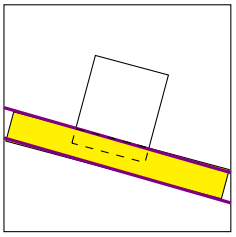

H.4.6 Pyrex side sawing

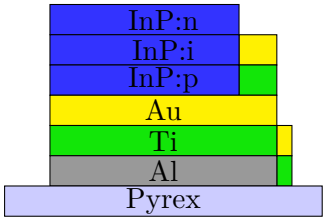

Goal: Cut a pyrex side to make the pyrex edge perfectly parralel to the active device, along the gold line
Method:

- Protect sample with AZ 52 14 (see appendix H.1)
- Sawing along the gold line
- Resist removal in aceton

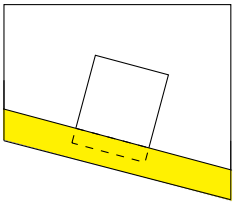

H.5 Nano structured front metal deposition

H.5.1 e-beam lithography resist spin coating

Goal: PMMA spin coating
Method:

- Spin-coating PMMA A5 (positive resist) (3000 rpm, 4000 rpm/s, 30")
- Annealing 30' at 160 °C

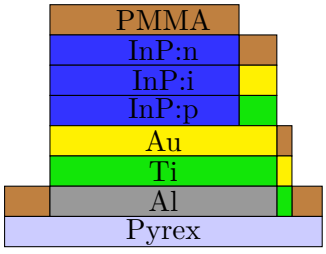

H.5.2 Al evaporation

Goal: Al deposition to increase surface reflection to ease e-beam lithography tracking
Method:

- Al evaporation, 50 nm at 1 nm.s^{-1}

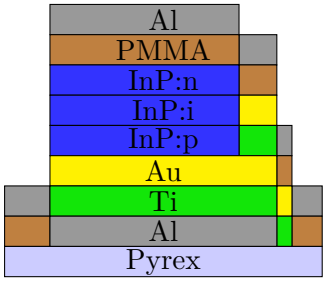

H.5.3 e-beam lithography

Goal: Create the nano-patterning
Method:

- e-beam lithography in itself is done by Nathalie Bardou.

Nota bene: In the next schemes, opening created to improve charge extraction is not represented anymore.

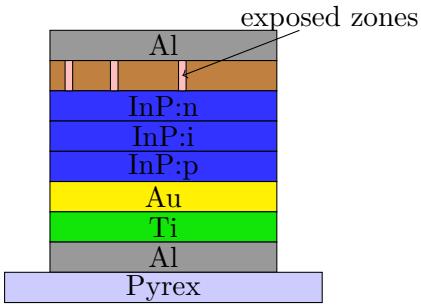

H.5.4 Aluminium removal

Goal: Remove aluminium
Method:

- Same than in appendix H.2

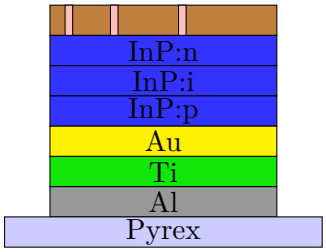

H.5.5 Development

Goal: Remove exposed resist
Method:

- Soak the sample in a mixture MIBK/isopropanol (150:50 in volume) for 1'
- Soak in isopropanol for 10", then dry immediatly

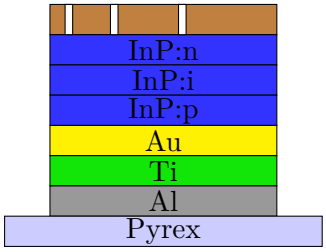

H.5.6 Oxygen Reactive Ion Etching

Goal: Remove residual resist
Method:

- Oxygen Plasma for 10"

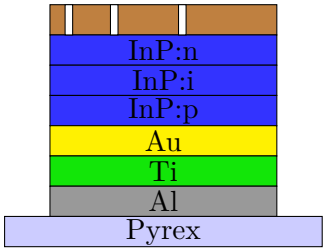

H.5.7 Deoxidation

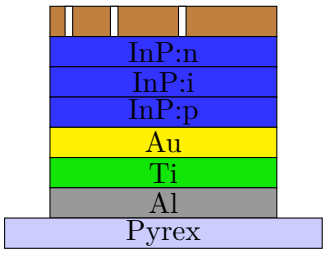

goal: Remove oxide deposited during Oxygen plasma
Method: See appendix H.1

H.5.8 Metalization

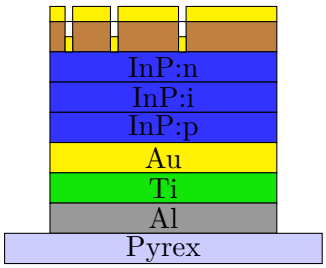

Goal: Create metal nano-patch
Method: See appendix H.1

- Evaporation Cr/Au, 20/400 Å

H.5.9 Lift-off

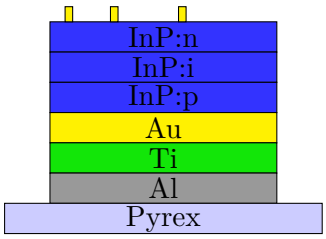

Goal: Remove unexposed PMMA
Method:

- Soak in trichloroethylene for 30' (minimum)
- Rinse in aceton, then dry

Résumé

Dans cette thèse nous évaluons la concentration optique sur cellules photovoltaïques micrométriques et nanométriques sans système de suivi de Soleil. Cette étude a deux objectifs principaux. La première partie est dédiée à l'évaluation de la faisabilité de la concentration optique sur des microcellules à base de Cu(In,Ga)Se2 via un concentrateur luminescent (LSC). Le LSC est bas-coût, concentre la lumière directe et diffuse, et est non imageant, ce qui très avantageux pour la concentration sur microcellules. Néanmoins, la sensibilité extrême aux non-idéalités explique la différence entre les performances théoriques et expérimentales. Un code de simulation est développé pour analyser ce système et ses mécanismes de perte. Un nouveau formalisme basé sur des données statistiques est proposé pour décrire les propriétés du LSC. Le couplage LSC/microcellules est effectué expérimentalement et des pistes d'amélioration explorées. La seconde partie tire profit de la fonction de conversion spectrale des LSC et développe un nouveau concept de nano-antenne photovoltaïque mono-résonant à base d'InP. Des simulations optiques montrent qu'un rendement de conversion de 10.7 % peut être atteint avec une épaisseur moyenne d'absorbeur de moins de 20 nm. Les étapes technologiques de fabrication sont identifiées et réalisées en salle blanche. Le fort ratio surface/volume nous a amené à étudier la passivation de l'InP par du polyphosphazène. Des mesures de luminescence montrent que la surface est stabilisée durablement. Les résultats de cette thèse démontrent que le couplage nano-photonique / LSC est prometteur, alliant de très faibles volumes à d'excellentes efficacités optiques.

Mots-clés: photovoltaïque, concentrateur luminescent, microcellule solaire, conversion spectrale, nano-photonique, piégeage de lumière

Abstract

In this thesis we explore light concentration on nano and micro photovoltaic cells without Sun tracking. This study has two main aims. The first part is dedicated to the evaluation of light concentration feasibility on Cu(In,Ga)Se2-based microcells with luminescent solar concentrator (LSC). LSC is cheap, allows both direct and diffuse light concentration and is non imaging, making it advantageous for microcells concentration. Yet, the extremely high sensitivity to non ideality explains the gap between theoretical and real systems. A simulation code is developed to analyze the system and its loss mechanisms. A new formalism based on statistical data is proposed to describe LSC properties. LSC and microcells coupling is experimentally achieved and improving tracks investigated. The second part takes advantage of the LSC down-shifting effect to propose a new mono-resonant InP-based photovoltaic nano-antenna. Optical modeling on this new device shows that 10.7 % efficiency can be obtained with an absorber averaged thickness lower than 20 nm. Technological process steps to fabricate this device are identified and realized in a clean-room environment. The high ratio surface over volume leads us to study InP passivation through a mono-atomic polyphosphazen film. Luminescent measurements show that passivated InP surface is long-term stabilized. The results of this thesis demonstrate that nano-photonic / LSC coupling is promising, enabling high optical efficiency in extremely low volume.

Keywords: photovoltaics, luminescent solar concentrator, micro solar cell, spectral conversion, nano-photonics, light trapping